Universität Stuttgart
Institut für Energieübertragung und Hochspannungstechnik, Band 33

Small-Signal Stability Modelling and Optimization of Microgrids

Small-Signal Stability Modelling and Optimization of Microgrids

Von der Fakultät
Informatik, Elektrotechnik und Informationstechnik
der Universität Stuttgart
zur Erlangung der Würde eines Doktor-Ingenieurs (Dr.-Ing.)
genehmigte Abhandlung

vorgelegt von
Simon Eberlein
aus Roth

Hauptberichter:	Prof. Dr.-Ing. K. Rudion
Mitberichter:	Prof. Dr.-Ing. D. Westermann
Tag der mündlichen Prüfung:	15.06.2021

Institut für Energieübertragung und Hochspannungstechnik
der Universität Stuttgart

2021

Bibliografische Information der Deutschen Nationalbibliothek:
Die Deutsche Nationalbibliothek verzeichnet diese Publikation in der Deutschen Nationalbibliografie, detaillierte bibliografische Daten sind im Internet über http://dnb.dnb.de abrufbar.

Universität Stuttgart
Institut für Energieübertragung und Hochspannungstechnik, Band 33

D 93 (Dissertation der Universität Stuttgart)

Small-Signal Stability Modelling and Optimization of Microgrids

Herstellung und Verlag: BoD - Books on Demand, Norderstedt
ISBN:

Abstract

The growing penetration of power systems with distributed energy resources entails new challenges for power systems. Microgrids are a model of future low inertia power systems due to the large share of distributed energy resources. This work focuses on the small-signal stability of islanded microgrids.

Modal analysis is selected as the most appropriate method to assess the stability of microgrids due to its enhanced flexibility compared to other approaches, such as impedance or Lyapunov's direct method. In addition, numeric simulations are carried out to evaluate the power sharing between distributed energy resources after disturbances, such as load fluctuations.

Models for inverters, diesel synchronous machines and wind turbines with doubly-fed induction generators with grid-forming and grid-supporting droop controllers are implemented. Regarding wind turbines, two methods of synthetic inertia, either based on the phase-locked loop or the frequency gradient, are considered. Microgrids are modelled in the $dq0$ reference frame to enhance the numerical efficiency without loosing accuracy and to establish stable operating points for linearization and modal analysis.

An evolutionary algorithm tailored to optimization problems with a computationally intensive fitness evaluation is proposed. A binary search partitioning tree is at the core of the evolutionary algorithm and is used to evaluate and promote the diversity of the population, which distinctly enhances the performance for various optimization problems. The optimization and simulation framework consisting of the evolutionary algorithm and the aforementioned microgrid models is one of the main contributions of this work.

The evolutionary algorithm is used to optimize the controller parameters in various scenarios, ranging from small microgrids with only a few nodes to large benchmark microgrids. The optimization is based on a thorough parameter sensitivity analysis in order to identify all influential controller parameters. A large set of controller parameters is then optimized simultaneously.

It is shown that microgrids dominated by grid-forming inverters are very stable systems when well-designed and optimized controllers are used. In particular, the implementation of a virtual impedance is crucial for the stability. The impact of droop control variants and extensions found in literature, such as the transient or frame transformation

droop, is small in comparison. Microgrids with grid-supporting inverters are less stable and their dynamics mainly depend on the tuning of the phase-locked loop. Furthermore, the share of synchronous machines in the microgrid has a strong influence on the stability and the optimized values of the controller parameters. Moreover, it is shown that the synthetic inertia methods for wind turbines are compatible with the droop control and can enhance the stability of microgrids, especially when the methods are combined.

Model order reduction approaches are reviewed and validated under realistic condition, i.e. using the optimized parameter sets. It is seen that the neglect of the inner voltage and current control loops of grid-forming inverters, as often applied in literature, is not a valid assumption due to the influence of the voltage controller. Instead, a fifth order model is proposed in this work, which is shown to preserve the dominant modes. On the othe rhand, for the grid-supporting inverter, a simple current source model that neglects the LCL filter is a valid approximation. Simplifying the network lines with the phasor model or a first order Taylor expansion is feasible in LV networks due to the low time constants of LV lines.

Finally, the impact of inaccurate synchronization of the microgrid at the transition from islanded to grid-connected mode of operation is investigated. The loadings of microgrid components are particularly large when the voltage angles are not aligned in the moment the breaker closes. The impact of frequency or magnitude deviations is comparatively low.

The microgrid model and the modal analysis approach are easily extendable and should include further components, such as induction machine loads, in future. Moreover, unbalanced conditions and harmonics are to be included in the stability assessment as well as the parameter optimization.

Kurzfassung

Die zunehmende Integration erneuerbarer Energien führt zu neuen Herausforderungen für elektrische Energienetze. Mikronetze sind eine Blaupause für zukünftige elektrische Netze, mit einem hohen Anteil an verteilten Erzeugungsanlagen und geringer synchroner Erzeugung. Diese Arbeit behandelt die Kleinsignalstabilität von Mikronetzen im Inselbetrieb.

Modalanalyse wird als geeignete Methode zur Bewertung der Stabilität herangezogen, auf Grund der größeren Flexibilität im Vergleich zu anderen Ansätzen, wie beispielsweise der Impedanzmethode oder Lyapunovs direktem Verfahren. Zusätzlich werden numerische Simulationen durchgeführt, um die Leistungsaufteilung zwischen dezentralen Anlagen nach Störungen, wie zum Beispiel Lastsprüngen, zu bewerten.

Modelle von Wechselrichtern, Diesel-Synchronmaschinen und Windturbinen mit doppelt-gespeister Asynchronmaschine, sowie deren netzbildende oder netzstützende Regelkonzepte werden implementiert. In Bezug auf Windturbinen werden zwei Methoden der synthetischen Schwungmasse, zum einen basierend auf der Phasenregelschleife, zum anderen anhand des Frequenzgradienten, betrachtet. Die Mikronetze werden im $dq0$-Referenzsystem modelliert, um die numerische Effizienz zu erhöhen, ohne die Genauigkeit des Models zu beeinträchtigen, sowie um stabile Betriebspunkte und die Linearisierung und damit die Modalanalyse zu ermöglichen.

Ein evolutionärer Algorithmus, welcher speziell auf Optimierungsprobleme mit rechenintensiven Fitnessfunktionen zugeschnitten ist, wird entwickelt. Im Zentrum des Algorithmus steht ein Binary Search Partitioning Tree, welcher zur Evaluierung und Verbesserung der Diversität der Population verwendet wird. Hierdurch kann die Performanz für ein Reihe von Optimierungsprobleme wesentlich erhöht werden. Die Optimierungs- und Simulationsumgebung, bestehend aus dem evolutionärer Algorithmus und den beschriebenen Mikronetz-Modellen, ist einer der Hauptbeiträge dieser Arbeit.

Der evolutionäre Algorithmus wird dazu verwendet, die Reglerparameter in verschiedene Szenarien, von kleinen Mikronetzen mit wenigen Knoten bis hin zu großen Benchmark-Systemen, zu optimieren. Die Optimierung basiert auf einen ausführlichen Sensitivitätsanalyse, um sämtliche einflussreiche Parameter zu identifizieren. Eine breite Auswahl an Reglerparametern wird in der Folge simultan optimiert.

Es wird gezeigt, dass Mikronetze, welche durch netzbildende Wechselrichter do-

miniert werden, sehr stabil sind, wenn sorgfältig ausgelegte und optimierte Regler verwendet werden. Die Verwendung einer virtuellen Impedanz ist von entscheidender Bedeutung für die Stabilität. Der Einfluss verschiedener Varianten und Erweiterungen der Droop-Regelung, welche in der Literatur zu finden sind, ist dagegen vergleichsweise gering. Mikronetze mit netzstützenden Wechselrichtern zeigen eine geringere Stabilität und deren Dynamik hängt hauptsächlich von der Parametrierung der Phasenregelschleife ab. Weiterhin hat der Anteil an Synchronmaschinen einen bedeutsamen Einfluss auf die Stabilität, sowie auf die optimalen Werte der Reglerparameter. Zudem wird gezeigt, dass die Methoden zur synthetischen Schwungmasse von Windturbinen mit der Droop-Regelung kompatibel sind und die Stabilität von Mikronetzen verbessern können, insbesondere wenn die vorgestellten Methoden kombiniert werden.

Unter realistischen Bedingung, d.h. mit den optimierten Parametersätzen, werden anschließend Ansätze zur Modellreduktion validiert bzw. überprüft. Es zeigt sich, dass die Vernachlässigung der inneren Spannungs- und Stromregelschleifen von netzbildenden Wechselrichtern, welche in der Literatur häufig vorzufinden ist, wegen des Einflusses der Spannungsregelschleife, keine gültige Vereinfachung ist. In dieser Arbeit wird stattdessen ein Modell fünfter Ordnung hergeleitet, welches die dominanten Modi nahezu unbeeinflusst lässt. Die Annäherung des netzstützenden Wechselrichters als einfache Stromquelle, welche den LCL Filter vernachlässigt, ist hingegen gültig. Die Vereinfachung des elektrischen Netzes mit dem Phasor-Modell, oder einer Taylor-Entwicklung, ist valide, auf Grund der kleinen Zeitkonstanten der Niederspannungsleitungen.

Schließlich wird die Auswirkung der ungenauen Synchronisation des Mikronetzes mit dem Verbundnetz, beim Übergang zwischen Insel- und Verbundbetrieb, untersucht. Hohe Belastungen der Betriebsmittel im Mikronetz treten insbesondere dann auf, wenn die Spannungswinkel im Moment des Schalterschließens abweichen. Der Einfluss von Frequenz- und Amplitudenabweichungen ist hingegen vergleichsweise gering.

Das Mikronetzmodell und die Modalanalyse können leicht erweitert werden und sollten in Zukunft zusätzliche Komponenten, wie beispielsweise Verbraucher mit Asynchronmaschinen, einbeziehen. Weiterhin sollten unsymmetrische Zustände und Harmonische bei der Bewertung der Stabilität, sowie für die Parameteroptimierung berücksichtigt werden.

Acknowledgements

When I started this journey in 2014, little did I know what was in store for me. I would like to thank my family, who supported me not only while I was working on this dissertation, but throughout my entire education. I would like to thank my friends for the distractions and apologise to everyone I have not been able to see often enough in recent years due to time constraints.

I would like to thank Prof. Krzysztof Rudion in particular for supervising and providing the funding for this work, for proofreading my manuscripts and for the professional exchange. I thank Prof. Dirk Westermann for his interest and for taking over the co-report and Prof. Stefan Tenbohlen for the trust placed in me.

A special thanks goes to Annette Gugel, Nicole Schärli, Janja Schulz and Dr. Ulrich Schärli for their support and helpfulness in administrative matters and Janja also for her travel advise. My colleagues at the Institute of Power Transmission and High Voltage Technology were a great support, and it was a pleasure to join them on excursions and ski trips. I would like to thank in particlar Manswet Banka, Matthias Buchner and Deepak Deepak for proofreading of this work and the personal and professional exchange and also Tim Streubel for making an acceptable volleyball player out of a clumsy soccer player.

This dissertation would not have been possible without the help of students who contributed with their theses. Special mention should be made of the students who have contributed with their Master's Thesis. My thanks go to Marius Radloff, Karima Benimmar, Anya Heider, Anika Jandt, Bruno Hümmler, Daniel Contreras, Helena Hingerl, Christoph John and Ansgar Neumann.

Finally, I thank my current employer, DIgSILENT Gmbh, for the opportunity and the freedom to complete this dissertation in addition to my regular work.

Contents

1. Introduction **1**

1.1. Background . . . 1

1.2. Motivation . . . 4

1.3. Contributions of this Work . . . 5

1.4. Scientific Statement . . . 7

1.5. Outline . . . 8

2. Preliminaries on Microgrids, Stability and Model Reduction **9**

2.1. Introduction . . . 9

2.2. Microgrids . . . 9

2.2.1. Definition . . . 9

2.2.2. Benefits . . . 10

2.2.3. Current Research and Application . . . 11

2.2.4. Synchronization . . . 14

2.3. Stability . . . 15

2.3.1. Classification . . . 15

2.3.1.1. Conventional Power Systems . . . 15

2.3.1.2. Microgrids . . . 19

2.3.1.3. Time Frames . . . 22

2.3.2. Small-Signal Stability . . . 23

2.3.2.1. Modal Analysis . . . 23

2.3.2.2. Lyapunov's Direct Method . . . 29

2.3.2.3. Impedance-Based Stability . . . 30

2.3.2.4. Numerical Simulation . . . 32

2.3.2.5. Comparison . . . 34

2.4. Model Order Reduction . . . 35

2.4.1. Classification . . . 35

2.4.2. Singular Perturbation Theory . . . 36

3. Modelling **39**

3.1. Introduction . . . 39

3.2. Software . . . 39
3.3. Reference Frame Transformation . . . 40
3.4. Network . . . 42
3.4.1. Network Modelling for Inverter-Dominated Power Systems . . . 42
3.4.2. Example: Series RL Modelling in the $dq0$ Frame . . . 45
3.4.3. Model Order Reduction . . . 46
3.4.4. Line Model . . . 46
3.5. Phase-Locked Loop . . . 46
3.6. Distributed Energy Resources . . . 48
3.6.1. Classification . . . 48
3.6.2. Power Sharing Control . . . 50
3.6.2.1. Signal Measurement and Filtering . . . 50
3.6.2.2. Power Transmission over an $\mathbf{RL}$-Line . . . 52
3.6.2.3. Grid-Forming Droop Control . . . 53
3.6.2.3.1. Conventional Droop Control . . . 53
3.6.2.3.2. Inverse Droop Control . . . 54
3.6.2.3.3. Transient Droop . . . 54
3.6.2.3.4. Active Power Feed-Forward . . . 55
3.6.2.3.5. Virtual Frame Transformation . . . 56
3.6.2.3.6. Other Droop Variants . . . 57
3.6.2.4. Virtual Synchronous Machine and its Equivalence to Droop Control . . . 58
3.6.2.5. Virtual Impedance . . . 59
3.6.2.6. Grid-Supporting Droop Control . . . 60
3.6.3. Power Electronic Devices . . . 61
3.6.3.1. $\mathbf{LCL}$-filter . . . 62
3.6.3.2. Grid-Forming Power Electronic Devices . . . 64
3.6.3.2.1. Current Controller . . . 65
3.6.3.2.2. Voltage Control . . . 67
3.6.3.2.3. Model Order Reduction . . . 68
3.6.3.3. Grid-Feeding and Grid-Supporting Power Electronic Devices 71
3.6.3.3.1. Model Order Reduction . . . 73
3.6.4. Diesel Synchronous Generators . . . 74
3.6.4.1. Synchronous Machine . . . 75
3.6.4.2. Automatic Voltage Regulator . . . 79
3.6.4.3. Governor . . . 80

3.6.4.4. Virtual Impedance 81
3.6.5. Wind Power Plants 81
3.6.5.1. Basics of Type 3 Generator 81
3.6.5.2. Doubly-Fed Induction Generator Internal Voltage 82
3.6.5.3. Rotor Side Converter Control 83
3.6.5.4. Phase-Locked Loop Synthetic Inertia 84
3.6.5.5. Frequency Gradient Synthetic Inertia 85
3.6.5.6. Combined Synthetic Inertia 86
3.7. Loads 87
3.8. Synchrocheck 88
3.9. Composite Model 88

4. Optimization Algorithm and Framework 91
4.1. Introduction 91
4.2. Overview of Power System Optimization 92
4.3. Literature Review on Microgrid Stability Optimization 92
4.4. Problem Formulation 94
4.4.1. Objectives 94
4.4.2. Constraints 95
4.5. Fundamentals of Evolutionary Algorithms 96
4.5.1. Overview 96
4.5.2. Evolutionary Operators and Parameters 99
4.5.2.1. Selection 99
4.5.2.2. Crossover 101
4.5.2.3. Mutation 102
4.5.2.4. Handling of Constraints Violation 103
4.5.2.5. Niching 104
4.6. Binary Space Partitioning 105
4.6.1. Basics 105
4.6.2. Implementation 106
4.6.2.1. Tree Initialization 106
4.6.2.2. Adding Solutions 107
4.6.2.3. Closure of Subspaces 108
4.6.2.4. Mutation of Duplicate Solutions 109
4.6.2.5. Mutation with Guided Anisotropic Search 109
4.6.2.6. Diversity of Solutions 109
4.7. Overview of Implemented Evolutionary Algorithm 111

4.8. Parametrization . . . 112
4.8.1. Benchmark Cost Functions . . . 113
4.8.2. Optimized Parameter Set . . . 114
4.9. Simulation and Optimization Framework . . . 115

5. Case Studies 117
5.1. Introduction . . . 117
5.2. Test Systems . . . 118
5.2.1. Test System 1: Small Two-Node Microgrid . . . 118
5.2.2. Test System 2: Cigre Benchmark Microgrid . . . 118
5.2.3. Test System 3: Small Two-Node Microgrid with Synchrocheck . . . 119
5.3. Model Validation . . . 120
5.4. Case Study 1: Evolutionary Algorithm Performance . . . 121
5.5. Case Study 2: Parameter Sensitivity . . . 123
5.5.1. Grid-forming Droop Control . . . 123
5.5.1.1. Definition of Relevant Parameters . . . 123
5.5.1.2. Modal Analysis . . . 124
5.5.2. Grid-Supporting Droop Control . . . 126
5.5.2.1. Definition of Relevant Parameters . . . 126
5.5.2.2. Modal Analysis . . . 126
5.6. Case Study 3: Simultaneous Optimization of All Parameters . . . 127
5.6.1. Parameter Ranges for Optimizations . . . 128
5.6.2. Results . . . 128
5.6.2.1. Grid-Forming Droop Control . . . 128
5.6.2.2. Combination of Grid-forming and Grid-Supporting Droop Control . . . 130
5.7. Case Study 4: Benchmark Optimization of Two-Node Microgrid . . . 133
5.7.1. Benchmark Test Scenarios . . . 133
5.7.2. Results . . . 134
5.7.2.1. Optimized Parameter Sets . . . 134
5.7.2.1.1. Comparison of Droop Variants . . . 134
5.7.2.1.2. Frame Transformation Droop . . . 136
5.7.2.2. Time Domain Simulation . . . 138
5.7.2.3. Dominant Eigenvalues . . . 139
5.8. Case Study 5: Optimization of Cigre Benchmark Microgrid . . . 140
5.8.1. Benchmark Test Scenarios . . . 140

5.8.2. Results . . . 140
5.8.2.1. Optimized Parameter Sets . . . 140
5.8.2.2. Time Domain Simulation . . . 143
5.8.2.3. Dominant Eigenvalues . . . 143
5.9. Case Study 6: Model Order Reduction . . . 144
5.9.1. Grid-Forming Droop Control . . . 144
5.9.2. Grid-Supporting Droop Control . . . 148
5.10. Case Study 7: Optimization of Synthetic Inertia for Wind Power Plants . . . 149
5.10.1. Objectives . . . 149
5.10.2. Constraints . . . 151
5.10.3. Parameter Ranges . . . 151
5.10.4. Time Domain Simulation . . . 151
5.10.4.1. DFIG with Battery storage system . . . 151
5.10.4.2. DFIG with Synchronous Machine . . . 153
5.10.4.3. Optimized parameters . . . 154
5.11. Case Study 8: Synchronization . . . 155
5.11.1. Angle Deviation . . . 156
5.11.2. Frequency Deviation . . . 158
5.11.3. Amplitude Deviation . . . 159
5.11.4. Combination of Angle with Frequency/Amplitude Deviation . . . 159
5.11.5. Fast Synchronization . . . 160

6. Discussion 163
6.1. Summary and Conclusion . . . 163
6.2. Outlook . . . 167

A. Composite Microgrid Model Example 171
A.1. Inverter . . . 171
A.2. Network and Load Model . . . 174
A.3. Complete Microgrid Model . . . 175

B. State-Space Model of Grid-Forming Droop Controlled Inverter 177

C. Cigre Benchmark Microgrid Data 181

D. LV Power Electronic Device and Diesel Synchonous Machine Data 182

E. Synthetic Intertia for Wind Power Plants Data 183

List of Figures **185**

List of Tables **188**

Bibliography **189**

Abbreviations

AVR	Automatic voltage regulator
BSP	Binary search partitioning
DER	Distributed energy resource
DFIG	Doubly-fed induction generator
EA	Evolutionary algorithm
EMT	Electromagnetic Transient
FFD	Feed-forward droop
FTD	Frame transformation droop
GA	Genetic algorithm
GOV	Governor
HVDC	High voltage direct current
IPCC	Intergovernmental Panel on Climate Change
LPF	Low pass filter
LV	Low voltage
MV	Medium voltage
PED	Power electronic device
PLL	Phase-locked loop
POC	Point of coupling
PV	Photovoltaic
PWM	Pulse-width modulation
OD	Original droop
SBX	Simulated binary crossover
SM	Synchronous machine
TD	Transient droop
VI	Virtual impedance
VSM	Virtual synchronous machine

Symbols

abc	Power system phases
$\boldsymbol{A}$	State matrix
$\boldsymbol{B}$	Input matrix
$C,\ c$	Capacitor [F], [pu]
$C_f,\ c_f$	Filter capacitor [F], [pu]
$\boldsymbol{C}$	Output matrix
d	Direct axis
$\boldsymbol{D}$	Feed-forward matrix
f_{switch}	Switching frequency [Hz]
f_{res}	Resonance frequency [Hz]
FF_c	Feed-forward of current controller
FF_v	Feed-forward of voltage controller
H	Inertia constant [s]
I, ß	Current [A], [pu]
$\boldsymbol{I}$	Unity matrix
k_d	Damping coefficient
k_i	Integral gain
k_p	Proportional gain
$k_{i,c}$	Integral gain current controller
$k_{i,v}$	Integral gain voltage controller
$k_{p,c}$	Proportional gain current controller
$k_{p,v}$	Proportional gain voltage controller
k_{SI}	Proportional gain synthetic inertia
$\boldsymbol{K_s}$	Transformation matrix park transform
$\boldsymbol{K_a}$	Transformation matrix between arbitrary dq reference frames
$L,\ l$	Inductance [H], [pu]
$L_L,\ l_L$	Line inductance [H], [pu]
$L_{vi},\ l_{vi}$	Virtual inductance [H], [pu]

m_ω	Frequency droop coefficient
$m_{\omega,t}$	Transient frequency droop coefficient
$m_{\omega,ff}$	Feed-forward frequency droop coefficient
m_v	Voltage droop coefficient
$m_{v,t}$	Transient voltage droop coefficient
p	Participation factor
p_f	Number of field poles
$P,\ p$	Active power [W], [pu]
$P_L,\ p_L$	Line active power [W], [pu]
$P_{mea},\ p_{mea}$	Measured active power [W], [pu]
$R,\ r$	Resistor [Ω], [pu]
$R_L,\ r_L$	Line resistor [Ω], [pu]
$R_{Ground},\ r_{Ground}$	Ground resistor [Ω], [pu]
$R_{vi},\ r_{vi}$	Virtual resistor [Ω], [pu]
s	Laplace operator
s_E	Saturation
$S,\ s$	Apparent power [VA], [pu]
$S_L,\ s_L$	Line apparent power [VA], [pu]
q	Quadrature axis
$Q,\ q$	Reactive power [Var], [pu]
$Q_L,\ q_L$	Line reactive power [Var], [pu]
$Q_{mea},\ q_{mea}$	Measured reactive power [Var], [pu]
$T,\ t$	Torque [Nm], [pu]
T_f	Filter time constant [s]
T_a	Acceleration time constant [s]
u	Vector of system input
$V,\ v$	Voltage [V], [pu]
$X,\ x$	Reactance [Ω], [pu]
$X_L,\ x_L$	Line reactance [Ω], [pu]
$X_{vi},\ x_{vi}$	Virtual reactance [Ω], [pu]
$Z,\ z$	Impedance [Ω], [pu]
$Z_L,\ z_L$	Line impedance [Ω], [pu]
$Z_{vi},\ z_{vi}$	Virtual impedance [Ω], [pu]
Υ_{obj}	Objective function result
δ	Voltage angle
η_{div}	Penalty for diversity

λ	Eigenvalue
ω	Angular speed/frequency [rad/s]
ω_n	Nominal angular speed/frequency [rad/s]
ω_0	Set point angular speed/frequency [rad/s]
ϕ	Angle of impedance
ψ	Flux
σ	Standard deviation
θ	Voltage angle set point of controller/phase locked loop or rotor
ϱ_{cro}	Crossover rate
ϱ_{mut}	Mutation rate
ξ_{div}	Diversity weighting factor
ζ	Damping ratio
ζ_p	Damping factor

1. Introduction

1.1. Background

The interrelation between atmospheric CO_2 levels and temperature of the earth was first quantified by Arrhenius in 1896 [1]. Scientists increasingly predicted warming in the 1970s [2] and consensus began to form in the 1980s which lead to the establishment of the Intergovernmental Panel on Climate Change (IPCC) in 1988. A discernible human influence on the earth's temperature was carefully phrased by the IPCC in the 1990s and the 5^{th} IPCC synthesis report on climate change from 2014 [3] states that it is extremely likely that human influence has been the dominant cause of the observed temperature rise starting from the second half of the 20^{th} century. Greenhouse gas emissions through burning of fossil fuels are the main cause and the largest share has been contributed by developed countries [4].

11944 abstracts of peer-reviewed scientific literature from $1991 - 2011$ matching the topics 'global climate change' and 'global warming' were examined in [5]. 97.1% endorsed the consensus position that humans contribute to global warming. Nonetheless, the complex nature of global warming, uncertainties about the risks it poses and inevitable uncertainties in scientific research make it challenging for non-experts and laypersons to understand its causes. This has been used by interest groups to generate scepticism through organized campaigns from the outset [6]. Furthermore, due to the non-linearity and delay of the consequences of greenhouse gas emissions, countermeasures are implemented only very tentatively despite catastrophic consequences in the long term [3]. However, even based on economic considerations, immediate policies to slow emissions are mandatory [7, 8].

Renewable energies play a key role on the path to lowered emission targets and can also have positive socio-economic effects [9]. According to current policy, Germany aims at a share of at least 80% renewable energies within the total energy consumption by 2050 [10].

The integration of renewable energies into the electric power system is a major field of research [11]. A paradigm shift from large centralized thermal power plants to distributed energy resources (DER) is necessary. Renewable energy sources are typically connected to the distribution system, reflecting their dispersed nature. Moreover, DER are usually interfaced with the power network via power electronic devices (PED) in contrast to large conventional power plants, where synchronous machines (SM) are deployed. Examples of PED include photovoltaic plants or battery energy storage systems.

A 2014 report by the German Energy Agency (Deutsche Energie Agentur) [12] identifies the following consequences for the power system: The demand for minute reserve (Minutenreserve) is largely increased ($70 - 90\%$), whereas the demand for secondary control is marginally increased. Alternative concepts for the provision of balancing power are more suitable than must-run capacity of conventional power plants. Reactive power demand in the transmission system increases and DER should be able to provide reactive power even at times when they do not supply active power. The total short circuit capacity available is likely to remain constant, whereas it can alter significantly at individual nodes. Inertia of SM declines and must be provided by alternative sources. Furthermore, the report states that the required precision of models for dynamic studies of future power systems is an important field of research.

The last three aspects are directly linked to the deployment of PED. The overcurrent capacity of PED is between 1 and 2 pu [13], whereas SM can provide up to 8 times their nominal current. However, the overall capacity of PED is higher.

PED do not have rotating masses that are directly coupled with the electrical grid [14]. Hence, they do not provide inertia inherently. However, it is possible to emulate the inertia of SM in the control of PED, which is also referred to as artificial or synthetic inertia (SI). To that end, numerous control strategies have been proposed in literature in recent years [15]. Many controller types entail the ability of the PED to provide a voltage reference, in contrast to the current source behaviour of PED in today's power systems. Design, selection and tuning of appropriate controllers is a difficult task.

The contribution of wind power plants with doubly-fed induction generators (DFIG) in operation today to the system inertia is not significant, because the dynamics are dominated by the fast machine side converter. However, there is a lot of research effort for the design of SI controllers [16, 17].

Decades of experience have established features and standard models of SM, governors and excitation systems of varying orders that are known to capture the important modes for particular classes of problems. On the other hand, this experience does not exist for PED and they are often simply modelled as negative loads in stability studies, omitting their impact on power system dynamics [18]. The main reasons for this practice are the lack or limited access to well-validated, detailed PED models for the specific power system phenomena, insufficient information about the power system at the lower voltage

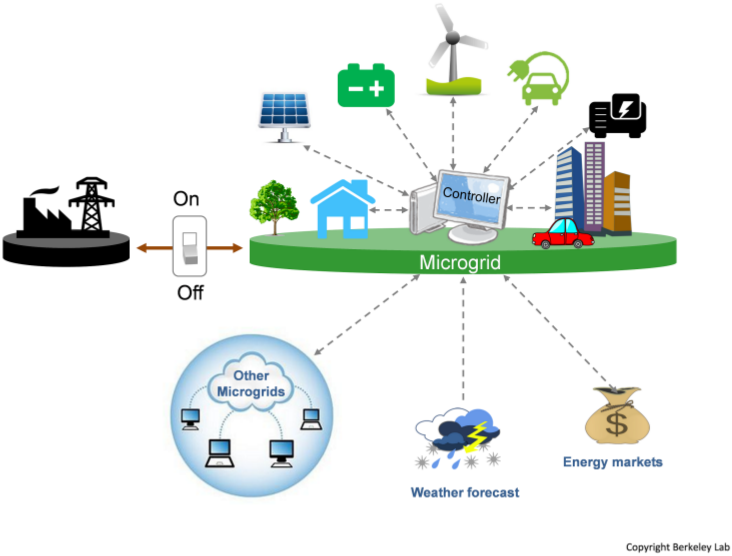

Figure 1.1.: Microgrid schematic [20].

levels and the lack of accepted (agreed) methodologies for the aggregation of PED [19].

Microgrids are parts of the distribution system that can be operated in grid-connected or in islanded mode [21], as illustrated in Fig. 1.1. In the latter case, the microgrid forms an autonomous cell, disconnected from the rest of the power system. This increases the reliability and allows for the uninterrupted supply of loads in the event of an outage in the bulk power system. It leads to further benefits if managed and coordinated efficiently. One characteristic is a high share of DER which makes microgrids a smaller scale model for future power systems. Hence, the problems described in the previous paragraphs can already be observed in concentrated form in microgrids today. Typical DER in microgrids are, besides wind and photovoltaic plants, also diesel powered SM.

The stability of islanded microgrids is subject to ongoing research and numerous control schemes have been proposed to ensure their small-signal stability [15]. Similar control approaches as in bulk power systems, emulating the inertia of SM, are applied. Many of them are enhancements to the widely applied droop control.

Another critical aspect of microgrid operation is the transition between islanded and grid-connected mode of operation. Unpredictable influences, such as measurement errors or load fluctuation, can cause imperfect alignment of the voltages of microgrid and bulk system when the connecting breaker is closed. Potential consequences are overcurrents and stress of microgrid components.

1.2. Motivation

Microgrids are a showcase for future power systems. The high share of DER raises issues, such as degraded stability, that will also affect the bulk power system once similar penetration rates are reached.

Although a wide variety of controller types for DER to improve the small-signal stability of microgrids has been proposed in literature, there is a lack of systematic evaluation and comparison of the various approaches. The performance of the designed controllers is generally compared to a very simple type of PED control, such as the droop control in its most basic form. There is a lack of performance comparison between the enhanced controller types.

Moreover, the superiority of controller types is usually only demonstrated for one study case with a certain, often rather small and simple, microgrid topology. However, controllers should be applicable in a wide range of scenarios with varying topologies, line lengths and network R/X ratios. In addition, they should comply with microgrids with various types of DER. Either only PED may be present, but also scenarios with PED and SM are possible. DFIG is usually investigated only in large-scale power systems, whereas few literature is found on DFIG in microgrids.

Furthermore, there is also a lack of systematic parameter sensitivity analysis, tuning and optimization in literature. Meaningful results will only be obtained if the evaluation of controller types is preceded by a thorough parameter optimization. Only then a fair comparison is possible. However, in most literature, the set of parameters that is optimized is limited to the parameters most influential, or assumed most influential. The parameter optimization should be accompanied by a sensitivity analysis which identifies all parameters relevant to the system stability.

Another aspect that has not been addressed in enough detail in literature is the validity of model order reductions for stability studies. For example, the neglect of the inner control loops of PED is generally assumed valid, although there is no prove to this concept. Especially, when PED controllers are optimized and tuned for fast response, slow and fast modes draw nearer to each other and the assumption may not be valid. Therefore, assumptions for order reductions should be validated by models with optimized controller parameters. Besides PED modelling, the necessary level of detail for network representation is another interesting aspect that needs further investigation.

An additional issue that has not been covered in detail in literature is the impact of imperfect alignment of the microgrid and bulk power system voltages at reconnection.

Although specifications for reconnection requirements exist, the theoretic background of the given boundaries for voltage deviations on both sides of the breaker at closing is unclear. It has not been examined so far how deviations outside the given boundaries affect the burden of microgrid components during this transition.

1.3. Contributions of this Work

This work is dedicated to the small-signal stability of islanded microgrids and has a broad scope, including various DER and controller types as well as design optimization approaches. A review of small-signal stability methods is provided and modal analysis is identified as the most suitable approach.

This is followed by a thorough analysis of the modelling of DER types, their controllers and the network. Modelling the network in the rotating $dq0$ frame is found to be an efficient, yet accurate approach for systems with high penetration of PED. The DER models include grid-forming, grid-supporting and grid-feeding inverters as well as wind turbines with doubly-fed induction generator (DFIG) and diesel SM. Several power sharing strategies based on droop control and virtual impedance (VI) are characterized. The tuning of inner loop controllers and the design of LCL filters is detailed. As regards DFIG wind turbines, SI strategies based on frequency gradient (df/dt) control and an approach that mimics the inertia of SM using a slowly reacting phase-locked loop (PLL) are depicted. Harmonics and unbalanced conditions are not the focus of this work and only balanced conditions are considered. However, most of the results of this work generally hold also for unbalanced conditions, because harmonics are filtered out from the controller input signals.

Model order reductions based on singular perturbation theory, such as the neglect of inner loop controllers and the simplification of the network differential equations, are reviewed. A new approach to the model order reduction of grid-forming PED that captures important dynamics of the voltage controller, while limiting the order to five states, is proposed.

A suitable optimization algorithm is required in order to optimize the controller parameters. Conventional optimization methods are not applicable due to the intricacy of the problem and the fact that a strictly mathematical formulation is not possible. Evolutionary algorithm (EA) is selected as an appropriate method on the grounds of the reduced likelihood to get trapped in local optima compared to other heuristic methods and due to its flexibility. A EA tailored to the optimization of DER controllers is proposed. It is designed to reach the optimum within a very limited number of fitness evaluations, because these are computationally intensive as they require numerical time domain simulation. A binary search partitioning (BSP) tree is at the core of the EA. It is used to avoid the repetitive evaluation of the same individual and, most importantly, to regulate the diversity of the population.

The efficient models and the EA are used to optimize the DER controllers. In a systematic approach, a thorough sensitivity analysis to identify all relevant controller parameters is conducted at first. Consequently, a large set of controller parameters, some of which so far not considered in literature, are incorporated in the optimization.

One optimization criterion is the efficient power sharing between DER to avoid overloading after contingencies, such as load fluctuations. The second criterion is the minimization of the real parts of dominant eigenvalues. Considered constraints are the accurate steady-state active and reactive power sharing between DER and the compliance with voltage and frequency limits.

Benchmark scenarios are developed to optimize and test the controllers and their parameters under various conditions. Line length and R/X ratio are varied. Microgrids with different types of DER are considered, containing only PED (including DFIG) or in addition SM. Several controller types for power sharing and SI are evaluated and compared.

Finally, the Cigre benchmark LV network with 38 nodes is considered. Controller parameters are optimized for this large-scale system and the resulting parameter sets are compared to the outcome of the benchmark optimizations. It becomes apparent that microgrids dominated by PED exhibit a high degree of small-signal stability, if the controllers are well-designed and all relevant parameters are optimized.

The optimized parameter sets are used to evaluate the validity of model-order reductions of the the network and PED under realistic conditions and for differing bandwidths of the cascaded PED control, i.e. power sharing, voltage and current control. It is shown that, whereas the approximation of the network is valid in LV microgrids, the often applied neglect of the inner loops of grid-forming inverters is not. On the other hand, the fifth order model proposed in this work well approximates the original 13^{th} order grid-forming model.

The last part of the case study section is dedicated to the synchronization of islanded microgrids. This can be regarded as a rather separate field of research, as it is more related to considerations of large disturbance stability. The burden of microgrid components are investigated for deviations between the voltages of the microgrid and the bulk power system at breaker closing. Frequency, magnitude and angle discrepancies and combinations are examined. The ranges of the deviations are beyond the accepted limits to investigate contingencies such as the very quick and inaccurate synchronization on the grounds of, for instance, looming instability in the microgrid. Voltage angle deviations

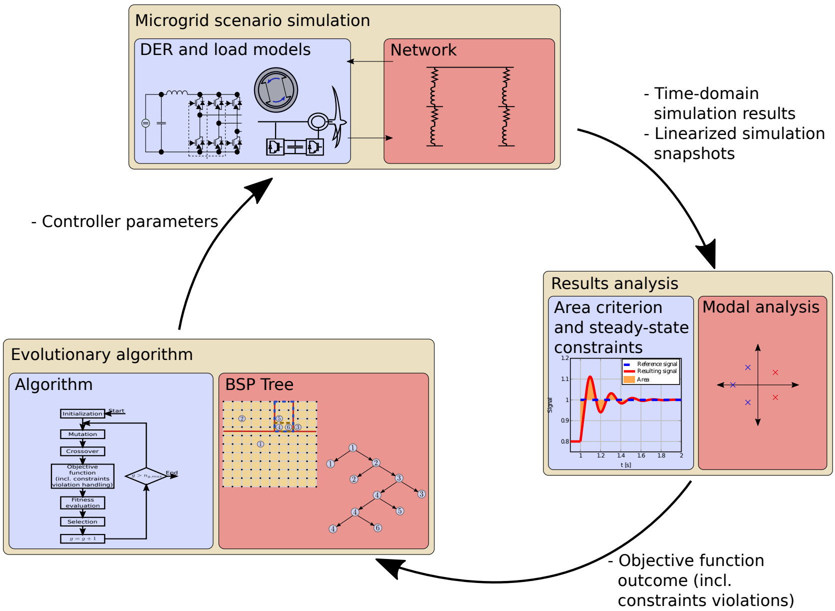

Figure 1.2.: Simulation and optimization framework.

at breaker closing are found to cause the most severe loadings of microgrid components, whereas magnitude and frequency deviations have a distinctly lower impact.

One of the main contributions of this work is the simulation and optimization framework illustrated in Fig. 1.2. It connects the optimization algorithm with the DER and network model. It forms the basis of the aforementioned controller parameter optimizations. Time-domain simulations of the microgrid are carried out and the results, including linearized model snapshots, are passed on to the results analysis. The results are evaluated according to the area criterion and modal analysis as well as constraints violations. The outcome is used in the objective function of the EA. The EA's performance is enhanced by the BSP tree. The optimized parameters of the EA are then handed over to the microgrid simulation which may consist of several scenarios. This iterative process is repeated until an optimal or close to optimal solution is found.

1.4. Scientific Statement

The following scientific statement is formulated to express the basic message of this work: **Islanded microgrids dominated by power electronic devices have a high level of small-signal stability, if the controllers are well-designed and all relevant parameters**

are optimized. Reduced-order models of grid-forming inverters should contain the dynamics of the voltage controller and neglecting the inner loops entirely is an oversimplification.

1.5. Outline

The rest of the thesis is organized as follows. Preliminaries on microgrids, stability and model order reduction are elaborated in Ch. 2. The microgrid and DER models are described in Ch. 3. Ch. 4 introduces the proposed optimization algorithm. Case studies are investigated in Ch. 5 and the discussion is presented in Ch. 6. An introductory section is provided at the beginning of each chapter.

2. Preliminaries on Microgrids, Stability and Model Reduction

2.1. Introduction

This preliminary chapter introduces the relevant basics of microgrids. The definition is presented and benefits, ranging from economic and technical to environmental and social, are described. Current research efforts and applications are elaborated. Another section is dedicated to the synchronization of islanded microgrids as this process is later simulated in the case studies.

The stability phenomena relevant for microgrids are categorized and compared to conventional power systems. The most widely used approaches to evaluate the small-signal stability of microgrids are introduced. Their advantages and disadvantages are compared.

The chapter closes with the description of model order reduction techniques. In particular, singular perturbation theory, which forms the basis of the model-order reduction techniques applied in this work, is elaborated.

2.2. Microgrids

2.2.1. Definition

Various definitions of the term 'microgrid' are found in literature. The following definition was offered in an EU microgrid research project [21]:

"Microgrids comprise LV distribution systems with distributed energy resources (DER) (micro-turbines, fuel cells, PV, etc.) together with storage devices (flywheels, energy capacitors and batteries) and flexible loads. Such systems can be operated in a non-autonomous way, if interconnected to the grid, or in an autonomous way, if disconnected from the main grid. The operation of microsources in the network can provide distinct benefits to the overall system performance, if managed and coordinated efficiently."

According to this definition, if MV facilities are involved for the connection of two LV microgrids, this is not designated one microgrid, but the operation of multi-microgrids.

[22] acknowledges that the term 'microgrid' is not uniformly defined in literature and lists the following characteristics according to a literature survey:

1. It is a connected subset of the LV or MV distribution system of an AC electrical power system.
2. It possesses a single point of connection to the remaining electrical power system. This point of connection is called point of common coupling.
3. It gathers a combination of generation units, loads and energy storage elements.
4. It possesses enough generation and storage capacity to supply most of its loads autonomously during at least some period of time.
5. It can be operated either connected to the remaining electrical network or as an independent island network. The first operation mode is called grid-connected mode and the second operation mode is called islanded, stand-alone or autonomous mode.
6. In grid-connected mode, it behaves as a single controllable generator or load from the viewpoint of the remaining electrical system.
7. In islanded mode, frequency, voltage and power can be actively controlled within the microgrid.

Microgrids can also be implemented as DC systems [23], which would implicate the removal of the property 'frequency control' from point 7.

The microgrid control offers the possibility to appear as a coordinated unit to the upstream network, which is the key feature that distinguishes it from LV systems with DER. The microgrid principle is not to be mistaken with the virtual power plant concept, as the microgrid elements are confined within the same local distribution network, the smaller size and the consumer interest. Its focus is the reliable supply of local consumption [24].

Two steady-state and two transient modes of operation are possible: Islanded, grid-connected and the transitions between them. During islanded operation, the load supply must be guaranteed by the local generation and the microgrid must remain stable. The microgrid frequency must be aligned to the frequency of the upstream network for the transition from islanded to grid-connected mode [25].

2.2.2. Benefits

The benefits of microgrids range from economic and technical to environmental and social [21]. Economic benefits are that microgrids can act as a hedging tool against potential risks of outage, load growth or price volatility. Furthermore, they serve as an initiator of local service and retail markets and can be an interest arbitrator for different stakeholders. Technical benefits include improved voltage quality due to coordinated reactive power control and active power curtailment, reduced losses, prevention of network congestion and enhanced reliability because of the islanding capability in the event of an outage in the upstream network. A requirement for the mentioned benefits is the existence of a coordination platform, either in centralized or in decentralized form. Finally, the social and environmental values are the reduction of emissions, the electrification of underdeveloped and remote areas and the raise of public awareness of energy saving and climate change [21].

As for today, the widespread implementation of microgrids has been hampered by technical challenges and high cost. The high initial investment cost for communication, the competition of DER and storage with low-cost large-scale power plants and the ongoing process of standardization are just some of the key barriers. An overview of current research in the field of microgrids with a focus on islanded operation is provided in the next section.

2.2.3. Current Research and Application

One of the key issues of islanded microgrid operation is the configuration of the protection equipment [26, 27]. The high share of PED entails lower short-circuit magnitudes. PED are able to provide fault current magnitudes between one and two times their rated current [13], whereas SM inject up to eight times their rated current [28]. Moreover, characteristic short-circuit current timescales of SM, such as the subtransient, transient and steady-state period, are not transferable to PED. Their current injection is largely dependent on the controller settings. Control of fault currents is especially demanding for grid-forming inverters, which exhibit voltage source behaviour (see Sec. 3.6.1). To avoid non-linearity by simply saturating inverter currents to protect the power electronics, other techniques such as the implementation of a VI were supposed [29]. The lack of inertia may also imply larger frequency fluctuations which requires the specific design of frequency relays [30].

Considering that many power system failures are not initiated by instability, but rather by a relatively minor disturbance that escalates through reactionary protection operation [31], microgrid protection devices are a major field of future research. Due to the lower fault current magnitude, conventional distribution protective devices cannot reliably protect microgrids. A commercial relay tailored to microgrids is still not available [32]. Therefore, it is resorted to existing options such as directional overcurrent, distance and differential relays.

Some widespread options for communication are power line communication, copper-wire line, fiber optics and a variety of wireless technologies such as GSM, GPRS, WiMax, WLAN and Cognitive Radio [33]. Important properties of these technologies are bandwidth, latency, range, security and reliability [34, 35]. Communication is imperative for the coordination among protection and control systems. Each disturbance can cause the response of multiple control and protection schemes. The traditional approach, where each controller reacts to a specific disturbance with fixed parameters that are set in advance on the basis of offline simulations, seems inapt. On the contrary, control strategies are developed based on online security assessment [36].

The islanding of parts of the distribution system is not necessarily a desired condition. Unintentional islanding can threaten the safety of line workers, violate frequency and voltage constraints, reduce probability of successful automatic reclosing and potentially damages utility and customer equipment [37]. Therefore, islanding detection methods are implemented in DER in order to disconnect in the event a distribution system island is formed. On the other hand, the DER must not disconnect automatically during intentional islanding events. Depending on the detection technique, microgrid parameters must be kept within certain thresholds to prevent tripping of the islanding detection.

Numerous islanding detection schemes are found in literature [38]. It is distinguished between passive and active techniques. Passive islanding techniques rely on the detection of parameter thresholds. Their advantages are inexpensiveness, easy implementation and no degradation of inverter power quality. Active techniques inject small disturbances at the inverter output to detect the response of the network. They have a smaller non detection zone compared to passive techniques, but deteriorate the output power quality and increase the controller complexity [39].

Research on intentional islanding and microgrid reconfiguration has gained increased attention in recent years. A non-dominated sorting genetic algorithm (GA) is utilized in [40] to reconfigure microgrids with the aim of minimizing the fuel consumption, ensuring the capability to feed the maximum possible demand and minimizing switching operation cost. Optimal formation of islands regarding load-shedding cost is conducted in [41] on the basis of mixed integer programming. The question of the optimal moment of islanding as a last resort to avoid cascaded failure is treated in [42]. The feasibility of adaptive load shedding for an intentional islanding case is studied in [43]. Particle swarm optimization is applied in [44] to split the distribution system into a number of islands followed by generation redispatch and load shedding. The reconfiguration of meshed networks considering the small-signal stability of droop-based islanded microgrids is covered in [45]. It is shown that the reconfiguration alters the line impedances between inverters and therefore affects

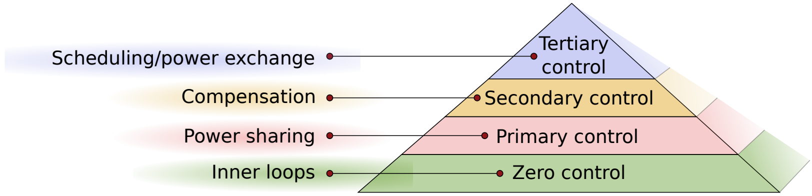

Figure 2.1.: Hierarchical microgrid control.

the stability. Criteria such as loss reduction, fault current magnitudes, voltage profile, feeder capacity and reliability improve with lower line impedances in meshed networks. Contrarily, the small-signal stability of droop controlled inverters deteriorates with lower line impedances.

An attempt to standardize the control levels was conducted in [46] by analogy to the classic system and is shown in Fig. 2.1. The microgrid control can be subdivided into four levels. The purpose of the primary control is to ensure the power sharing between the DER during fluctuations of generation and consumption as circulating active and reactive power can appear when two or more inverters are connected in parallel. It plays a vital role in securing the small-signal stability of the islanded microgrid and is covered in detail in Sec. 3.6.2. The primary control is likely to cause voltage frequency and voltage magnitude deviations which are compensated by the secondary controller. The aim is to regulate the deviations toward zero after each change of load and generation [47, 48, 49].

The tertiary control is the highest level of control and caters to the optimized scheduling of the generation and consumption in the microgrid. In grid-connected mode of operation, it also controls the power exchange with the upstream power system [50, 51]. In addition, there are also decentralized control approaches [51] where each DER controller optimizes its operation independently, collaborating or competing with other microsources. This type of organization lends itself to microgrids with various ownerships and optimization goals.

[46] additionally defines the zero level control, which refers to the inner loop controllers of the units, such as voltage and current controllers of PED.

Despite major research efforts, widespread application of microgrids capable of islanded operation has not taken place yet. SMA [52] is one of the few vendors that offer battery inverters compatible with decentralised multi-master control, that holds the promise of easily extendable microgrids which are resistant to single point failures and allow integration of many types of energy sources [53].

The multi-agent system approach has been deployed in two European microgrids, the German 'Am Steinweg' project and on the Greek island of Kythnos [54]. The reader may

Table 2.1.: Microgrid reconnection requirements [59].

Rated power [MVA]	$\lvert\Delta f\rvert$ [Hz]	$\lvert\Delta v\rvert$ [pu]	$\lvert\Delta\delta\rvert$ [°]
$0 - 0.5$	0.3	0.1	20
$0.5 - 1.5$	0.2	0.05	15
$1.5 - 10$	0.1	0.03	10

consult a recent review [55] for an exhaustive list of existing and experimental microgrid systems. Total microgrid capacity was estimated 1.4 GW in 2015 and is expected to expand to 5.7 GW by a conservative estimate or 8.7 GW under an aggressive scenario by 2024 [56].

2.2.4. Synchronization

Among the critical aspects of microgrid operation is the transition between islanded and grid-connected mode. One scenario is the reconnection with the bulk power system that was switched back online after a power failure [57]. This transition can burden the components. Possible high currents or generator torques may trigger the protection system or affect the ageing of the equipment.

In preparation for the reconnection, the microgrid frequency is synchronized with the bulk power system resorting to a synchrocheck controller. Phase, amplitude and frequency are never exactly aligned with the bulk power system due to measurement errors, fluctuating loads and generation in the microgrid, varying frequency and amplitude of the bulk power system or the response time and tolerance of circuit breakers [58]. During network reconstruction, the microgrid can also be reconnected with another small grid cell with fluctuating loads and generation instead of the rather stable bulk power system. Another scenario is that looming instability or imbalance between load and generation require the microgrid to reconnect as quickly as possible. In this case, a balance must be struck between the period of time until the breaker is closed and the accuracy of the voltage alignment at closing.

Maximum frequency, voltage and angle deviation requirements for microgrid reconnection with the bulk power system for various power categories are given in Table 2.1. The implications of deviations outside the ranges stated in Table 2.1 are investigated in this work.

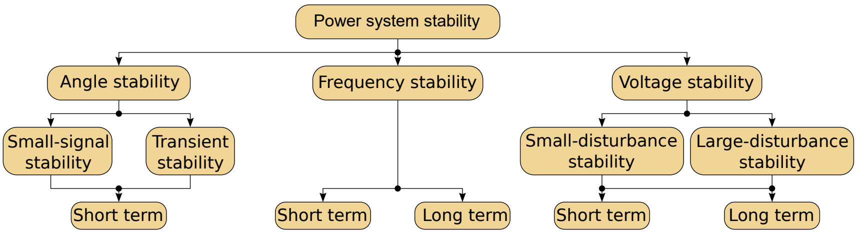

Figure 2.2.: Stability classification of conventional power systems [62].

2.3. Stability

2.3.1. Classification

2.3.1.1. Conventional Power Systems

Stability of conventional power systems is generally defined as the quality of a power system to remain in a state of operating equilibrium under normal operating conditions and to restore a viable state of equilibrium after undergoing a disturbance [60]. An interesting historical overview on literature covering power system stability is presented in [61] and a historical review of stability problems is given in [60]. Fig. 2.2 provides an overview of stability phenomena.

In traditional power systems dominated by SM, the stability problem has mainly been one of preserving synchronous operation. Synchronism depends on power-angle relationships and the dynamics of SM rotor angles. On the other hand, instability may also be encountered due to collapse of load voltage and is, therefore, an issue of voltage control. The response of only a limited amount of equipment present in the power system may be important for the evaluation of stability after being subject to a certain disturbance. Hence, the classification into various categories greatly facilitates the understanding of stability problems and the identification of relevant components [60, 62].

Rotor angel stability refers to electromechanical oscillations inherent in power systems with SM. It is characterized by the variation of the power output of SM when their rotor oscillates. Under steady-state conditions, the rotor speed of a SM remains constant and there is equilibrium between the output electrical torque and the input mechanical torque. If this equilibrium is upset following a disturbance and one generator temporarily runs faster than the another, its rotor's angular position will advance relative to slower machines.

The relationship between active power transmitted over a line represented by a pure series reactance x_{Line} and the voltages at its terminals is given as

$$P = \frac{v_1 v_2}{x_{Line}} \sin\delta, \tag{2.1}$$

where v_1 and v_2 are the terminal voltage magnitudes and δ is the angular separation. Depending on this power-angle relationship, part of the load is transferred from the slow to the fast machine. Resulting from the sinusoidal shape, an increase in angular separation is accompanied by a decrease in power transfer beyond an angular limit of $\delta = 90^\circ$ and leads to instability.

System stability depends on the existence of two components of the electrical torque of SM. The change in electrical torque ΔT_e of a SM following a perturbation is resolved into two components as follows:

$$\Delta T_e = T_S \Delta\delta + T_D \Delta\omega, \tag{2.2}$$

where T_S is the synchronizing torque coefficient and $T_S\Delta\delta$ is the synchronizing torque component, which is proportional to the rotor angle perturbation $\Delta\delta$. T_D is the damping torque coefficient and $T_D\Delta\omega$ is referred to as the damping torque component, which is proportional to the rotor speed deviation $\Delta\omega$. Instability in form of an aperiodic drift follows from the lack of sufficient synchronizing torque. On the other hand, oscillatory instability is a consequence of the lack of sufficient damping torque.

It is common to characterize the rotor angle stability phenomena in terms of two categories for convenience in analysis [60]:

- Small-signal (or small-disturbance) stability is the property of the power system to preserve synchronism under small disturbances such as little variations in generation and loads. Linearization of system equations is permissible for purposes of analysis as the disturbances are considered sufficiently small. In power systems dominated by SM, the small-signal stability is largely a problem of insufficient damping of oscillations. Oscillations localized at a small part of the power system are termed local modes or machine system modes. They are associated with the swinging of units of a generating station relative to the rest of the power system. Oscillation of a group of machines in one part of the system against machines in other parts are referred to as inter area modes. When generating units and other control modes are the main cause of oscillations, the term control modes is used. The usual causes are the poor tuning of AVRs, governors, HVDC converters and static var compensators. Another type are torsional modes which are associated with turbine-generator shaft system rotational components. They are a consequence of interaction with series-capacitor-compensated lines, excitation controls, speed governors and HVDC controls.

- Transient stability is the property to preserve synchronism when subject to a severe transient disturbance. Short circuits of different types, such as phase-to-ground, phase-to-phase-to-ground or three-phase are the contingencies usually considered. The non-linear power-angle relationship influences the resulting system response, which involves large excursions of generator rotor angles. Both the initial operating state and the severity of the disturbance affect the transient stability. In general, the post-disturbance steady state is different from that prior to the disturbance and the study period of interest is limited to three to five seconds after the disturbance.

Both small-signal and transient rotor angle stability are classified as short term phenomena [62].

Voltage stability is the property of a power system to maintain acceptable voltages at all buses after being subject to a perturbation and under normal operating conditions. Instabilities are characterized by a progressive and uncontrollable drop in voltage as a result of an increase in load demand, for instance. Often, the main factor leading to instability can be identified as the inability to meet the reactive power demand. The analysis of the problem is based on the voltage drop due to the power flowing through predominantly reactive impedances in the transmission network. Whereas voltage instability is essentially a local phenomenon, its consequences may have widespread impact leading to a sequence of accompanying events and voltage collapse in a significant part of the power system [63].

It is again helpful to classify the subclasses small-disturbance and large-disturbance voltage stability:

- Small-disturbance voltage stability is concerned with small perturbations and is determined by the characteristics of loads and controls at a certain point in time. Static analysis can be effectively used to identify stability margins and examine a wide range of system conditions [64].

- Large-disturbance voltage stability covers the systems property to control voltages after large disturbances such as loss of generation or system faults. This involves interactions of continuous and discrete controls and protections as well as load characteristics. It requires the investigation of the non-linear dynamic performance of system considering time frames extending from a few seconds to tens of minutes. Hence, the performance needs to be examined with long-term dynamic simulations.

Angle and voltage instabilities often go hand in hand. However, to understand the underlying causes and develop appropriate design and operating procedures, the distinction is necessary [60, 62].

Voltage stability problems usually have time frames of a few seconds up to tens of minutes. Dynamics of HVDC converters, electronically controlled loads and induction motors are involved in short term voltage stability and the analysis involves the solution of appropriate system differential equations. Short-circuits close to loads are of interest in contrast to angle stability [62].

Slower acting equipment such as thermostatically controlled loads, generator current limiters and tap-changing transformers contribute to long term voltage stability. The study period extends up to several minuted.Stability is not determined by the severity of the initial disturbance, but rather by the resulting outage of equipment. The causes of instability are small-signal instability of the post-disturbance steady state or lack of attraction toward the stable post-disturbance equilibrium. Static analysis is used to identify stability margins and to investigate a range of system conditions and scenarios. It should be complemented by quasi-steady-state time-domain simulations where the impact of controller time constants is relevant [62].

The ability to maintain steady frequency despite imbalance between load and generation after a severe system upset is referred to as frequency stability. It is associated with the ability to restore the balance between load and generation, while avoiding unintentional load disconnection. Otherwise sustained frequency swings and resulting tripping of generation and loads can occur. Frequency stability can invoke actions of processes that are not modelled in voltage stability studies or conventional transient stability, such as slow boiler dynamics or Volts/Hertz protection of generators. Such situations are commonly associated with the conditions after splitting into islands of large interconnected power systems. In comparison to rotor angle stability, frequency stability is determined by the mean frequency of an island rather than the relative motion of machines. The reasons causing frequency instability are generally insufficient coordination of control and protection equipment, inadequate generation reserve or improper equipment response [62].

The characteristic time frames of frequency stability phenomena range from fraction of seconds, involving devices such as generator controls or underfrequency load shedding, to minutes, where devices such as load voltage regulators and prime mover energy supply are dominant. An undergenerated island with inadequate load shedding is an example of short term frequency instability. Long term frequency stability involves more complex phenomena associated for example with boiler protection or turbine overspeed controls [62].

2.3.1.2. Microgrids

There are some distinct differences between microgrids and conventional power systems which also affect the observed stability phenomena [65]. Microgrid feeders are relatively short and are operated at low or medium voltage levels with high R/X ratios. Consequently, the intrinsic coupling between voltages and reactive power and angles and active power is less distinct. The low short circuit capacity entails that a small change in microgrid configuration, e.g. the start up of a genset, can result in comparatively large frequency and voltage perturbations. Furthermore, the smaller size leads to higher uncertainty due to fluctuations in load and generation. Loading is typically unbalanced with up to 100 % difference between phases [66].

The differing characteristics also result in different types of stability problems. Transient and voltage stability issues typically occur more frequently than frequency stability problems in conventional systems. In microgrids, however, the lower inertia makes maintaining frequency stability more challenging. Frequency and voltage are strongly coupled in microgrids and instability is manifested by fluctuations in all system variables. The conventional classifications into angle, frequency and voltage stability is, therefore, not adequate.

Based on this discussion, it becomes apparent that the classification of stability phenomena in conventional power systems does not properly reflect the conditions in microgrids and new categories need to be identified. Possible identifiers are the relative size of the disturbance, the time-span, the physical cause, the methodology to analyse or predict the instability or the physical components that are involved in the process. The IEEE PES Task Force on Microgrid Stability puts the emphasis on the type of equipment and/or controllers involved [65].

A microgrid is defined stable if, after being subject to a disturbance, all state variables recover to a (possibly new) steady-state that satisfies the operational constraints and without the necessity of any involuntary load shedding. If loads are disconnected only in order to isolate faulted elements, the microgrid is considered stable if it meets the aforementioned criteria [65].

As illustrated in Fig. 2.3, the stability is divided into phenomena pertaining to equipment control system and to active and reactive power sharing and balance. In either category, the instability can be short- or long-term. Heavily loaded microgrids may show undamped oscillations with small load changes in the long term. On the other hand, poor coordination of power sharing schemes can quickly lead to oscillations beyond acceptable limits in the short term. The disturbances correspond to any exogenous inputs. Operational mode or set-point adjustments as well as load changes for example, are considered small

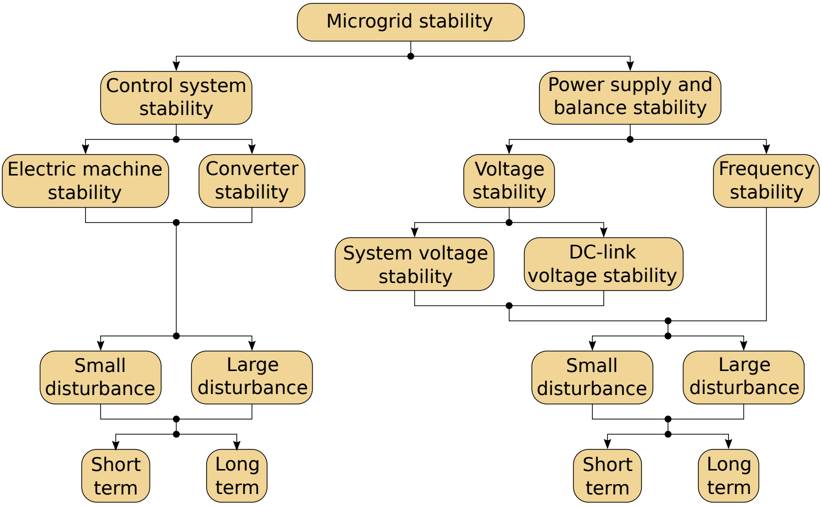

Figure 2.3.: Classification of microgrid stability [65].

disturbances. Disturbances such as unplanned transitions from grid-connected to islanded mode of operation, loss of generations units or short-circuits are referred to as large disturbances [65].

Power supply and balance stability are connected to the maintenance of power balance and the effective sharing of load demand among the DER, while satisfying operational requirements. This is associated with contingencies such as violation of DER limits, loss of a generation unit, poor power sharing among multiple DER or involuntary no-fault tripping. This may jeopardize the system frequency and cause large excursions at a high rate of change [67].

A large load step followed by inadequate system and protection response is one example. Undamped oscillations that last for a few seconds up to minutes can occur [68], which is rarely observed in conventional systems. The duration of such phenomena depends on the time it takes for the frequency protection to operate.

Voltage collapse in the form of a slow and sustained decay, as seen in conventional systems, is not an issue in microgrids due to the relatively short line lengths and smaller voltage drops. However, any changes in DER terminal voltages are almost immediately reflected in the rest of the system [69]. This necessitates proper coordination of DER (e.g. reactive power/voltage droop) to avoid high reactive power flows. Delayed voltage recovery after faults can also be a problem. Induction motors absorb high amounts of reactive power during voltage sags to re-magnetize, which may not be available [70].

Voltage stability is also an issue on the DC side of PED. Especially when operating close to the active power limit, undamped ripples can occur in the voltage across the DC-link capacitor when the reactive power demand increases [71].

Examples for short-term voltage instabilities include fast dynamic changes in the active/reactive power demand. Gradual steady state increase in demand and DER output limits being reached is an example for long-term voltage instability.

The second major grouping is the control system stability, which pertains to inadequate control schemes and/or poor tuning of equipment controllers. With regard to electric machine stability, the ability to return to synchronism was the major concern in conventional systems. However, this is less of an issue in microgrids as SM show high resiliency for faults even when relative angles are large and even if the fault is sustained for a long time as demonstrated in [72]. Synchronizing and damping torque problems have not been reported when SM are equipped with reasonably tuned AVRs and governors. Hence, SM instability in microgrids is mainly associated with inept tuning of AVRs and governors [65].

Converter stability is concerned with small- and large-perturbation instabilities of PED. Small-perturbation stability is a major issue for inner voltage and current control loops. Their tuning is challenging. High harmonic oscillations in the range hundreds of Hz or kHz may occur [73] in contrast to the low-frequency oscillations caused by outer power sharing controllers, which are attributed to power supply and balance stability. Besides inner loop tuning, high-frequency switching can trigger resonance of LCL filters. The bandwidth of PLLs of grid-feeding PED also plays a vital role in microgrid stability [74]. Another serious concern is the tripping of PED after large disturbances due to under-frequency and under-voltage protection schemes.

This work is dedicated mainly to small-disturbance/small-signal stability issues. A clear assignment to the categories described cannot be made. In fact, it will be shown that the inner loop controllers and PLL tuning have a significant impact on the power sharing and the time scales are not clearly separated. Hence, as defined above, control system stability has a certain impact on power supply and balance stability. However, as harmonics are not considered and the focus is placed on the power sharing of DER, the most appropriate categorisation for this work is power supply and balance stability. Droop control is used which affects both voltage and frequency stability. DC-link voltage stability is not considered as the DC capacitor is assumed large and the supply from the energy source is supposed to meet the AC side demand.

The part of this work dedicated to microgrid synchronization and the stress of microgrid components at breaker closing can be assigned to the category large disturbance

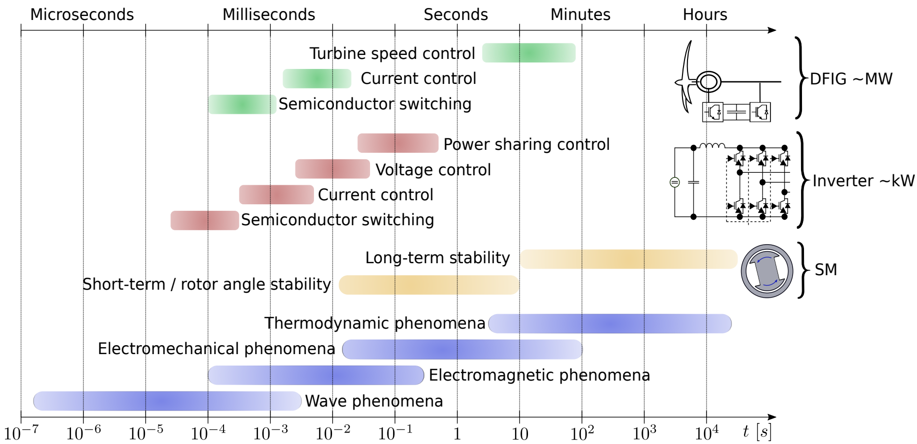

Figure 2.4.: Time frames of dynamic phenomena.

frequency stability.

2.3.1.3. Time Frames

Fig. 2.4 gives an overview of the time frames of basic power system dynamics phenomena, stability problems due to SM and controllers of DER investigated in this work. Power system dynamic phenomena may be resolved into four groups, based on their physical character: Wave, electromagnetic, electromechanical and thermodynamic. Although some dynamics belong to two or more groups while others lie on the boundary between groups, this broad classifications is convenient, but by no means absolute.

The fastest dynamics pertain to wave effects corresponding to the propagation of electromagnetic waves due to switching operations or lightning strikes. Electromagnetic dynamics are located in the machine windings following a perturbation. These dynamics are also involved in the response of protection systems or the interaction between electrical machines and the network [14]. Electromechanical phenomena are characterized by the oscillation of rotating masses of generators and motors after a disturbance and the prime mover control. Boiler control action in steam power plants are involved in the slow thermodynamic phenomena [61]. Apparently, one single model cannot accommodate the wide range of bandwidths in Fig. 2.4 [75].

The short and long term rotor angle stability of conventional power systems dominated by SM was discussed in Sec. 2.3.1.1. It becomes apparent that the dynamics of the controller of inverters in the kW class have a higher bandwidth than the dynamic phenomena affecting the stability of SM. This is the reason why the dynamics of network lines should generally not be neglected in the dynamic stability investigation of inverter-dominated power systems. The fast dynamics of the inner control loops interact with the network dynamics and the approximation to use algebraic equations for the network model can neglect important modes [76]. The bandwidth of the current controller should be ten times smaller than the switching frequency of the semiconductors and is usually around 1 kHz. The voltage controller ought to be about 3 to 5 times slower than the current controller. The power sharing control is the outermost controller of the cascade and its bandwidth is usually selected between 2 and 10 Hz [77].

The switching frequency of the DFIG is lower compared to the former inverter example in the kW range, due to the higher rated power in the MW range. This reduces the losses. Semiconductor switching is between about 1 and 8 kHz and the bandwidth of the current controller is again about 10 times lower, whereas the turbine speed control response can take up to several tens of seconds [78]. Grid-forming control, which necessitates a voltage control loop, is not considered for DFIG in this work.

2.3.2. Small-Signal Stability

The problem of predicting the small-signal stability of microgrids with high share of inverters has attracted researchers from various fields and so, several approaches have evolved. Reviews of some of the methods are presented in [79, 80, 81]. Three of the most widely applied approaches are introduced in the following sections.

2.3.2.1. Modal Analysis

Modal analysis is based on the state-space representation of dynamic systems. A set of n first order nonlinear ordinary differential equations of the following form describe the behaviour of a dynamic system:

$$\dot{x}_i = f_i(x_1, x_2, ..., x_n; u_1, u_2, ..., u_r; t) \text{ where } i = 1, 2, ..., n, \tag{2.3}$$

where n is the order of the system and r is the number of inputs. By using vector-matrix notation, this can be rewritten

$$\dot{x} = f(x, u, t). \tag{2.4}$$

The column vector x is denoted as the state vector and its entries x_i are the state variables. The column vector u represents the inputs to the system. Time is denoted by t, $\dot{x}$ is the derivative of a state variable x with respect to time. It is referred to a time-invariant system if the derivatives of state variables are not explicit functions of time:

$$\dot{x} = f(x, u) \tag{2.5}$$

The output variables of the system may be expressed in terms of state variables and input variables as

$$y = g(x, u), \tag{2.6}$$

where y is the column vector of outputs and g is a vector of nonlinear functions relating state and input variables to output variables.

At any instant of time t_0, the state of a system represents the minimum amount of information that is necessary to determine its future behaviour without reference to the input before t_0. State variables are any set of n linearly independent system variables that describe the state of the system. An n-dimensional euclidean space called state space may be used to represent the system state. The system state will change with time, whenever the system is not in equilibrium or the input is non-zero.

In the equilibrium, all derivatives $\dot{x}_1, \dot{x}_2, ..., \dot{x}_n$ are simultaneously zero. The equilibrium point must satisfy the equation

$$f(x_0) = 0, \tag{2.7}$$

where x_0 is the state vector x at the equilibrium point.

A system is linear if the functions $f_i (i = 1, 2, ..., n)$ in (2.5) are linear. Whereas a linear system has only one equilibrium state, more than one equilibrium points may exist for a nonlinear system. The input and the initial state has no influence on the stability of a linear system. On the other hand, the stability of a nonlinear system is dependent on the type and magnitude of input as well as the initial state. A nonlinear system is called locally or small-signal stable if it remains within a small region surrounding the equilibrium point when subject to a small perturbation. Finite stability is given when the state of a system remains within the finite region R. The criterion for global stability is that R includes the entire finite space.

By linearizing the nonlinear system equations about the equilibrium, local stability conditions can be investigated. Assuming that x_0 is the initial state vector and u_0 the input vector with respect to the equilibrium point, (2.5) becomes

$$\dot{x}_0 = f(x_0, u_0) = 0. \tag{2.8}$$

Perturbing the system from the above state results in:

$$x = x_0 + \Delta x; \quad u = u_0 + \Delta u, \tag{2.9}$$

where the prefix Δ represents a small deviation. The new state is described according to (2.5):

$$\dot{x}_0 + \Delta\dot{x} = f[(x_0 + \Delta x), (u_0 + \Delta u)] \tag{2.10}$$

Due to the small perturbations, the nonlinear functions $f(x, u)$ can be approximated in terms of first order Taylor's series expansion and it is obtained that

$$\Delta\dot{x}_i = \frac{df_i}{dx_1}\Delta x_1 + ... + \frac{df_i}{dx_n}\Delta x_n + \frac{df_i}{du_1}\Delta u_1 + ... + \frac{df_i}{du_r}\Delta u_r \tag{2.11}$$

with $i = 1, 2, ...n$. Likewise, referring to (2.6), it can be written that

$$\Delta y_j = \frac{dg_j}{dx_1}\Delta x_1 + ... + \frac{dg_j}{dx_n}\Delta x_n + \frac{dg_j}{du_1}\Delta u_1 + ... + \frac{dg_j}{du_r}\Delta u_r, \tag{2.12}$$

where $j = 1, 2, ..., m$. This leads to the linearized forms of (2.5) and (2.6):

$$\Delta\dot{x} = \boldsymbol{A}\Delta x + \boldsymbol{B}\Delta u \tag{2.13}$$

$$\Delta y = \boldsymbol{C}\Delta x + \boldsymbol{D}\Delta u \tag{2.14}$$

where

$$\begin{gathered}
\boldsymbol{A} = \begin{bmatrix} \frac{df_1}{dx_1} & \cdots & \frac{df_1}{dx_n} \\ \vdots & \ddots & \vdots \\ \frac{df_n}{dx_1} & \cdots & \frac{df_n}{dx_n} \end{bmatrix}, \quad \boldsymbol{B} = \begin{bmatrix} \frac{df_1}{du_1} & \cdots & \frac{df_1}{du_r} \\ \vdots & \ddots & \vdots \\ \frac{df_n}{du_1} & \cdots & \frac{df_n}{du_r} \end{bmatrix}, \\
\boldsymbol{C} = \begin{bmatrix} \frac{dg_1}{dx_1} & \cdots & \frac{dg_1}{dx_n} \\ \vdots & \ddots & \vdots \\ \frac{dg_m}{dx_1} & \cdots & \frac{dg_m}{dx_n} \end{bmatrix}, \quad \boldsymbol{D} = \begin{bmatrix} \frac{dg_1}{du_1} & \cdots & \frac{dg_1}{du_r} \\ \vdots & \ddots & \vdots \\ \frac{dg_m}{du_1} & \cdots & \frac{dg_m}{du_r} \end{bmatrix},
\end{gathered} \tag{2.15}$$

where Δx is the state vector of dimension n, Δy is the output vector of dimension m, Δu is the input vector of dimension r, A is the state or plant matrix of size $n \times n$, B is the control or input matrix of size $n \times r$, C is the output matrix of size $m \times n$, D is the feed-forward matrix which defines the proportion of input which appears directly in the output of size $m \times r$. These partial derivatives are formed around the equilibrium point where the small perturbation is analysed. The state equations in the frequency domain are obtained using the Laplace transform with the Laplace operator s:

$$s\Delta x(s) - \Delta x(0) = \boldsymbol{A}\Delta x(s) + \boldsymbol{B}\Delta u(s) \tag{2.16}$$

$$\Delta y(s) = \boldsymbol{C}\Delta x(s) + \boldsymbol{D}\Delta u(s). \tag{2.17}$$

The formal solution of the state equations shows that the poles of $\Delta x(s)$ and $\Delta y(s)$ are the roots of the equation [60]

$$\det(s\boldsymbol{I} - \boldsymbol{A}) = 0, \tag{2.18}$$

where $\boldsymbol{I}$ is the unity matrix. This is referred to as the characteristic equation and the values of s which satisfy the above conditions are known as eigenvalues λ of the matrix A. The system is asymptotically stable if the eigenvalues have negative real parts and it is unstable if at least one of the eigenvalues has a positive real part, which is also referred to as the Routh-Hurwitz criterion. On the basis of the first order approximation, it is not possible to generally determine the stability if the eigenvalues have real parts equal to zero. A mode is non-oscillatory if its eigenvalue is real. Hence, a negative real eigenvalue corresponds to a decaying mode. The faster the decay, the larger the eigenvalue's magnitude. Aperiodic instability is represented by a positive real eigenvalue. Oscillatory modes are present in systems with complex eigenvalues given as conjugate pairs. The frequency of oscillation is derived from the imaginary component, whereas the damping depends on the real component. Therefore, for a complex pair of eigenvalues $\lambda = \sigma \pm j\omega$. The frequency of oscillation in Hz is given by $f = \frac{\omega}{2\pi}$. The damping ratio ζ is often used as a measure for oscillatory modes in power systems

$$\zeta = \frac{-\sigma}{\sqrt{\sigma^2 + \omega^2}}. \tag{2.19}$$

The damping ratio ζ determines the rate of decay of the amplitude of the oscillation with respect to cycles of oscillation.

For an eigenvalue λ_i, there exists at least one non-zero vector ϕ_i which satisfies (2.20). The vector ϕ_i is called a right eigenvector of the eigenvalue λ_i [82].

$$\boldsymbol{A}\phi_i = \lambda_i \phi_i. \tag{2.20}$$

For an eigenvalue λ_i, there exists at least one non-zero vector Ψ_i which satisfies (2.21). In this case, the vector Ψ_i is called a left eigenvector of the eigenvalue λ_i.

$$\boldsymbol{A}^T \Psi_i = \lambda_i \Psi_i \quad (\text{or } \Psi_i^T \boldsymbol{A} = \lambda_i \Psi_i^T). \tag{2.21}$$

A right eigenvector indicates on which variables a mode is more observable and, therefore, carries mode observability information. It reflects relative magnitudes and relative phases of the corresponding system variables. A left eigenvector indicates by modulation of which system variables the mode is more controllable and, therefore, carries mode controllability information and determines the dominance of its mode. Participation factors, transfer function residues and mode sensitivities can be derived from eigenvectors and they contain rich information about the dynamic properties of a system under study.

A shortcoming of right and left eigenvectors is that their elements are dependent on units and scaling associated with the state variables, which hampers the identification of the relationship between the states and the modes. Therefore, a matrix referred to as the participation matrix P was introduced [83], which combines the right and left eigenvectors to derive a measure of the association between the state variables and the modes:

$$\boldsymbol{P} = [p_1, p_2, \ ... p_n], \tag{2.22}$$

with

$$p_i = \begin{bmatrix} p_{1i} \\ p_{2i} \\ \vdots \\ p_{ni} \end{bmatrix} = \begin{bmatrix} \phi_{1i}\Psi_{i1} \\ \phi_{2i}\Psi_{i2} \\ \vdots \\ \phi_{ni}\Psi_{in} \end{bmatrix} \tag{2.23}$$

where ϕ_{ki} is the k^{th} entry of the right eigenvector ϕ_i and Ψ_{ik} is the kth entry of the left eigenvector Ψ_i. The element $p_{ki} = \phi_{ki}\Psi_{ik}$ is referred to as the participation factor. It represents the relative participation of the k^{th} state variable in the i^{th} mode, and vice versa. It is beneficial that p_{ki} is dimensionless due to the effect of multiplying elements of the left and right eigenvectors. The participation factor combines controllability and observability and is also a measure of the sensitivity of the eigenvalue λ_i to the diagonal elements a_{kk} of the state matrix A:

$$p_{ki} = \frac{d\lambda_i}{da_{kk}}. \tag{2.24}$$

A literature review on the usage of modal analysis for microgrid stability assessment is provided in the following and advantages and shortcomings of the method are revealed. By direct comparison to numeric time domain simulation, modal analysis features a number of advantages [82]. It reveals rules behind complicated phenomena of system dynamics through a systematic approach, whereas in simulation method various disturbances are applied and plotted responses are observed in a trial-and-error approach. Modal analysis allows for the detailed and individual analysis of weakly damped and unstable modes. The pattern of each mode is indicated unambiguously. However, modes of different frequencies and damping are mixed in time domain simulation, which hinders the evaluation of the results. The systematic approach behind modal analysis can reveal information about the proper tuning of controllers or the siting of damping controllers, for instance through participation factors. In contrast, simulation results lack such systematic information.

On the other hand, simulation has a wide field of application, whereas modal analysis is only suitable for small-signal stability. Numeric simulation also captures non-linearities and its results may be more intuitive to some engineers. A drawback of modal analysis is that it requires detailed modelling of the entire system and these data may not always be available. Moreover, models become increasingly complex for larger systems [82].

Modal analysis has been widely applied in the stability analysis of islanded microgrids. [84] investigates the small-signal stability of a microgrid with droop-controlled inverters when the droop gains are varied. It is concluded that the stability mainly depends on the smallest electrical distance (impedance) between two inverters occurring in the microgrid. Hence, the stability deteriorates with smaller electrical distances between grid-forming inverters. This contrasts with large interconnected power systems with SM, where longer lines impair the stability.

The stability of an existing MV microgrid on a physical island is analysed in [48], considering primary, secondary and tertiary control. Diesel powered SM are the grid-forming units that interact with grid-supporting battery storage systems. The time delay of communication is incorporated in the stability analysis. A microgrid comprising various components such as a wind turbine with asynchronous machine, a SM and battery storage systems is regarded in [85]. The prediction of the dynamics is successfully verified by time-domain simulation. A number of DER types, such as SM, wind turbines with full-size converter and battery storage systems, are also investigated in [86]. The dynamics of the governor and AVR are neglected.

[87] examines the stability of microgrids with droop-controlled diesel SM and inverters, neglecting the line dynamics. The droop gains of the diesel SM dominate the stability. Similar analysis is conducted in [88]. It is concluded that smaller droop gains of the SM and a non-linear droop with derivative term of the inverter improve the stability. Moreover, the influence of the operating point on the dominant modes is found to be minor. This observation is confirmed in [89, 90] concluding that the system does not exhibit a high degree of non-linearity. On the other hand, [91] argues that the linearisation around an operating point is not suitable to ensure global stability and that the lack of exact modelling parameters impedes the small-signal analysis. Hence, an online approach based on Singular Entropy Matrix Pencil method [92] is proposed, where the modes are

continually extracted from measurement data.

The small-signal stability of microgrids with grid-forming and grid-feeding inverters is examined in [93]. The upshot is that the dynamics of grid-forming droop controlled and grid-feeding inverters are nearly decoupled. An energy management system that provides optimized droop coefficients every 15 seconds is implemented in [94] and some worst case scenarios are identified. [90] optimizes droop gains not only with regard to stability, but also considers rate of change of frequency relays. A trade-off is made between stability and limiting of frequency transients. Hopf Bifurcation is utilized in [95, 96] to allow for an efficient determination of parameter ranges with stable system behaviour.

2.3.2.2. Lyapunov's Direct Method

Lyapunov stability is widely used in control theory [97]. Furthermore, Lyapunov stability is an important characteristic of an equilibrium point of a dynamic system. The method attempts to prove stability directly resorting to suitable functions which are defined in the state space. It can be formalized by the following definitions [60]:

- The equilibrium of (2.5) is stable if there exists a positive definite function $V(x_1, x_2, ..., x_n)$ such that its total derivative $\dot{V}$ with respect to (2.5) is not positive.
- The equilibrium of (2.5) is stable if there exists a positive definite function $V(x_1, x_2, ..., x_n)$ such that its total derivative $\dot{V}$ with respect to (2.5) is negative definite.
- The system is stable in that region in which $\dot{V}$ is negative semi definite, and asymptotically stable if $\dot{V}$ is negative definite.

For further information on the applications of Lyapunov's direct method, the reader is referred to [98].

The main advantage of Lyapunov-based techniques is that they quantify the magnitude of the deviations or excursions the system can sustain by estimating the domain of asymptotic stability. This facilitates the design and optimization of control and protection systems and provides an estimate of the size of disturbance that can be tolerated. The large-signal non-linear stability analysis has a much broader domain of validity compared to the small-signal linear analysis. A large-signal stable system is also small-signal stable, whereas the opposite is not inevitably true [99].

The large size of interconnected power systems hinders the application of Lyapunov's method. On the other hand, the manageable size of microgrids facilitates the usage. However, the number of publications on large-signal stability studies of microgrids is limited compared to small-signal stability studies. Numeric simulation is a more common means of large-signal studies than Lyapunov-based techniques [100].

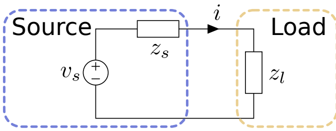

Figure 2.5.: Source and load subsystems for impedance-based stability analysis.

One of the main drawbacks is that there is no general systematic method to define the Lyapunov's function $V(x)$ and it can be easily computed only for comparatively simple systems [101]. This necessitates system simplifications [102] which are not applicable to all types of controllers and networks.

The stability of a very small microgrid consisting only of an inverter and a load is investigated with Lyapunov's method in [103]. An islanded microgrid with grid-forming droop controlled inverters is analysed in [97]. To apply the method, lines are assumed purely inductive. [104] simplifies the model by neglecting the inner current and voltage loop of the inverter and using a Taylor approximation for the line dynamics. It is seen that the parameters of the interconnection line between grid-forming inverters play a dominant role for the system stability. The criteria for stability found in [104] are applied to a small microgrid in [105] by testing the criteria for each pair of droop controlled inverters.

2.3.2.3. Impedance-Based Stability

The impedance-based approach entails that each load and source is described by its input and output impedance. In order for the interconnected source-load system to be stable, the ratio of the source output impedance to the load input impedance must satisfy the Nyquist stability criterion. It was first presented in [106] for DC systems and was expanded to AC in [107]. Fields of application are the the design of switching-mode power supplies with input filters, as well as more complex DC distributed power systems [108]. The method was generalized for AC power systems in [79].

As given in Fig. 2.5, the system is partitioned into the source subsystem represented by its Thevenin equivalent circuit which consists of an ideal voltage source in series with an output impedance z_s, whereas the load subsystem is modelled by its input impedance z_l. With almost all power electronic circuits being non-linear, this linear approximation is valid only for small-signal analysis. The current $i(s)$ flowing from the source to the load is then

$$i(s) = \frac{v_s(s)}{z_l(s) + z_s(s)}. \qquad (2.25)$$

This can be rearranged resulting in [109]

$$i(s) = \frac{v_s(s)}{z_l(s)} \frac{1}{1 + z_s(s)/z_l(s)}. \tag{2.26}$$

The source voltage is assumed stable when unloaded and the load current is assumed stable when powered from an ideal source. It follows that both $v_s(s)$ and $1/z_l(s)$ are stable. The stability of the current then depends on the stability of the second term on the right-hand side of (2.26):

$$H(s) = \frac{1}{1 + z_s(s)/z_l(s)}. \tag{2.27}$$

It is observed that $H(s)$ resembles the close-loop transfer function of a negative feedback control system with a unity forward gain and a feedback gain of $z_s(s)/z_l(s)$. Analysis by linear control theory shows that $H(s)$ is stable if and only if $z_s(s)/z_l(s)$ satisfies the Nyquist stability criterion [106].

It is important to note that the source is assumed to be a voltage source that is stable when unloaded. Grid connected inverters, however, are often controlled in the current-injection or grid-feeding mode and do not show voltage source behaviour. An impedance-based stability criterion for current-source system is developed in [109]. It is seen that a current source should have a high parallel output impedance in contrast to voltage source systems, where the output series impedance should be low in order to ensure stable operation over a wide range of loads.

One shortcoming of the impedance-based method is the limited observability of certain states as a consequence of its dependence on the definition of local source-load subsystems. This entails the necessity to investigate the stability at several subsystems interfaces, if a more general statement on the system stability is to be made. Therefore, critical locations have to be identified, where the application of the method reveals the influence of a controller or a passive component on the stability [110]. Another disadvantage is that the physical insight into the model gets lost when the impedance model is built.

An advantage is that the impedance-based analysis captures all the small-signal features of the real system, including the PWM, for instance. It can therefore predict sustained harmonic oscillations of voltage source converters. Hence, it is recommended in [110] to ensure the global stability resorting to eigenvalue-based analysis and to avoid sustained harmonic oscillation at local AC-DC interfacing points by impedance-based analysis. Another benefit is that the system model is readily obtained in the form of a linear network. Analysing system stability at a local point of the network merely involves the computation of the equivalent load and source subsystem impedance based on linear network theory [79]. If an analytical impedance model cannot be derived, the input and output impedance can be obtained through measurement or by numerical simulation. Furthermore, analysis can point to possible solutions, indicating how the input and output impedances should be reshaped to stabilize the system.

The stability of an AC distribution system based on power electronics is investigated in [111] using the impedance method in the dq frame. The transformation into the dq frame results in two decoupled DC systems and impedance specification criteria developed for DC systems can be readily applied. The dq reference frame is also utilized in [112] for impedance-based analysis of networks with a high share of DER in combination with HVDC. The influence of the PLL bandwidth on the stability of three-phase inverters in weak grids is investigated in [113, 114]. The non-linear low-frequency dynamics of PLLs are also analysed in [115] laying the basis to determine the impact of large penetration levels of DER. [116] optimizes the current controller and the PLL parameters of a grid-feeding inverter in a weak grid. Damping methods for inverter LCL filter are investigated in [117] and future trends are identified. [118] focuses on oscillatory phenomena between wind farms and HVDC. It is stated that, as a rule of thumb, the system operates stably when the bandwidth of the HVDC rectifier (which is the source) is faster than the bandwidth of the wind farm inverters (load).

2.3.2.4. Numerical Simulation

Numerical simulation is used in this work for the purpose of results illustration. Moreover, it is used to evaluate the ability of a system to quickly reach a steady-state after perturbations. Another application is the microgrid reconnection with the bulk power system and the evaluation of the component loadings in this process.

Depending on the nature of the study, components can be represented by ordinary differential equations, differential-algebraic equations or partial differential equations in power system transient studies. If the focus is placed on the local distribution of electromagnetic fields along a transmission line, a distributed parameter representation with partial differential equations will be used. When the interconnection of electromagnetic fields of different components is of concern, the lumped parameter description of the interconnecting lines is sufficient. The electromagnetic transients can even be omitted if the purpose of the analysis are the slower and more system wide electromechanical transients [119]. A closer look at the network representation in LV microgrids used in this work is taken in Sec. 3.4.

Power system models comprise slow continuous dynamics, like the frequency regulation of SM, as well as fast dynamics like controllers of inverters of PED. Relay logics of protective devices or switched loads exhibit also discrete dynamics. Being interconnected, the mathematical representation ought to capture the continuous and discrete nature of the components. Linearity is another important aspect of the mathematical representation of a system. Power systems contain a number of sources of nonlinearities. A pervasive example is the power transfer over the line impedance which is described by trigonometric functions as exemplified in (2.1) for active power and a purely inductive line. Power systems are, therefore, an important class of hybrid systems, described as large-scale, nonlinear systems with fast/slow continuous and discrete states [119].

The software Matlab/Simulink [120], which is based on a causal modelling approach, is used in this work. The main difference to non-causal (sometimes also called acausal) modelling, such as the Modellica language [121], lies in the distinct definition of input and output variables. In non-causal modelling, systems are built by simply connecting the interface of subsystems. The software automatically and conveniently detects the variables to be exchanged between subsystems and the user simply specifies the model equations which need to be satisfied. On the other hand, in causal modelling, rigid variable input and output relations need to be defined for each subsystem [119].

In time-domain simulations, the nonlinear system behaviour is approximated by piecewise linear system behaviour. To obtain the system state over time, computational efficient methods and algorithms for linear systems are applied. Their efficiency is dictated by the degree of system nonlinearities. Discrete events can be thought as transitions from one continuous dynamic system to another, affecting the set of differential algebraic equations.

The suitability of numerical integration methods is highly dependent on the characteristics of the simulated system. It is necessary to solve a large nonlinear and stiff set of differential-algebraic equations for the combined simulation of the various timescale phenomena occurring in microgrids. The major characteristics of a numerical simulation method are its numerical stability, accuracy and efficiency. Commonly used methods are Backward Euler, trapezoidal method and Gear's method [119]. For enhanced efficiency, strategies such as automatic step size control, application of dishonest Newton method (keeping the Jacobian matrix constant over a number of iterations) and sparse matrix solution techniques are frequently used. The step size should be adjusted small enough if the states vary rapidly and can be chosen large after transients have decayed to increase the efficiency. Matlab's ode23tb solver for stiff systems is used in this work. It is an implementation of an implicit Runge-Kutta formula, where the first stage is a trapezoidal rule step an the second stage is a backward differential formula of order two [119].

Table 2.2.: Summary of approaches to stability analysis.

Numerical simulation	Lyapunov's direct method
+ Intuitive method + Wide field of application + Supports all types of models and controllers (discrete, nonlinear, unbalanced) − Computationally expensive for complex systems − Various disturbances have to be simulated and evaluated in a trial-and-error approach − Modes of different frequencies and damping are mixed, no systematic information	+ Estimates the domain of asymptotic stability or ensures global stability + Broad domain of validity − No general systematic method to define Lyapunov's function − Necessitates model simplifications
Impedance method	**Modal analysis**
+ Captures all small-signal features, including PWM, harmonics, etc. + Impedance model is readily obtained analytically, through numerical simulation or measurement + Provides information how input and output impedances should be reshaped to stabilize system − Limited observability of certain states − Necessity to investigate several source-load subsystems − Physical insight into the model gets lost	+ Systematic and flexible approach + Individual and detailed analysis of modes revealing rules behind complicated phenomena + Delivers information for proper controller tuning and siting of devices − Analyses only linearised system at operating point (no global stability) − Requires detailed information on model parameters − Models become complex for larger systems

A closer look at the advantages and disadvantages of the numeric simulation approach is also taken in Sec. 2.3.2.1 on modal analysis.

2.3.2.5. Comparison

Table 2.2 summarizes the advantages and disadvantages of the approaches described. Modal analysis is the most widely applied approach in literature and is also selected as the main method for this work. The primary reason is its flexibility and the fact that the model can be easily extended for any DER type. Furthermore, the method is easily combined with numeric simulation, as done in this work, using the non-linear model of the system for the simulation and linearized snapshots for modal analysis. Another important advantage for this work is that the impact of control parameter variations and model simplifications on the dominant modes can be analysed in detail and visualized in eigenvalue plots.

2.4. Model Order Reduction

2.4.1. Classification

Model simplifications reduce the computational cost of numeric simulation and pave the way for stability analysis with Lyapunov's method. Reduced complexity can also give better insight into key factors influencing stability. Moreover, the reduced accuracy lowers the chances of modelling errors when exact power system data are not available.

Three categories of model order reduction techniques are identified according to [122, 123]:

- Parameter optimizations
- Polynomial approximations
- State truncations

Gray/black-box system identification is an example of parameter optimization, where parameter sets of reduced-order models are optimized to minimize errors of response data between reduced and original models.

The basis of polynomial approximation is the matching of moments or Markov parameters between the original and reduced-order models, which are applied to transfer function models. The original state-space model is usually transformed to reconfigure the states according to observability, controllability or response time in state truncation methods. Examples are balanced transformation and singular perturbation theory, which is detailed in the next Section.

Prony method is used in [124] to propose black-box models for microgrids on the basis of voltage, current and output power measurements. Gray-box system identification with particle swarm optimization is applied in [125] to obtain equivalent frequency and active power dynamics of a microgrid.

Polynomial approximation in the form of discarding fast states first, but adding back a reduced representation of their interaction with the slow states is used in [126].

The fast modes can be added back to the reduced model by pole-zero truncation [127], extracting the dominant transfer functions of the fast subsystem.

2.4.2. Singular Perturbation Theory

Singular perturbation theory is frequently used to reduce the order and complexity of power system models and is also applied in this work. The modelling of large-scale power systems has been thoroughly investigated and a certain degree of simplification has been established in literature. A straightforward model order reduction follows from a distinct separation of time-scales. One important example is the neglect of line and SM stator dynamics in phasor simulation of interconnected power systems. Although the large time constants of SM are often stated as the main reason for the validity of the phasor simulation approach in literature, it is interesting that some new research points out that the validity rather follows from the large values of the impedances between generators in interconnected power systems [104].

However, there is a lack of experience and systematic studies of microgrids and inverter modelling with proper validation and verification [104]. In power converter design, the speed of slow states is limited from below due to the absence of inertia, whereas fast states are confined from above by the limitation of switching frequency and filters. Therefore, the interaction between fast and slow states can be significant as their timescales may actually be quite close [126]. Pushing inverter control parameters to extremes in order to allow for a fast response of the cascaded control exacerbates the interaction between slow and fast states.

Despite their very fast nature, the impact of network dynamics in microgrids was pointed out in [128, 129]. [130] shows that the full-order model predicts instability, whereas a reduced-order (Kuramoto's) model forecasts stable behaviour over a wide range of parameters, which corroborates the inaccuracy of oversimplified models. On the one hand, a natural time-scale separation exists in microgrids, for instance between the droop controller and the inner control loops of inverters. However, it follows from literature that even very fast states can influence the slow modes [104] and the justification of exclusion of certain degrees of freedom based on simple timescale ratio could be an oversimplification.

A general method for stability analysis of multiple timescale systems based on singular perturbation theory is presented in the following. As elaborated in Sec. 2.3.2.1, the dynamics of a system at an operating point can be described by a set of first-order differential equations linearized around the equilibrium point:

$$\Delta\dot{x} = \boldsymbol{A}\Delta x, \tag{2.28}$$

where x is a set of system variables and A is the corresponding Jacobian matrix. The simplification aims at eliminating the "fast" states x_f and to consider only the relevant slow states x_s. Hence, the system

$$\left[\begin{array}{c} \Delta\dot{x}_s \\ \hline \Delta\dot{x}_f \end{array}\right] = \left[\begin{array}{c|c} \boldsymbol{A_{ss}} & \boldsymbol{A_{sf}} \\ \hline \boldsymbol{A_{fs}} & \boldsymbol{A_{ff}} \end{array}\right] \left[\begin{array}{c} \Delta x_s \\ \hline \Delta x_f \end{array}\right] \tag{2.29}$$

is separated into two subsystems corresponding to slow and fast states:

$$\Delta\dot{x}_s = \boldsymbol{A_{ss}}\Delta x_s + \boldsymbol{A_{sf}}\Delta x_f, \tag{2.30}$$

$$\epsilon\Delta\dot{x}_f = \boldsymbol{A_{fs}}\Delta x_s + \boldsymbol{A_{ff}}\Delta x_f, \tag{2.31}$$

where ϵ is a set of parameters designating fast degrees of freedom [131]. One possible way to simplify the system is to fully neglect the left-hand side of 2.31 [84], i.e. set ϵ to zero, and inserting (2.31) into (2.30) leading to

$$\Delta\dot{x}_s = (\boldsymbol{A_{ss}} - \boldsymbol{A_{sf}}\boldsymbol{A_{ff}^{-1}}\boldsymbol{A_{fs}})\Delta x_s, \tag{2.32}$$

which represents the zero's order approximation of the perturbation approach. The accuracy of the model can be enhanced by considering the next order, stating that the first derivative of Δx_f is non-zero, while the second derivative is negligible [104, 132]. It follows that

$$\Delta x_f \approx \Delta x_f^{(0)} + \Delta x_f^{(1)}, \tag{2.33}$$

where the superscripts in brackets designate the orders of derivatives. Inserting into (2.31) results in

$$\epsilon\Delta\dot{x}_f^{(0)} + \epsilon\Delta\dot{x}_f^{(1)} = \boldsymbol{A_{fs}}\Delta x_s + \boldsymbol{A_{ff}}\Delta x_f^{(0)} + \boldsymbol{A_{ff}}\Delta x_f^{(1)}. \tag{2.34}$$

Neglecting second order terms and separating the zero and first order terms leads to

$$\boldsymbol{A_{fs}}\Delta x_s + \boldsymbol{A_{ff}}\Delta x_f^{(0)} = 0, \tag{2.35}$$

$$\epsilon\Delta\dot{x}_f^{(0)} = \boldsymbol{A_{ff}}\Delta x_f^{(1)}, \tag{2.36}$$

and finally

$$\Delta x_f^{(0)} = -\boldsymbol{A_{ff}^{-1}}\boldsymbol{A_{fs}}\Delta x_s, \tag{2.37}$$

$$\Delta x_f^{(1)} = -\boldsymbol{A_{ff}^{-1}}\epsilon\boldsymbol{A_{ff}^{-1}}\boldsymbol{A_{fs}}\Delta\dot{x}_s. \tag{2.38}$$

Inserting the last two equations as an approximation for Δx_f in (2.30) yields

$$(\boldsymbol{I} + \boldsymbol{A_{sf}} \boldsymbol{A_{ff}^{-1}} \epsilon \boldsymbol{A_{ff}^{-1}} \boldsymbol{A_{fs}}) \Delta \dot{x}_s = (\boldsymbol{A_{ss}} - \boldsymbol{A_{sf}} \boldsymbol{A_{ff}^{-1}} \boldsymbol{A_{fs}}) \Delta x_s, \tag{2.39}$$

where $\boldsymbol{I}$ represents a unity matrix. From this general expression it can be concluded that the stability of such a system is guaranteed if the full state matrix $(\boldsymbol{I}+\boldsymbol{A_{sf}} \boldsymbol{A_{ff}^{-1}} \epsilon \boldsymbol{A_{ff}^{-1}} \boldsymbol{A_{fs}})^{-1} (\boldsymbol{A_{ss}} - \boldsymbol{A_{sf}} \boldsymbol{A_{ff}^{-1}} \boldsymbol{A_{fs}})$ satisfies the Routh-Hurwitz criterion.

3. Modelling

3.1. Introduction

This section details the microgrid component models used for simulation and modal analysis. It starts with the selection of a suitable modelling and simulation software. A whole section is dedicated to reference frame transformations as they are pervasive in power system modelling. Furthermore, several approaches to efficiently and yet accurately model the network line dynamics are elaborated. Going beyond the typical phasor and natural abc-frame models, the $dq0$ model and a reduced first order Taylor approximation are depicted.

The modelling of PLLs is described as they are used in DER as well as loads. The major part of this chapter deals with the DER modelling. At first, power sharing strategies that are applicable to all types of DER are introduced. A special focus is placed on different droop control strategies and VI. Differences and similarities between the power sharing approaches are pointed out. Afterwards, the DER types PED, diesel SM and DFIG wind power plants are discussed. LCL filter design and the tuning of inner control loops are detailed. Model-order reduction techniques found in literature are introduced and a new approach that preserves the dynamics of the voltage controller for grid-forming PED is proposed.

The dynamic impact of loads is not the focus of this work and a simple model is used. The model of the synchrocheck, which controls the voltage at the point of coupling at microgrid synchronization with the bulk system, is introduced. The chapter closes with the depiction of an example model of a microgrid in the dq-frame.

Only three-phase systems are treated in this thesis. To simplify the diagrams, the single-phase representation is usually shown.

3.2. Software

Simulink [120] software is used for numerical simulation as well as linearization of the state-space model at certain operating points in this work. Simulink offers more flexibility compared to other options, including commercial software. Its control systems toolbox also comes with many useful features for linear system analysis.

However, it was found that its SimPowerSystems toolbox with specialized technology for power system modelling is not efficient enough for the purposes of this work. Moreover, it is not free of bugs. Therefore, all models are build from basic simulink blocks, such as integrators, gains or state-space models (one exception is the DFIG wind power plant, where the built-in model is used). In combination with the network modelling approaches introduced later in this chapter, this drastically improved numerical simulation performance. Simulink's graphical modelling approach can be helpful at times, but also increases the time and effort for the scripting automation of recurring tasks, such as the network construction.

3.3. Reference Frame Transformation

Reference frame transformations are used in many contexts of power system modelling, control and analysis. Their original application were AC machines to eliminate time-varying inductances [133]. They are advantageous for component controllers as the transformation into a synchronously rotating reference frame leads to static variables during steady-state operation. This is also taken advantage of for efficient simulation of power systems as larger integration time steps are possible.

The transformation of three phase variables x_{abc} from the stationary to the arbitrary reference frame, also referred to as the Park transform, can be expressed as [134]

$$x_{dq0} = \boldsymbol{K_s} x_{abc}, \tag{3.1}$$

where

$$x_{dq0}^T = [x_d \; x_q \; x_0], \tag{3.2}$$

$$x_{abc}^T = [x_a \; x_b \; x_c], \tag{3.3}$$

$$\boldsymbol{K_s} = \frac{2}{3} \begin{bmatrix} cos(\theta) & cos(\theta - \frac{2\pi}{3}) & cos(\theta + \frac{2\pi}{3}) \\ sin(\theta) & sin(\theta - \frac{2\pi}{3}) & sin(\theta + \frac{2\pi}{3}) \\ \frac{1}{2} & \frac{1}{2} & \frac{1}{2} \end{bmatrix}. \tag{3.4}$$

The velocity and angular position of the arbitrary reference frame are related as

$$\frac{d\theta}{dt} = \omega_s. \tag{3.5}$$

The factor $2/3$ preserves the amplitude of the signals. Other variants of the Park transform

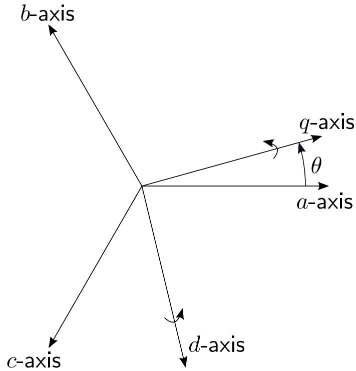

Figure 3.1.: Natural abc and rotating dq (zero sequence omitted) reference frame.

exist that follow the power invariant principle. The inverse transformation is

$$\boldsymbol{K_s^{-1}} = \begin{bmatrix} cos(\theta) & sin(\theta) & 1 \\ sin(\theta - \frac{2\pi}{3}) & sin(\theta - \frac{2\pi}{3}) & 1 \\ sin(\theta + \frac{2\pi}{3}) & sin(\theta + \frac{2\pi}{3}) & 1 \end{bmatrix}. \tag{3.6}$$

In symmetrically configured systems, the zero sequence component x_0 can be omitted. The reference frames are illustrated in Fig. 3.1.

The transformation of the variables x_{dq} from an arbitrary reference with the angle θ_1 to another with the angle θ_2 is formulated as

$$x_{DQ} = \boldsymbol{K_a} x_{dq}, \tag{3.7}$$

where

$$\boldsymbol{K_a} = \begin{bmatrix} cos(\theta_{diff}) & -sin(\theta_{diff}) \\ sin(\theta_{diff}) & cos(\theta_{diff}) \end{bmatrix}, \tag{3.8}$$

and $\theta_{diff} = \theta_1 - \theta_2$. The inverse transformation is

$$\boldsymbol{K_a^{-1}} = \begin{bmatrix} cos(\theta_{diff}) & sin(\theta_{diff}) \\ -sin(\theta_{diff}) & cos(\theta_{diff}) \end{bmatrix}. \tag{3.9}$$

3.4. Network

3.4.1. Network Modelling for Inverter-Dominated Power Systems

The dynamic behaviour of large-scale power systems is becoming more complex with the increased penetration of DER and especially PED. This development has led to several modelling approaches attempting to facilitate the analysis of dynamic phenomena [135].

A technique to model the power system in time domain used in classical EMT simulation is the native abc reference frame, resulting in the sinusoidal waveform depicted in Fig. 3.2a.), assuming that there are no harmonics present. This is the most general approach as it is valid over a wide range of frequencies and can be applied to unbalanced systems.

The dynamics of power systems have been dominated by large SM with high inertia and slow dynamic response in the past. On the basis of time-varying phasor models (also referred to simply as phasor models) neglecting the line dynamics, the dynamic processes of large-scale interconnected power systems were successfully analysed. A key assumption of this approach is that AC quantities can be mapped to quasi-constant signals, because phasors are slowly changing in comparison to the system frequency. This entails that the resulting models have a well-defined operating point, are time-invariant in steady-state and can be described using purely algebraic equations, neglecting fast line dynamics. Resulting from these advantages, the widespread use of quasi-static models has historically enabled studies of machine stability, inter-area oscillation and other slow dynamic phenomena [28, 136, 137].

With the advent of small DER and fast acting PED, new challenges have emerged. Voltage and current signals contain increasing amounts of harmonics and can exhibit fast amplitude and phase variations which are neglected in phasor simulation [119]. To bridge this gap, several alternative modelling techniques have been proposed, among them approaches that apply a transformation into the $dq0$ reference frame. Although in

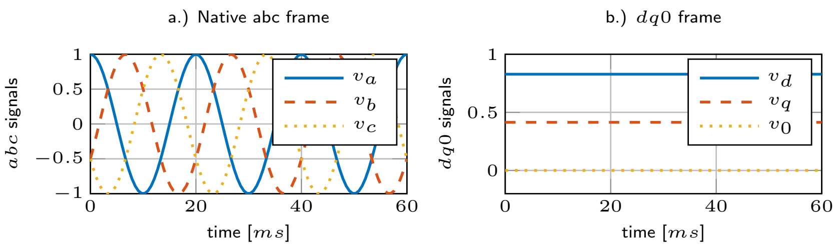

Figure 3.2.: Comparison of signals in the abc and $dq0$ frame.

Table 3.1.: Summary of approaches for dynamic modelling of power networks [135].

	Operating point / small signal analysis	High frequency dynamics	Asymmetric networks	Numerical efficiency
abc	×	$\surd$	$\surd$	×
Time var. phasor	$\surd$	×	×	$\surd$
$dq0$	$\surd$	$\surd$	×	$\surd$
Dynamic phasor	$\surd$	$\surd$	$\surd$	see text

some literature this is described as an entirely new approach, actually the same frame transformation is used for time varying phasors. The novelty is that the transients are not neglected as described below.

These approaches based on the $dq0$ transformation share with time-varying phasors the advantage of a well defined operating point and map AC-signals to quasi-constant signals, as shown in Fig. 3.2. Additionally, they are derived from physical representations directly and are inherently transient, remaining accurate at high frequencies. A drawback of $dq0$ quantities is that they are not as general as abc-based models and are beneficial mainly when the system is symmetrically configured.

Time-varying phasor and $dq0$-based models are compared in [138, 139] and it is shown that even if the frequencies in the time-varying phasor model are smaller than the nominal frequency ω_n, this does not automatically imply that the quasi-static model correctly describes the system. It is claimed that, as a rule of thumb, the quasi-static approximation is not valid, if the dominant states of the $dq0$ model are unstable. Consequently, time-varying phasor models can be inaccurate in the distinctly important margin between stability and instability. It is demonstrated in [128, 129] that network dynamics, despite their fast nature, have a significant impact on the dynamics of inverter dominated LV microgrids. However, the R/X ratios ($R/X \approx 1$ in [128] and $R/X \approx 0.16$ in [129]) of the examined power lines are much smaller than in conventional LV systems.

Dynamic phasors are another modelling technique that has become increasingly popular. They represent voltage and current signals by Fourier series expansion, where harmonic components are evaluated over a moving time window [140, 141]. In order to allow for an accurate representation of the system while using a relatively large numerical step size, the system is approximated with nearly periodic quantities. This allows for an efficient simulation of harmonic components, which cannot be achieved with $dq0$-based models. Dynamics phasor simulation is compared with abc-based modelling in [140]. It is seen that dynamic phasor simulation is about ten times more efficient although the number of states is larger. The higher model order is compensated by the larger numerical step size. In [142, 128] dynamic phasor models tailored to droop controlled microgrids are

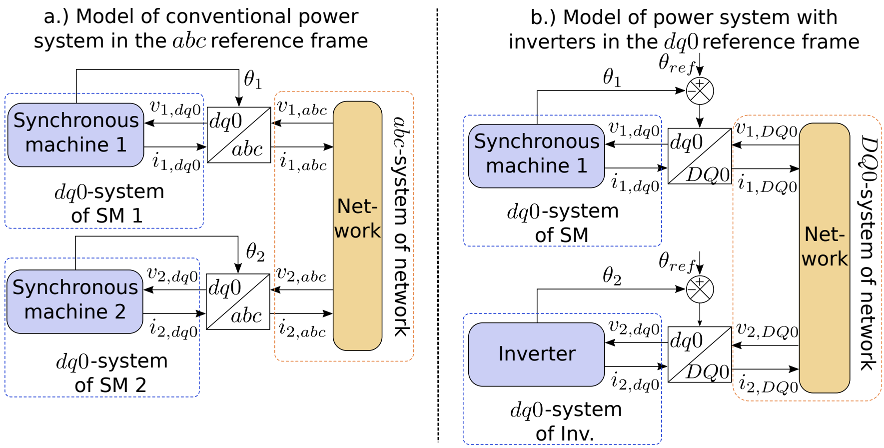

Figure 3.3.: Reference frames in power system simulation.

proposed. Dynamic phasors can also be used for asymmetric systems [143] and asymmetric faults [144].

The characteristics of the various modelling approaches are summarized in Table 3.1. In this work, the $dq0$-based approach is chosen, as only symmetric system conditions are investigated and harmonics are not considered.

For further clarification of the $dq0$ transform, the modelling of the power network in the abc and the $dq0$ reference frame are compared in Fig. 3.3. In case of the conventional abc-based model, two SM that are modelled in their individual $dq0$ reference frame are exemplified. The network is modelled in the native abc frame and the rotor angles θ_1 and θ_2 are used for the $abc/dq0$ transformations.

In case of the $dq0$ frame in Fig. 3.3b.), a SM and an inverter are exemplified. Both are modelled in their individual $dq0$ frame, similar to Fig. 3.3a.), but the power network is also modelled in its individual $DQ0$ frame instead of the native abc frame. The $DQ0$ frame refers to the reference frame rotating with the angle θ_{ref} of the power grid in this work.

The angle θ_{ref} serves as a common reference for the $dq0/DQ0$ transformation. The angle of the $dq0$ frame of one DER or the average angle of the $dq0$ frames of all DER may be chosen as the reference angle θ_{ref}. Note that if the linear passive elements of the network in Fig. 3.3 are approximated by algebraic equations, the $dq0$ model becomes the time-varying phasor model. The open-source software introduced in [145] is used to build the $dq0$ network model in this work.

For further insight on how to model large networks in the $dq0$ frame and with first

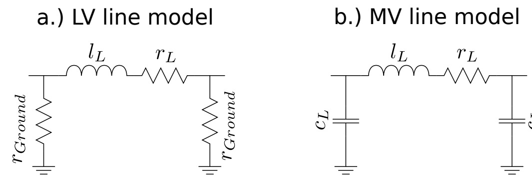

Figure 3.4.: Single line diagrams of LV and MV line models.

order approximation, the reader is referred to [132, 146, 135].

3.4.2. Example: Series RL Modelling in the $dq0$ Frame

Linear passive elements form the basis for modelling of a large variety of more complex components. To get insight into the $dq0$ modelling, the dynamic model of a symmetric three-phase series RL element as shown in the line model in Fig. 3.4a.) (omitting the ground resistor) is exemplified here [135]. The series RL model in the native abc reference frame can be expressed as

$$\frac{d}{dt} i_{abc,12} = \frac{1}{l_L}(v_{abc,1} - v_{abc,2}) - \frac{r_L}{l_L} i_{abc,12}, \tag{3.10}$$

where $i_{abc,12}$ is the vector of the three phase currents between two nodes with the three phase voltage vectors $v_{abc,1}$ and $v_{abc,2}$.

The differentiation of the $abc/dq0$ transformation from (3.4) for currents results in

$$\frac{d}{dt} i_{dq0} = \frac{d\boldsymbol{K_s}}{dt} i_{abc} + \boldsymbol{K_s} \frac{d}{dt} i_{abc}. \tag{3.11}$$

Observe that

$$\frac{d\boldsymbol{K_s}}{dt} i_{abc} = \boldsymbol{\mathcal{W}} \boldsymbol{K_s} i_{abc} = \boldsymbol{\mathcal{W}} i_{dq0}, \tag{3.12}$$

where

$$\boldsymbol{\mathcal{W}} = \begin{bmatrix} 0 & \omega_s & 0 \\ -\omega_s & 0 & 0 \\ 0 & 0 & 0 \end{bmatrix}, \tag{3.13}$$

with ω_s being the fundamental frequency.

Using (3.10) and (3.12), (3.11) can be written as

$$\frac{d}{dt} i_{dq0,12} = \boldsymbol{\mathcal{W}} i_{dq0,12} + \frac{1}{l_L}(v_{dq0,1} - v_{dq0,2}) - \frac{r_L}{l_L} i_{dq0,12}. \tag{3.14}$$

Omitting the zero sequence, it follows that the d- and q-component of the voltage over a series RL model are expressed as

$$v_{d,1} - v_{d,2} = -\omega_s l_L i_q + l_L \frac{d}{dt} i_d + r_L i_d, \tag{3.15}$$

$$v_{q,1} - v_{q,2} = \omega_s l_L i_d + l_L \frac{d}{dt} i_q + r_L i_q. \tag{3.16}$$

3.4.3. Model Order Reduction

Staying with the example from the previous section, for the time-varying phasor model, which is used in conventional stability analysis, the voltages become

$$v_{d,1} - v_{d,2} = -\omega_s l_L i_q + r_L i_d, \tag{3.17}$$

$$v_{q,1} - v_{q,2} = \omega_s l_L i_d + r_L i_q. \tag{3.18}$$

Direct comparison with (3.15) and (3.16) reveals that the $dq0$-based model has an additional derivative term describing high-frequency effects. The time-varying phasor model is the singular perturbation approximation of the $dq0$ model. The time derivative is neglected, but the model is equivalent at frequencies that are significantly below the fundamental frequency.

This quasi-static model is extended to higher frequencies in [132], by using a first-order Taylor approximation of the dynamic equations. The model is based on the simplification of the frequency dependent network admittance matrix. It combines the advantages of high bandwidth and a well-defined operating point. Since the mathematical derivation of the model is not trivial, it is referred to [132] for further information.

3.4.4. Line Model

The line models used in this work are shown in Fig. 3.4. The pi-model is used both for LV and MV lines. In case of the LV lines, the shunt capacitor is neglected. However, to establish a voltage at the terminals, a very high resistance r_{Ground} ($\approx 10\ k\Omega$) is implemented [76]. For MV lines, the shunt capacitor is applied.

3.5. Phase-Locked Loop

PLLs are used in DER and loads to measure the frequency and angle of a single or multi-phase signal. The synchronous reference frame PLL for three-phase signals is illustrated in Fig. 3.5a.) [147]. It is the most popular and widely used technique owing to its simple structure and robustness [148]. The signal, for example a three-phase voltage

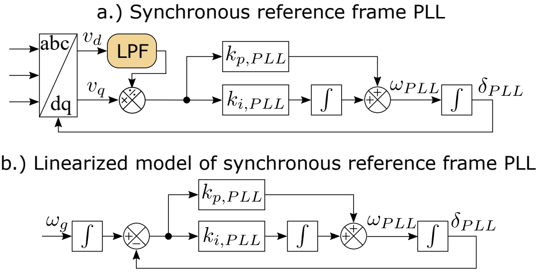

Figure 3.5.: PLL models.

measurement, is transformed from the natural abc-frame into the $dq0$-reference frame, omitting the zero sequence. The PI-controller regulates the frequency ω_{PLL} and the resultant angle δ_{PLL} aiming at nullifying the quadrature component v_q. If v_q is zero, the $dq0$-reference frame is in phase with the signal in the abc-reference frame. In order to be insensitive to signal magnitude variations, v_q is normalized. For the normalization, an estimation of the signal amplitude is used. It is obtained by low-pass filtering of v_d.

The linearized model in Fig. 3.5b.) and the approximated transfer function describing the actual input-output relationship of the grid and PLL frequency are deduced in [149, 147]:

$$\omega_{PLL}(s) = \frac{k_{p,PLL}s + k_{i,PLL}}{s^2 + k_{p,PLL}s + k_{i,PLL}}\omega_g(s). \tag{3.19}$$

It becomes apparent that the synchronous reference frame PLL can be approximated as a standard second order transfer function.

Due to its widespread application, the synchronous reference frame PLL is adopted in this work. The PI-controller parameters are tuned to achieve an optimal damped second-order system with a settling time of 500 ms [150]. The normalized second-order transfer function can be written as

$$PLL_{2nd} = \frac{2\xi_d\omega_{2nd}s + \omega_{2nd}^2}{s^2 + 2\xi_d\omega_{2nd}s + \omega_{2nd}^2}, \tag{3.20}$$

where $\omega_{2nd} = \sqrt{k_{i,PLL}}$ and $\xi_d = \frac{k_{p,PLL}\sqrt{k_{i,PLL}}}{2k_{i,PLL}}$.

Using the approximation from [151], the settling time of the second-order system is

$$t_{sett} = \frac{4.6}{\xi_d\omega_{2nd}}. \tag{3.21}$$

By combination of (3.21) with the normalized coefficients from (3.20), the PI-controller parameters can be set depending on the settling time:

$$k_{p,PLL} = \frac{9.2}{t_{sett}} = 18.4, \tag{3.22}$$

$$k_{i,PLL} = \frac{4.6^2}{(t_{sett}\xi_d)^2} = 169.3, \tag{3.23}$$

where $\xi_d = \frac{1}{\sqrt{2}}$ to achieve an optimal damped second-order system.

Although it is claimed in [152] that the synchronous reference frame model of the PLL is accurate enough, there is no consensus in literature on how to model PLLs for stability studies, despite significant research efforts. In [126] an additional low-pass filter (LPF) for harmonic suppression is implemented for v_q. PLLs are usually designed to enhance the performance of the DER, whereas the effect on the system stability is rarely taken into account [153]. There is a trade-off between fast response and stability regarding the parameter tuning of PLLs [154, 155]. The performance of PLLs in a weak grid environment was studied in [156]. It is shown that the PLL controller gains are limited by the short-circuit ratio. Various PLL techniques are compared in [157] and the synchronous reference frame PLL gives the best results. On the other hand, [158] identifies that the synchronous reference frame PLL has disadvantages when harmonics are present and that an enhanced PLL with an adaptive filter is preferable.

3.6. Distributed Energy Resources

3.6.1. Classification

DER can be classified with respect to their grid-interface and their control target. This work considers three types of grid-interfaces that heavily influence the system dynamics:

- Inverters,
- SM with diesel engines and
- DFIG of wind turbines.

The control targets are specified as grid-feeding, grid-supporting and grid-forming [159]. This section explicates the generic structure of these control targets, independent from the grid-interface. How the control targets are implemented in the specific grid-interface is elaborated in the following sections.

Grid-feeding control is also referred to as grid-following, current control or PQ-control in literature [22]. The simplified control structure is illustrated in Fig. 3.6a.), representing the three-phase grid by a single line. In essence, the grid-feeding control acts

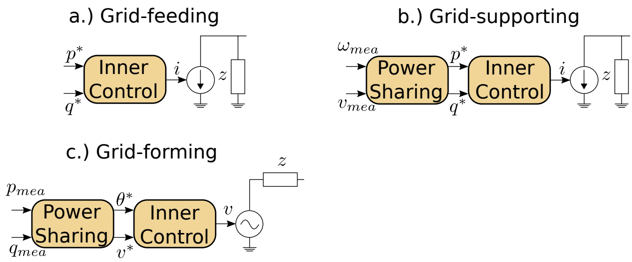

Figure 3.6.: DER controller types.

as a current source with a parallel impedance. The current set by the inner controller depends on active and reactive power set points p^* and q^*, respectively. A typical example of a grid-feeding DER is a renewable energy source, where the active and reactive power set points are taken from a maximum power point tracker. It must be pointed out that a synchronous machine in PQ-control mode exhibits rather voltage than current source characteristics, due to the rotor inertia. Nevertheless, it is referred to as a grid-feeding synchronous machine, if the control target is to supply a certain active and reactive power in this work.

The structure of the grid-supporting control in Fig. 3.6b.) is similar to the grid-feeding, since it also shows current source behaviour. The difference is that the set points for the active and reactive power are derived from a power sharing controller, which forms a cascaded control with the inner controller. Although other input variables are possible, the measured frequency w_{mea} and voltage amplitude v_{mea} are used in this work. The aim is to stabilize the system by counteracting deviations of these variables from their nominal values, which indicates a system disturbance, load change or the overloading of other DER.

Grid-forming is the third control target depicted in Fig. 3.6c.). It deviates from the other structures as it exhibits voltage source behaviour. The target is to set a certain voltage magnitude v^* and angle θ^*. The set points are again derived from the power sharing control, which is dependent on the measured active power output p_{mea} and reactive power output q_{mea} of the DER. At least one DER in an islanded microgrid must be grid-forming to provide a voltage reference for the other DER.

It is to be noted that other definitions of the control targets exist in literature. For example, in [89] grid-forming is defined as voltage source behaviour with constant amplitude and frequency, whereas the control structure in Fig. 3.6c.) is denoted grid-supporting-grid-forming control. A closer look at the power sharing control is taken in the next section.

3.6.2. Power Sharing Control

The power sharing control has a crucial influence on the system dynamics as it is the slowest controller of the cascade. As observed in Fig. 3.6b.) and c.), it is the outermost controller of the cascade and therefore needs to have a larger time constant than the inner controller. Its main purposes is to distribute the power of load fluctuations among DER to avoid overloading and possible damage, while ensuring the small-signal stability of the microgrid. Literature reviews of power sharing strategies in microgrids, which are also referred to as primary control strategies, are provided in [15] and [160].

Three main types of power sharing controllers have been developed rather independently. They share the common feature of emulating the dynamics of synchronous machines to some extent. Droop control and its variants are the most widely used strategies and are covered in Sec. 3.6.2.3. The virtual synchronous machine (VSM) is introduced in Sec. 3.6.2.4. The synchronverter was introduced in [161] and is characterized by a detailed representation of the synchronous machine equations. The concept was expanded by self-synchronization [162], a damping correction loop [163] and VI [164]. The dynamic stability of a synchronverter dominated microgrid was investigated in [96] using bifurcation theory. To the author's knowledge, no distinct advantage of the synchronverter concept over the droop control regarding stability that would justify the increased modelling complexity has been presented so far. Therefore, this power sharing strategy is not followed in this work.

3.6.2.1. Signal Measurement and Filtering

The measurement signals ω_{mea} and v_{mea} for grid-supporting and p_{mea} and q_{mea} for grid-forming control, which are used as inputs for the power sharing control, need to be filtered for the following reasons:

1. The power sharing controller is the outermost controller in the cascade and, therefore, its bandwidth must be significantly smaller than the inner controller's (see Sec. 3.6.3.2.2).
2. Droop control is predicated on the quasi-static steady-state relationship between power flow and voltage angle in a mostly reactive network and has a finite bandwidth.
3. To eliminate unwanted measurement noise.
4. To eliminate particular harmonics, for example at double fundamental frequency due to asymmetric conditions.

In general, the last requirement is the limiting factor for bandwidth of the filter.

Practitioners and researchers consent on the definition of the instantaneous active power p_{mea} and reactive power q_{mea} in a three phase system under symmetric, but not necessarily steady-state conditions [165]:

$$p_{mea}(t) = \frac{3}{2}(v_d(t)i_d(t) + v_q(t)i_q(t)), \tag{3.24}$$

$$q_{mea}(t) = \frac{3}{2}(v_d(t)i_q(t) - v_q(t)i_d(t)). \tag{3.25}$$

The proper definition of the instantaneous reactive power in asymmetric conditions, however, is still a controversial research field [166].

In the vast majority of literature on power sharing/droop control, a simple first order LPF is deployed to cater to harmonics and asymmetric conditions. Measurement delay is negligible for this consideration and the bandwidth of the filter usually ranges between 2 and 10 Hz [77]. In existing research, little attention has been paid to the design of the LPF [167, 168], although it has a major impact on the system dynamics, as will be shown in Sec. 5.5. Moreover, it allows for some degree of freedom in its design, because it does not alter the steady-state in contrast to other design parameters, such as the droop coefficients [169].

The overall system stability of parallel connected inverters is affected by a low bandwidth of the LPF. Enhanced LPF methods have been proposed to allow for higher bandwidths. The second-order harmonics due to asymmetric conditions are filtered using a band-stop filter in [170]. A second order Butterworth LPF is used in [171] to attain enhanced attenuation of harmonics. Other higher order filters, such as Chebyshew and Bessel filters, were successfully deployed to improve the filter performance [168]. Whereas it would also be possible to use moving average technique, this has the disadvantage of no simple s-domain model for controller design [172, 173].

Only symmetric conditions at fundamental frequency are investigated in this work and the evaluation of various filter types is beyond the scope. Nonetheless, the impact of higher bandwidth filters on the stability should be considered, as proven by the recent research effort in this field. Hence, the LPF time constant is a parameter to be incorporated in the optimization of droop controllers. However, the selection of a suitable higher order filter remains an important field of future research and a simple first order LPF with cut-off frequency ω_c is used in this work.

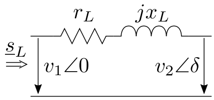

Figure 3.7.: Power flow over an RL-line.

3.6.2.2. Power Transmission over an RL-Line

To clarify the ideas behind the power sharing strategies, the power flow over an RL-line as shown in Fig. 3.7 is described. When the line impedance is defined as $\underline{z}_L = z_L e^{j\phi} = r_L + jx_L$, the apparent power $\underline{s}_L$ of the line becomes [174]

$$\underline{s}_L = p_L + jq_L = \underline{v}_1 \underline{i}_L^* = \underline{v}_1 (\frac{\underline{v}_1 - \underline{v}_2}{\underline{z}_L})^* = v_1 (\frac{v_1 - v_2 e^{-j\delta}}{z_L e^{-j\phi}}) = \frac{v_1^2}{z_L} e^{j\phi} - \frac{v_1 v_2}{z_L} e^{j(\phi-\delta)}. \tag{3.26}$$

The active and reactive power are

$$p_L = \frac{v_1}{z_L} cos\phi - \frac{v_1 v_2}{z_L} cos(\phi - \delta), \tag{3.27}$$

$$q_L = \frac{v_1}{z_L} sin\phi - \frac{v_1 v_2}{z_L} sin(\phi - \delta). \tag{3.28}$$

This can be rewritten as

$$p_L = \frac{v_1}{r_L^2 + x_L^2} \left[r_L (v_1 - v_2 cos\delta) + x v_2 sin\delta \right], \tag{3.29}$$

$$q_L = \frac{v_1}{r_L^2 + x_L^2} \left[-r_L v_2 sin\delta + x_L (v_1 - v_2 cos\delta) \right], \tag{3.30}$$

which can be reorganized to

$$v_2 sin\delta = \frac{x_L p_L - r_L q_L}{v_1}, \tag{3.31}$$

$$v_1 - v_2 cos\delta = \frac{r_L p_L - x_L q_L}{v_1}. \tag{3.32}$$

Assuming that the angle δ is small, then $sin\delta \approx \delta$ and $cos\delta \approx 1$. r_L may be neglected if the line is predominantly inductive, i.e. $x_L \gg r_L$, which finally leads to:

$$\delta \approx \frac{x_L p_L}{v_1 v_2}, \tag{3.33}$$

$$v_1 - v_2 \approx \frac{x_L q_L}{v_1}. \tag{3.34}$$

It is seen that for the given assumptions, the voltage angle δ is related to the active power p_L, whereas the difference in voltage magnitude depends on the transmitted reactive power q_L. On the other hand, if the line is predominantly resistive, the relationship is reversed and the active power is coupled with the difference in magnitude, whereas the reactive power is interdependent with the angle. This can be derived by assuming a small angle δ and neglecting the line inductance x_L in (3.31) and (3.32).

3.6.2.3. Grid-Forming Droop Control

3.6.2.3.1. Conventional Droop Control

Grid-forming droop control is the most widely used power sharing strategy for inverters in islanded microgrids. It was first introduced in [175]. The conventional grid-forming droop control assumes that the network lines are inductive. As was shown in Sec. 3.6.2.2, this results in the interdependency between frequency and active power and between voltage magnitude and reactive power. Therefore, the frequency ω_{droop} and voltage magnitude $v_{droop,d}$ of the DER are controlled as follows:

$$\omega_{droop} = \omega_0 - m_\omega(p_{LPF} - p_0), \tag{3.35}$$

$$v_{droop,d} = v_0 - m_v(q_{LPF} - q_0), \tag{3.36}$$

where p_{LPF} and q_{LPF} are the low-pass filtered active and reactive power output of the DER, respectively. p_0 and q_0 are active and reactive power set points, respectively, which can, for example, originate from a microgrid central controller that aims at optimizing the secondary control of the microgrid. ω_0 and v_0 are usually set to their nominal values, i.e. 1 pu, but can also provide another degree of freedom for the microgrid central controller. m_ω and m_v are the active and reactive power droop coefficients, respectively. They determine to what extend ω_{droop} and $v_{droop,d}$ alter, when the active and reactive power outputs of the DER change. The set point for the voltage angle can be calculated by multiplying ω_{droop} by the nominal angular speed ω_n and integrating. The voltage magnitude is equivalent to $v_{droop,d}$, because $v_{droop,q}$ is set to zero.

The applicability of the conventional droop control in low voltage microgrids was proven with a simplified stability analysis in [176]. The assumption of predominantly inductive lines is not valid in LV microgrids. On the other hand, the grid-side filter inductance of the inverter favourably decreases the R/X ratio of the impedance between DER. In addition, VI can be used to decrease the R/X ratio, as will be shown below. Furthermore, the conventional droop control is compatible with the inherent coupling between frequency and active power of SM.

Some drawbacks of the droop control are [160]:

- Frequency and voltage magnitude fluctuate and exhibit deviations from their nominal values in steady-state. There is an inherent trade-off between frequency and voltage regulation and load sharing accuracy. Larger droop coefficients result in better load sharing, while aggravating the stability [177] and causing larger steady-state deviations.

- Nonlinear loads and harmonic power sharing were not considered in the original droop method. This results in harmonic circulating currents and power quality problems. Furthermore, the dynamic response is delayed due to the filtering of the measured active and reactive power [178].
- The reactive power sharing accuracy is affected by the voltage drop over the line impedances. If the impedances between parallel inverters and loads differ, (3.36) does not guarantee exact reactive power sharing according to the droop coefficient, as there are unequal voltage drops over the network lines. As a consequence, large circulating currents can occur [179, 180].

Numerous variations of the conventional droop control that can enhance the performance have been suggested in literature [160] and are elaborated in the following sections.

3.6.2.3.2. Inverse Droop Control

The inverse droop control assuming predominantly resistive lines is proposed in [181, 182]. The frequency depends on the reactive power and the voltage magnitude on the active power in this method:

$$\omega_{droop} = \omega_0 - m_\omega(q_{LPF} - q_0), \tag{3.37}$$

$$v_{droop,d} = v_0 - m_v(p_{LPF} - p_0). \tag{3.38}$$

While this ensures better stability for highly resistive networks, one disadvantage is that the active power sharing is inaccurate here, resulting from line impedance voltage drops. Precise active power sharing usually has a higher priority than exact reactive power sharing [21]. Moreover, there is an inherent coupling between the frequency and active power for synchronous machines which is not compatible with the inverse droop.

3.6.2.3.3. Transient Droop

The combination of the static droop function with a transient droop function was first proposed in [77]:

$$\omega_{droop} = \omega_0 - m_\omega(p_{LPF} - p_0) - m_{\omega,t}\frac{dp_{mea}}{dt}, \tag{3.39}$$

$$v_{droop,d} = v_0 - m_v(q_{LPF} - q_0) - m_{v,t}\frac{dq_{mea}}{dt}, \tag{3.40}$$

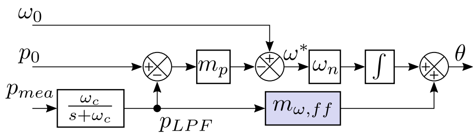

Figure 3.8.: Droop control with feed-forward gain.

where $m_{\omega,t}$ and $m_{q,t}$ are active and reactive power transient droop coefficients and p_{mea} and q_{mea} are the measured active and reactive power before the LPF, respectively. As a pure derivative term is not recommended in practice, a high-pass filter is usually employed. Its cut-off frequency can be chosen equal to the LPF of the conventional droop, which is also adopted in this work. This controller has since been often used in literature [183, 184] and proven to enhance the stability, especially when synchronous machines are present in a microgrid [88].

3.6.2.3.4. Active Power Feed-Forward

The frequency feed-forward gain $m_{\omega,ff}$ presented in Fig. 3.8 was implemented in some early publications on droop control [176] to stabilize the active power droop. The inverter voltage angle correlates with the filtered active power output in the frequency domain as follows:

$$\theta = \frac{1}{s}(\omega_0 - m_\omega(p_{LPF} - p_0)) - m_{\omega,ff}p_{LPF}, . \tag{3.41}$$

The voltage angle according to the transient droop from (3.39) in Sec. 3.6.2.3.3 in the frequency domain can be written as:

$$\theta = \frac{1}{s}(\omega_0 - m_\omega(p_{LPF} - p_0) - m_{\omega,t}sp_{mea}), \tag{3.42}$$

If a high-pass filter with the same cut-off frequency as the LPF is utilized ($sp_{mea} \approx \frac{s\omega_c p_{mea}}{s+\omega_c} = sp_{LPF}$) instead of a pure derivative, this can be brought to the form:

$$\theta = \frac{1}{s}(\omega_0 - m_\omega(p_{LPF} - p_0)) - m_{\omega,t}p_{LPF}. \tag{3.43}$$

(3.43) is equal to (3.41), if $m_{\omega,t} = m_{\omega,ff}$. Hence, the active power droop control is similar when using the feed-forward or the transient droop. However, an advantage is that no derivative or high-pass filter are necessary, which may cause problems for discrete controllers when harmonics are present in the microgrid and entails a phase shift and delay.

Moreover, both methods differ in the reactive power droop. Here, no integrator is present as in case of the angle and frequency relation in (3.41). Therefore, the conventional reactive power droop from (3.36) is employed.

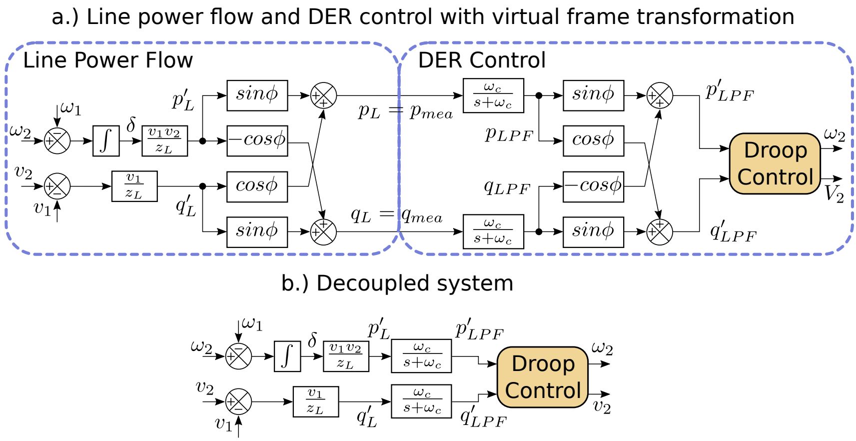

Figure 3.9.: Virtual frame transformation with simplified line power flow.

3.6.2.3.5. Virtual Frame Transformation

In LV networks, the conventional droop is not efficient due to the high R/X ratio. To overcome this issue, a "modified" active and reactive power p'_{LPF} and q'_{LPF} were proposed in [174], by using an orthogonal linear rotational transformation matrix T_{VF}, that depends on the impedance $z_L e^{j\phi}$ of the between DER and load:

$$\begin{bmatrix} p'_{LPF} \\ q'_{LPF} \end{bmatrix} = \boldsymbol{T_{VF}} \begin{bmatrix} p_{LPF} \\ q_{LPF} \end{bmatrix} = \begin{bmatrix} sin\phi & -cos\phi \\ cos\phi & sin\phi \end{bmatrix} \begin{bmatrix} p_{LPF} \\ q_{LPF} \end{bmatrix} = \begin{bmatrix} x_L/z_L & -r_L/z_L \\ r_L/z_L & x_L/z_L \end{bmatrix} \begin{bmatrix} p_{LPF} \\ q_{LPF} \end{bmatrix} \tag{3.44}$$

It can be shown [174] that applying this transformation to (3.31) and (3.32) is equivalent to the following relationship for the RL-line in Fig. 3.7:

$$sin\delta = \frac{z_L p'_L}{v_1 v_2} \tag{3.45}$$

$$v_1 - v_2 cos\delta = \frac{z_L q'_L}{v_1}, \tag{3.46}$$

where p'_L and q'_L are shown in Fig. 3.9. Going on the assumption that the voltage difference $v_1 - v_2$ and the angle δ are small, the angle depends only on p'_L, whereas the voltage difference is dependent only on q'_L. Accordingly, defining the "modified" active and reactive powers p'_L and q'_L allows to independently influence the grid frequency and voltage magnitude when used in the droop control.

Fig. 3.9a.) clarifies the relationships. It illustrates the simplified power flow over the RL-line and the DER controller, which sets the voltage v_2 at the end of the line. ω_1

and ω_2 are the frequencies of the corresponding voltages v_1 and v_2, respectively. It is assumed that the voltage magnitude v_2 and the frequency ω_2 are set by a droop controller of the DER. The trigonometric functions cancel each other out. The resulting decoupled system is shown in Fig. 3.9b.).

A shortcoming of this controller is that the network impedance angle ϕ is unknown in general and the decoupling is therefore not guaranteed. Moreover, the line angle between DER and loads differs and is also dependent on the present load scenario. Using differing angles for the frame transformation in each DER leads to unequal power sharing. To tackle this issue, a fixed angle of $45°$ is proposed in [185], based on the optimization of the system stability under various conditions.

The virtual frame transformation was also used in [186]. An alternative virtual frequency-voltage frame was proposed in [187] and [188], but a mathematical derivation to prove the decoupling of power flows is not presented. Hence, the above described frame transformation is adopted in this work due to its simple design process and clear physical meaning.

3.6.2.3.6. Other Droop Variants

A number of other droop variants have been proposed in literature, many of them applying a quadratic or other non-linear function in the droop equation [189, 190, 191, 192]. In [191], a non-linear droop is suggested to improve the reactive power sharing, while preserving the dynamic stability. [192] suggests online adjustment of the active power droop coefficient and the LPF time constant to comply with rate of change of frequency relays and enhance the frequency response.

In order to decouple the droop dynamics, network impedance estimation is conducted in [179]. A new type of droop method is proposed in [193], where the virtual flux is drooped instead of inverter output voltage. Inner loop controllers are not necessary in this method, but a common load bus is needed and it cannot be applied in all microgrid topologies. Another variant found in literature is the angle droop control [194]. Here, the voltage angle is used instead of the frequency in the active power droop, which enhances the stability and avoids frequency deviations in steady-state. However, at least some low-bandwidth communication must be present, because the DER need to share a common reference angle.

In [195] a high-pass filter is implemented for the measured active and reactive power instead of a LPF. As a consequence, the impact of the droop control is only relevant during transients and there is no steady-state deviation of frequency and magnitude. However, this does not guarantee steady-state power sharing.

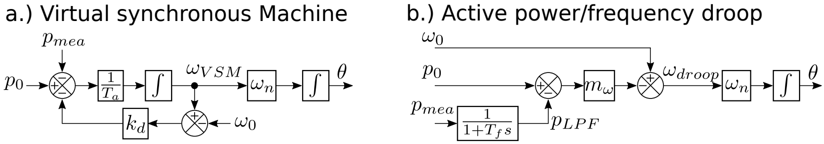

Figure 3.10.: Comparison of virtual synchronous machine and droop control.

3.6.2.4. Virtual Synchronous Machine and its Equivalence to Droop Control

Several variants of the VSM have been proposed in literature [196, 197, 198, 199, 200]. Reviews on VSM implementations are provided in [201, 202, 203]. The parametrization through small-signal stability analysis at an infinite bus is conducted in [204, 205]. Particle swarm optimization is used for the online optimization of VSM parameters in [206]. Similarities between VSM and droop control have been reported in [207, 208]. Even the conditions for the equivalence of VSM and the active power/frequency droop have been pointed out in [209].

A common feature of all VSM is a numerical model of the mechanical part of a synchronous machine that provides the references for the operation of the inverter. The accuracy of the emulation of the synchronous machine varies and the simplest form is arguably the reproduction of the traditional swing equation. The block diagram is shown in Fig. 3.10a.). The angle θ is the reference for the grid-forming control and ω_0 is usually set to the nominal frequency. The dynamics can accordingly be represented by

$$T_a s\omega_{VSM} = p_0 - p_{mea} - k_d(\omega_{VSM} - \omega_0), \tag{3.47}$$

where T_a is the acceleration time constant, ω_{VSM} is the rotor speed of the VSM and k_d is the damping coefficient. The active power/frequency droop equation including the LPF, as depicted again in Fig. 3.10b.), takes the following form when isolating the measured active power:

$$p_{mea} = (1 + T_f s)(\frac{1}{m_\omega}(\omega_0 - \omega_{droop}) + p_0), \tag{3.48}$$

where $T_f = 1/\omega_c$ is the filter time constant. Expanding the products of (3.48) leads to:

$$p_{mea} = \frac{T_f(s\omega_0 - s\omega_{droop})}{m_\omega} + \frac{\omega_0 - \omega_{droop}}{m_\omega} + T_f s p_0 + p_0. \tag{3.49}$$

By eliminating the derivatives of constant terms, this can be simplified to:

$$\underbrace{T_f \frac{1}{m_\omega} s\omega_{droop}}_{\text{Inertia term}} = p_0 - p_{mea} - \underbrace{\frac{1}{m_\omega}(\omega_{droop} - \omega_0)}_{\text{Damping term}}. \tag{3.50}$$

It becomes apparent that Eq. (3.50) has the same form as (3.47). The equivalence is given if the following conditions are met [209]:

$$T_a = T_f \frac{1}{m_\omega}, \quad k_d = \frac{1}{m_\omega}. \tag{3.51}$$

The effect of the time constant of the LPF T_f is analogous to the virtual inertia. Hence, the inherently unstable control of a VSM with zero inertia corresponds to a droop controller without LPF. Furthermore, the damping gain k_d is inversely linked to the droop gain m_ω.

The analysis provides a new perspective for the droop control and further insight to the functional meanings of parameters. The question whether VSM are more intuitive due to their similarities with synchronous machines [208] is mostly a matter of taste. The droop control can readily be tuned to emulate the damping and inertia of a specific synchronous machine and traditional stability analysis based on the swing equation can be applied to conventional droop controllers. An advantage of the droop control is that a large variety of modifications exists to comply with the specific application. Moreover, higher order filters can be applied as discussed in Sec. 3.6.2.1.

3.6.2.5. Virtual Impedance

A VI can enhance the performance of grid-forming inverters. As the droop control relies on predominantly inductive lines, a large coupling inductor could be utilized for the LCL-Filter to decrease the R/X ratio. However, this comes at a higher cost. An alternative is to implement a virtual inductor or a VI in the controller, which is illustrated in the single line diagram of the LCL-filter in Fig. 3.11. The grid-forming inverter controls the voltage v_c at the filter inductor. The application of an algebraic VI entails the calculation of the voltage drop over an impedance $\underline{z}_{vi} = r_v + j\omega l_v$ caused by the coupling inductor current $\underline{i}_{L2}$:

$$\Delta\underline{v}_{vi} = \underline{v}_c - \underline{v}_{c,vi} = \underline{i}_{L2}\underline{z}_{vi} = \underline{i}_{L2}(r_{vi} + j\omega l_{vi}). \tag{3.52}$$

This voltage drop is subtracted from the set value of the filter capacitor voltage (the control variable of the voltage controller) to simulate the existence of the VI. In (3.52), an algebraic VI [210, 174] is exemplified. It has also been suggested to use a transient VI with differential equations resorting to a high-pass filter for the derivative [211]. One advantage of an algebraic VI is that its magnitude is the same at all frequencies, which results in decreased harmonic voltage drops compared to transient impedances. Moreover, differential computations with high frequency noise amplification or a high-pass filter with phase shift and delays are avoided [212]. As the algebraic VI only takes effect at the fundamental frequency, multiple cross-coupling feedback controllers, which are individually

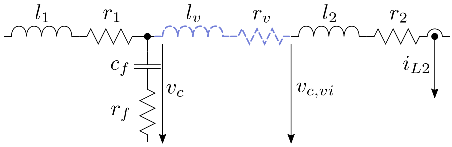

Figure 3.11.: LCL-filter with VI.

tuned at low-order harmonics can be implemented for the sharing of non-linear loads [213].

Besides better stability due to an adjustable R/X ratio, VIs also allow for better reactive power sharing at steady state (assuming conventional droop), if similar impedance values are used for the DER. Accurate reactive power sharing is falsified by differing line impedances. The VI assimilates the effective line impedance, as the DER share a common portion of their effective line impedance, if the same VI is chosen for the DER.

VIs are not only helpful to improve the dynamic and steady state power sharing, but also to limit fault currents, suppress harmonics and increase the damping of parallel inverters. An algebraic type VI is used in [180] to enhance the dynamics, reactive power sharing and harmonic suppression in a radial microgrid. Parameters of an algebraic VI are optimized in [214] with particle swarm optimization according to several criteria resorting to weighting factors. A GA is used in [215] to optimize the static power sharing. A virtual negative resistor is implemented in [216] to compensate for highly resistive lines. In [212] the VI is optimized with modal analysis according to the eigenvalue and damping. Better reactive power sharing by a VI with distributed communication is attained in [217] and low-bandwidth communication is used for the same purpose in [218].

A transient VI is used in [195] and the reactive power sharing is not attained through droop control, but by the adjustment of the VI according to the reactive power output. When there is a short-circuit in the microgrid, the fault currents can be limited by adding a transient VI [29]. Using a VI is advantageous compared to a simple saturation of the fault currents, as the control remains linear. In [89] a transient VI is implemented and the steady-state influence of the VI is discarded in order to avoid steady-state voltage drop.

3.6.2.6. Grid-Supporting Droop Control

The grid-supporting droop control sets the output active and reactive power of the DER depending on the measured and filtered frequency and voltage magnitude, respectively. This is attained by isolating the power instead of the frequency or voltage magnitude in the grid-forming droop equations (3.35) and (3.36), which results in

$$p_{droop} = p_0 - \frac{1}{m_\omega}(\omega_{LPF} - \omega_0), \tag{3.53}$$

$$q_{droop} = q_0 - \frac{1}{m_v}(v_{LPF} - v_0), \tag{3.54}$$

where p_{droop} and q_{droop} are the set values for the active and reactive power that are forwarded to the inner controller, ω_{LPF} and u_{LPF} are the measured and low-pass filtered voltage frequency and magnitude, ω_0 and v_0 are usually set to the nominal values of frequency and voltage and provide a degree of freedom, respectively. p_0 and q_0 are set by the secondary controller of the microgrid central controller.

In steady state, the active and reactive power output of a grid-supporting droop controlled DER is equal to a grid-forming droop controlled DER, when the parameters are the same. This is obvious as the grid-supporting droop control is deduced from the grid-forming droop control by simply exchanging input and output variables. The dynamic behaviour, however, differs distinctly. The grid-supporting droop exhibits current source and the grid-forming voltage source behaviour. When the load changes in an islanded microgrid for example, the grid-forming droop controlled DER instantaneously take on the major share of the load alteration. They change their frequency and voltage accordingly. The grid-supporting droop controlled DER then react to this alteration and adjust their active and reactive power until a new equilibrium is found. Note that this is only veritable for PED. For SM, the machine dynamics as well as governor and AVR exert a dominant influence.

3.6.3. Power Electronic Devices

The diagram of the three phase inverter used in this work is depicted in Fig. 3.12. The DC-source represents a battery cell or a PV module, for example. If there is a large DC-circuit inductor l_{DC} in series, the inverter is labelled current source inverter. If a large capacitor c_{DC} across the DC bus dominates the DC circuit dynamics, it is called voltage source converter [219]. However, the usage of the term voltage source converter is not consistent in literature which causes confusion. It is sometimes used synonymic to grid-forming inverter [22]. According to the definition above, a grid-forming inverter with a large DC-capacitor is correctly labelled voltage controlled voltage source inverter.

The DC-voltage is converted to AC through a two-level inverter bridge with power electronic switches, such as insulated gate bipolar transistors [220]. To decrease the size of the filter, alternative converter topologies are subject of current research. Multi-level converters, such as neutral point clamped and cascaded converter, have the benefit of reducing the voltage step changes and therefore the size and cost of the filter for a given current ripple. However, this comes at the expense of increased cost of the power electronics and higher system complexity [221]. Unbalanced loads or single-phase

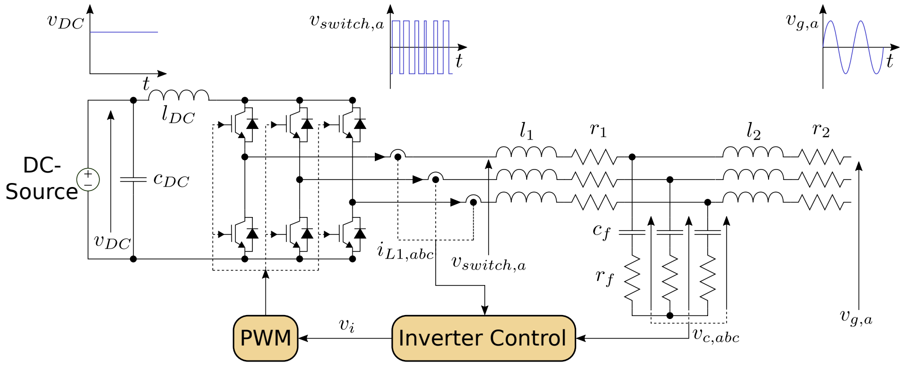

Figure 3.12.: Overview of inverter with LCL-filter.

connected generation often found in microgrids necessitate the inverter to provide a neutral line to allow for a current path and minimise the coupling effect among the phases [219].

The pulse width modulation (PWM) converts the voltage on the AC side of the bridge, which is set by the inverter control, to pulses that drive the power electronics. A variety of modulation techniques exist, including hysteresis modulation, pulse density modulation and space-vector modulation.

It is presumed in this work that the DC source is always capable of providing the required voltage for the converter bridge and the dynamics of the DC-circuit are negligible, which is an assumption commonly found in literature [76]. Moreover, only the fundamental frequency is of interest for the small-signal stability analysis. Hence, the PWM and the converter bridge are simply represented by an ideal voltage source that is set by the inverter control output v_i, which is also referred to as the averaged model [222].

An LCL-filter is used to filter the harmonic content resulting from the switching of the semiconductors with the aim of passing only the fundamental frequency to the grid. The evolution of the voltage waveform is illustrated in Fig. 3.12. The filter is covered in the next section. The inverter control dominates the system dynamics and will be elaborated in the subsequent sections. The inverter side inductor current $i_{L1,abc}$ and the filter capacitor voltage $v_{c,abc}$ are used as input to the control in Fig. 3.12, but it is to be mentioned that other feedback variables are possible [223].

3.6.3.1. LCL-filter

Although this work does not aim at optimizing the filter, realistic parameters need to be implemented as the filter components influence the system stability. In general, there is a trade-off between damping of harmonics and fast dynamic performance [224]. LCL-filters are the preferred choice because of the enhanced decoupling between active and reactive power and a smoother interface between parallel sources in comparison to LC-filters [225]. This is a result of the additional inductor between the filter capacitor c_f and the grid. A similar procedure as in [226] is adopted to design the filter.

To begin with, the inverter-side filter l_1 is sized with respect to a predefined maximum allowable current ripple Δi_r:

$$\Delta i_r = \frac{v_{DC} t_1}{3 n l_1}, \text{ where } t_1 = \frac{\sqrt{3} m_{max}}{8 f_{switch}}, \tag{3.55}$$

where $n = 1$ or 2 assuming a two-level or three-level inverter, respectively. v_{DC} is the nominal DC-link voltage, m_{max} is the maximum modulation factor and f_{switch} is the switching frequency of the power electronics. It is possible to choose the required minimum inverter-side filter inductor l_1 by setting a maximum permissible current ripple of $\Delta i_r = 15 - 25\%$ with regard to the nominal current. A value $i_r = 20\%$ is selected in this work.

The grid-side inductor l_2 is set to 25% [226] of the inverter-side inductor l_1 as it does not have to dampen the whole harmonic current spectrum [227] in a second step. The filter capacitor c_f may be designed as a proportion of the rated power of the inverter [228] depending on the reactive power requirements. Alternatively, the filter resonance frequency f_{res} can be chosen with respect to the guidance rule in (3.56).

$$10 f_g \leq f_{res} \leq \frac{f_{switch}}{10}, \tag{3.56}$$

where f_g is the grid nominal frequency (50 Hz). The switching frequency f_{switch} is usually above 6 kHz in low voltage applications and 10 kHz is chosen in this work. (3.57) can now be used to calculate the filter capacitor.

$$\omega_{res} = \frac{1}{\sqrt{l_f c_f}} \Rightarrow c_f = \frac{1}{\omega_{res}^2 l_f}, \tag{3.57}$$

where $\omega_{res} = 2\pi f_{res}$ and l_f is the parallel connection of the grid side and inverter side inductors:

$$l_f = \frac{l_1 l_2}{l_1 + l_2}. \tag{3.58}$$

Active [229] or passive damping may be applied to dampen the transient dynamics. A commonly used passive damping resistor in series with the shunt capacitor is used in this work. Its size can be calculated according to

$$r_f = 2\zeta_p \sqrt{\frac{l_f}{c_f}}, \tag{3.59}$$

Table 3.2.: Example parameters for a LCL filter of a 10 kW inverter in a 400 V system.

Par.	f_{switch}	m_{max}	V_{dc}	n	Δi_r	ζ_p	f_{res}
Value	10 kHz	1.15	700 V	1	0.2	0.3	500 Hz
Par.	L_1	R_1	L_2	R_2	C_f	R_f	
Value	1.5 mH	$0.1\ \Omega$	0.36 mH	$0.03\ \Omega$	$70\ \mu$H	$2.75\ \Omega$	

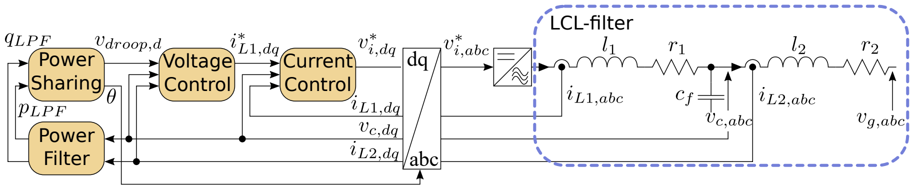

Figure 3.13.: Overview of grid-forming droop controlled inverter with LCL-filter.

where ζ_p is the dominant damping factor. In order to yield an acceptable compromise between damping and attenuation it is set to 0.3 [227]. Example LCL filter parameters for 10 kW inverter in a 400 V system are given in Table 3.2.

3.6.3.2. Grid-Forming Power Electronic Devices

The control principle of a grid-forming PED is depicted in Fig. 3.13 with a single line diagram of the LCL-filter. In this and all following figures, the damping resistor r_f of the filter capacitor c_f is not shown. The abc/dq-transformation is at the center of the model and the entire cascaded control is implemented in the dq-reference frame. The voltage and current controller regulate each axis separately, as will be shown in the following chapters. The output power of the inverter is forwarded to the power sharing controller. The power sharing controller passes the set values for the filter capacitor voltage $v_{droop,d}$ to the voltage control. In case that a VI is incorporated, the voltage drop from (3.52) would be subtracted from this voltage set values. The filter capacitor voltage is controlled through the adjustment of the inverter-side current i_{L1}. Therefore, the output of the voltage controller are the set values $\underline{i}^*_{L1,dq}$ which are transmitted to the current control.

The voltage and current controller are also referred to as the inner loops [208]. In some literature the inner loops are omitted and a direct open loop PWM signal generation is implemented, where the power sharing output reference voltage is directly fed into the PWM [161]. However, the inner loops serve important protective functions by limiting the currents of the power electronic converters during short circuits and are therefore the

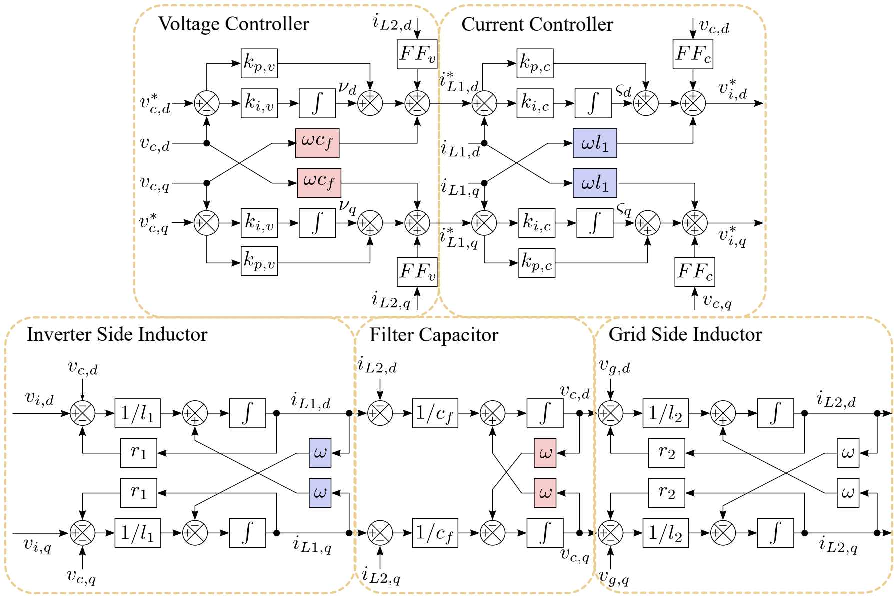

Figure 3.14.: Overview of grid-forming droop controlled inverter with LCL-filter.

preferred option [89]. Furthermore, as will be shown in Sec. 5, they affect or even enhance the stability and damping.

An overview of the inner control loops and the physical model of the LCL-filter is given in Fig. 3.14. Note that the inner loops as well as the filter are modelled in the dq-reference frame. The controllers are detailed in the following sections.

3.6.3.2.1. Current Controller

The current controller comprises PI-controllers for both axes, the decoupling and the feed-forward of the capacitor voltage $v_{c,dq}$ with the feed-forward gain FF_C (see Fig. 3.13). The current over l_1 is dependent on the voltage difference between $v_{i,dq}$ and $v_{c,dq}$. The feed-forward anticipates the reaction of the PI-controllers when $v_{c,dq}$ fluctuates which stabilizes the control.

The tuning of the current controller is explicated in the following. The decoupling is introduced to eliminate the mutual influence of the current $i_{L1,dq}$ in both axes. Consequently, two decoupled, first-order linear systems are derived for the inverter side inductor (assuming $FF_c = 1$):

$$l_1 \frac{di_{L1,d}}{dt} = -r_1 i_{L1,d} + v_{i,d} \tag{3.60}$$

$$l_1 \frac{di_{L1,q}}{dt} = -r_1 i_{L1,q} + v_{i,q}. \tag{3.61}$$

For the loop gain $l_{CL}(s)$ of the PI-controller and the inverter-side inductor, it follows that [230]

$$l_{CL}(s) = \left(\frac{k_{p,c}}{l_1 s}\right) \frac{s + k_{i,c}/k_{p,c}}{s + r_1/l_1}. \tag{3.62}$$

There is a plant pole fairly close to the origin at $s = -r_1/l_1$. Therefore, the magnitude and phase of the loop gain begin to drop at a relatively low frequency. By setting $k_{i,c}/k_{p,c} = r_1/l_1$, the PI-controller is tuned to cancel the pole. Finally, assuming the loop gain $l_{CL}(s) = k_{p,c}/(l_1 s)$, the closed loop transfer function of the d-component becomes

$$\frac{i_{L1,d}}{i^*_{L1,d}} = \frac{1}{T_{CL}s + 1}, \tag{3.63}$$

if

$$k_{p,c} = l_1/T_{CL}, \tag{3.64}$$

$$k_{i,c} = r_1/T_{CL}, \tag{3.65}$$

where T_{CL}, which is a design choice, is the time constant of the resultant closed-loop system [230]. $1/T_{CL}$ is the bandwidth of the current controller and ought to be substantially smaller than the switching frequency, e.g. ten times. On the other hand, a small T_{CL} is needed for a rapid current controller response. T_{CL} is selected 2 ms in this work.

The feed-forward loops can propagate a significant amount of harmonics [89] that can be suppressed by phase-lead low-pass filters [219], which are not depicted in Fig. 3.14. Moreover, several alternatives for the PI-controllers are proposed in literature, which improve the performance under unbalanced conditions and the presence of harmonics [219]. On the one hand, positive and negative sequence currents can be dealt with by separate PI-controllers to cater to unbalance. On the other hand, H_∞ ("H-infinity") techniques offer significant improvement in terms of THD. However, the main shortcoming is the trade-off between fast dynamics and low THD.

A widely applied controller type is the proportional resonant control. Its transfer function is given by

$$C_{PR}(s) = k_{p,PR} + k_{i,PR}\frac{s}{s^2 + \omega^2}, \tag{3.66}$$

where ω is the resonant frequency and $k_{p,PR}$ and $k_{i,PR}$ are proportional and integral gains, respectively. This controller is capable of eliminating the steady-state error when tracking a sinusoidal signal as it has a high gain around the resonant frequency. It can be implemented in the abc- or $\alpha\beta$-frame and is therefore less complex compared to the PI-controller and lower THD can be achieved [219]. The resonant frequency should be maintained close to the system frequency. Adaptive mechanisms can be employed when the frequency in the microgrid varies significantly. Proportional resonant controllers were shown to be more stable in weak grids in comparison to PI-controllers in [154].

Current deadbeat controllers [166] are also widely applied in inverter control. The general idea is that the controlled variable reaches its required value within fixed periods of sampling. It is possible to obtain fast dynamic response, but the controller is sensitive to parameter variations and non-linear loads [219].

Another research field is the choice of the feedback variable (in this work i_{L1}) for the current controller. [231] gives an overview of the various possibilities and proposes a superior control principle that uses the filter capacitor current as feedback variable. [223] compares the characteristics of converter-side and grid-side inductor current control. Converter-side current control is not recommended in [221], stating problems such as filter resonance that causes under damped transient response oscillations, large overshoot and poor voltage harmonic disturbance rejection.

In this work, PI-controllers are used as harmonics are not considered and the whole system is modelled in the dq-frame, which inherently forbids the usage of proportional resonant controllers as they are either implemented in abc or $\alpha\beta$ frame. At the fundamental frequency, the PI-controller in the dq frame is equivalent to the proportional resonant controller [219]. Due to the widespread application, the converter side inductor current is used as the feedback signal.

3.6.3.2.2. Voltage Control

The structure of the voltage controller is similar to the current controller. PI-controllers for each axis, the decoupling and the feed-forward of the output current $\underline{i}_{L2,dq}$ with the feed-forward gain FF_v are implemented. The current $\underline{i}_{L2,dq}$ flows from the capacitor to the grid and its fluctuations cause alterations of the capacitor voltage. Therefore, the load adaptability is enhanced and the action of the PI-controllers is anticipated by the feed-forward [232]. In comparison to the current controller, the bandwidth of the voltage controller is usually 3 to 5 times lower [77].

Aspects of tuning of the voltage controller are elaborated in the following. The closed loop transfer function of the voltage controller ($v_{c,d}/v_{c,d}^{*}$) for varying parameter sets is depicted in Fig. 3.15. The cut-off frequency is at about 100 rad/s. The magnitude gradually increases between 200 and about 10^4 rad/s, from where it drops due to the limited bandwidth of the current controller.

Larger values for $k_{p,v}$ lead to an increased gain at high frequencies. The selection of the proportional gain is a trade-off between fast response and limitation of harmonic

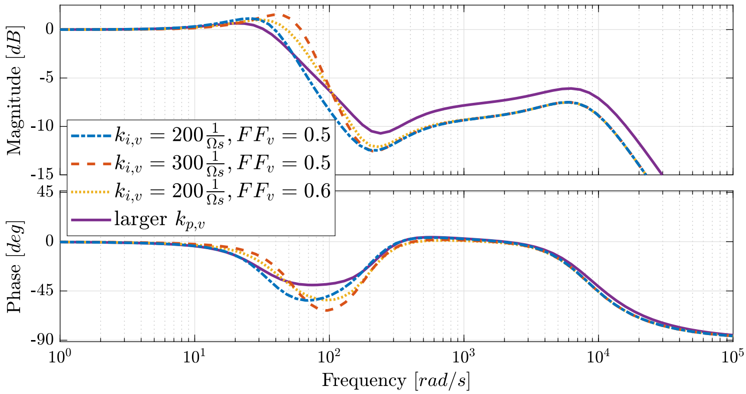

Figure 3.15.: Magnitude and phase response of the closed loop transfer function of the voltage controller ($v_{c,d}/v^*_{c,d}$).

propagation. It is set to $3\ \Omega^{-1}$ in this work.

When the integral gain $k_{i,v}$ is increased to $300\ \frac{1}{\Omega s}$, the cut-off frequency becomes higher, whereas harmonics are not affected. The effect of raising the feed-forward gain FF_v from 0.5 to 0.6 is similar. Fig. 3.16 illustrates the phase response of the transfer function $i_{L2,d}/v^*_{c,d}$. Droop control is predicated on the assumption that power lines are inductive and inductive behaviour is also desirable for the cascaded control. Hence, $i_{L2,d}$ should lag $v^*_{c,d}$ by 90° at fundamental frequency. Both the increase of $k_{i,v}$ and FF_v result in a more inductive system compared to the base case ($k_{i,v} = 200\ \frac{1}{\Omega s}$,$FF_v = 0.5$), whereas a larger $k_{p,v}$ is counterproductive.

In conclusion, the impact on the dynamic behaviour of $k_{i,v}$ and FF_v reveals similarities. The optimization of the controller should incorporate both parameters as their combination improves the dynamics, which will also be shown in Ch. 5.

[225] investigates the universal applicability of cascaded inner loop controllers and concludes that a proportional resonant controller should be used for voltage controller and a proportional controller for the current loop. The influence of the feed-forward of the grid-side inductor current is examined in [232]. It becomes apparent that the feed-forward gain has a strong impact on the stability and is one of the controller parameters to be optimized.

As harmonics are not considered, PI-controllers are a reasonable choice in this work.

3.6.3.2.3. Model Order Reduction

There is a lack of systematic approaches in literature to determine the validity of model

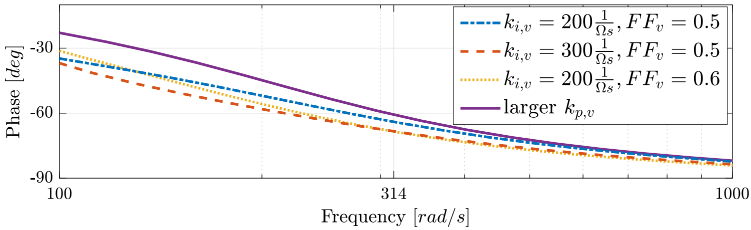

Figure 3.16.: Phase response of the closed loop transfer function $i_{L2,d}/v^*_{c,d}$.

order reductions of PED. In particular, the neglect of the inner control loops of grid-forming converters, as often applied in literature, has not been investigated in detail and may be an oversimplification [233].

This issue was addressed in [126] with a polynomial approximation approach. Fast states of the inner loops are discarded first and then a reduced-order representation is added back to model their interaction with the slow states. The reduced-order representation of the fast states is obtained by pole-zero truncation. However, feed-forward terms of the voltage controller, which have a significant impact on the dominant modes, as will be shown in Ch. 5.5.1.2, are not considered.

This work follows the reduction approach based on singular perturbation. The fast states of the control cascade are simplified. Fig. 3.17 compares the original 13^{th} order grid-forming PED model (power filter: 2 states, power sharing/conventional droop: 1 state, voltage control: 2 states, current control: 2 states, LCL-filter modelled in dq reference frame: 6 states) with simplified representations (VI control is not shown).

The current loop, which includes the current control and the converter side inductor, has a high-bandwidth and can either be fully neglected or represented by a first order lag with the time constant T_{CL}, as explained in Sec. 3.6.3.2.1. This reduces the order by four or two states, respectively.

Another approach often found in literature is to neglect both current and voltage loop. In this case, only the grid-side conductor of the LCL filter remains. The model order is reduced by another 4 states, resulting in a 5^{th} order model. It is proposed in [104] to approximate the grid-side inductor by a first-order Taylor expansion, leading to a third order model. Furthermore, the grid-side inductor can also be approximated by the phasor model.

A new approach to model the inner loops and LCL filter is proposed in this work. Starting from the neglect of the current loop in Fig. 3.17b.), the capacitor c_f is approximated by a phasor model. The purpose of c_f is to filter the high frequency harmonic noise from the power electronic switching and its impact on the dominant modes

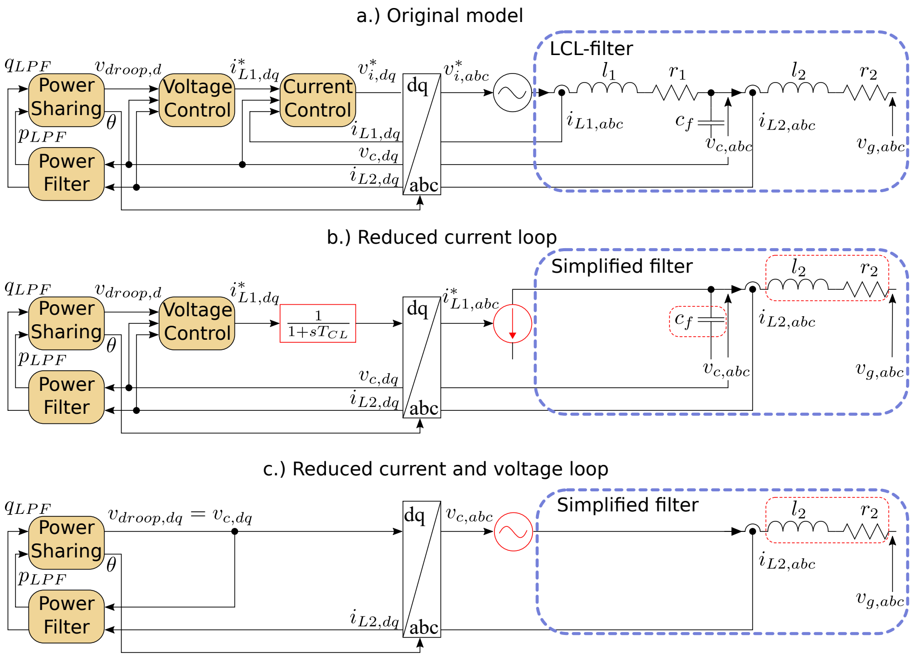

Figure 3.17.: Model order reduction of grid-forming inverter.

is minor. In contrast to the model in Fig. 3.17c.), the voltage control is not reduced as it affects the dominant modes, as will be shown in Ch. 5. The grid-side conductor l_2 is approximated by a first-order Taylor series.

Whereas the time constants of LV lines are relatively small due to the high R/X ratio, the time constant (L/R) of the grid-side inductor is larger and it may affect the slower modes. Hence, its approximation may not be valid, especially when the phasor model is used. To alleviate the problem, a modification of the microgrid model based on the wye-delta transform is proposed in this work.

A single line diagram of an example microgrid with two PED, two loads and two lines is shown in Fig. 3.18a.). For the PED, only the filter capacitor and the impedance of the grid-side inductor $\underline{z}_{L2}$ are shown. Two simplifications are applied in Fig. 3.18b.). On the one hand, PED 1 is connected at the end of a line and impedances $\underline{z}_{L2}$ and $\underline{z}_{Line1}$ are merged. This not only reduces the overall number of impedances, the time constant of the resultant impedance will also be the average of the time constants of $\underline{z}_{L2}$ and $\underline{z}_{Line1}$. Hence, the high time constant of $\underline{z}_{L2}$ is avoided or at least alleviated by the high R/X ratio of the LV line.

On the other hand, there is no additional line between PED 2 and load 2, whereby

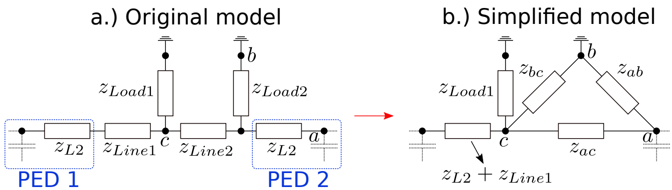

Figure 3.18.: Microgrid simplification.

the above described procedure is not possible here and $\underline{z}_{L2}$ cannot be merged with any line impedance. However, nodes a, b and c form a wye connection, which can be transformed to a delta connection. This way, the impedance $\underline{z}_{L2}$, with its large time constant, can be omitted.

This is demonstrated by an example with actual values, assuming the impedances $\underline{Z}_{L2} = (0.03 + j0.11)\ \Omega$ (typical for an inverter with 10 kVA), $\underline{Z}_{Load2} = (14.68 + j4.40)\ \Omega$ ($S_{Load2} = 10$ kVA, power factor of 0.95 inductive) and $\underline{Z}_{Line2} = (0.062 + j0.016)\ \Omega$ (typical LV line with 100 m length). The resulting impedances after the wye-delta transform are

$$\underline{Z}_{ab} = \frac{\underline{Z}_{L2}\underline{Z}_{Load2} + \underline{Z}_{L2}\underline{Z}_{Line2} + \underline{Z}_{Load2}\underline{Z}_{Line2}}{\underline{Z}_{Line2}} = (20.87 + j31.10)\ \Omega, \tag{3.67}$$

$$\underline{Z}_{ac} = \frac{\underline{Z}_{L2}\underline{Z}_{Load2} + \underline{Z}_{L2}\underline{Z}_{Line2} + \underline{Z}_{Load2}\underline{Z}_{Line2}}{\underline{Z}_{Load2}} = (0.09 + j0.12)\ \Omega, \tag{3.68}$$

$$\underline{Z}_{bc} = \frac{\underline{Z}_{L2}\underline{Z}_{Load2} + \underline{Z}_{L2}\underline{Z}_{Line2} + \underline{Z}_{Load2}\underline{Z}_{Line2}}{\underline{Z}_{L2}} = (20.97 + j1.52)\ \Omega. \tag{3.69}$$

$\underline{Z}_{ab}$ has the largest time constant with 4.7 ms, whereas the time constant of Z_{L2} is 11.7 ms. Hence, the phasor approximation will be more accurate after the wye-delta transform.

The PED control uses the output current over $\underline{z}_{L2}$. It can be derived by adding the currents over $\underline{z}_{ab}$ and $\underline{z}_{ac}$. The procedure described requires that loads are modelled as impedances as well as the wye topology at the coupling point of the DER. The latter is for instance also available with a T-connection to a line.

3.6.3.3. Grid-Feeding and Grid-Supporting Power Electronic Devices

The grid-feeding and grid-supporting PED are covered together in this section due the structural resemblance of their controllers. Two variants of the grid-feeding control with an LCL filter are depicted in Fig. 3.19 [234, 93, 235]. The damping resistor r_f of the filter capacitor c_f is not shown. Similar to the grid-forming control, the abc/dq-transform is at the centre of the model, but the transformation angle is measured by a PLL here. The PLL measures the angle of grid voltage $v_{g,abc}$.

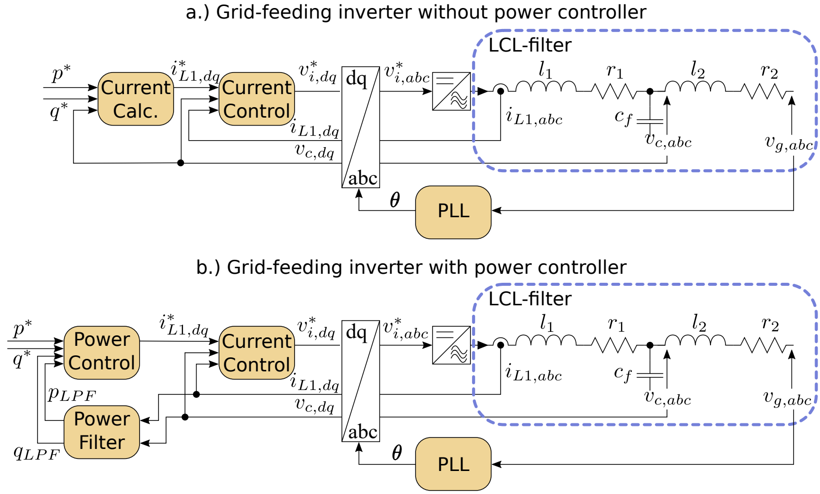

Figure 3.19.: Overview of different types of grid-feeding inverters with LCL-filter.

In Fig. 3.19a.), the current reference $i^*_{L1,dq}$ is calculated from the capacitor voltage $v_{c,LPF,dq}$ and the set values for p^* and q^* in the 'Current Calc.'-block as follows:

$$i^*_{L1,d} = \frac{2}{3}\frac{p^* v_{c,d} + q^* v_{c,q}}{v^2_{c,d} + v^2_{c,q}} \tag{3.70}$$

$$i^*_{L1,q} = \frac{2}{3}\frac{p^* v_{c,q} - q^* v_{c,d}}{v^2_{c,d} + v^2_{c,q}}. \tag{3.71}$$

It is seen that the current $i_{L1,dq}$ is the control variable. It determines the power that is supplied from the inverter-side branch of the LCL-filter. However, the reactive power consumption of the capacitor affects the power that is supplied to the grid. The reactive power consumption of the the filter capacitor c_f can be compensated by recalculating the reactive power set value as follows:

$$q^*_{comp} = q^* + \frac{3}{2}(v^2_{c,d} + v^2_{c,q})\omega_0 c_f. \tag{3.72}$$

A LPF may be necessary to filter the harmonics in the measured voltage v_c [234]. The model and tuning of the current controller and also the LCL filter design are similar to the grid-forming inverter.

Another control strategy for grid-feeding inverters frequently applied in practice is illustrated in Fig. 3.19b.). It comprises an additional power controller, often a PI-controller, that controls the output power of the inverter. Its inputs are the set values for active

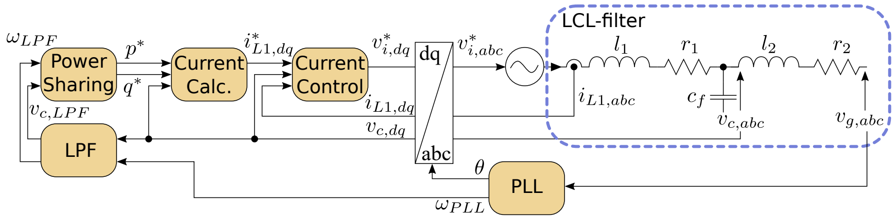

Figure 3.20.: Overview of grid-supporting inverter with LCL-filter.

and reactive power and their low-pass filtered measurement p_{LPF} and q_{LPF}. The output serves as the reference value of the current control. The compensation from (3.72) can also be used here.

It is shown in [236] that the control concept with the additional power controller is slower and less stable. The stability of an islanded microgrid with grid-forming droop controlled and grid-feeding inverters is investigated in [93]. It is found that the influence of grid-feeding inverters on the small-signal stability of the system is minor.

The overview of a grid-supporting inverter is depicted in Fig. 3.20. It is similar to 3.19 a.). To enhance the stability of the grid-supporting control, the power controller from 3.19b.) is omitted in this work. The references for active and reactive power output of the inverter originate from the power sharing control described in Sec. 3.6.2.6. The measured frequency ω_{LPF} and voltage magnitude ($\sqrt{v_{c,d}^2 + v_{c,q}^2}$) are low-pass filtered and then forwarded to the power sharing controller. Sec. 3.6.2.1 on the measurement filtering is also applicable to the grid-supporting inverter, except that the input variables are the measured frequency and voltage magnitude.

3.6.3.3.1. Model Order Reduction

Fig. 3.21 compares the original 13^{th} order grid-supporting PED model (low pass filter: 2 states, power sharing/droop: 1 state, current control: 2 states, PLL: 2 states, LCL-filter modelled in dq reference frame: 6 states) with simplified representations.

The current loop is simplified similar to the grid-forming model in Fig. 3.17b.). A further reduction is to additionally neglect the filter capacitor and grid-side inductor, which means that the current supplied to the grid is directly set. Consequently, the capacitor voltage cannot be used as input to the current calculation and is replaced by the grid voltage v_g. This way, the model order reduces to 7. For both simplified models, the first order lag must be present, because of the interdependency between the supplied current (i_{L1} or i_{L2}) and the measured voltage (v_c or v_g). It leads to instability if not decoupled by the first order lag.

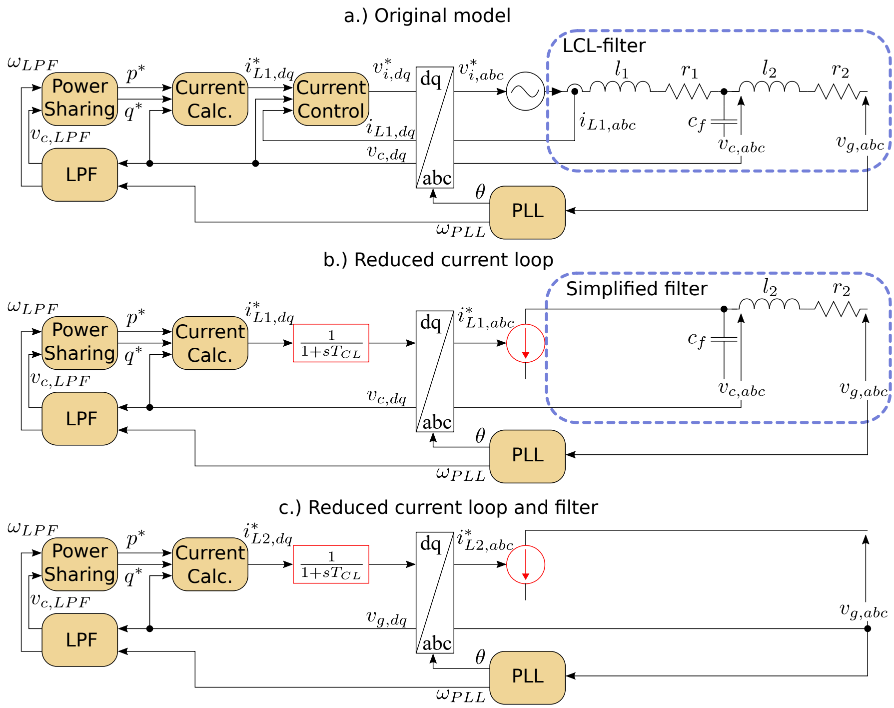

Figure 3.21.: Model order reduction of grid-supporting inverter.

Similar simplifications can of course also be applied to the grid-feeding PED, but are not made use of in this work.

3.6.4. Diesel Synchronous Generators

Diesel engine powered SM, which are also referred to as gensets, have been typically assigned the role of grid-forming units in a microgrid [237]. Due to their flexibility, battery storage systems have become an alternative to fulfil this role. Having several flexible grid-forming units in a microgrid enhances the resilience.

Grid-forming and grid-feeding control are used for SM in this work. The control principles are shown in Fig. 3.22 together with a single line diagram of the grid connection of the SM. In the grid-forming mode, the low-pass filtered active and reactive power output are forwarded to the power sharing controller. Due to the large time constants, the transient droop (Sec. 3.6.2.3.3) and the active power feed-forward droop (Sec. 3.6.2.3.4) control are not suitable for SM. The frame transformation droop (Sec. 3.6.2.3.5), however, also takes effect on slower mechanisms and the static power sharing. Hence, frame

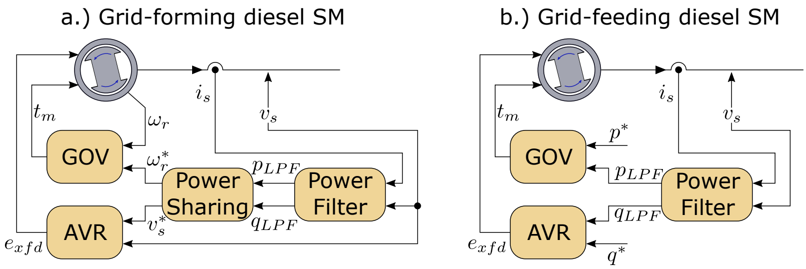

Figure 3.22.: Grid-forming and grid-feeding SM.

transformation droop enhances the flexibility and is applied for SM in this work.

The inputs of the governor are the desired rotor frequency ω_r^* and actual rotor frequency ω_r and its output is the mechanical torque of the SM rotor t_m. The AVR controls the stator voltage v_s by adjusting the field winding voltage e_{xfd} of the SM. In case of the grid-feeding control in Fig. 3.22, the GOV controls the active power and the AVR the reactive power. SM, AVR and GOV are detailed in the subsequent sections for the grid-forming control mode. The models are similar in grid-feeding control, except for the input of AVR and GOV.

In present interconnected power systems, the power system stability is closely connected to the synchronism of SM. The electrical and electromechanical behaviour of the majority of synchronous machines can be modelled using the equations of the three-phase salient-pole synchronous machine [134]. The modelling and analysis of synchronous machines has always been a challenging task. It is covered in a number of books [60, 134, 238, 239, 240]. The detailed mathematical model of a synchronous machine will be described in this section.

3.6.4.1. Synchronous Machine

The schematic of the cross section of three-phase two-pole synchronous machine is illustrated in Fig. 3.23. The field and armature are the essential elements of the machine. Alternating voltages are induced in the armature windings by the rotating field winding f_d, which carries direct current. Additionally, there are two damper windings $k_{q,1}$ and $k_{q,2}$ in the rotor q-axis and one damper winding $k_{d,1}$ in the d-axis. All windings are represented by a single loop in Fig. 3.23.

Assuming the uniform rotation of the magnetic field, voltages displaced by $120°$ in time phase will be induced in the three-phase armature windings due to their distribution of $120°$ apart in space. Depending on the number of field poles p_f, the synchronous

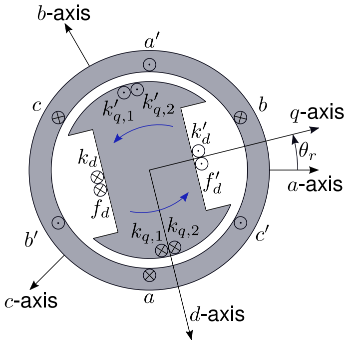

Figure 3.23.: Cross section of three-phase two pole SM.

mechanical speed n of the rotor in revolutions per minute is given by

$$n = \frac{120 f_n}{p_f}, \tag{3.73}$$

where f_n is the nominal frequency. The following assumptions are made for the development of the synchronous machine equations [60]:

- Regarding the mutual effects with the rotor, the stator windings are sinusoidally distributed along the air gap between stator and rotor
- The rotor inductances are not affected by the stator slots when varying the rotor position
- The magnetic hysteresis and magnetic saturation are negligible

If the equations of the SM are established in the natural abc-frame, they contain inductance terms which vary with the rotor angel θ_r, which in turn varies in time with the rotor frequency ω_r. If an appropriate transformation of stator variables is applied, a much simpler form with a clearer presentation of the physical relationships is attained. Therefore, the stator variables are transformed into the $dq0$-reference frame, that rotates with the rotor angle θ_r.

The state equations of the stator and rotor windings can then be expressed as follows [134]:

$$s\psi_{qs} = \omega_n[v_{qs} - \frac{\omega_r}{\omega_n}\psi_{ds} + \frac{r_s}{x_{ls}}(\psi_{mq} - \psi_{qs})], \tag{3.74}$$

$$s\psi_{ds} = \omega_n[v_{ds} + \frac{\omega_r}{\omega_n}\psi_{qs} + \frac{r_s}{x_{ls}}(\psi_{md} - \psi_{ds})], \tag{3.75}$$

$$s\psi_{0s} = \omega_n(v_{0s} - \frac{r_s}{x_{ls}}\psi_{0s}), \tag{3.76}$$

$$s\psi_{kq1} = \omega_n \frac{r_{kq1}}{x_{lkq1}}(\psi_{mq} - \psi_{kq1}), \tag{3.77}$$

$$s\psi_{kq2} = \omega_n \frac{r_{kq2}}{x_{lkq2}}(\psi_{mq} - \psi_{kq2}), \tag{3.78}$$

$$s\psi_{fd} = \omega_n[\frac{r_{fd}}{x_{md}} e_{xfd} + \frac{r_{fd}}{x_{lfd}}(\psi_{md} - \psi_{fd}), \tag{3.79}$$

$$s\psi_{kd} = \omega_n[\frac{r_{kd}}{x_{lkd}}(\psi_{md} - \psi_{kd})], \tag{3.80}$$

where ψ_{qs}, ψ_{ds} and ψ_{0s} are the stator fluxes in the d-, q- and 0-axis, respectively. ψ_{kq1}, ψ_{kq2}, ψ_{fd} and ψ_{kd} are the fluxes in the first and second damper winding in the $q-$ axis, the field winding and the damper winding in the d-axis, respectively. ψ_{md} and ψ_{mq} are the mutual fluxes in the d- and q-axis, respectively. v_{ds}, v_{qs} and v_{0s} are the stator voltage in the d-, q- and 0-axes, respectively. r_s, r_{kd}, r_{lkq1}, r_{kq2} and r_{fd} are the resistances of the stator, the damper winding in the d-axis, the first and second damper winding the q-axis and the field winding, respectively. x_{ls}, x_{lkq1}, x_{lkq2}, x_{lkd} and $x_l fd$ are the stator leakage reactance, the reactances of first and second damper winding in the q-axis, the reactance of the damper winding in the d-axis and the reactance of the field winding, respectively. e_{xfd} is the exciter voltage in the field winding.

The magnetizing flux linkages are expressed in terms of winding flux linkages in order to have a proper state model, which yields [134]:

$$\psi_{md} = x_{ad}(\frac{\psi_{ds}}{x_{ls}} + \frac{\psi_{fd}}{x_{lfd}} + \frac{\psi_{kd}}{x_{lkd}}), \tag{3.81}$$

$$\psi_{mq} = x_{aq}(\frac{\psi_{qs}}{x_{ls}} + \frac{\psi_{kq1}}{x_{lkq1}} + \frac{\psi_{kq2}}{x_{lkq2}}) \tag{3.82}$$

where

$$x_{aq} = (\frac{1}{x_{mq}} + \frac{1}{x_{ls}} + \frac{1}{x_{lkq1}} + \frac{1}{x_{lkq2}})^{-1} \tag{3.83}$$

$$x_{ad} = (\frac{1}{x_{md}} + \frac{1}{x_{ls}} + \frac{1}{x_{lfd}} + \frac{1}{x_{lkd}})^{-1}. \tag{3.84}$$

The stator currents are the output of the machine model and can be described as:

$$i_{ds} = \frac{1}{x_{ls}}(\psi_{ds} - \psi_{md}) \tag{3.85}$$

$$i_{qs} = \frac{1}{x_{ls}}(\psi_{qs} - \psi_{mq}) \tag{3.86}$$

$$i_{0s} = \frac{1}{x_{ls}}\psi_{0s} \tag{3.87}$$

The mechanical part of the machine can be described by defining the per unit rotor

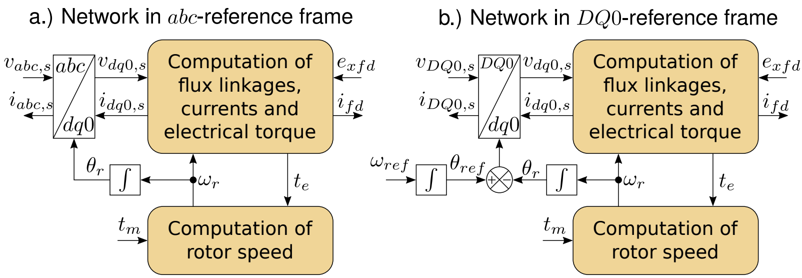

Figure 3.24.: Reference frames for SM coupling with the power system.

speed ω_r as

$$\omega_r = -\frac{\omega_n}{2Hs}(t_e - t_m), \tag{3.88}$$

where H is the inertia constant in seconds and t_e and t_m are the mechanical and electrical torques, respectively. The electrical torque is defined as

$$t_e = \psi_{ds} i_{qs} - \psi_{qs} i_{ds}. \tag{3.89}$$

The simulation of the SM is shown in block diagram form in Fig. 3.24 [134]. If the network is modelled in the natural abc-reference frame, the rotor angle θ_r is used for the $abc/dq0$-transformation. The flux linkages are computed according to (3.74) - (3.80), the currents in accordance to (3.85) - (3.87) and the electrical torque as defined in (3.89). The exciter voltage e_{xfd} is needed as an input for the computation of the flux linkages and the field winding current i_{fd} may be needed for the simulation of the exciter.

The mechanical torque for the computation of the rotor speed originates from the governor model. If the network is modelled in the $DQ0$-reference frame, the $abc/dq0$-transformation is replaced by a transformation between the synchronous reference frame of the network and the rotor reference frame. The angle for this $DQ0/dq0$-transformation is the difference between the angle of the network, which is the reference angle θ_{ref}, and the rotor θ_r. If the system is symmetric, the zero sequence can be omitted from the equations.

Simplified models are often used to reduce the complexity of the model and the computational effort. A common simplification is to neglect the stator transients [134, 241]. In this work, however, stator transients are taken into account due to possible interactions with the fast dynamics of PED. Moreover, it is not recommended to apply simplifications in small low-power systems [134].

SM may be equipped with a power electronics front end which enables the non-synchronous operation of the engine. In this way, increased power density and higher

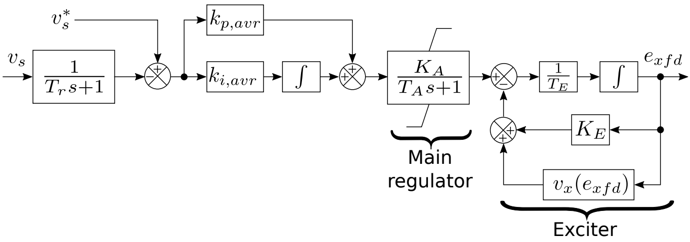

Figure 3.25.: AVR model AC5A to control stator voltage v_s.

efficiency can be achieved [242]. On the other hand, the inverter increases the overall cost of the system, reduces the reliability and hampers the provision of short circuit currents. SM are coupled with the network directly in this work.

3.6.4.2. Automatic Voltage Regulator

Two different AVR models are used in this work, depending on the voltage level. For LV applications, the model shown in Fig. 3.25 is implemented. It is similar to the AC5A system with a brushless exciter [243] except that a PI-controller is used [226, 89]. It is widely applied by the industry and commonly used for small sized SM. The measured stator voltage is filtered by a first order lag with the time constant T_r. The output of the PI-controller is fed into the main voltage regulator which consists of another first order lag with the time constant T_A and the gain K_A. The exciter in Fig. 3.25 is modelled depending on the time constant T_E, the exciter gain K_E and the saturation which is a function of the exciter output voltage e_{xfd} according to (3.90) [244].

$$v_x = e_{xfd} s_E(e_{xfd}). \tag{3.90}$$

The saturation $s_E(e_{xfd})$ is defined as

$$s_E(e_{xfd}) = \begin{cases} e_{xfd} \frac{s_E(e_{xfd,2})}{e_{xfd,2}} & for\ e_{xfd} < e_{xfd,2} \\ s_E(e_{xfd}) + (e_{xfd} - e_{xfd,2}) \frac{s_E(e_{xfd,1}) - s_E(e_{xfd,2})}{e_{xfd,1} - e_{xfd,2}} & for\ e_{xfd} > e_{xfd,2}. \end{cases} \tag{3.91}$$

The saturation function is also illustrated in Fig. 3.26.

For the MV diesel SM, the field controlled alternator rectifier (AC1A) model illustrated in Fig. 3.27 is utilized [245]. Besides the measurement filter, it consists of an alternator main exciter with non-controlled rectifiers and a damping filter. The field winding current i_{fd} is an additional input.

Large thermal power plants are usually equipped with power systems stabilizers to

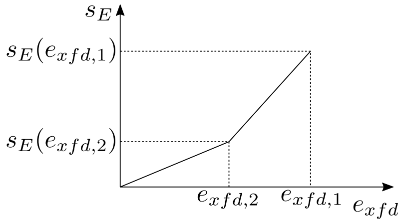

Figure 3.26.: AVR saturation function.

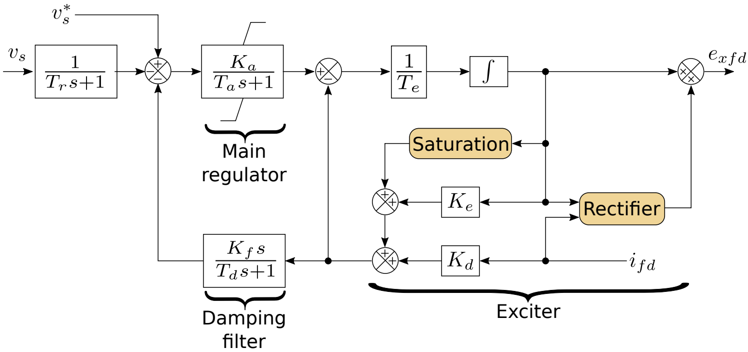

Figure 3.27.: AVR model AC1A to control stator voltage v_s.

dampen rotor oscillations by means of field voltage control. However, the application of power system stabilizers is not common for diesel SM.

3.6.4.3. Governor

As for the AVR, differing models are used for the GOV depending on the voltage level. The governor of the LV diesel SM is depicted in Fig. 3.28. Focusing on electricity production, it is sufficient to use a much lower order model than available models that consider thermodynamic aspects. A PI-controller is employed to regulate the frequency [226, 89]. The control signal is transformed into a fuel current by the current driver gain K_3. A limited first order lag represents the actuator. The time constant τ_2 varies and is a complicated function of the fuel temperature. Its variation can be ignored for simplicity. The engine combustion system comprising a number of cylinders is represented by a dead time element. The dead time, which is assumed constant, represents two components for each individual cylinder: The power stroke delay, which varies randomly, and the ignition delay, which depends on the generator speed [246].

The GOV for the MV system is illustrated in Fig 3.29 [247]. The combustion engine

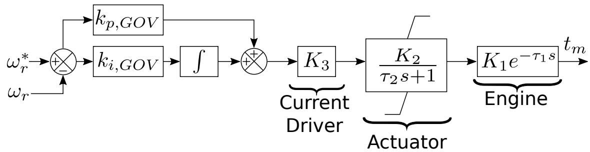

Figure 3.28.: Governor for LV applications.

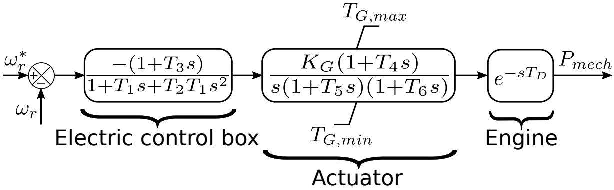

Figure 3.29.: Governor for MV applications.

is again represented by a dead time [248]. Further components are the electrical control box and the actuator.

3.6.4.4. Virtual Impedance

VI was developed for inverter control. However, it is also used in the SM control in this work to allow for maximum flexibility of the controller. VI not only influences the transient behaviour, but also improves the steady state power sharing as described in Sec. 3.6.2.5. The set point for the stator voltage v_s^* is adapted by subtracting an absolute voltage value $\Delta v_{vi,SM}$:

$$\Delta v_{vi,SM} = |\underline{i}_s \underline{z}_{vi,SM}| = |\underline{i}_s (r_{vi,SM} + j\omega l_{vi,SM})|. \tag{3.92}$$

3.6.5. Wind Power Plants

3.6.5.1. Basics of Type 3 Generator

A type 3 variable speed wind turbine with DFIG is used in this work and its simplified structure and control is depicted as a single line diagram in Fig. 3.30. In addition, there is a transformer to connect the 690 V of the stator to the 20 kV medium voltage network. Simulink's build-in model is applied to represent the DFIG [249], which implements a fifth order model for the induction machine [250]. The averaged model [222] is again used for grid-side and rotor side converters. Hence, they are represented by an ideal voltage source. The grid side converter controls the DC voltage to remain stable. The control of the rotor side converter is elaborated in Sec. 3.6.5.3.

3.6.5.2. Doubly-Fed Induction Generator Internal Voltage

Controlling the internal voltage of the DFIG to adjust the active power when the grid frequency varies is the essence of all inertia support methods. In order to enhance the understanding of the dynamic interaction between DFIG and grid, the internal voltage of the DFIG is elaborated in the following. The description of the synthetic internal voltage is inspired by the SM model, where the rotating exciter field induces voltages in the stator windings. According to the DFIG machine model in the dq reference frame, the stator side circuit equation is [251]

$$\underline{v}_{s,dq} = -r_s \underline{i}_{s,dq} + \frac{d\underline{\psi}_{s,dq}}{dt} + j\omega_1 \underline{\psi}_{s,dq} \tag{3.93}$$

where $\underline{i}_{s,dq}$ is the stator current, $\underline{v}_{s,dq}$ is the stator voltage, r_s is the stator resistance and ω_1 is the rated angular speed. The stator flux can be written as

$$\underline{\psi}_{s,dq} = -l_s \underline{i}_{s,dq} + l_m \underline{i}_{r,dq} \tag{3.94}$$

where i_r is the rotor current, l_s is the stator inductance and l_m is the mutual inductance. Combining (3.93) and (3.94) gives

$$\underline{v}_{s,dq} + r_s \underline{i}_{s,dq} + l_s \underline{i}_{s,dq} j\omega_1 + \frac{dl_s \underline{i}_{s,dq}}{dt} = \frac{dl_m \underline{i}_{r,dq}}{dt} + j\omega_1 l_m \underline{i}_{r,dq}. \tag{3.95}$$

The stator current transient can be neglected in the electromechanical timescale [252]. Moreover, as the rotor current is controlled by the rotor side converter with a high bandwidth, rotor current transient dynamics can also be neglected [251], which yields

$$\underline{v}_{s,dq} + r_s \underline{i}_{s,dq} + j\omega_1 l_s \underline{i}_{s,dq} = j\omega_1 l_m \underline{i}_{r,dq}. \tag{3.96}$$

The actual rotor current is equal to the rotor current reference in the electromechanical timescale, when neglecting the rotor current transient. Consequently, the rotor side converter actually controls the internal voltage of the DFIG directly. Therefore, the dynamics are similar to the voltage behind reactance model of SM, because this internal voltage directly determines the dynamics of the DFIG in the electromechanical timescale.

The fact that the DFIG is not only connected to the grid through the stator, but also through the grid side converter, has been omitted so far. The bandwidth of its control loop is high and its impact can be neglected for the internal voltage. The impact of the grid side converter can be merged into the mutual impedance, taking into account that the grid side converter delivers the slip power, as elaborated in [251]. The grid side converter can be merged into the internal voltage by defining the internal impedance $x_d = \omega_1 l_s$ and

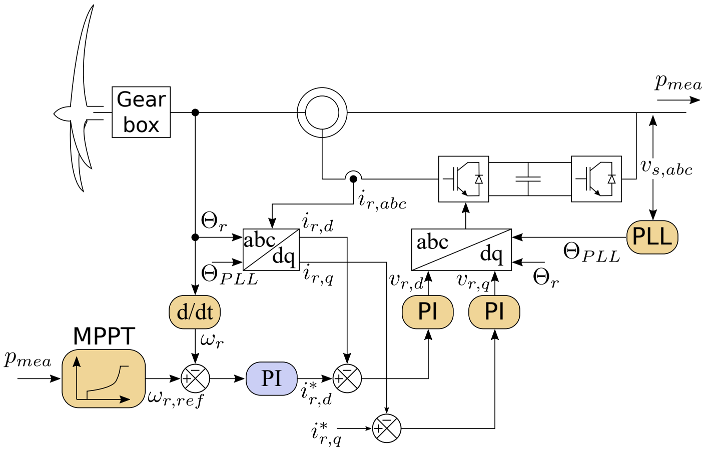

Figure 3.30.: DFIG wind power plant control.

by changing the internal impedance to $x_d/(1 - s_{slip})$ in the q-axis circuit, where s_{slip} is the slip of the DFIG.

3.6.5.3. Rotor Side Converter Control

The maximum power point tracker (MPPT) determines the reference angular speed of the rotor $\omega_{r,ref}$ according to the measured active power p_{mea}. The direct axis rotor current reference $i_{r,d}$, which regulates the active power, is obtained from a PI-controller which has the angular speed error as input. The current loop comprises PI-controllers for both axes and controls the voltage of the rotor side converter. With a bandwidth of 100 Hz, it is the fastest control loop of the cascade. The reference of the q-axis rotor current is zero, as the reactive power reference of the DFIG is always zero in this work, the focus lies on SI and active power support.

In order to provide sustained active power for frequency regulation, deloaded mode of operation has to be applied [253, 254, 255]. In deloaded operation, the DFIG is not controlled in accordance to the angular speed reference, but to supply a certain active power, which is below the optimal operating point. Hence, the input of the PI-controller (blue in Fig. 3.30) is not the angular speed error, but the active power error. The plant is operated at a suboptimal operating point, forcing it to deliver less active power than it is actually capable to generate at a given moment. Depending on the wind speed, the deloaded operating point is either obtained by adjusting the rotor speed or the pitch angle [256].

This is illustrated in Fig. 3.31. For moderate wind speeds, the rotor speed is

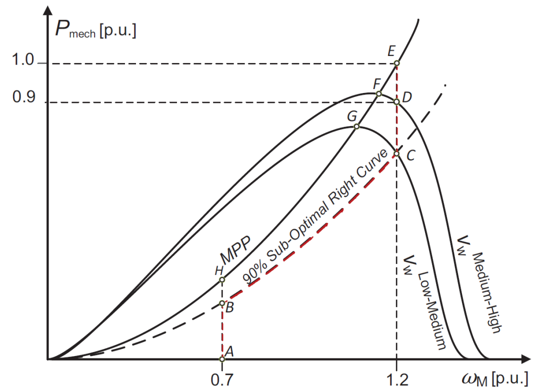

Figure 3.31.: Deloaded operation for several operating points [257].

adjusted higher than the optimal operating point, shifting from G to C. In this way, kinetic energy can be released from the rotor in case of a frequency disturbance. Shifting the operating point to a lower rotor speed relative to the optimum would cause instability, since the release of active power for frequency response would further slow down the rotor. For higher wind speeds where the rotor speed is at its maximum, usually 1.2 pu, the pitch angle is used to regulate the output power at a suboptimal operating point, whereas the rotor speed is kept constant. The operating point is shifted from E to D by increasing the pitch angle. To provide additional active power for frequency response, the pitch angle is decreased again.

The wind speed is set to 10.5 m/s in all simulations in this work. The pitch controller is active at this wind speed. The focus of this work is not on the optimization of the deloaded operation but of the inertia provision. The fast dynamics of the inertia provision can be regarded as decoupled from the significantly slower rotor speed and pitch angle control.

Inertial response and primary frequency control in isolated power systems are analysed in [256] with a special focus on the turbine operating point.

3.6.5.4. Phase-Locked Loop Synthetic Inertia

The PLL detects the angle Θ_{PLL} of the stator voltage $v_{s,abc}$. Θ_{PLL} is used to transform the voltages and currents into the dq-reference frame. The PI-controller of the PLL adjusts the angular speed of the PLL ω_{PLL} to the fluctuating grid frequency ω_{grid}, aiming at the quadrature component $v_{q,PLL}$ to be zero.

Fig. 3.32 clarifies this process. The stationary case is shown in a.). The quadrature

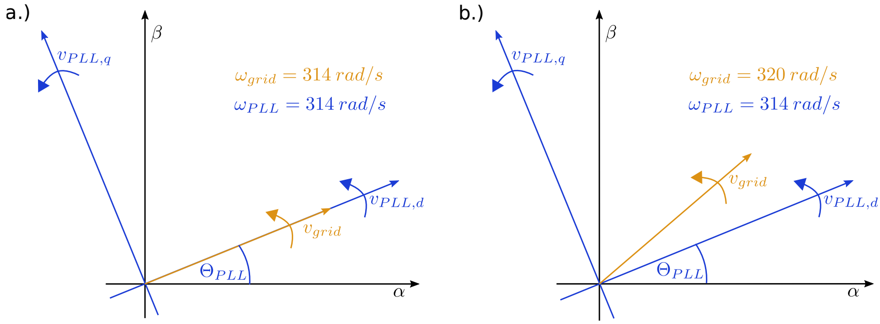

Figure 3.32.: PLL dynamics.

component is zero and the dq-frame of the PLL is aligned to the grid voltage. The grid voltage has undergone a transient change in b.). To bring the quadrature component back to zero, the PI-controller will adjust ω_{PLL}. This procedure is similar to the dynamics of the rotor angle of a SM during frequency transients, considering that Θ_{PLL} determines the angle of the DFIG internal voltage described in Sec. 3.6.5.2. When the PI-controller of the PLL is tuned to slowly react to grid frequency changes, DFIG can provide synthetic inertia (SI) and shows similar response to frequency transients as SM.

One advantage of this SI variant is that no high-pass filtered frequency measurement, as in the case of frequency gradient inertia and which can lead to instability [17], is necessary. Furthermore, similarities with SM dynamics allow for the utilization of control strategies related to those in conventional power systems, where a lot of experience exists.

The PLL dominates the internal voltage phase motion in a vector controlled DFIG. Therefore, manipulating the PLL parameters is a very direct way of controlling the output active power [258]. There is still lack of literature focusing on the impact of PLL in stability studies [259]. Significant influence of PLL on small-signal stability was stated in [260, 261]. Systematically manipulating PLL parameters to provide SI was first introduced in [16].

3.6.5.5. Frequency Gradient Synthetic Inertia

Another means of providing SI often found in literature [262] is the frequency gradient SI. It is another way to imitate the inertia in the equation of motion of SM. It has been applied in commercial wind turbines [263]. The active power is controlled in proportion to the frequency gradient:

$$\Delta p = -k_{SI}\frac{df_{PLL}}{dt}, \tag{3.97}$$

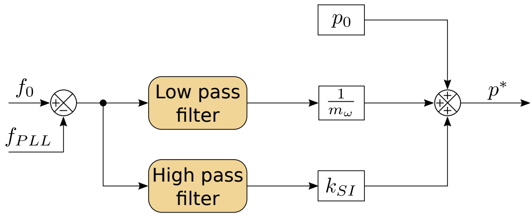

Figure 3.33.: Combination of frequency gradient SI and grid-supporting droop control.

where k_{SI} is the proportional factor of the SI and f_{PLL} is the frequency measured by the PLL. A high pass filter with the time constant T_{SI} is employed as it is not possible to use the pure derivative in practice. There is a trade-off between rapid inertia response and controller stability and the selection of the proportional factor and the time constant is a difficult task [264, 265, 266]. [17] reports stability issues of this controller type. It is suggested to use a time constant of at least 1 s for the high-pass filter to guarantee stability. In this work, a compromise between the values found in literature [264] and the stability limit identified in [17] is made by selecting $T_{SI} = 0.5$ s. Deriving an optimal value for T_{SI} is not the focus of this work and remains an open question for future research.

The frequency gradient SI can be merged with grid-supporting droop control as shown in Fig. 3.33. The variable p_0 is the active power set point of the deloaded operation and p^* is the resulting active power set point. Reactive power droop is not applied by the DFIG.

The frequency response of full-size converter, DFIG and active stall induction generator wind power plants on a physical island are examined in [267]. Dynamic penetration limits could be relaxed substantially by the combination of droop control and frequency gradient inertia.

3.6.5.6. Combined Synthetic Inertia

The possibility to combine both means of providing SI is investigated in this work, as they complement one another in terms of response time. Active power provision by a slow PLL is not immediately at its maximum as the active power output is proportionate to angle between internal and stator voltage. For example, when the grid frequency decreases, this angle starts to grow and alongside the active power rises.

The response of the frequency gradient SI depends on the PLL bandwidth and the time constant of the high-pass filter and is usually quicker than the method with slow PLL. Therefore, it is advantageous to combine both methods.

As opposed to the slow PLL method, the frequency gradient SI necessitates a PLL with reasonably fast response. It is, therefore, helpful to implement two PLLs with differing bandwidth.

3.7. Loads

The focus is placed on the interaction and stability of DER in this work. The load model is kept simple.

Static load models [268, 269] with constant impedance are used for one thing in transient EMT simulations in the abc frame. Then again, they are not feasible for other parameter optimization studies due to their voltage dependency. For example, the undesired voltage dependency causes the optimization algorithm to favour controller parameters that result in voltages with low magnitudes. This decreases the disruption by load switching events as the actual power variation is reduced. Consequently, oscillations are attenuated. This is an optimization goal in this work. However, it originates from the load model here and not some superior controller parameter set.

Instead, a constant active and reactive power current source model is generally used, which is also referred to as a pq-load. The supplied current is given as follows, similar to the current calculation of the grid-feeding inverter:

$$i^*_{Load,d} = \frac{2}{3}\frac{p^* v_{POC,d} + q^* v_{POC,q}}{v^2_{POC,d} + v^2_{POC,q}}, \tag{3.98}$$

$$i^*_{Load,q} = \frac{2}{3}\frac{p^* v_{POC,q} - q^* v_{POC,d}}{v^2_{POC,d} + v^2_{POC,q}}, \tag{3.99}$$

where v_{POC} is the voltage at the point of coupling. The resulting algebraic loop is avoided by implementing a LPF with a time constant of 5 ms for the supplied current $\underline{i}^*_{Load,dq}$. The time constant is chosen higher than the current controller's to avoid interference.

Load modelling is named as an important aspect of future microgrid stability research in [22]. It is essential for the ability to predict the operation of protective devices and potential protection induced cascading failures [31]. However, simple static load models are still widely applied according to a survey [270, 271].

It was shown that droop controlled inverters and active loads are almost completely decoupled in LV microgrids in [93], which justifies the simplification in this work. The active loads in [93] are modelled similar to the grid-feeding inverter in Sec. 3.6.3.3, but additionally incorporate the DC link.

It is reported in [272] that directly coupled induction machines make up about a quarter of loads in MV systems and can cause lightly damped oscillations in microgrids with droop controlled inverters. Controller parameters of dynamic loads may be optimized

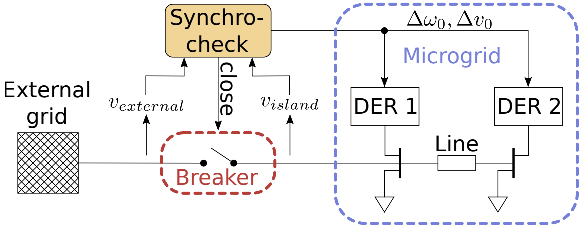

Figure 3.34.: Voltages alignment of microgrid and external grid with synchrocheck.

for system stability, but to the detriment of induction machine control [273]. It is shown in [274] that composite loads, consisting of static loads and induction machines, have a general tendency to enhance the damping of low-frequency oscillatory modes but deteriorate the damping of medium-frequency oscillatory modes.

3.8. Synchrocheck

As elaborated in Sec. 2.2.4, the synchronization of the islanded microgrid with an external grid is one of the critical aspects of microgrid operation. A synchrocheck is used for the synchronization, as shown in Fig. 5.3. It measures the voltage at both sides of the switch that separates the microgrid from the external grid. A PI-controller is then deployed to control the voltage frequency and amplitude set points of the DER in the microgrid. For droop controlled DER, ω_0 and v_0 from the droop equations (3.35) and (3.36) are adjusted [275]. This rather simple synchronization process is adequate for this work, because the focus is placed on the transients and loadings when the breaker closes after synchronization. The external grid is modelled as a stiff voltage source. Any protective devices that might trigger during the process are not modelled.

3.9. Composite Model

An example of a linearized LV microgrid model in the $dq0$-reference frame is presented to provide further insight into the $dq0$ modelling approach. The microgrid with two grid-forming droop controlled DER is illustrated in Fig. 3.35a.) and its composite state-space model is depicted in Fig. 3.35b.). The frequency of PED 1 is used as the reference frequency. Besides the PED, other DER could also be implemented.

It is started from the individual state-space models of the inverters, network and loads, which are then assembled to form the complete model. This procedure is also referred to as the component connection method [276]. The description presented in [76,

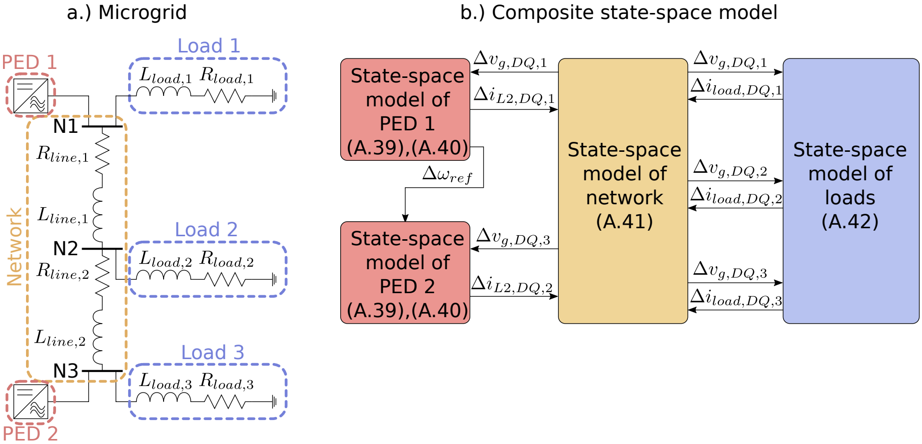

Figure 3.35.: Example microgrid and composite state-space model.

277] and [278] is closely followed. The example is presented in App. A. PEDs are used in this example network. However, they could be replaced with the diesel SM introduced in this chapter.

The simulation and optimization framework, which links the models described in this chapter to the optimization algorithm of Ch. 4, is elaborated in Sec. 4.9.

4. Optimization Algorithm and Framework

4.1. Introduction

The intricacy of the introduced models and the complexity of the parameter optimization problems dealt with in this thesis demand an optimization algorithm that is tailored to the problem. The optimization problems are characterized by a computationally intensive fitness evaluation, as numeric time-domain simulation is necessary. Evolutionary algorithm (EA) is selected as a suitable optimization algorithm and is elaborated in this chapter.

Firstly, an overview of power system optimization methods and applications is provided in this chapter. Next, the objectives and constraints of the controller optimization problem are formulated. The main optimization criteria are the eigenvalue real parts of the system and area criterion, which is a measure for the ability of the system to rapidly reach a new steady state following a disturbance. The main constraints are evaluated at steady-state and include the accuracy of the power sharing between DER as well as limited voltage magnitude and frequency deviations from their nominal values.

Subsequently, a literature review of control parameter optimization in microgrids is provided. Shortcomings of previous approaches are pointed out.

The fundamentals of EA are discussed, detailing various approaches for the evolutionary operators selection, crossover and mutation. Moreover, the handling of constraints violations and approaches for niching to enhance the diversity of the population are explicated. A particular characteristic of the proposed EA is the BSP tree. It is used to improve the mutation, avoid duplicate individuals and promote the diversity of the population.

Finally, the parametrization of the EA is elaborated, which has a huge impact on its efficiency and is a difficult task as the number of possible combinations is numerous and parameters are interdependent. Benchmark cost functions are used for the EA parameter selection, because the actual optimization problems are too computationally intensive for the necessary large number of EA runs.

The chapter closes with an overview of the simulation and optimization framework which connects Ch. 3 on modelling with Ch. 4 on optimization.

4.2. Overview of Power System Optimization

Some of the main fields subject to optimization in power systems are [279]:

- Optimal reconfiguration of distribution networks
- Thermal unit commitment/hydrothermal coordination
- Uncertainty analysis
- Economic dispatch/optimal power flow
- Reactive source allocation
- Expansion planning
- Maintenance scheduling

A wide variety of techniques to solve these problems exists, including conventional and modern optimization methods. Three groups are identified [280]:

1. Conventional optimization techniques
   - Linear programming, network flow programming, nonlinear programming, quadratic programming, newton method, mixed-integer programming
2. Intelligent search methods
   - Evolutionary algorithms, tabu search, artificial neural network, particle swarm optimization
3. Nonquantity approaches to address uncertainties in objectives and constraints
   - Fuzzy set applications, analytic hierarchical process, probabilistic optimization

The optimization problems in this work are characterized by their increased complexity. Numeric simulations are necessary to evaluate a solution to the problem. A strict mathematical formulation of the problem is not possible. It is, therefore, resorted to a EA on the grounds of its flexibility in problem solving.

4.3. Literature Review on Microgrid Stability Optimization

The optimization of microgrid parameters regarding system stability can be classified into online and offline tuning [281, 282]. In online tuning, the control parameters are adjusted during the operation of the system. It is possible to to adapt to changing circumstances such as the line impedance between DER and loads when the consumption fluctuates. To this end, an adaptive neuro-fuzzy inference system for droop controlled inverters is proposed in [283]. Linear programming is utilized in [169] to optimize the stability of DER resorting to low-bandwidth communication. It is also stated that there is a general trend towards decentralization of controller optimization. The control parameters of a microgrid with virtual synchronous machines are optimized during operation using particle swarm optimization in [206]. The criteria are the damping ratio, the largest occurring real part of the eigenvalues and the voltage angle deviations with respect to the centre of inertia.

The focus of this work is on offline tuning, where it is desired to obtain a fixed parameter set in advance to guarantee the stable operation under various conditions. The small-signal stability of DER is optimized offline using Markov chains and Markov jump linear systems for a MV feeder in [284]. Particle swarm optimization is used in [285] to optimize droop controlled DER in a small microgrid. The total harmonic distortion and the area criterion for power sharing are considered in the fitness function. Grid-supporting droop control is optimized in [286] with particle swarm optimization. [191] also resorts to particle swarm optimization to optimize a nonlinear droop with respect to power sharing and cost reduction. The inverter control and the filter parameters are optimized in [287] in a small microgrid with particle swarm optimization. The optimization criteria are the minimization of the largest eigenvalue real part and the power sharing. The feasible range and the optimal value of an algebraic type VI are investigated in [214] resorting to particle swarm optimization. Several criteria are incorporated using weighting factors.

Inverter control with VI is optimized with differential evolution for a small LV microgrid in [210]. A feasible range for the controller parameters is detected in [278] with modal analysis. A GA is then used to find optimal values within this range depending on the power sharing and area criterion. The droop coefficients, the proportional gain of the voltage controller and the integral gain of the current controller are identified as the most influential control parameters. A non-dominated sorting GA, which is a multi-criteria optimization method, is used in [288] to optimize the placement of droop based inverters taking into account the small-signal stability and the network losses. It is shown that other aspects of the microgrid performance, such as losses, voltage profile and reactive power sharing, deteriorate with better small-signal stability. Larger impedances of the connection between grid-forming inverters enhance the stability, but weaken the other criteria. The non-dominated sorting GA is also utilized in [40] for the optimal reconfiguration of droop based islanded microgrids with respect to static criteria.

This review reveals the following characteristics of previous works: The optimization focuses on few parameters that are most influential to the microgrid stability, such as the droop coefficients or the VI. Other parameters with significant influence, for instance the power measurement filter time constant or the feed-forward gain of the voltage controller, are not taken into consideration. It is frequently relied on the droop control in its simplest form, although variants of the droop control and VIs can enhance the performance. Furthermore, the interaction of different controller types, such as grid-forming and grid-supporting, is rarely investigated as most works focus on a single type of control. Moreover, most of the considered microgrids consist of only a small number of nodes. The optimized parameter sets are tested only for a very limited number of use cases, i.e. few operating points are considered and microgrid parameters, such as line length or R/X ratio, are not varied. Hence, the general applicability is not proven.

4.4. Problem Formulation

4.4.1. Objectives

As shown in the literature review of microgrid stability optimization in Sec. 4.3, DER controller parameters are often optimized with respect to the power sharing, largest occurring eigenvalue real part or damping. Further criteria are monetary cost, network losses and other static criteria. In this work, it is focused on the minimization of the largest occurring eigenvalue real part and the area criterion for power sharing.

The real parts of the dominant eigenvalues determine the decay of transients and the ability of a system to rapidly reach a new steady-state operating point. This criterion is preferred over the damping coefficient, because the main goal in inverter-dominated networks is to avoid overloading and violations of component constraints during transients. Therefore, the first priority is the rapid decay of the envelope rather than oscillation damping. Furthermore, as will be seen in Chapter 5 on case studies, extensive oscillation is not an issue in inverter-dominated networks.

The second objective deployed in this work is depicted in Fig. 4.1. To ensure the quick alignment with the reference signal, the area is minimized as illustrated. In this work, the signal is the active or reactive power of a DER. The minimization problem is formulated as follows:

$$\Upsilon_{obj} = Min\Big(\sum_{i=1}^{n}\sum_{k=1}^{l}\int_{t_{step,k}}^{t_{step,k}+t_{settle,k}} |p_{DER,i}(t) - p_{DER,i}(t_{step,k}+t_{settle,k})| + |q_{DER,i}(t) - q_{DER,i}(t_{step,k}+t_{settle,k})|\Big), \tag{4.1}$$

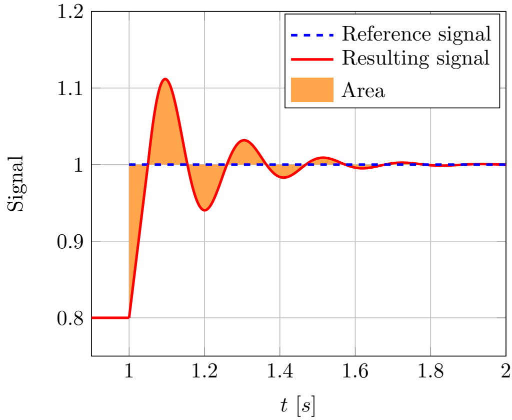

Figure 4.1.: Benchmark functions

where $i = \{1, ..., n\}$ is the DER index and n the number of considered DER, $k = \{1, ..., l\}$ is the load step number and l is the total number of load steps, $p_{DER,i}(t)$ is the active power of DER i, $q_{DER,i}(t)$ is the reactive power of DER i and $t_{step,k}$ is the time of the load step k. $p/q_{DER,i}(t_{step,k} + t_{settle,k})$ is seen as the steady state reference, assuming that the steady state is reached within the settling time $t_{settle,k}$ after a load step. These steady-state values of active and reactive power vary depending the controller parameters.

The area criterion clearly sets the focus on the power sharing of DER and the avoidance of overloading, whereas the stability of the system is not the primary objective. However, the area criterion and eigenvalue real part minimization are complementary. The area criterion is introduced because inverter dominated networks are very stable when using thoroughly optimized controller parameter sets as shown in Chapter 5. This inherent stability allows to focus on power sharing and omitting component overloading, while keeping the dominant eigenvalues in a stable domain by setting a certain maximum real part constraint.

Differing objectives are used for the SI optimization of wind power plants. These will be elaborated in the case study in Sec. 5.10.

4.4.2. Constraints

The steady-state power sharing between DER is dominated by the power sharing control as described in Sec. 3.6.2. The power sharing is inaccurate due to the voltage drop over the power lines. To ensure that the distribution discrepancy is limited, the steady-state active and reactive power difference between the DER is limited. Unless otherwise stated, a maximum of 0.1 pu and 0.2 pu is allowed for active and reactive power, respectively. The limit for the reactive power is a bit more relaxed as it is connected to the voltage in the conventional droop. In addition, accurate steady-state active power sharing can be considered more important due to the cost of the energy provided (or curtailed).

The steady-state voltage deviations at any node with a load is constrained to $+/-0.1$ pu which is a typical value LV systems. The frequency discrepancy at steady-state is limited to 500 mHz. This value is chosen because a frequency droop coefficient m_ω of 0.01, which corresponds to a 500 mHz deviation at 1 pu active power discrepancy, is often found in literature.

These constraint violations are incorporated in the cost as described in Sec. 4.5.2.4. Note that individuals that cause instability of the simulated system are inherently identified as violations of constraints as they cannot be evaluated.

The constraints for the SI optimization of wind power plants will be defined in the case study in Sec. 5.10.

4.5. Fundamentals of Evolutionary Algorithms

Evolutionary algorithms mimic the biological processes of reproduction, recombination, mutation and selection and are assigned to artificial intelligence. No differentiations of the constraints or the objective function are needed in contrast to conventional methods. Variants of EAs are evolutionary programming and evolutionary strategy [289]. They are also closely related to GAs. The distinct feature of the proposed EA that draws the line to GA is the BSP tree, which utilizes the history of all individuals in the previous generations.

The evolution is a process in which individuals belonging to a species show optimized behaviour in order to solve problems characterized by chance, temporality, chaos and non-linear interactivities. Conventional optimization techniques have difficulties in solving this type of problem. Advantages of EAs are their flexibility and their robust response to changing circumstances [279]. Furthermore, the method lends itself to multi-criteria optimization [290]. EAs have one of the lowest probabilities to get trapped in local optima among heuristic methods [279]. However, they perform rather poorly in finding optimal or very close to optimal solutions. Another shortcoming of EAs is their relatively high computational intensity.

4.5.1. Overview

Figure 4.2 depicts flowchart of a basic EA. At first, an initial population consisting of a number of individuals is created. Each of the individuals represents a solution to the

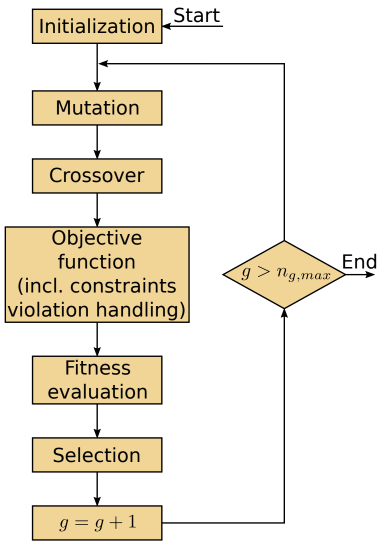

Figure 4.2.: Basic flowchart of a EA.

problem, often selected purely random. In the subsequent iterations, a variation and a selection process is conducted.

The variation process features the random genetic processes mutation and crossover. Each individual is assigned a fitness value evaluating the quality of its solution. The objective function and the fitness function of a EA are not to be confused. The objective function characterizes the performance of an individual independent from other individuals. It incorporates the goodness of the solution regarding the optimization problem and penalties for constraint violations. The outcome of the objective function is also referred to as the cost in this work. The aim of the optimization is to minimize the cost.

The fitness function measures the reproduction opportunities within the population. It may incorporate additional information, such as the diversity of an individual compared to the rest of the population. An approximation can be used if the evaluation of the fitness value is computationally demanding.

Note that the term 'fitness' implies that its maximization is the optimization goal. Optimization problems in this work are minimization problems. It is, therefore, convenient to use the term 'fitness' rather as a measure that needs to be minimized. Hence, better individuals are associated with lower fitness in this work.

During the selection, individuals with better fitness are preferred and have an increased chance to pass their information on to the population of the next generation (iteration). The iterations are performed until a stop criterion is fulfilled. This can be

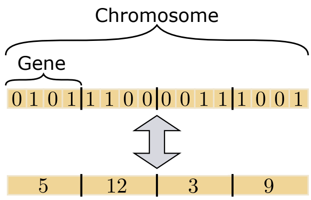

Figure 4.3.: Encoding of chromosomes

a maximum number of generations or when the difference in the average fitness value between subsequent generations falls below a certain threshold. In this way, an asymptotic convergence towards optimal solutions is pursued [279].

The variety of selection methods, evolutionary operators (mutation, crossover and selection) and representations of individuals is manifold [291]. The representation of individuals refers to the encoding of the information individuals contain, which may have a considerable influence on the algorithm's performance. Figure 4.3 illustrates examples for binary and integer representation. Inspired by biology, an attribute of an individual is called gene and a number of attributes referring to related features is named a chromosome. The parameters of an individual are mapped into a finite string of symbols that represent possible solutions in the problem space. A binary, real-valued or character-based symbol alphabet can be used. Integer or continuous values are usually chosen for complex applications. This also facilitates the definition of problem specific operators [279].

Until the end of the 1990's, the assumption that binary representation is superior was prevalent, but has not been supported by empirical results [292, 293]. There is no superior choice of the genetic operators [294], neither holding across all problems nor for a specific type of problem as was shown by mathematical analysis [295]. On the contrary, it was also shown that unspecialised algorithms are outperformed by specialized algorithms in a specific problem domain [296]. The human operator has extensive freedom to adapt the evolutionary approach to the problem.

Some of the advantages of EA are their flexibility and broad applicability, as was mentioned before. The problem space can be disjoint and contain infeasible regions. The same procedure is applicable to mixed-integer problems, discrete combinatorial problems, continuous-valued parameter optimization problems and so forth, without essential alteration. The problem formulation may involve arbitrary linear and non-linear objective functions and constraints. Differentiations are omitted during computation [279].

Although conventional methods outperform EAs for simple, convex problems, it was shown in [297] that their performance can be significantly better for complicated multimodal problems and their chance to get trapped in local optima is lower. EAs can also be hybridized with other methods, for example fuzzy systems or neural networks [298]. Furthermore, EAs are suitable for parallel processing, what makes the method feasible for distributed processing computers. Whereas the computationally intensive evaluation of fitness values is a highly parallel process, only the selection requires some serial processing.

The ability for self-optimization is another interesting feature. Classic methods depend on the appropriate setting of exogenous parameters to tune the optimization algorithm. However, this setting can be a part of the search process in evolutionary computation itself, (e.g. the mutation rate adjusts to the diversity of the population) [279].

4.5.2. Evolutionary Operators and Parameters

The following sections detail the essential operators of evolutionary algorithms: Selection, crossover and mutation.

4.5.2.1. Selection

Selection decides which individuals pass their information on to the population of the next generation. The convergence to local or global optima is dominated by the selection pressure. It dictates the average fitness in a population. The change in each generation's mean fitness is highly dependent on the population fitness variance [279]. On the one hand, a high selection pressure (preference for good individuals) enhances convergence speed. On the other hand, low selection pressure decreases the chance to get trapped in local optima. Therefore, selection schemes should be designed as a trade-off between the preservation of population diversity and convergence.

Numerous selection schemes have been proposed in literature. They can be classified into two groups [279]: Proportionate-based schemes apply the selection with respect to the relative fitness values of individuals. Secondly, in ordinal-based methods, the rank of the individual within the population based on comparison of fitness values is the criterion for selection. The latter are sometimes deemed superior, because they omit the dominance of super fit individuals according to their fitness and, therefore, inherently preserve the diversity of the population [279].

In proportionate-based selection [299], the fitness values are normalized with respect to the range between the best and worst individuals:

$$Fit_{scaled,i} = \frac{Fit_i - Fit_{worst}}{Fit_{best} - Fit_{worst}}, \tag{4.2}$$

where $Fit_{scaled,i}$ is the scaled fitness of individual i, Fit_i is the initial fitness of individual

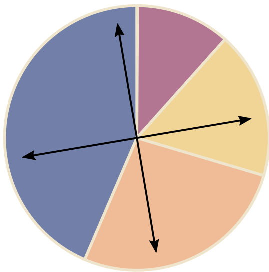

Figure 4.4.: Example for stochastic universal sampling.

i, Fit_{best} is the fitness of the best individual and Fit_{worst} is the fitness of the worst individual in the population.

The individuals are usually selected successively until the mating pool is full in proportionate-based selection. The better the fitness, the more likely it becomes for an individual to be selected. One individual may be selected several times. The stochastic nature of this procedure can lead to a bias in the selected pool. This is avoided in stochastic universal sampling [300], which is illustrated in Fig. 4.4. The sizes of the segments in the pie chart are proportionate to the fitness of the individuals. The number of arrows corresponds to the number of individuals in the mating pool. The angles between the arrows are equal. The arrows are rotated randomly and individuals with an arrow in their segment are selected. In the example in Fig. 4.4, the fittest individual is selected twice in stochastic universal sampling, whereas it may be selected up to four times in simple proportionate-based selection, due to stochastic uncertainties.

To avoid the dominance of very fit individuals and preserve the diversity of the population, individuals are selected according to their rank instead of their fitness in rank-based selection. The selection probability depending on the rank is calculated as follows:

$$L_r = \frac{2}{n_p}(1 - \frac{r-1}{n_p - 1}), \tag{4.3}$$

where L_r is the selection probability of the individual with rank r and n_p is the number of individuals in the population.

Tournament selection also counts among rank-based selection. A number of individuals are drawn randomly from the population and the best ranked among them are selected for the intermediate population. As an example, six individuals are drawn randomly from the population and the two with the best fitness are selected. This procedure is repeated until the mating pool is complete.

A subset comprising of the best individuals is chosen in truncation selection. Then, individuals are selected with the same probability from this subset.

When every individual is assigned a selection probability according to its rank, the linear correlation between rank and selection probability is assured and it is referred to as linear ranking selection. In accordance, exponential ranking selection weights the probabilities exponentially with the rank.

In combination to these techniques, elitist selection can be implemented. The best individuals of the preceding generation are automatically transferred to the new mating pool to ensure that the best solutions are preserved. The remaining individuals are chosen according to one of the selection techniques previously described.

4.5.2.2. Crossover

Crossover mixes the genes of two or more individuals. It is characterized by its disruptiveness, as it can split the information of individuals. The proportion of the parental population that performs crossover is specified by the crossover rate ϱ_{cro}. Individuals not selected for crossover remain unaltered, which means that one parent chromosome goes to one offspring and the other to the other offspring.

Some commonly applied crossover mechanisms are depicted in Fig. 4.5. One-point crossover in Fig. 4.5a.) was applied in traditional EAs [279]. Chromosomes are split at a randomly chosen point between two genes. The offspring consists of the genes left of this point from one parent, and right of this point from the other parent. The procedure with two points works similar and is illustrated in Fig. 4.5b.). This can be extended to m-point crossover, with the number of genes in a chromosome minus one being the maximum of m. The disruptiveness and the diversity of the offspring increases with m. It is referred to uniform crossover if each gene is randomly picked from either of the two parental chromosomes, which is very disruptive. The ordering of the genes is irrelevant in uniform crossover, whereas for smaller m, neighbouring genes have a higher likelihood of being picked from the same parent. Depending on the optimization problem, this may not be a desired characteristic of the crossover, affecting its randomness [301].

The diversity can be promoted by utilizing a weighted convex combination such as the arithmetic crossover:

$$x_{child} = \rho x_{parent,1} + (1 - \rho) x_{parent,2}, \tag{4.4}$$

where $x_{parent,i}$ are the values of the respective gene of parent i, ρ is a random value between 0 and 1 and x_{child} is the value of the child. The child introduces new values that diverge from the parents' values. Other options include the possibility to calculate the average value of the parental genes or the square-root of their product [279].

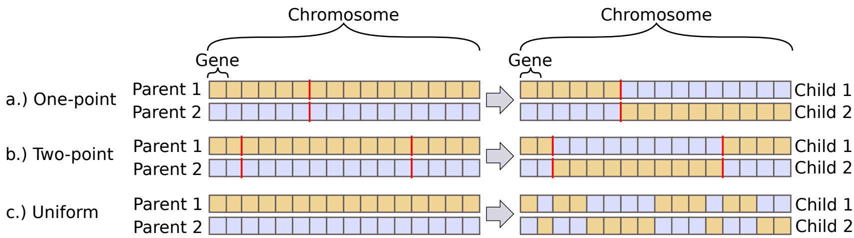

Figure 4.5.: Crossover mechanisms.

Arithmetic is an example of an interpolating crossover. Mechanisms that extrapolate are also possible. An important example is the simulated binary crossover (SBX). It allows to simulate a one-point binary crossover, even if other representations than binary are used [302]. In [303] it was found to be one of the best crossover methods for real coded presentation. The parental values are rather diverse and the offspring can take on a wide variety of values and explore the search space at an early stage of the algorithm. Once the population has largely converged to an optimum, the parental values are similar resulting in offspring values close to the parental values in order to contract the search space around the optimum. The SBX entails the calculation of the spread factor ϖ:

$$\varpi = \begin{cases} 2h^{\frac{1}{\varrho+1}} & , for \ h \leqslant 0.5 \\ \frac{1}{2(1-h)}^{\frac{1}{\varrho+1}} & , for \ h > 0.5. \end{cases} \tag{4.5}$$

h is chosen randomly between 0 and 1 and the recombination parameter ϱ determines the variation of the children around the parents. A larger ϱ causes children that are more similar to their parents. The children are then derived depending on the parents values and the spread factor:

$$x_{child,1} = 0.5x_{parent,1}(1+\varpi) + 0.5x_{parent,2}(1-\varpi) \tag{4.6}$$

$$x_{child,2} = 0.5x_{parent,1}(1-\varpi) + 0.5x_{parent,2}(1+\varpi) \tag{4.7}$$

4.5.2.3. Mutation

The influence of mutation is more pronounced at later stages of the algorithm, when the individuals have become increasingly similar and for objective functions with many local optima. The mutation rate ϱ_{mut}, i.e. the probability of a gene to alter its value, normally ranges between 0.001 and 0.05 and its setting is more critical than the crossover rate [279]. To enhance the efficiency and influence the diversity, it may be advisable to apply a variable mutation rate. An approach is to implement high values at the beginning to promote the exploration of the whole problem space and to decrease the value for the fine-tuning at the end.

Two mutation mechanisms are used in this work, which either add a normally or a uniformly distributed value to the original value. A normally or Gauss distributed value is added according to the following equation:

$$x_{mutated} = x_{initial} + \frac{1}{\sqrt{2\pi}\sigma} exp(-\frac{1}{2\sigma^2}h), \tag{4.8}$$

where σ is the standard deviation and h is the arithmetical mean, which is set to zero. Similarly, a uniformly distributed value between -1 and 1 is added in uniform mutation. Note that real valued encoding is used in this work. The optimized parameters can take on values between 0 and 1, which stand for the upper and lower boundary of the parameter range, respectively. If a parameter is out of range after mutation, it is set to the boundary value, i.e. 0 or 1.

4.5.2.4. Handling of Constraints Violation

The application of operators such as crossover and mutation entail the production of infeasible individuals that violate the constraints imposed by the search space. In the context of power systems, an example of a constraint is voltage band. This trespassing can be handled in four different ways [279]: The parameters of the operators can be manipulated in order to obtain only feasible individuals, the affected individuals can be repaired or discarded and penalty functions can be applied to exacerbate the fitness.

The first three approaches do not allow for any infeasible solutions in the population, which is not necessarily an advantage. In contrast, this can be a shortcoming, especially for highly constrained problems. Good solutions are often located close or on the boundary to infeasible regions and the "tunnelling" through infeasible segments should be encouraged. Therefore, these approaches are not recommended, because comparatively sound solutions may be lost as a result of potentially minor constraints violations.

On the other hand, the application of penalty functions allows to search through infeasible regions. The design of penalty functions, however, is a difficult task. The preferred method in this work is to allow infeasible individuals in the population. An algorithm is implemented that ensures that the cost deteriorate with the degree of violations and are always higher than the cost of the worst individual without violations.

The constraint violations described in Sec. 4.4.2 are ordered according to their severity: An unstable simulation model is regarded as the worst violation. This is followed

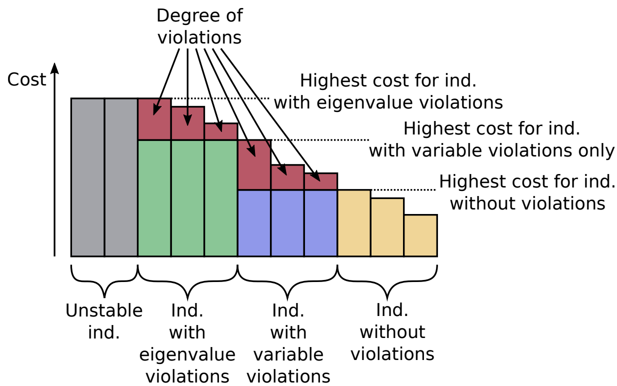

Figure 4.6.: Constraints Handling.

by violations of eigenvalue constraints. Variable constraint violations, such as power sharing discrepancies, are considered least severe.

The algorithm for the assignment of penalties is exemplified in Fig. 4.6 and is implemented as follows: The outcome of the objective function (cost) of the worst individual without any violations is taken. To this value, the degree of violation of the least severe constraint violation, i.e. variable constraint, is added to calculate the cost of individuals that violate the variable constraint only. Next, the highest cost of any individual that only violates the variable constraint is taken, as calculated before. This value is added to the degree of violations with the next level of severity, i.e. eigenvalue violations, for all individuals that violate this constraint. Finally, the highest cost of any individual with eigenvalue violations, as calculated before, is also assigned to the individuals with unstable simulation models.

In this way, it is assured that individuals with violations are always assigned higher cost than those without. Individuals with violations are ordered according to the severity of their violation type.

4.5.2.5. Niching

Similar to many other optimization techniques, a frequent problem of EAs is the convergence to local optima. In case few very fit individuals happen to dominate the population, their improved reproduction opportunities strongly decrease the diversity of the population. In contrast, slow finishing is not desirable as well. It is the consequence of insufficient improvement in the offspring when the difference between average and best individuals is small [279]. The goal of niching methods is to mitigate these effects.

Another agent named genetic drift [304] reduces the population diversity, similar to the selection pressure. Here, the reproduction chance is not increased due to better fitness, but as a result of the stochastic nature of the selection operator. To exemplify this, one can think of a small population of ten individuals that differ only in one gene, which has no influence on the fitness. The random nature of the selection will lead to a significant bias towards one type of individual sooner or later. This bias will become stronger over time, as the individuals of one type have increased reproduction probabilities on account of their higher numbers. This self-energizing effect will finally cause the extinction of the other type. Even if several equal peaks exist, the EA would end up converging to a single one.

Hence, the inclusion of multiple optima in the search is desirable, even if multi-objective optimization is not the main goal. Niching methods aim at extending the standard EA by establishing subpopulations in the vicinity of local and global optima to explore multiple optima [279].

One approach is to enhance an individual's fitness value in proportion to its diversity in comparison to other individuals within the population. This method is called fitness sharing.

It is also possible to segment the population into disjoint sets, which are referred to as islands. Each island is a separated EA, although promising individuals may be exchanged after certain intervals, which are called eras. In this way, the likelihood of few very fit individuals dominating the whole population is decreased. Each islands may converge to a different optimum.

Another option is to automatically delete the individual that resembles an offspring the most from a randomly chosen subset of the population, when this offspring is created. This is referred to as crowding. In restricted mating, the recombination of dissimilar individuals is omitted as it is presumed that similar parents produce offspring that resembles them and mating dissimilar individuals would result in unfit offspring, as it is too disruptive [279].

4.6. Binary Space Partitioning

4.6.1. Basics

Binary space partitioning (BSP) is used in this work to store and retrieve data of all the individuals in the history of the EA. This is useful in many ways, as will be detailed in this section. BSP was originally developed in the context of computer graphics, for instance to efficiently access spatial information about the objects in a scene [305]. The

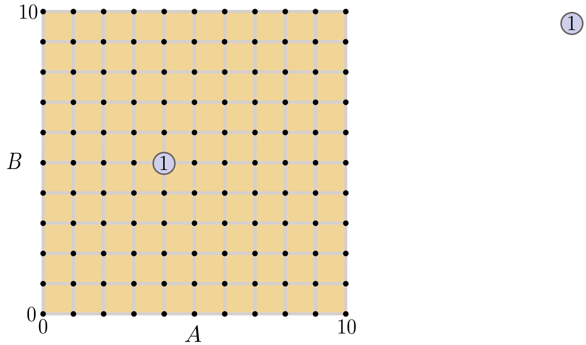

Figure 4.7.: Solution space (left) and root of BSP (right) [309].

implementation in this work resembles a k-dimensional tree [306].

The BSP tree can be used to implement a non-revisiting EA, which omits the repeated fitness evaluation of identical individuals [307]. Individuals that have already occurred in a former generation are detected and mutated. This is reasonable if the fitness evaluation is computationally more intensive than the detection of identical individuals. Hence, an efficient method to detect and alter recurring individuals is required. The diversity of the population is also promoted in this way. A recurring individual is mutated and takes on values close to its initial values, as elaborated below. The BSP tree serves the purpose of efficiently storing and retrieving individuals in its tree-like structure in order to detect recurring individuals.

The history driven EA [308] is an advancement of the non-revisiting EA. It is characterized by an alternative mutation named guided anisotropic search. In this mutation, individuals are led to nearby local optima. The BSP tree is again helpful here as explained below.

4.6.2. Implementation

4.6.2.1. Tree Initialization

To provide insight to the implementation of the BSP tree, its structure is exemplified assuming a two-dimensional solution space with variable A and B. The method may be transferred to arbitrary number of dimensions.

In the initialization of the tree, the solution space is required and the resolution must be determined. The resolution is necessary to transfer solutions into integers that can be processed by the tree. Pertaining to the two-dimensional example, it is assumed that gene A ranges between 0 and 10 and gene B between 0 and 100. Assuming that

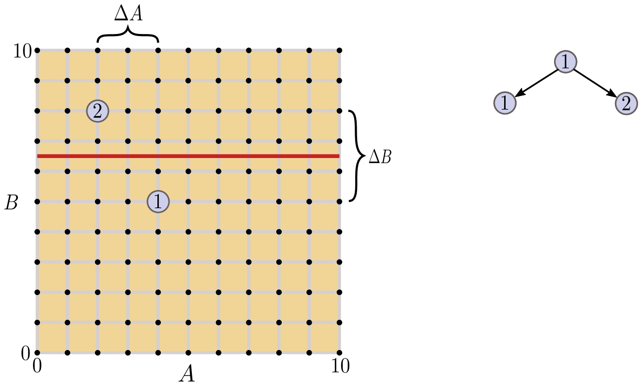

Figure 4.8.: Solution space (left) and BSP tree with two solutions (right)[309].

gene A has a resolution of 1 and gene B has a resolution of 10, the solution space can be reduced to 121 solutions instead of an infinite number, as is illustrated in Fig. 4.7. Each intercept point represents a solution of the optimization problem. The choice of the resolution is critical for the efficiency of the EA. The lower the impact of the variation of a gene on the fitness, the larger the resolution is to be set.

4.6.2.2. Adding Solutions

The first solution $(4; 50)$, also denoted as the root, is now added to the tree as depicted in Fig. 4.7. This solution corresponds to the point $(4; 5)$. From now on, solutions are specified referring to the resolution of the tree. The solution is assigned the whole solution space as its subspace.

The next solution to be added is $(2; 8)$. It divides the solution space into two subspaces as illustrated in Fig. 4.8. The first one ranges between $(0 : 10; 0 : 6, 5)$ and the second one between $(0 : 10; 6.5 : 10)$.

The separation of the solution space depends on the distance of the solutions in the dimensions, which are denoted ΔA and ΔB in Fig. 4.8. The dimension with the larger distance is used for the separation, in this case ΔB. If this results in a boundary that is located on a grid line, the boundary is placed arbitrarily on one side to unambiguously determine the subspaces. Two leafs are added to the tree, representing the former solution of the entire subspace (in this case solution 1) and the newly added (in this case solution 2). They are added so that the left solution in the separating dimension always has the smaller value.

Another solution $(8; 7)$ is added next as given in Fig. 4.9. At first, its correct place

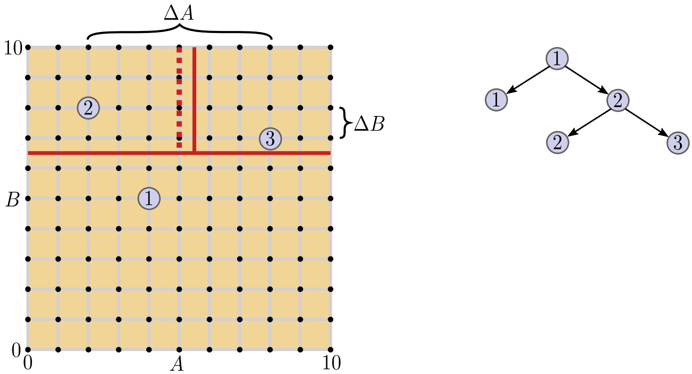

Figure 4.9.: Solution space (left) and BSP tree with three solutions (right)[309].

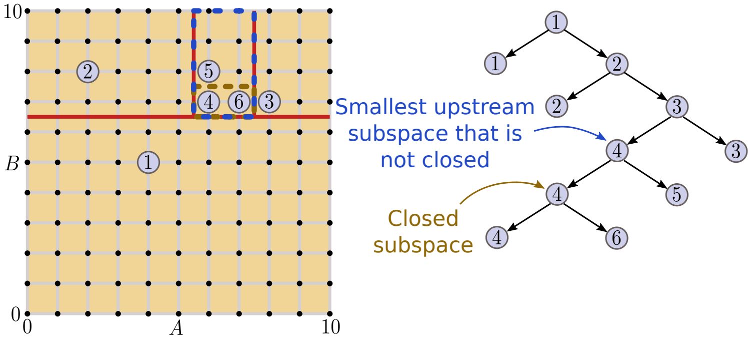

Figure 4.10.: Solution space (left) and BSP tree with a closed subspace (right)[309].

in the tree must be found. Starting from the root, it is checked whether the new solution lies within the subspace of the right or the left leaf. This is done until a leaf is encountered that does not possess further branches, meaning that the new solution is part of this leaf's subspace. The new solution is located in the subspace of solution 2 and added as described. The boundary is located on a grid line and needs to be shifted arbitrarily to the right (as shown in Fig. 4.9) or the left. Further solutions are added in a similar fashion.

4.6.2.3. Closure of Subspaces

A subspace is declared full (or closed), if all its solutions have been added. To efficiently detect duplicate solutions, the algorithm remembers which subspaces are closed. A duplicate solution can then be detected in an upstream leaf, avoiding the search up to the final leaf. This is depicted in Fig. 4.10, where the solutions $4, 5$ and 6 have been added. The solution 6 closes the subspace of the upstream leaf.

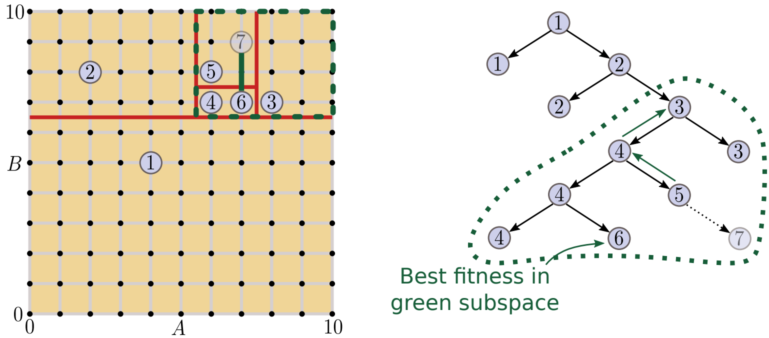

Figure 4.11.: Mutation with guided anisotropic search [309].

4.6.2.4. Mutation of Duplicate Solutions

If a duplicate solution is detected, it is mutated. In the non-revisiting EA [307], the new value is located in the smallest upstream subspace that is not closed and contains the original solution. For instance, if the solution 4 would be added again, it would be mutated to lie inside the dashed blue subspace at some random empty position as illustrated in Fig. 4.10.

4.6.2.5. Mutation with Guided Anisotropic Search

For the implementation of the guided anisotropic search [308], the leafs are assigned the result of the objective function for its solution. In Fig. 4.11, a new solution (7) is added to the example, which is mutated with guided anisotropic search. As a first step, the leaf with the subspace that contains solution 7 is searched. From this leaf (5), it is proceeded a number of layers in the upstream direction. The number of layers is set to 2 in this work. The resulting subspace (3) is denoted the neighbourhood and is marked green in Fig. 4.11.

Now, the fittest solution within this neighbourhood is identified. It is assumed to be solution 6 in this example. The mutated value is selected at an arbitrary position between the original value and solution 6 as marked in Fig. 4.11. The new value is rounded according to the resolution. If it is a duplicate solution, it is mutated as described in Sec. 4.6.2.4.

4.6.2.6. Diversity of Solutions

Diversity of the individuals within the population decreases the chances to get trapped in local optima. A measure for the diversity of an individual from BSP tree data is developed

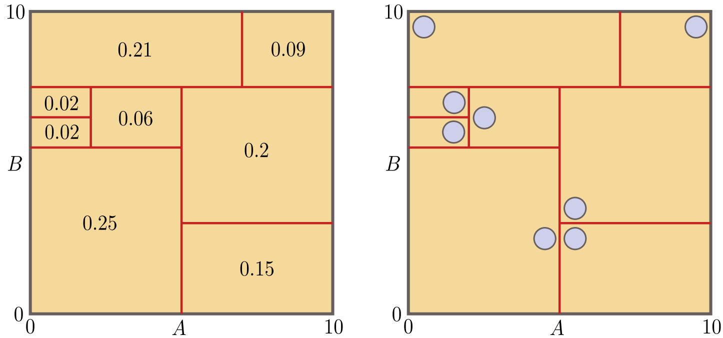

Figure 4.12.: Diversity of solutions according to the size of their subspace [309].

in this work. The diversity of an individual corresponds to the size of its subspace, relative to the entire solution space. For example, if the solution space comprises 100 solutions, and the subspace of the individual contains 15 solutions, its diversity is 0.15.

Fig. 4.12 illustrates the diversity measure for various individuals and their subspaces for a two-dimensional problem. It is to be mentioned that the purpose of the figure is to demonstrate the division into subspaces and was not created according to the rules of the BSP tree. The intention is to showcase and exaggerate the problem described in the following.

It becomes apparent in Fig.4.12 b.) that the measure for the diversity is not exact. Individuals may be located at an arbitrary position within their subspace. There is a chance that two similar solutions are located next to each other, but are assigned a high diversity due to their extensive subspaces. However, this constellation does not occur very frequently and the large space towards the other directions justifies the enhanced diversity of these individuals. They are at least at the border to an unexplored part of the solution space. In conclusion, the described diversity is not exact, but is accurate enough for the purpose of the EA.

The incorporation of the diversity in the fitness evaluation is elaborated in the following. To promote the diversity of the population, a penalty which is inversely proportional to the diversity is added to the fitness of an individual. As previously mentioned, the higher the fitness, the worse the individual. The size of subspaces ρ_{ss} as described above ranges between 0 and 1. Hence, subtracting the size from 1 is a measure for the lack of diversity. This measure is then scaled according to the maximum and minimum cost (objective function outcome) of any individual and multiplied with the diversity weighting factor ξ_{div}:

$$\eta_{div} = (1 - \rho_{ss})(max(cost) - min(cost))\xi_{div}, \tag{4.9}$$

where η_{div} is the penalty that is added to the fitness.

4.7. Overview of Implemented Evolutionary Algorithm

A real coded EA is implemented in this work, meaning that the optimized parameters are represented by real numbers. The values range between 0 and 1, which represent the lower and upper boundary of the optimization range of a parameter, respectively. For example, if a parameter is optimized in the range between 12 and 18, it is actually represented by numbers between 0 and 1 in the algorithm. The encoded value 0.5 would correspond to the actual value of 15.

The flow chart of the implemented EA is shown in Fig. 4.13. The population can be separated into islands. Apart from several options for the implementation of the genetic operators (mutation, crossover and selection), the BSP tree and its features are at the core of EA. The BSP tree is updated with the result for the objective function of each individual. All individuals of former generations with their respective objective function value are stored. With this data, the diversity with respect to the historic progression is incorporated in the fitness evaluation. The other way in which the BSP tree is utilized is the mutation with guided anisotropic search as elaborated in Sec. 4.6.2.5. On the one hand, the guided anisotropic search is used in the mutation block. On the other hand, it is used when a duplicate individual is detected.

The fitness is calculated incorporating the objective function result Υ_{obj} (see Sec. 4.4.1 and 4.8.1), and the penalty for the lack of diversity η_{div}:

$$Fit = \Upsilon_{obj} + \eta_{div}. \tag{4.10}$$

Note that the penalty for constraint violations is included in the objective function outcome Υ_{obj} (see Sec. 4.5.2.4 and Sec. 4.4.2).

The mutation variants implemented are Gauss and uniform as described in Sec. 4.5.2.3. The options for crossover from Sec. 4.5.2.2 are one-point, uniform, simulated binary or arithmetic. Tournament, rank-based, fitness-proportional, stochastic universal (rank-based or fitness-proportional) selection mechanisms are implemented as explicated in Sec. 4.5.2.1.

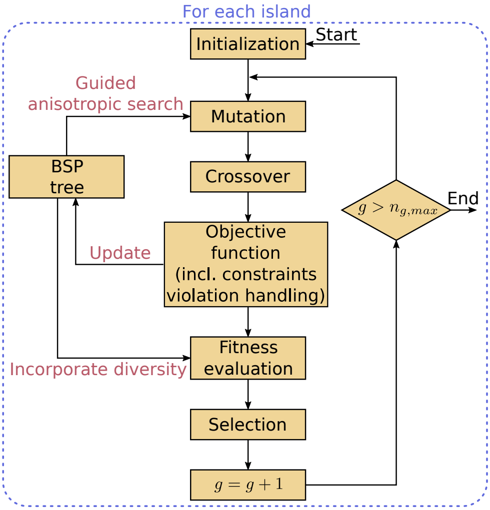

Figure 4.13.: Flowchart of implemented EA.

4.8. Parametrization

The parametrization of a EA, i.e. the selection of parameters such as the mutation rate or the type of recombination, is a difficult task [310]. The parameter set has to be applicable to a large variety of problems and solution spaces that occur in the domain of DER controller optimization. The proposed EA hinges on numerous parameters that influence the outcome interdependently. A parallel optimization, i.e. a EA that optimizes the EA parameters, is not practicable due to the large number of parameters and the various dependencies. Self-optimization is also not an option in this case. The EA in this work is designed to converge within a very limited number of fitness evaluations and self-optimization adjusts too slow.

In conclusion, the only feasible way to select the parameters is by optimizing one parameter after another. To this end, benchmark optimization problems are used, because the fitness evaluation would be too costly when applied to practical problems that entail numeric simulations. As the EA operators depend on chance, the viability of parameter sets must be evaluated multiple times. To end up with meaningful results, each parameter set is evaluated 100 times for each benchmark function. The number of fitness evaluations for each run of the EA is set to 1000. This is a relatively low figure which is attributable to the fact that the EA is to be optimized for problems where the fitness evaluation is computationally intensive.

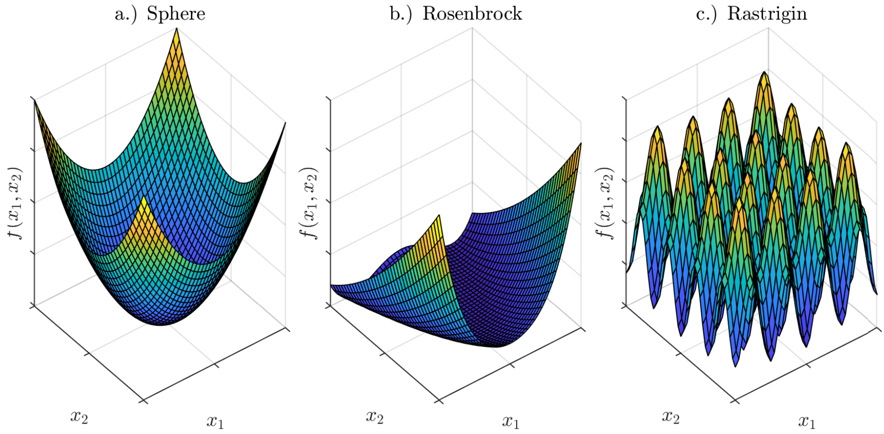

Figure 4.14.: Benchmark functions

4.8.1. Benchmark Cost Functions

The parameter selection is conducted using the benchmark functions sphere, Rosenbrock and Rastrigin [311]. They are illustrated in Fig. 4.14 for two dimensions. They are commonly employed to benchmark optimization algorithms.

The Sphere function is convex and unimodal and is described by

$$\Upsilon_{obj}(\boldsymbol{x}) = \sum_{i=1}^{d} x_i^2, \tag{4.11}$$

where d is the number of dimensions. Its global minimum is at $(0, 0)$ for the two dimensional case. The domain is $x_{1/2} \ \epsilon \ [-100 \ \ 100]$ in this work.

The Rosenbrock function, which is also referred to as the valley function, is unimodal and the global optimum lies in a narrow, parabolic valley:

$$\Upsilon_{obj}(\boldsymbol{x}) = \sum_{i=1}^{d-1} 100(x_{i+1} - x_i^2)^2 + (x_i - 1)^2. \tag{4.12}$$

Its global minimum is at $(1, 1)$, assuming $d = 2$. The domain is $x_{1/2} \ \epsilon \ [-29 \ \ 31]$ in this work.

The Rastrigin function is more complex and multimodal with several local minima:

$$\Upsilon_{obj}(\boldsymbol{x}) = 10d + \sum_{i=1}^{d} x_i^2 - 10cos(2\pi x_i). \tag{4.13}$$

Table 4.1.: Optimized parameters for a microgrid with two grid-forming inverter.

Population	Size	10
	Number of islands	1
Selection	Type	Proportionate to fitness
	Weighting of diversity ξ_{div}	1
Crossover	Mode	Arithmetic
	Crossover rate ϱ_{cro}	1
Mutation	Type	Gauss
	Mutation rate ϱ_{mut}	0.05
	Standard deviation σ	0.5

The global minimum is at $(0, 0)$ for the two dimensional case. In this work, the domain is $x_{1/2} \,\epsilon\, [-5.12 \;\; 5.12]$.

4.8.2. Optimized Parameter Set

As mentioned, due to their large number, it is not possible to optimize all EA parameters in parallel. Therefore, the parameters are optimized successively. The performance of the EA is evaluated for the benchmark functions described in Sec. 4.8.1. The parameters are optimized one after another, while the others are kept constant. At first, the genetic operators mutation, crossover and selection are optimized. Afterwards, the optimal population size and number of islands are derived. A detailed description is omitted here, as this is a rather lengthy process. The reader is referred to [309] for an elaborate depiction of the process.

The optimized parameters are given in Table 4.1. The population size is relatively small with only 10 individuals. This is attributable to the low number of fitness evaluations. The subdivision of the population with such a low number of individuals is not productive, which is why there is only one island. The optimal selection type is proportionate to fitness and the weighting of the diversity is 1, meaning that the cost and diversity are equally weighted in the fitness evaluation. Incorporating the diversity in the fitness evaluation has a particularly large impact on the performance [309]. This holds for the more complex benchmark functions Rastrigin and Rosenbrock in particular. Arithmetic crossover is chosen and the crossover rate $\varrho_{cro} = 1$, meaning that the chromosomes of all individuals take part in the crossover. Gauss mutation with a standard deviation $\sigma = 0.15$ and a mutation rate of $\varrho_{mut} = 0.05$ performs best.

Mutating duplicate individuals improves the outcome. However, using the guided anisotropic search for duplicate individuals or as the default mutation mechanism does not result in any improvements in comparison to Gauss mutation.

4.9. Simulation and Optimization Framework

Having introduced the microgrid model in Sec. 3 and the optimization algorithm in Sec. 4, an overview of the simulation and optimization framework is given in Fig. 4.15, which is at the core of this work.

The microgrid model comprises the DER and load models including their controllers. Droop variants and VI are used for the PED and SM and SI is used for DFIG. The DER and load models exchange data (i.e voltages and currents) with the network model. Several implementations of the network model are possible, representing simplifications and differing reference frames. Network topology and line data, such as R/X ratio, are varied in the simulation scenarios to evaluate the controller parameters and the placement of the DER.

The time-domain simulation results and linearized simulation snapshots are used for the evaluation of the area criterion and modal analysis, respectively. The objective function outcomes, including constraints violations, are used in the EA, which features various implementations of genetic operators as well as constraints violations handling, niching and the fitness evaluation of the individuals. Furthermore, the BSP tree forms part of the EA. It enables the evaluation of the diversity of individuals, the mutation with guided anisotropic search and prohibits the recurrence of equal individuals.

The selected individuals with the DER controller parameters are passed on to the microgrid scenario simulation, where multiple simulations may be carried out to test each individual for various microgrid conditions.

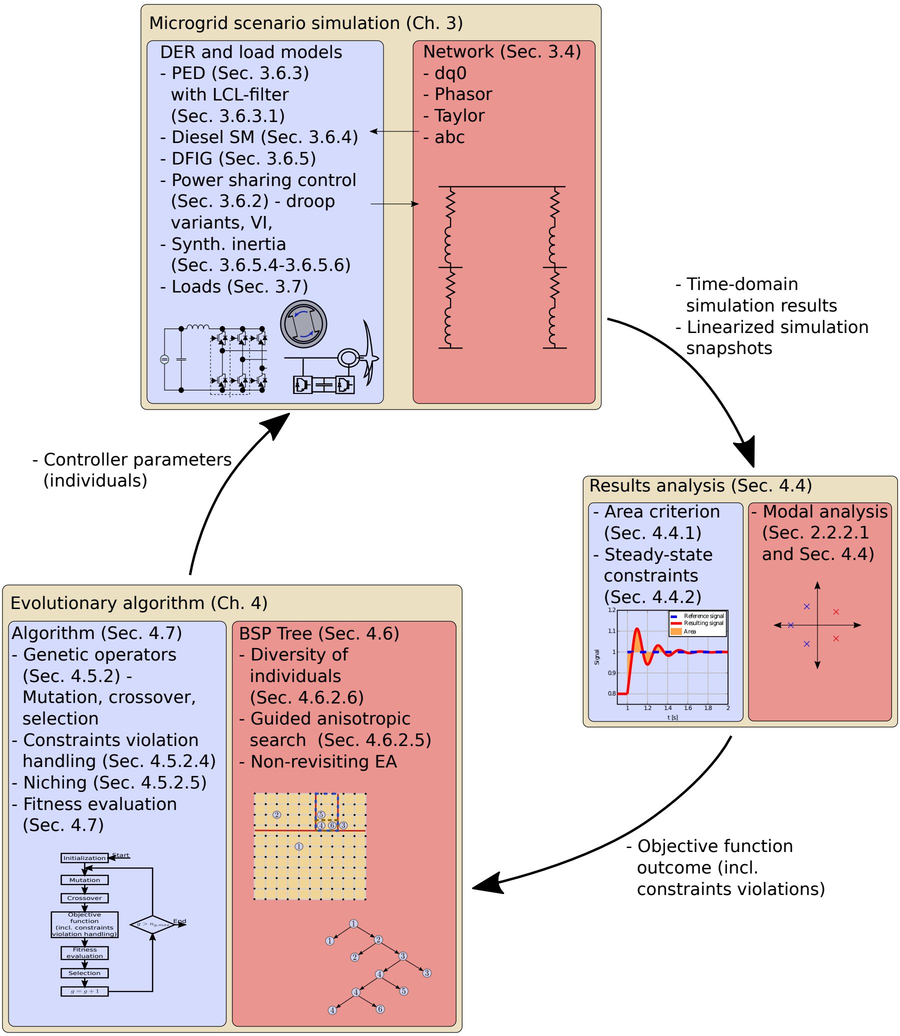

Figure 4.15.: Simulation and optimization framework.

5. Case Studies

5.1. Introduction

The optimization algorithm from Sec. 4 is applied to the models described in Sec. 3 in this chapter. Aspects that have so far not been addressed in literature on microgrid small-signal stability optimization, as identified in Sec. 4.3, are investigated.

At first, the test networks are described. Then, the models from Sec. 3 are validated through comparison with Simulink's SimPowerSystems toolbox [120].

The performance of the EA introduced in Sec. 4 is compared to a conventional EA in case study 1. Benchmark functions and a microgrid control parameter optimization problem are taken as examples.

A sensitivity analysis of PED is carried out in order to identify relevant parameters for the optimization in case study 2. Grid-forming and grid-supporting droop controlled PED are regarded and their interaction is investigated.

Case study 3 is the first optimization study. The simultaneous parameter optimization of all control parameters that were found to be relevant in the sensitivity analysis, including potentially influential inner loop parameters and the measurement filter cut-off frequency is conducted. Conventional droop control in combination with VI is applied and a small microgrid with two nodes is regarded.

Whereas the previous optimization is carried out for a small microgrid with fixed parameters, various droop types are later optimized and compared in benchmark scenarios in case study 4. In these scenarios, line length and R/X ratio are varied in a small microgrid to take into account varying microgrid conditions. Moreover, the interaction of PED and SM is analysed. To reduce the complexity of the optimization, the voltage controller parameters are fixed, using the outcome from the previous study case.

Finally, controller parameters and the location of DER are optimized for the Cigre LV benchmark microgrid [312] with 38 nodes in case study 5. The results are compared to the previous benchmark scenarios.

The optimized parameter sets are used to verify PED and network reduction approaches under realistic conditions in case study 6. Eigenvalues and results of time domain simulations for reduced models are compared to the original high-order models.

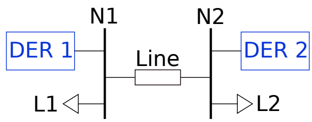

Figure 5.1.: Small microgrid with two nodes.

Case study 7 is dedicated to the optimization of the SI of wind power plants for MV microgrids with PED or SM. The combination of SI methods and droop control is discussed.

In the final case study 8, it is looked at the inaccurate synchronization of microgrids with the bulk power system and the resultant loadings for the microgrid components.

5.2. Test Systems

5.2.1. Test System 1: Small Two-Node Microgrid

The small microgrid with two nodes from Fig. 5.1 is used in many case studies in this work. There is a DER and a load at each node. Line length and R/X ratios are varied in the case studies. The setup captures the main dynamics of more complex microgrid topologies despite its simple structure. The approach of using small microgrids with two or three nodes to analyse the controller stability is often found in literature [313, 314, 315, 86, 316, 105, 102, 96, 91, 29, 183].

One benefit of this simple topology is the decreased simulation effort. Furthermore, the correlation of certain microgrid properties, such as the R/X ratio of lines or their length, with controller performance is facilitated by a simple structure. In more complex topologies with various line lengths and R/X ratios, these correlations cannot be represented uniquely. In addition, the simple topology is suitable to represent worst-case scenarios with either very long or very short lines. The DER controllers are further challenged by the increased disruptiveness of load switching compared to larger systems with a number of relatively smaller loads.

5.2.2. Test System 2: Cigre Benchmark Microgrid

The second test system that is used in this work is the Cigre benchmark LV microgrid with 38 nodes depicted in Fig. 5.2 [312]. The data of the lines, PV plants and loads are given in Appendix C. The largest load in the network is load 1 and PV 1 is largest PV plant in the network. It also contains four DER (nominal powers: $S_{n,DER1} = 25$ kVA, $S_{n,DER2} = 40$ kVA, $S_{n,DER3} = 30$ kVA, $S_{n,DER4} = 35$ kVA).

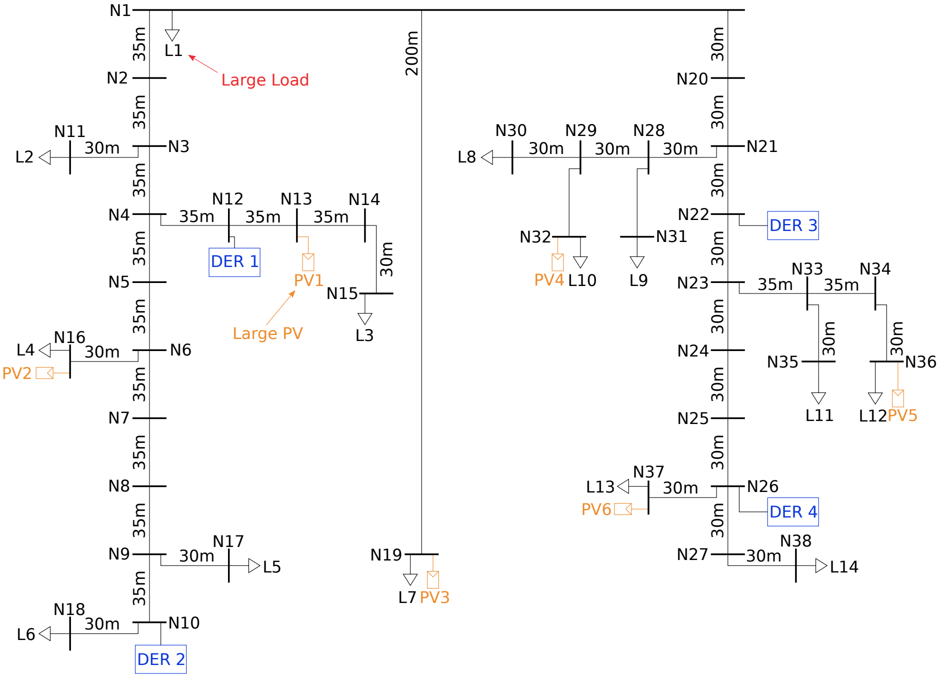

Figure 5.2.: Cigre benchmark LV network [312].

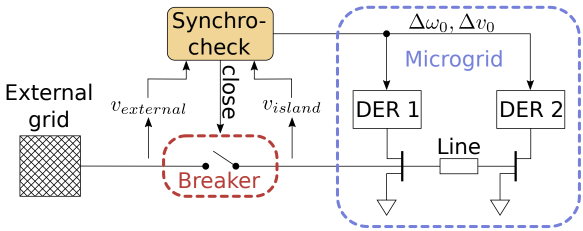

Figure 5.3.: Voltages alignment of microgrid and external grid with synchrocheck.

5.2.3. Test System 3: Small Two-Node Microgrid with Synchrocheck

To simulate the effects of inaccurate synchronization, the two-node microgrid is equipped with a synchrocheck that controls the breaker between microgrid and the external grid. The microgrid with synchrocheck was introduced in in Sec. 3.8 and is shown again in Fig. 5.3 for the sake of clarity.

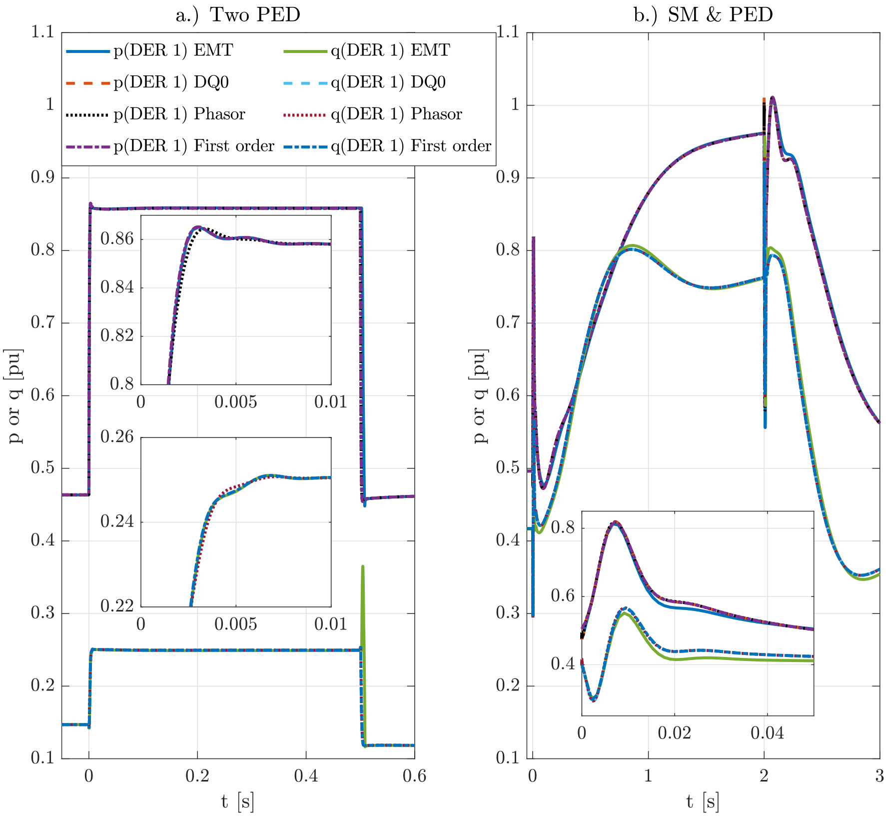

Figure 5.4.: Model validation results.

5.3. Model Validation

The network model in the $dq0$-frame as well as its approximations described in Sec. 3.4 and the model of the SM from Sec. 3.6.4.1 are validated by comparing them to Simulink's Simscape power system toolbox [120], which features EMT simulation. The small microgrid with two nodes from Sec. 5.2.1 is simulated either with two PED or with one PED and one SM ($S_{n,DER} = 10$ kW). The DER Data are given in App. D. The line length is 100 m and the R/X-ratio is 3.9 ($R'_L = 0.624$ Ω/km, $X'_L = 0.16$ Ω/km). There are two static loads ($S_{n,Load} = 10$ kW, power factor: 0.95 (ind.)) at each node.

The active and reactive power of DER 1 for the case with two PED are depicted in Fig. 5.4a.). When load 2 is switched on at $t = 0$ s, no visible difference is perceived between the EMT model, the $dq0$ network model and the first order approximated model curves. As expected, the phasor approximation leads to slight deviations due to the neglect

Table 5.1.: Optimized parameters for a microgrid with two grid-forming inverter.

		Optimized	Conventional		
	Number of Fitness Evaluations	1000	1000	5000	10000
Sphere	Mean cost	0.0001	0.3209	0.0008	0.0000
	Cost variance	0.0002	1.2753	0.0060	0.0000
	Optimum found [%]	82.27	53.46	86.99	93.29
Rosenbrock	Mean cost	0.0611	0.3938	0.0110	0.0000
	Cost variance	0.2276	0.6138	0.0995	0.0002
	Optimum found [%]	57.63	30.41	78.64	89.67
Rastrigin	Mean cost	0.0931	7.9341	6.7453	3.9959
	Cost variance	0.2169	10.9869	8.8629	7.2135
	Optimum found [%]	36.27	10.43	17.73	19.25

of the network dynamics. When load 1 is switched off, the EMT model differs from the other simulations due to the delayed breaker opening at the current zero crossing of the phases. This means that the load disconnection is delayed in the EMT simulation.

Fig. 5.4b.) compares the Simulink built-in SM model to the SM model described in Sec. 3.6.4.1. The AVR from Sec. 3.6.4.2 and governor from 3.6.4.3 for LV networks are used for the $dq0$ as well as the Simulink EMT model. Load 2 is switched on at $t = 0$ s and load 1 is turned off at $t = 2$ s. The curves of the $dq0$ network model and its phasor and first order approximations are on top of each other, because the line dynamics do not affect the slow modes of the SM. They have perceptible deviations from the EMT model. The causes of the deviations cannot be clearly identified as the exact implementation of the Simulink built-in SM model is not known. Yet the dynamics are similar.

5.4. Case Study 1: Evolutionary Algorithm Performance

To demonstrate the effectiveness of the proposed EA, its performance is compared to a conventional EA. By conventional, it is referred to a EA where the parameters from Table 4.1 are used, but features in connection with the BSP tree (mutation of duplicate individuals, incorporation of the diversity in the fitness evaluation) are not applied. Furthermore, simulated binary crossover is used instead of arithmetic crossover, which is a choice often made in literature [303].

The results for the benchmark functions introduced in Sec. 4.8.1 are shown in Table 5.1. Three parameters are used to evaluate the performance of the two EA types for 100 runs. The mean cost is the mean difference to the optimum. The cost variance and the percentage that finds the global optimum assess the reliability of the EA. The global optimum is considered to be found, when the cost is smaller than 0.1.

The optimized EA was designed to excel when the number of fitness evaluations is small, such as 1000. For such a low number of evaluations, the optimized EA performs significantly better than the conventional EA. It is notable that the likelihood of finding the optimum is more than three times higher in case of the optimized EA for the most complicated benchmark function (Rastrigin). The optimum is found at about every third run (36.27%) and the variance is low, showing that the algorithm reliably detects solutions in the proximity of the global optimum.

As larger numbers of fitness evaluations are usually applied in the conventional EA, the results for 5000 and 10000 evaluations are given in Table 5.1. For 5000 evaluations the results are better than the optimized EA for the simpler benchmark functions (sphere and Rosenbrock). However, in case of the Rastrigin function, even with 10000 evaluations the conventional EA's performance does not come close to the optimized EA. Improvements between 5000 and 10000 evaluations are minor. This is a sign that the conventional EA gets trapped in local optima. It highlights the necessity to lead the EA to various optima by promoting the diversity of the population, which is one of the features of the optimized EA as described in Sec. 4.6.2.6.

Fig. 5.5 compares the cost of the best individual in the population (logarithmic scale) for the generations of one run for Rastrigin's function. Both EAs perform rather similar during the very first generations. At around generation 30, the conventional EA gets trapped in a local optimum and subsequently shows hardly any improvement. Due to the promotion of the diversity in the population, the optimized EA is able to search several optima and steadily lowers the cost.

Finally, the performance of the EA is demonstrated for a practical control parameter optimization problem from this work. The problem from Sec. 5.7 (TD, area criterion, all cases) is taken as an example. It is one of the most demanding optimization problems in this work. Unlike benchmark functions, this problem is highly constrained and the EA may not even find a solution without violations.

For 100 runs, the optimized EA finds at least one solution without violations in 96 cases, whereas the conventional EA achieves this only in 87 cases. The average cost are 0.62 for the optimized and 0.79 for the conventional EA.

The EA was designed to generally perform well for low numbers of fitness evaluations. In the following optimizations, the number of fitness evaluations, i.e. the generations, are adjusted according to the complexity of the problem. It was sometimes necessary to increase the number of fitness evaluations to reliably find the optimal solution.

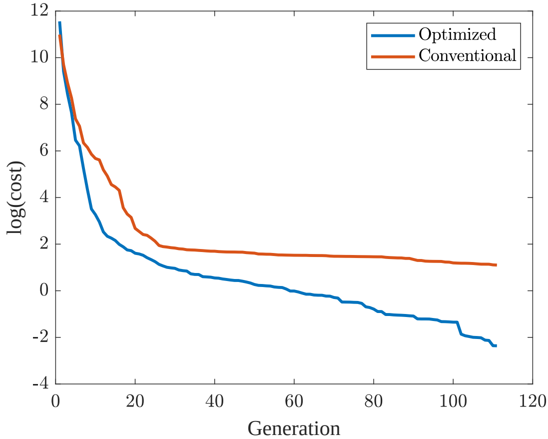

Figure 5.5.: Cost over the generations for microgrid optimization.

5.5. Case Study 2: Parameter Sensitivity

This section takes a detailed look at the parameter sensitivity of the dominant modes of grid-forming and grid-supporting droop controlled inverters. In many literature only a limited number of control parameters is regarded when investigating the stability of microgrids. It is usually assumed that the droop coefficients are the most influential parameters [317, 282][1].

5.5.1. Grid-forming Droop Control

5.5.1.1. Definition of Relevant Parameters

As mentioned, a broad scope of parameters is incorporated in the sensitivity analysis. The inner loops affect the control system stability, which is mainly concerned with harmonic stability according to the definition of the IEEE Task Force on microgrid stability [65]. The fast current loop is tuned as described in Sec. 3.6.3.2.1 and does not significantly take effect on the dominant modes. The voltage controller is slower and may affect the complex interactions in the cascaded control. Hence, the controller gains $k_{p,v}$ and $k_{i,v}$ and the feed-forward gain FF_v are investigated, although their impact is usually not considered in literature.

The droop control, with the droop coefficients m_ω and m_v, and the measurement filter, with the cut-off frequency ω_c, pertain to the power supply and balance stability [65].

[1] The presented sensitivity analysis was conducted by the author of this work.

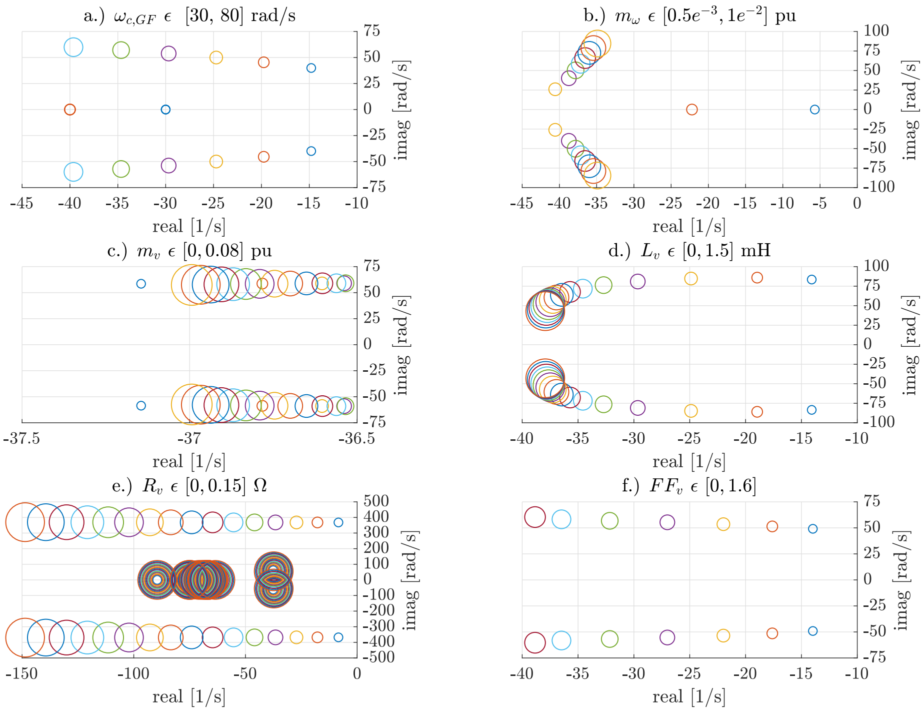

Figure 5.6.: Dominant eigenvalues of the microgrid with two grid-forming inverters for various parameter ranges (parameters increase with marker size).

This is the outermost part of the cascaded control and has a strong impact. However, the filter cut-off frequency is often regarded as a fixed parameter in literature.

The VI affects the power supply stability as well as the control system stability, as will be shown. The virtual resistor R_v damps high frequency modes that originate from the interaction of voltage controllers of parallel DER. The virtual inductor L_v influences mainly the power sharing.

5.5.1.2. Modal Analysis

Fig. 5.6 depicts the dominant eigenvalues for various parameter ranges for the small two node microgrid introduced in Sec. 5.2.1 with two grid-forming droop controlled inverters ($S_{n,DER} = 10$ kW) and two pq-loads ($S_{n,Load} = 10$ kW, power factor: 0.95 (ind.)). The line length is 100 m and the R/X ratio is 3.9 ($R'_L = 0.624$ Ω/km, $X'_L = 0.16$ Ω/km). Parameter values increase with the marker size. Unless otherwise stated, the parameters from App. D are used.

The filter cut-off frequency $\omega_{c,GF}$ is varied between 30 and 80 rad/s in Fig. 5.6a.). The stability margin increases with $\omega_{c,GF}$ and the system is very sensitive to this parameter.

The dominant eigenvalues for the variation of the frequency droop coefficient m_ω are depicted in Fig. 5.6b.). Eigenvalues move away from the imaginary axis with increased m_ω. An oscillatory pair of eigenvalues becomes dominant for large values of m_ω and the damping decreases towards larger values.

The voltage droop coefficient m_v is varied between 0 and 0.08 pu in Fig. 5.6c.). At first, the system becomes less stable for increased values, but this effect is then reversed. In general, the impact is minor.

Regarding the virtual inductance in Fig. 5.6d.), the observed oscillatory pair of eigenvalues becomes better damped and more stable for larger values. It is interesting to see that the affected modes have similar time-scales and damping compared to the ones influenced by the filter cut-off frequency and the droop coefficients.

A lightly damped oscillatory mode close to the y-axis is provoked by low magnitudes of the virtual resistor in Fig. 5.6e.) and it rapidly becomes more stable with increased values. Analysis of participation factors reveals that the modes originate from the interaction of the voltage controllers of the parallel inverters.

In Fig. 5.6f.), the impact of the feed-forward gain FF_v is illustrated. Large values lead to enhanced stability and the system is very sensitive to this parameter. The time-scales of the modes are similar to the modes affected by the droop coefficients.

The influence of some further parameters and design choices was investigated and the results are summarized without showing the eigenvalues plots. A minor impact is attributed to the feed-forward gain of the current controller FF_c. Selecting either the set values $v^*_{c,dq}$ or the measurement values $v_{c,dq}$ for the decoupling in the voltage controller hardly affects the dynamics. In contrast, using the set value $i^*_{L1,dq}$ for the current controller decoupling leads to instability. Hence, the measured values $i_{L1,dq}$ should be used. The choice of the reference angle, which may be selected form one of the PED or as their average, has a very minor impact.

In conclusion, it does not comply with the complex dynamic interactions of the system to regard only few influential parameters, such as the droop coefficients. In fact, FF_v or L_v affect similar modes as m_ω and their impact is more pronounced compared to m_v. The tuning of the PI-controller of the voltage loop and its impact are discussed in Sec. 3.6.3.2.2.

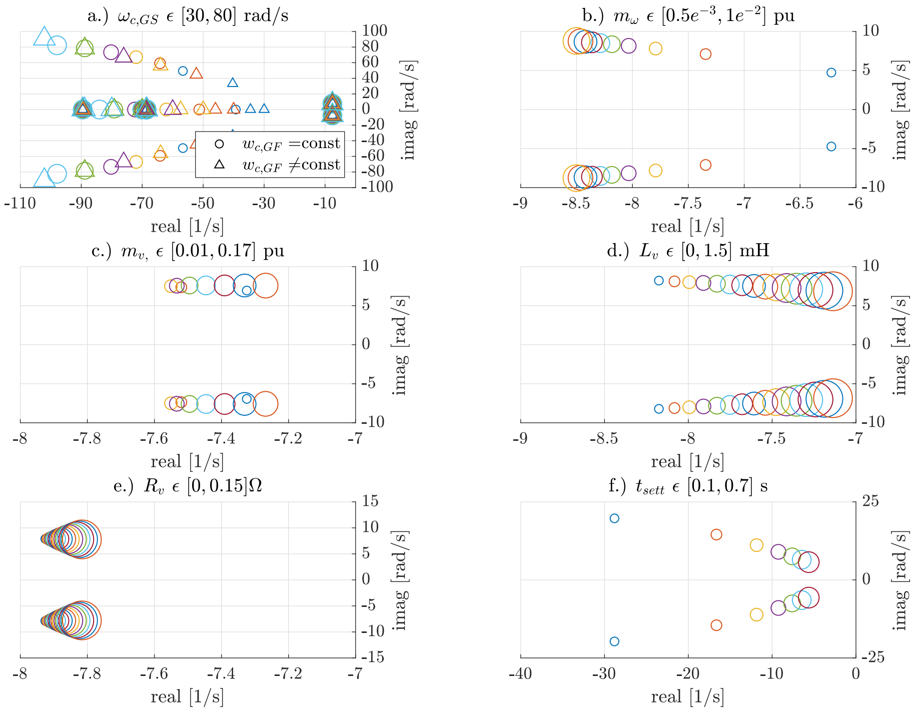

Figure 5.7.: Dominant eigenvalues of the microgrid with one grid-forming and one grid-supporting inverter for various parameter ranges (parameters increase with marker size).

5.5.2. Grid-Supporting Droop Control

5.5.2.1. Definition of Relevant Parameters

Relevant control parameters are assigned to the stability categories defined in [65]. The fast current controller is tuned in accordance to Sec. 3.6.3.2.1. Therefore, the only remaining parameters pertaining to the control system stability are the PI-controller parameters of the PLL.

The power supply and balance stability is influenced by the droop coefficients and the filter cut-off frequency.

5.5.2.2. Modal Analysis

The small two node microgrid is investigated again. One PED in an islanded microgrid must be in grid-forming mode of control to provide the voltage reference. The other

PED is now controlled with grid-supporting droop control. Unless otherwise stated, the parameters from App. D are used.

The impact of varying the filter cut-off frequency of the grid-supporting (GS) PED, while the cut-off frequency of the grid-forming PED is either kept constant or also varied, is given in Fig. 5.7a.). The dominant eigenvalues are hardly affected and an oscillatory pair moves away from the imaginary axis.

In the subsequent plots, the droop coefficients of both PED are varied simultaneously. Stability deteriorates for small m_ω , whereas the eigenvalues are rather stable for large magnitudes. The influence of m_v is minor. Modes first dissociate from the imaginary axis, but this trend is then reversed.

Growing values of L_v and R_v slightly aggravate the stability, but the impact of the VI of the grid-forming PED (there is no VI in grid-supporting control) is much smaller compared to the case with two grid-forming PED.

Fig. 5.7f.) depicts the influence of settling time of the PLL, which is seen to be strong. The oscillatory mode moves deep into the stable region when the PLL is tuned aggressively. These results contrast with the findings in [150], where the influence of harmonics is incorporated and the impedance method is used. However, harmonics are not considered in this work which is why aggressive PLL tuning does not lead to instability. Instead, a fast PLL decreases the response time of the cascaded control.

It becomes apparent that the dominant eigenvalues are less affected by most parameters. The dynamics are dominated by the settling time of the PLL.

5.6. Case Study 3: Simultaneous Optimization of All Parameters

This section discusses the simultaneous optimization of all control parameters of the grid-forming and grid-supporting droop controlled inverter that where found to have a significant impact on the system dynamics according to the sensitivity analysis in Sec. 5.5. The objective is the area criterion as described in Sec. 4.4.1 and the voltage, frequency and power sharing constraints as described in 4.4.2 are applied. In addition, the largest occurring real part of an eigenvalue must be below -5 1/s.

Again the two node microgrid from Sec. 5.2.1 with two PED and two pq-loads is investigated. The line length is 100 m and the R/X ratio is varied to analyse its impact. Load 1 is initially connected and load 2 disconnected. At $t_{step,1} = 1$ s, load 2 is switched on and at $t_{step,2} = 3$ s load 1 is disconnected.

Table 5.2.: Parameter ranges for the simultaneous optimization.

Par.	$w_{c,GF}/w_{c,GS}$	$k_{i,v}$	L_v	R_v
Range	$[15, 75]$ rad/s	$[50, 600] \frac{1}{\Omega s}$	$[0, 2]$ mH	$[0, 0.4]$ Ω
Par.	$m_{\omega,GF}/m_{\omega,GS}$	$m_{v,GF}/m_{v,GS}$	FF_v	
Range	$[0.0001, 0.01]$ pu	$[0, 0.16]$ pu	$[0, 1.2]$	

5.6.1. Parameter Ranges for Optimizations

The selected parameter ranges for the optimization reflect the outcome of the sensitivity analysis and are shown in Table 5.2. The upper boundary of the filter cut-off frequency is set to 75 rad/s to allow for proper filter as elaborated in Sec. 3.6.2.1. The steady-state frequency deviation is limited to 500 mHz at 1 pu active power deviation by selecting a maximum frequency droop coefficient m_ω of 0.01 and m_v ranges between 0 and 0.16 pu. Although it hardly affects the dominant modes, it also influences the steady-state reactive power sharing.

The VI also takes effect on the steady-state reactive power sharing. The impact on stability and damping is limited for larger value and the ranges are chosen between 0 and 2 mH and 0.4 Ω. The proportional gain $k_{p,v}$ of the voltage controller is not part of the optimization and is fixed to $3\ \Omega^{-1}$ to limit harmonic propagation, as described in Sec. 3.6.3.2.2. The voltage controller's integral gain ranges between 50 and $600\ \frac{1}{\Omega s}$ to obtain a bandwidth between the droop and current controller's. The feed-forward gain FF_v is limited to 1.2 to restrict harmonic propagation.

5.6.2. Results

To take a closer look at the impact of the line R/X ratio and the cut-off frequency ω_c, the optimizations are carried out for $R/X = 7.7$ ($R'_L = 0.642\ \Omega$/km, $X'_L = 0.083\ \Omega$/km) or $R/X = 3.9$ ($R'_L = 0.624\ \Omega$/km, $X'_L = 0.16\ \Omega$/km) and for the ranges $\omega_c = [15, 75]$ or $\omega_c = [15, 30]$.

5.6.2.1. Grid-Forming Droop Control

Optimized parameter sets of the grid-forming controller are depicted in Table 5.3. The cut-off frequency is always at its upper boundary to ensure the fast response of the droop control. Integral gain $k_{i,v}$ tends to be larger when $\omega_{c,GF}$ is high, because this also implies

Table 5.3.: Optimized parameters for a microgrid with two grid-forming inverters.

$R/X = 7.7$, $\omega_{c,GF} = [15, 75]$ rad/s	Par.	$\omega_{c,GF}$	$k_{i,v}$	L_v	R_v	$m_{\omega,GF}$	$m_{v,GF}$	FF_v
	Val.	75 rad/s	210 $\frac{1}{\Omega s}$	0.68 mH	0.12 Ω	0.005 pu	0 pu	1.04
$R/X = 7.7$, $\omega_{c,GF} = [15, 30]$ rad/s	Par.	$\omega_{c,GF}$	$k_{i,v}$	L_v	R_v	$m_{\omega,GF}$	$m_{v,GF}$	FF_v
	Val.	30 rad/s	180 $\frac{1}{\Omega s}$	0.88 mH	0.12 Ω	0.006 pu	0 pu	1.08
$R/X = 3.9$, $\omega_{c,GF} = [15, 75]$ rad/s	Par.	$\omega_{c,GF}$	$k_{i,v}$	L_v	R_v	$m_{\omega,GF}$	$m_{v,GF}$	FF_v
	Val.	75 rad/s	200 $\frac{1}{\Omega s}$	0.86 mH	0.1 Ω	0.0055 pu	0 pu	1.04
$R/X = 3.9$, $\omega_{c,GF} = [15, 30]$ rad/s	Par.	$\omega_{c,GF}$	$k_{i,v}$	L_v	R_v	$m_{\omega,GF}$	$m_{v,GF}$	FF_v
	Val.	30 rad/s	140 $\frac{1}{\Omega s}$	1.1 mH	0.1 Ω	0.006 pu	0 pu	1.08

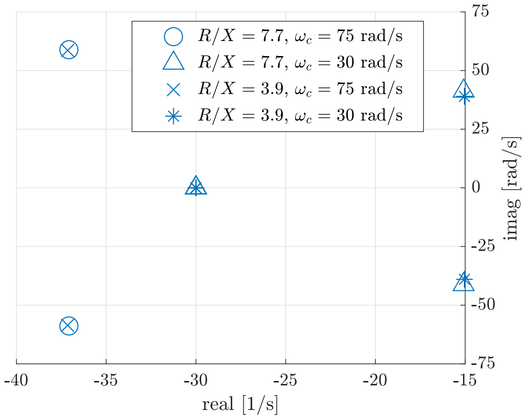

Figure 5.8.: Comparison of dominant eigenvalues of grid-forming inverters for optimized parameter sets.

a faster response of the voltage controller. FF_v is slightly above 1 and larger when $\omega_{c,GF}$ is smaller.

Lower values of $\omega_{c,GF}$ lead to slightly larger $m_{\omega,GF}$. Voltage droop coefficient $m_{v,GF}$ is always zero which implies that the VI dominates the reactive power sharing. This outcome is reasonable because there is no measurement filter involved in the VI loop leading to a fast response. The virtual inductor tends to be larger when R/X is smaller and the virtual resistor lies around $0.1\ \Omega$ or slightly larger.

Fig. 5.8 illustrates the dominant eigenvalues for the optimized parameter sets. The real part of the eigenvalue pairs is considerably smaller when the cut-off frequency is 75

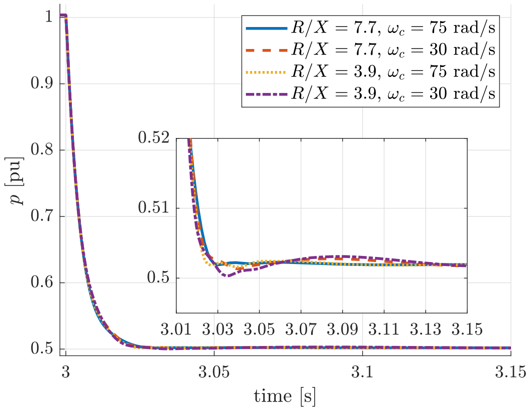

Figure 5.9.: Comparison of time-domain simulation results of grid-forming inverters for optimized parameter sets.

rad/s, independent from the R/X ratio. A lower R/X ratio does not necessarily cause the system to be more stable. The real parts of the eigenvalues are far away from the constraint of -5 1/s. It becomes apparent that the power sharing is improved along with the stability.

Fig. 5.9 compares time-domain simulation results of inverter 1 after load 1 is disconnected and the the active power of PED 1 decreases from about 1 to 0.5 pu. With optimized parameter sets, the response is rapid in all scenarios and the alignment with the steady-state value is fast in particular when $\omega_{c,GF}$ and the R/X ratio are large. Note that time constants of lines become smaller with higher R/X ratios.

The results for the area criterion hardly differ in all scenarios. The area is about 1% larger when $\omega_{c,GF} = 30$ rad/s compared to $\omega_{c,GF} = 75$ rad/s and a larger R/X ratio decreases the area by about 1% for both cut-off frequencies. The optimized parameters are more dependent on $\omega_{c,GF}$ than on the R/X ratio, because parameters resemble one another for the same range of $\omega_{c,GF}$.

5.6.2.2. Combination of Grid-forming and Grid-Supporting Droop Control

Simultaneous optimization of grid-supporting and grid-forming droop parameters has not been carried out in literature yet. Table 5.4 shows the optimized parameter sets.

Although their impact on dominant modes is minor according to sensitivity analysis, the measurement filter cut-off frequencies $\omega_{c,GF}$ and $\omega_{c,GS}$ always reach their upper boundary. The frequency droop coefficient m_ω is smaller compared to the case with two grid-forming PED and always takes on a value of 0.002 pu. The voltage coefficient $m_{v,GF}$

Table 5.4.: Optimized parameters for a microgrid with two grid-forming inverter.

$R/X = 7.7$, $\omega_{c,GF} = [15, 75]$ rad/s	Par.	$\omega_{c,GF}/\omega_{c,GS}$	$k_{i,v}$	L_v	R_v	$m_{\omega,GF}/m_{\omega,GS}$	$m_{v,GF}/m_{v,GS}$	FF_v
	Val.	$75/75\,\frac{rad}{s}$	$250\ \frac{1}{\Omega s}$	0.72 mH	$0.34\ \Omega$	0.002/0.002 pu	0/0.124 pu	1.12
$R/X = 7.7$, $\omega_{c,GF} = [15, 30]$ rad/s	Par.	$\omega_{c,GF}/\omega_{c,GS}$	$k_{i,v}$	L_v	R_v	$m_{\omega,GF}/m_{\omega,GS}$	$m_{v,GF}/m_{v,GS}$	FF_v
	Val.	$30/30\,\frac{rad}{s}$	$370\ \frac{1}{\Omega s}$	1.4 mH	$0.34\ \Omega$	0.002/0.002 pu	0/0.15 pu	1.16
$R/X = 3.9$, $\omega_{c,GF} = [15, 75]$ rad/s	Par.	$\omega_{c,GF}/\omega_{c,GS}$	$k_{i,v}$	L_v	R_v	$m_{\omega,GF}/m_{\omega,GS}$	$m_{v,GF}/m_{v,GS}$	FF_v
	Val.	$75/75\,\frac{rad}{s}$	$340\ \frac{1}{\Omega s}$	0.7 mH	$0.36\ \Omega$	0.002/0.002 pu	0/0.128 pu	1.16
$R/X = 3.9$, $\omega_{c,GF} = [15, 30]$ rad/s	Par.	$\omega_{c,GF}/\omega_{c,GS}$	$k_{i,v}$	L_v	R_v	$m_{\omega,GF}/m_{\omega,GS}$	$m_{v,GF}/m_{v,GS}$	FF_v
	Val.	$30/30\,\frac{rad}{s}$	$490\,\frac{1}{\Omega s}$	1.4 mH	$0.36\ \Omega$	0.002/0.002 pu	0/0.153 pu	1.08

is again zero, whereas for the grid-supporting device it is either around 0.125 or 0.15 pu, depending on the cut-off frequency. The grid-supporting inverter has no VI and the reactive power sharing is entirely regulated by $m_{v,GS}$, which explains the large values.

Smaller cut-off frequencies again lead to a larger virtual inductor, whereas the resistor is always around $0.35\ \Omega$. The feed-forward gain is around 1.1 or slightly larger.

Similar to the case with two grid-forming PED, the parameter sets resemble one another for similar ranges of ω_c, highlighting the major influence of this parameter. Fig. 5.10 depicts the dominant eigenvalues. The influence of the R/X ratio is again minor and the impact of ω_c is more pronounced. This is also observed in Fig. 5.11, which shows the active power of the grid-forming inverter after load 2 is connected. The return to steady-state is quicker with higher cut-off frequencies and the overshoot is generally large. This is a consequence of the current source characteristic of the grid-supporting controller. Most of the load is initially taken over by the grid-forming inverter due to its voltage source behaviour. The grid-supporting PED subsequently reacts to the frequency/voltage changes of the grid-forming PED. The result of the area criterion is more than two times larger compared to the case of two grid-forming PED when $\omega_c = 75$ rad/s and $R/X = 3.9$.

Direct comparison of the Fig. 5.10 and 5.8 reveals that the combination of grid forming inverters provides larger stability margin than in case where a grid supporting inverter is introduced.

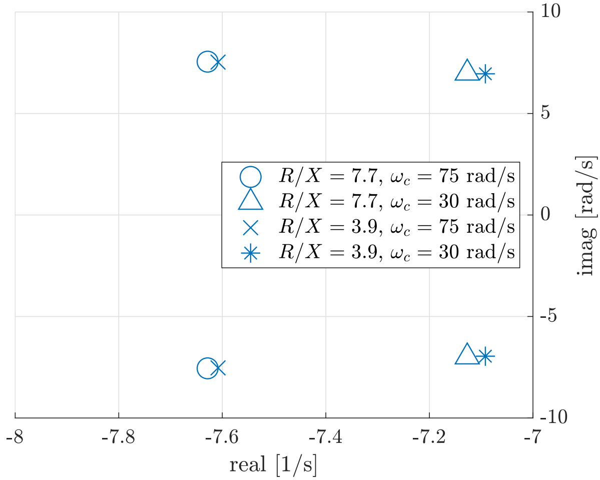

Figure 5.10.: Comparison of dominant eigenvalues of one grid-forming and one grid-supporting inverter for optimized parameter sets.

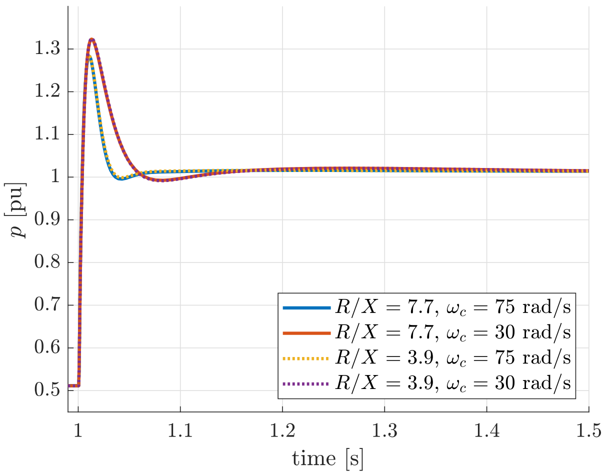

Figure 5.11.: Comparison of time-domain simulation results of one grid-forming and one grid-supporting inverter for optimized parameter sets.

5.7. Case Study 4: Benchmark Optimization of Two-Node Microgrid

5.7.1. Benchmark Test Scenarios

In this section, variants of the grid-forming droop control are optimized and compared based on benchmark tests. DER are exposed to various conditions in LV microgrids, which are simulated using benchmark tests. Again, the simple two-node microgrid from Sec. 5.2.1 is used. However, the DER controllers are benchmarked in various scenarios.

To analyse their interaction, the DER at both nodes ($S_n = 10$ kVA) can either be two PED or one PED and one SM wit the data given in App. D. The length of the line is either 30 or 400 m. Long lines aggravate the steady-state power sharing because of the larger voltage drop, whereas short lines and low impedance between DER affect the stability [288, 45]. The R/X ratio is set to 3.9 or 7.7, similar as in Sec. 5.6.

Line length and R/X ratios are varied in the benchmark scenarios. This results in four cases, because there are four combinations of line length and R/X ratio. The four cases are tested for combinations of two PED or one PED and one SM. Furthermore, there is a combined scenario named "all cases", where the same control parameters are tested for the combination of two PED as well as the combination of PED and SM, which then sums up to eight cases. This scenario benchmarks the control parameter sets for a large variety of microgrid applications.

To evaluate the transient response and steady-state behaviour of the primary control, loads in the microgrid are varied every 5 s in four steps. Load 1 ($S_n = 10$ kVA, power factor 0.95 inductive) is initially connected and load 2 ($S_n = 10$ kVA, power factor 0.95 inductive) disconnected. Load 2 is switched on at $t = 5$ s and the reactive power of load 1 is turned off at $t = 10$ s. The active power of load 1 is turned off at $t = 15$ s and at $t = 20$ s, the reactive power of load 2 is turned off.

The constraints for active and reactive power sharing and voltage deviations described in Sec. 4.4.2 are applied again. For the combination of PED and SM, the maximum real part of any eigenvalue is set to -1 1/s, because the time constants of SM are higher. For two PED, the maximum is again -5 1/s. Besides the area criterion, the largest occurring eigenvalue is minimized when SM are present to optimize the stability margin.

To lower the complexity of the optimization problems, some parameters that were optimized in the previous study case in Sec. 5.6 are assumed to be constant. According to the optimization in Sec. 5.6.2, the integral gain of the voltage controller $k_{i,v}$ is set to 200 $\frac{1}{\Omega s}$. The feed-forward gain FF_v is set to 1, which is slightly lower than the optimized values to limit harmonics propagation. ω_c is always at its upper boundary in

Table 5.5.: Parameter ranges for optimization.

Par.	m_ω	m_v	L_v	R_v	$m_{\omega,t}$	$m_{v,t}$
Range	$[0, 0.016]$ rad/s	$[0, 0.16] \frac{1}{\Omega s}$	$[0, 0.15]$ pu	$[0, 0.03]$ pu	$[0, 1]10^{-3}$ pu	$[0, 1]10^{-3}$ pu
Par.	ϕ	$k_{p,AVR}$	$k_{i,AVR}$	$k_{p,GOV}$	$k_{i,GOV}$	
Range	$[0, 90]°$	$[0, 0.16]$ pu	$[0, 1.2]$ pu	$[0, 10]$ pu	$[0, 1200]$ pu	

the optimizations in Sec. 5.6.2. It is set to 60 rad/s, which corresponds to the upper end of the values found in literature [77]. Higher order filters with even larger cut-off frequencies remain an open field of research. Only grid-forming droop control is regarded as this control type is considered superior due to the high overshoot when grid-supporting control is involved (see Fig. 5.11).

The ranges of the optimized parameters are given in Table 5.5.

5.7.2. Results

5.7.2.1. Optimized Parameter Sets

5.7.2.1.1. Comparison of Droop Variants

Table 5.6 and Table 5.7 depict the parameter sets for optimizations according to the benchmark scenarios. Three droop variants are considered: The transient droop (TD) as described in Sec. 3.6.2.3.3, the feed-forward droop (FFD) from Sec. 3.6.2.3.4 and the virtual frame transformation droop (FTD, Table 5.7) elaborated in Sec. 3.6.2.3.5. Only grid-forming droop controllers are regarded due to their promising outcome in Sec. 5.6. Considered scenarios are a microgrid with 2 PED and with one PED & SM, each with 4 cases due to the variation of the R/X ratio and line length. In addition, the former scenarios are combined ('All cases') leading to a total of 8 cases for this scenario, i.e. the parameter set is optimized for 8 simulation cases. The optimization according to the area criterion is regarded first.

The frequency droop coefficient is close to 0.009 pu in all cases as a result of the frequency deviation constraint. The 2 PED scenario of the FTD is an exception. The angle ϕ_{PED} is at $3°$ which is similar to an inverse droop. As the inverse droop is based on a high R/X ratio, $R_{v,PED}$ is very large and $L_{v,PED}$ is zero. The voltage droop coefficient $m_{v,PED}$ takes on relatively small values in all scenarios and for all droop types. This shows again that the voltage should rather be regulated by the VI and not the voltage

Table 5.6.: Resulting parameter sets for optimization with respect to area criterion or eigenvalue real parts* for TD and FFD.

	TD			FFD		
	2 PED	PED & SM	All cases	2 PED	PED & SM	All cases
$m_{\omega,PED}$ [pu]	0.0095	0.009/0.008*	0.0095	0.0095	0.008/0.0055*	0.009
$m_{v,PED}$ [pu]	0.042	0.008/0.02*	0.02	0.014	0.01/0.04*	0
$L_{v,PED}$ [mH]	1	1/0.4*	0.8	1.8	1/1*	1.8
$R_{v,PED}$ [Ω]	0.16	0.64/0.88*	0.52	0.12	0.48/0.4*	0.6
$m_{\omega,t,PED}$[10^{-3} pu]	0.13	0.06/0.12*	0.09	-	-	-
$m_{v,t,PED}$[10^{-3} pu]	0.5	0.4/0.36*	0.48	-	-	-
$m_{\omega,ff,PED}$ [pu]	-	-	-	0.031	0.027/0.026*	0.015
$m_{\omega,SM}$ [pu]	-	0.0095/0.008*	0.0095	-	0.008/0.005*	0.009
$m_{v,SM}$ [pu]	-	0.1/0.06*	0.152	-	0.124/0.076*	0.16
$L_{v,SM}$ [mH]	-	0.2/1.8*	1.8	-	1/1.4*	2
$R_{v,SM}$ [Ω]	-	0.52/0.8*	0.24	-	0.28/0.12*	0.24
ϕ_{SM} [°]	-	84/75*	75	-	78/75*	75
$k_{p,AVR}$ [pu]	-	0.14/0.06*	0.16	-	0.2/0.06*	0.18
$k_{i,AVR}$ [pu]	-	0.18/0.12*	0.2	-	0.22/0.12*	0.22
$k_{p,GOV}$ [pu]	-	2.8/2*	2.8	-	5/1.6*	6.2
$k_{i,GOV}$ [pu]	-	240/260*	220	-	280/200*	280
Average area	0.0203	1.1747	0.5920	0.0205	1.1811	0.5947
Max(Re(eigenvalues))* [1/s]	-	−2.0072*	-	-	−1.9620*	-

droop coefficient. The virtual inductor $L_{v,PED}$ takes on values between around 1 to 2 mH and $R_{v,PED}$ is usually about 0.5 Ω. $R_{v,PED}$ is lower in case of two PED. The FTD is an exception as mentioned.

The values of the transient droop coefficients $m_{\omega,t,PED}$ and $m_{v,t,PED}$ are around $0.1 \cdot 10^{-3}$ and $0.5 \cdot 10^{-3}$ pu, respectively. The feed-forward gain tends to be larger for the two PED scenario. The angle ϕ_{PED} of the FTD is low in case of two PED, as mentioned. In the other scenarios, it is $90°$ which makes it equivalent to the conventional droop.

Regarding the SM, droop coefficient $m_{\omega,SM}$ is in the same range as $m_{\omega,PED}$. On the other hand, $m_{v,SM}$ is much larger than $m_{v,PED}$. Higher droop coefficients entail a more rapid response of the slow SM system. The virtual inductance $L_{v,SM}$ normally ranges between 1 and 2 mH, but can also be much smaller. The virtual resistor $R_{v,SM}$ is smaller compared to the PED and lies between 0.24 and 0.52 Ω.

The ranges of the proportional gain of the AVR $k_{p,AVR}$ and $k_{i,AVR}$ are narrow and go from 0.14 to 0.28 and from 0.18 to 0.32, respectively. The variation of the governor proportional gain $k_{p,GOV}$ is rather large and ranges between 2.8 and 6.4, whereas there is little variation in the integral gain $k_{i,GOV}$.

Except for scenario with two PED, where the FTD is advantageous, the average result of the area criterion of the simulated cases is the lowest for the transient droop.

Table 5.7.: Resulting parameter sets for optimization with respect to area criterion or eigenvalue real parts* for FTD.

	FTD		
	2 PED	PED & SM	All cases
$m_{\omega,PED}$ [pu]	0.015	0.008/0.0055*	0.009
$m_{v,PED}$ [pu]	0	0.016/0.042*	0.004
$L_{v,PED}$ [mH]	0	0.4/0.7*	1.7
$R_{v,PED}$ [Ω]	1.2	0.38/0.08*	0.56
δ_{PED} [°]	3	90/69*	90
$m_{\omega,SM}$ [pu]	-	0.008/0.0045*	0.009
$m_{v,SM}$ [pu]	-	0.108/0.064*	0.148
$L_{v,SM}$ [mH]	-	0/0.8*	1
$R_{v,SM}$ [Ω]	-	0.24/0.16*	0.4
ϕ_{SM} [°]	-	81/84*	78
$k_{p,AVR}$ [pu]	-	0.28/0.08*	0.16
$k_{i,AVR}$ [pu]	-	0.32/0.16*	0.18
$k_{p,GOV}$ [pu]	-	6.4/2.6*	4.4
$k_{i,GOV}$ [pu]	-	300/280*	240
Average area	0.0199	1.1873	0.5988
Max(Re(eigenvalues))* [1/s]	-	−2.0009*	-

When SM are present, the area is increased considerably. Comparing the three droop types, the outcome for the areas hardly differ and their performance is rather similar.

The optimized parameter sets for the minimization of the maximum occurring eigenvalue real part for the microgrid with PED & SM are also given in Table 5.6 and Table 5.7. It is reasonable to optimize with respect to eigenvalues here, because the stability margin is lower when SM are present.

Both for PED and SM, the values of m_ω are decreased in comparison to the area criterion optimization. For the SM, m_v is decreased whereas the virtual inductor $L_{v,SM}$ is increased. The advantages of the FTD are exploited by setting the angle ϕ of the PED to $69°$. The GOV and AVR are tuned less aggressively. Maximum eigenvalue real parts are similar for the droop types, but slightly increased for the FFD.

5.7.2.1.2. Frame Transformation Droop

The FTD can adjust the droop control to network conditions, such as the angle of the network impedance, either online or offline. Therefore, it is a promising approach for various microgrid topologies and a closer look is taken at each case when optimized

Table 5.8.: Optimized parameter sets for the FTD optimization.

	2 PED			
	length = 30 m		length = 400 m	
	$R/X = 7.7$	$R/X = 3.9$	$R/X = 7.7$	$R/X = 3.9$
$m_{\omega,PED}$ [pu]	0.0085	0.009	0.015	0.015
$m_{v,PED}$ [pu]	0	0	0	0
$L_{v,PED}$ [mH]	0	0	0	0
$R_{v,PED}$ [Ω]	0.56	0.58	1.24	1.24
δ_{PED} [°]	9	3	3	3
Area	0.0183	0.0183	0.0210	0.0211

	PED & SM			
	30 m		400 m	
	$R/X = 7.7$	$R/X = 3.9$	$R/X = 7.7$	$R/X = 3.9$
$m_{\omega,PED}$ [pu]	0.009	0.009	0.008	0.01
$m_{v,PED}$ [pu]	0.004	0	0.014	0
$L_{v,PED}$ [mH]	0.5	0.4	0	0.9
$R_{v,PED}$ [Ω]	0.52	0.36	0.4	0.64
ϕ_{PED} [°]	90	90	90	87
$m_{\omega,SM}$ [pu]	0.0095	0.0095	0.008	0.0095
$m_{v,SM}$ [pu]	0.072	0.044	0.104	0.144
$L_{v,SM}$ [mH]	0	0	0	0.6
$R_{v,SM}$ [Ω]	0.4	0.32	0.18	0.16
ϕ_{SM} [°]	84	84	81	84
$k_{p,AVR}$ [pu]	0.24	0.28	0.24	0.16
$k_{i,AVR}$ [pu]	0.26	0.34	0.28	0.18
$k_{p,GOV}$ [pu]	6.8	7	8	6.8
$k_{i,GOV}$ [pu]	280	280	300	260
Area	1.1026	1.1089	1.1096	1.1080

with respect to the area criterion. Table 5.8 shows the results of the optimization for a microgrid with two PED or with one PED and one SM. A certain line length and R/X ratio is regarded in each case.

Similar to the optimizations in the previous section, the droop coefficient $m_{\omega,PED}$ is around 0.009 when the line length is 30 m for cases where two PED are present. It increases to 0.015 pu for longer line lengths.

Droop coefficient $m_{v,PED}$ and virtual inductor $L_{v,PED}$ are zero, independent from the line length. The virtual resistance $R_{v,PED}$ strongly depends on the line length and

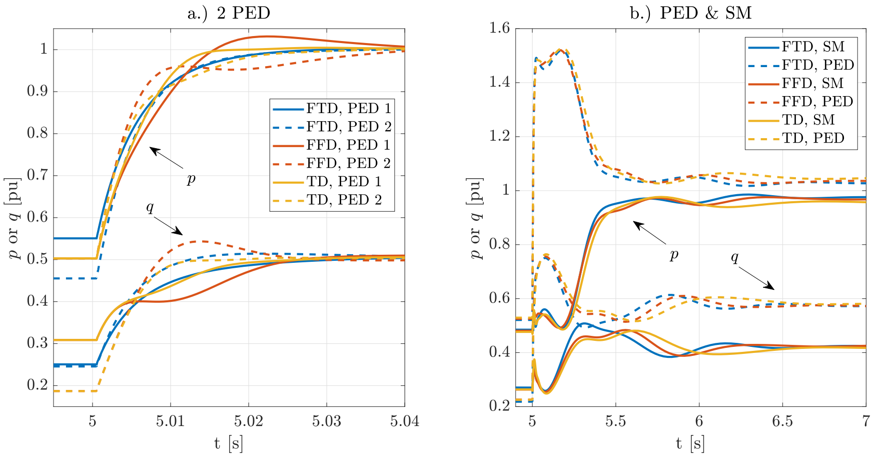

Figure 5.12.: Response to load step.

increase for longer lines. Inverse droop characteristics are observed due too the low angle ϕ_{PED}. The area hardly depends on the R/X ratio, but is smaller for shorter lines.

Droop coefficient $m_{\omega,PED}$ is again around 0.009 and $m_{v,PED}$ is relatively small in all cases for a microgrid with one PED and one SM. The virtual resistor $R_{v,PED}$ is close to $0.5\ \Omega$ and $L_{v,PED}$ is always below 1 mH. The angle ϕ_{PED} takes on values at or close to $90°$.

Similar to the PED, $m_{\omega,SM}$ is also at around 0.009. Particularly for longer lines, $m_{v,SM}$ is significantly larger than $m_{v,PED}$. $R_{v,SM}$ and $L_{v,SM}$ are relatively small. Governor and AVR have similar controller parameters as in the optimizations of the previous section. The areas are smaller compared to the average areas of similar scenarios in Sec. 5.7.2.1.1.

5.7.2.2. Time Domain Simulation

Fig. 5.12 depicts the response to the connection of load 2 at $t = 5$ s for 2 PED and PED & SM (line length $= 400$ m, $R/X = 7.7$), when the area criterion is the optimization criterion for the parameter sets (see Table 5.7).

It is interesting to observe that for the FTD in Fig. 5.12a.), the reactive power is accurately shared at steady-state ($t < 5$ s) as the frequency is a global variable, whereas active power sharing is inaccurate. This follows from the inverse droop characteristics. All droop variants quickly align with their steady-state value within only about two cycles, whereas the FTD exhibits a very smooth and overdamped behaviour.

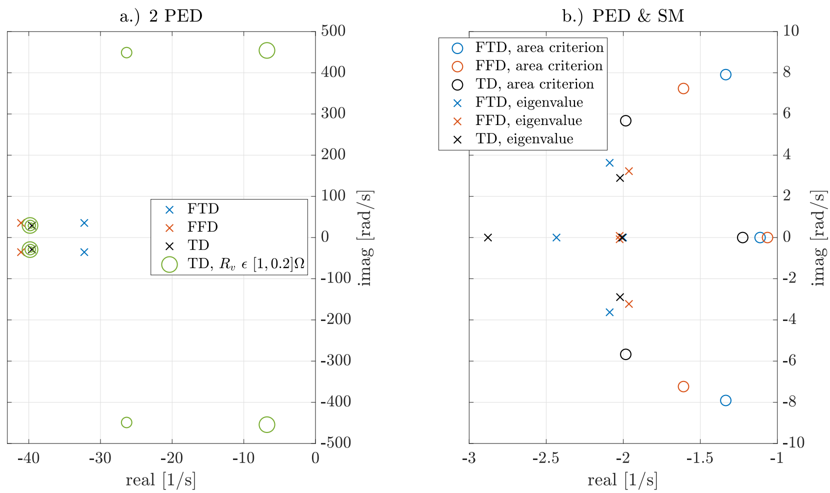

Figure 5.13.: Dominant eigenvalues when optimized according to area criterion or eigenvalue real part.

Due to the larger time constants of SM, the time-scale for PED & SM in Fig. 5.12b.) is much larger. The PED initially takes on a larger share of the load because of its voltage source characteristics and its location at the same node as the switched load. Hence, it is overloaded following the load step. The steady-state is reached after about 2 s. The observed difference between the droop variants are minor again.

5.7.2.3. Dominant Eigenvalues

The dominant eigenvalues for the cases simulated in Fig. 5.13 (only the line length is reduced to 30 m which impairs the stability) are illustrated in Fig. 5.13. The eigenvalues are located far inside the left half-plane in Fig. 5.13a.), pertaining to the scenario with 2 PED. The FTD has the largest eigenvalue real part. On the other hand, it performed best in power sharing according to the area criterion. Hence, eigenvalue and area criterion optimization are not necessarily coherent. The virtual resistor $R_{v,PED}$ is varied between 1 and $0.2\ \Omega$ (larger circles imply lower resistance) to highlight its influence. An oscillatory mode occurs that moves towards the unstable region quickly. When a PED and a SM is present, eigenvalues are much closer to the imaginary axis. Oscillatory modes are observed for all droop variants. When optimized with respect to area criterion, the damping ratio is the lowest for FTD and the largest for the TD. When optimized according to eigenvalue real part, dominant modes are at around 2 1/s. Furthermore, the damping is improved for all droop types.

5.8. Case Study 5: Optimization of Cigre Benchmark Microgrid

5.8.1. Benchmark Test Scenarios

In this section, it is looked at the Cigre benchmark LV microgrid introduced in Sec. 5.2.2. It contains four DER which are optimized in this section. DER data are given in App. D.

The parameters are optimized for scenarios where all the DER are grid-forming PED or where one DER is a SM. When there are only PED, a high load and a high PV case is incorporated, i.e. two simulations are evaluated in the objective function. For scenarios where there is one SM, only the high load case is analysed, because it is unrealistic that a SM is connected when the PV generation exceeds the load in the microgrid in the high PV case. Four load/generation steps are simulated, which represent worst case fluctuations. At first, the largest PV plant in the microgrid (PV 1) is disconnected and then reconnected again. Afterwards, the largest load (load 1) is switched off and on again.

In the case where one DER is a SM, not only the controller parameters are optimized, but also the placement of the SM. This means that either of the four DER can be the SM, whereas the other three are PED. The analysed droop variants are the TD and the FTD due to their promising performance in Sec. 5.7. Moreover, the original droop (OD) without any controller design enhancements (also no VI) is investigated. The same set of controller parameters is applied to all PED in the microgrid. Furthermore, the same constraints as for the optimization of the small microgrid in Sec. 5.7 are applied. The ranges of the optimized parameters are given in Table 5.5.

5.8.2. Results

5.8.2.1. Optimized Parameter Sets

The optimized parameter sets and the results for the optimization criteria are given in Table 5.9. Besides the average area and maximum eigenvalue real parts resulting from the optimized parameter sets of this section, also the outcome using the parameter sets from the benchmark optimization of Sec. 5.7 is shown.

The droop coefficients $m_{\omega,PED}$ and $m_{\omega,SM}$ are again around 0.01 or slightly larger. Hence, maximum possible values that do not violate the frequency deviation constraint are preferable. An exception is the OD scenario with 4 PED where the value is smaller because the system tends to become unstable for higher values. Reactive power droop coefficients tend to be larger compared to the small microgrid in Sec. 5.7. The OD is an exception with a small value. The cut-off frequency is shown for all droop types, although it was only optimized for the OD, because setting it to 60 rad/s leads to an unstable

Table 5.9.: Parameter sets for optimization with respect to area criterion or eigenvalue real parts* and comparison of results using parameters from Sec. 5.7^{+}.

	TD		FTD		OD	
	4 PED	3 PED & SM	4 PED	3 PED & SM	4 PED	3 PED & SM
$m_{\omega,PED}$ [pu]	0.011	0.0105/0.01*	0.013	0.0115/0.013*	0.0025	0.012/0.009*
$m_{v,PED}$ [pu]	0.096	0.038/0.035*	0.03	0.083/0.0255*	0.0047	0.061/0.069*
ω_c [rad/s]	60	60	60	60	15	12/9*
$L_{v,PED}$ [pu]	0.1319	0.088/0.0565*	0.1319	0.0848/0.0157*	-	-
$R_{v,PED}$ [pu]	0.015	0.016/0.014*	0.019	0.02/0.012*	-	-
$m_{\omega,t,PED}$ [10^{-3} pu]	0.71	0.71/0.41*	-	-	-	-
$m_{v,t,PED}$[10^{-3} pu]	0.28	0.5/0.24*	-	-	-	-
ϕ_{PED} [°]	-	-	42	90/84*	-	-
$m_{\omega,SM}$ [pu]	-	0.0135/0.0095*	-	0.013/0.011*	-	0.0135/0.0095*
$m_{v,SM}$ [pu]	-	0.1185/0.0475*	-	0.1085/0.0255*	-	0.1165/0.0915*
$L_{v,SM}$ [pu]	-	0.0126/0.11*	-	0.0314/0.0377*	-	0.0063/0*
$R_{v,SM}$ [Ω]	-	0.0138/0.0104*	-	0.016/0.015*	-	0.0048/0*
ϕ_{SM} [°]	-	90/87*	-	90/87*	-	90/90*
$k_{p,AVR}$ [pu]	-	0.4/0.3*	-	0.48/0.3*	-	0.54/0.16*
$k_{i,AVR}$ [pu]	-	0.56/0.64*	-	0.56/0.66*	-	0.7/0.32*
$k_{p,GOV}$ [pu]	-	7.8/8*	-	8/9*	-	6.2/7.6*
$k_{i,GOV}$ [pu]	-	700/840*	-	840/660*	-	580/640*
Average area	0.078	1.0583	0.0677	1.0856	0.6668	1.4594
Average area^{+}	0.13^{+}	2.8669^{+}	0.0768^{+}	2.7339	-	-
Max(Re(eig.))* [1/s]	-	−2.1993*	-	−2.244*	-	−2.1296
Max(Re(eig.))*$^{+}$ [1/s]	-	−0.8336*$^{+}$	-	−0.5262*$^{+}$	-	-

system here. The outcome between 9 and 15 1/s makes the OD slow to react.

The virtual inductor $L_{v,PED}$ tends to be larger compared to the small microgrid (note that the values are given in pu because of the differing nominal power of the DER). $m_{v,SM}$ is again smaller, when optimized with respect to eigenvalue real part. In case of 4 PED, the angle ϕ_{PED} is at 42°, unlike the small microgrid, where it is 3°. An explanation is that the main feeder lines in the microgrid (lines between node 1 and 10 and between 1 and 27) have a relatively low R/X ratio. For the SM, angle ϕ_{SM} is always close to 90°. AVR and GOV are tuned significantly more aggressively compared to the small microgrid. This is a consequence of the lower proportion of SM in the microgrid. It enables stability to be maintained due to the stabilizing effect of the high share of grid-forming PED even with a very aggressive tuning.

As mentioned, the algorithm also optimizes the position of the SM. In all scenarios with SM, it is placed at node 12. This is the ideal place for the SM, because it is close to the load and generation fluctuations of Load 1 and PV 1, respectively. Grid-forming PED initially take on a larger share of the load because their voltage source behaviour is more pronounced compared to the SM. This is mitigated by placing the SM close to the

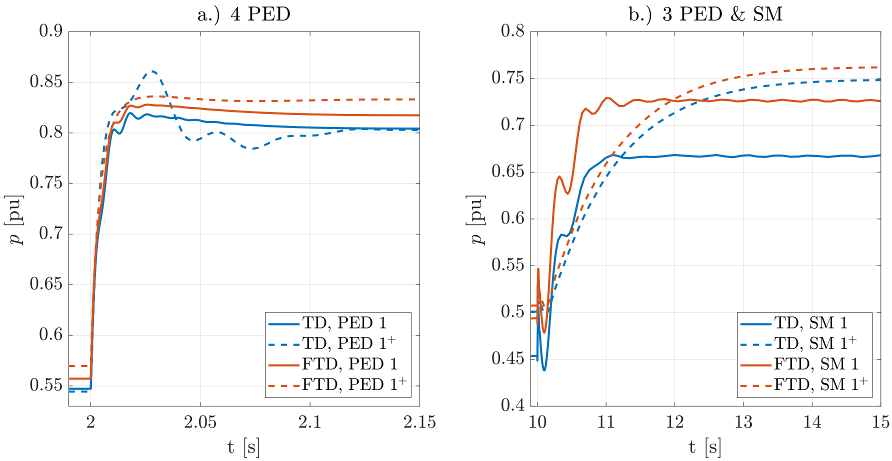

Figure 5.14.: Response to load step ($^+$parameters from Sec. 5.7).

fluctuation and where it takes a higher share.

The outcome for the optimization criteria is distinctly better when the parameters from the optimization in this section are used compared to the parameter sets from the benchmark scenarios in Sec. 5.7 as seen in Table 5.9. The average area is about 2-3 times larger when parameters from the small microgrid optimization are used. An exception is the scenario with 4 PED of the FTD, where the areas are similar. Pertaining to the eigenvalue optimization, however, parameter sets from Sec. 5.7 for FTD strongly decrease the stability margin.

The OD was not regarded in Sec. 5.7. In comparison to the other droop types, OD always performs worse. Especially for the 4 PED scenario, the area is tremendously larger. When the SM is present, differences to other droop types become less distinct.

In conclusion, the parameter sets found in the benchmark optimization of the small, two-node microgrid cannot simply be transferred to this larger microgrid. This holds for microgrids with SM in particular, where the proportion of SM among all DER has a strong impact and AVR and GOV can be tuned more aggressively when the share of SM is low. On the other hand, the parameter sets from the small microgrid do not violate any constraints. The OD yields poor results especially when only PED are connected, which again corroborates the positive impact of the VI.

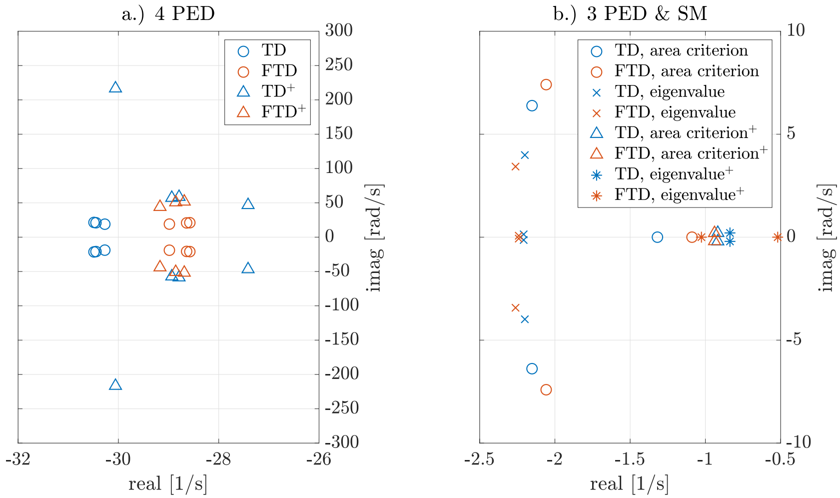

Figure 5.15.: Dominant eigenvalues when optimized according to area criterion or eigenvalue real part ($^+$parameters from Sec. 5.7).

5.8.2.2. Time Domain Simulation

The outcome of time-domain simulations for the active power of PED/SM 1 at node 12 is presented in Fig. 5.14 for the scenarios with 4 PED or with 3 PED and SM, when optimized with regard to area criterion. The OD is not considered due to the poor outcome and extensive oscillation.

In case of 4 PED, the settling time is prolonged compared to the small microgrid with 2 PED (Fig. 5.12a.)) for all droop types and parameter sets. The discrepancy between using the parameter sets from the large and small microgrid optimization is minor for the FTD, but very distinctive for the TD. Here, an additional higher frequency oscillation is observed.

Regarding the scenario with 3 PED and SM, the settling time is significantly lower using the parameter sets from the large microgrid optimization, particularly for the TD. However, it is still longer compared to the small microgrid (Fig. 5.12b.)). High frequency oscillations due to the aggressive tuning of the AVR are seen. On the other hand, when using the parameters from Sec. 5.7, an almost first order behaviour is observed.

5.8.2.3. Dominant Eigenvalues

The dominant eigenvalues for the scenarios are given in Fig. 5.15. When only PED are present, eigenvalues generally tend to be closer to the imaginary axis compared to the outcome for the small microgrid in Fig. 5.13. FTD is more stable and less oscillatory compared to TD. A pair of high frequency (ca. 220 rad/s) oscillatory modes occurs for the TD, when using the parameter sets from the small microgrid optimization. From analysis of participation factors, it is concluded that the pair originates from voltage controller interaction. The low damping is a consequence of the low value for the virtual resistor, as seen in Table 5.6 ($0.16\ \Omega$, i.e. 0.01 pu). A larger number of PED in a microgrid seems to aggravate the damping and the interaction of their voltage controllers. Nonetheless, eigenvalues are still well inside the left half pane.

Regarding the scenario with a SM, the results for the optimization towards area criterion and with respect to eigenvalue are shown. The least stable eigenvalues occur when the parameter sets from Sec. 5.7 are used. It is interesting that optimizing with respect to eigenvalues does not result in lower real parts compared to optimizing according to the area for the parameters from Sec. 5.7. On the other hand, modes are well damped conforming with the observed first order behaviour in Fig. 5.14b.).

Deploying the parameters from the large grid optimization, differences between the droop types are small. The largest real parts are below -2 1/s when optimized with respect to eigenvalues. The damping ratio of the oscillatory modes is about 50% when optimized towards eigenvalues and 29% when optimized towards area criterion.

5.9. Case Study 6: Model Order Reduction

Model order reduction approaches from literature and those proposed in this work are analysed and validated in this section. The optimized control parameters from Sec. 5.6 are used to test the simplifications under realistic parameter conditions.

5.9.1. Grid-Forming Droop Control

The simple two-node microgrid introduced in Sec. 5.2.1 is again used. The line length is 100 m and the R/X ratio is 3.9 ($R'_L = 0.624\ \Omega$/km, $X'_L = 0.16\ \Omega$/km). Fig. 5.16 compares the dominant eigenvalues for grid-forming droop controlled inverters for cut-off frequencies of $\omega_{c,GF} = 75$ or $\omega_{c,GF} = 30$ rad/s. In comparison to the original model, the outcome is hardly affected when the current loop is approximated by a first order lag ('CL≈PT1'). The damping is slightly increased when neglecting the current loop entirely ('no CL'). A tangible difference is seen when not considering the inner loops at all ('no IL'). The cascaded control is slowed down when $\omega_{c,GF}$ is smaller and the impact of the dynamics of the inner loops is less pronounced. As a consequence, the deviations of eigenvalues are smaller for $\omega_{c,GF} = 30$ rad/s.

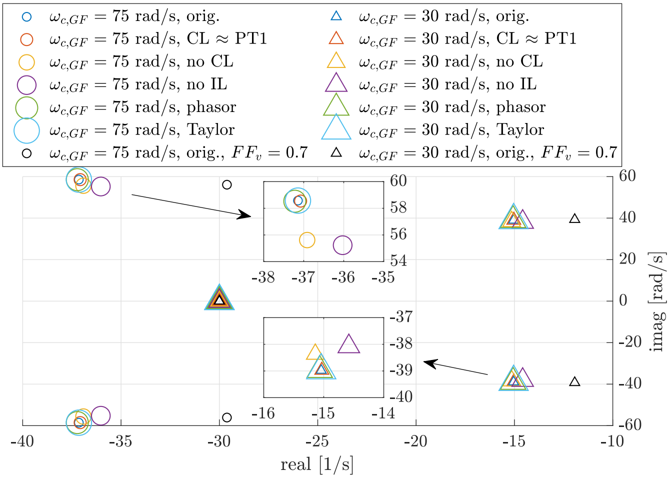

Figure 5.16.: Comparison of dominant eigenvalues of two grid-forming inverters for model simplifications.

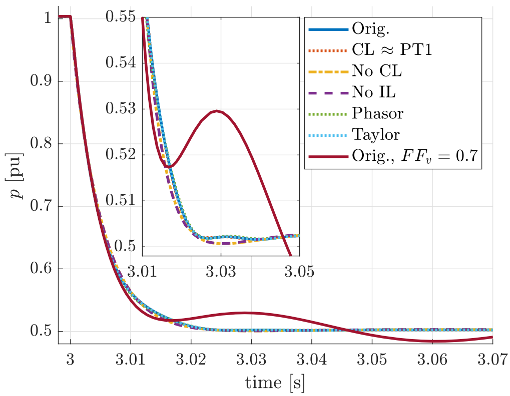

Figure 5.17.: Comparison of time domain simulation results of two grid-forming inverters for model simplifications.

Eigenvalues are generally close to the original model for network simplifications. This holds for the first-order Taylor approximation in particular. The time constants of the line dynamics are small due to the high R/X ratio in LV networks and there is little interference with the dominant modes of cascaded PED control.

Additionally, the dominant modes of the original model with a feed-forward gain FF_v of 0.7, which is a value often seen in literature and which limits the propagation of harmonics [76] in comparison to larger values, are shown in Fig. 5.16. The impact is

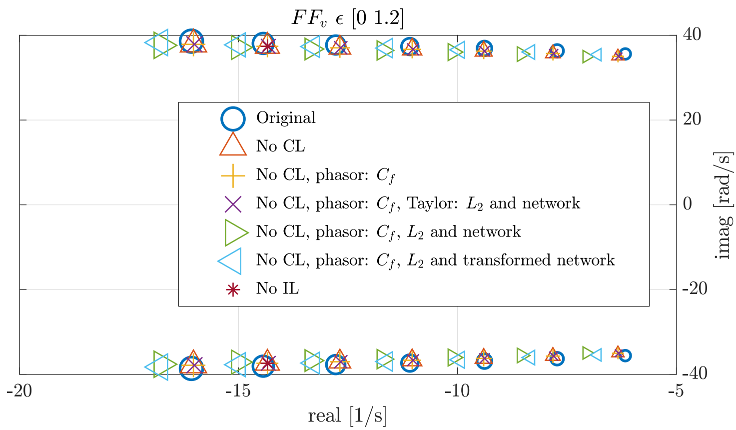

Figure 5.18.: Comparison of dominant eigenvalues for grid-forming inverters for model simplifications and $w_c = 30$ rad/s.

tremendous and the system becomes less stable. Neglecting the inner loops entirely is an unacceptable approximation here, because the model is then independent from FF_v. Therefore, the validity of this approximation is very sensitive towards control parameter variations and only holds for the optimized parameter set.

Fig. 5.17 illustrates the active power of PED 1 in time domain simulations after a load disconnection. For network simplifications in particular and also when the current loop is approximated by a first order lag, deviations from the original model are minor. In contrast, deviations are significant when the current loop or the entire inner loops are omitted. A very different outcome is observed when varying FF_v. In conclusion, the neglect of the voltage controller is an oversimplification in general.

In Sec. 3.6.3.2.3, a model reduction approach that preserves the dynamics of the voltage controller (and the impact of FF_v) is introduced. Furthermore, topology transformations that reduce the largest occurring time constants of simplified elements are proposed. These approaches are validated in the following, using the microgrid introduced in Fig. 3.18.

Fig. 5.18 illustrates the dominant eigenvalues for $\omega_c = 30$ rad/s and FF_v is varied between 0 and 1.2. Again, neglecting the current loop ('No CL') leads to slight deviations from the original model. Additionally approximating the filter capacitor C_f with a phasor model and the grid-side inductor by a first-order Taylor model does not significantly increase the difference to the original model.

On the other hand, using the phasor approximation for the network leads to considerably larger deviations. The proposed network transformation from Sec. 3.6.3.2.3

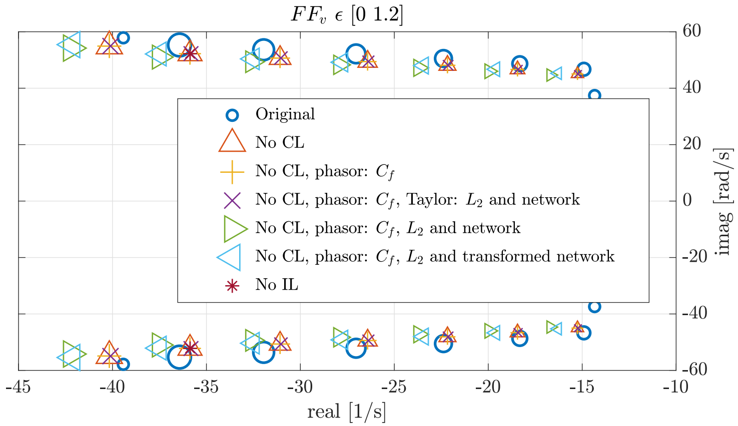

Figure 5.19.: Comparison of dominant eigenvalues for grid-forming inverters for model simplifications and $w_c = 75$ rad/s.

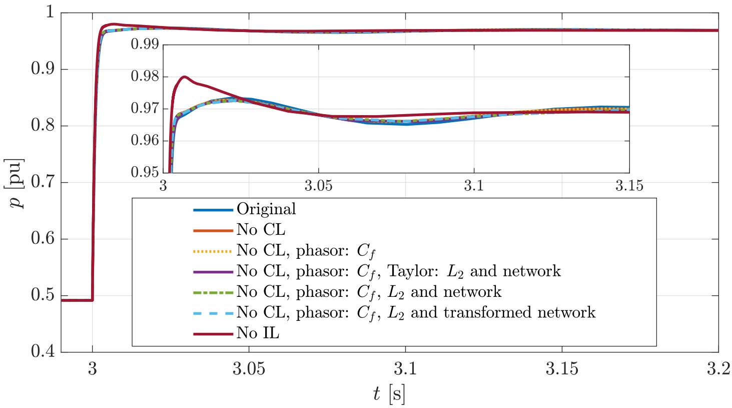

Figure 5.20.: Comparison of time domain simulations for grid-forming inverters for model simplifications with $\omega_c = 75$ rad/s and $FF_v = 0.2$.

can alleviate this to some extent, particularly for low values of FF_v. It is again observed that neglecting the inner loops only approximated the model well when FF_v is around unity (the pair of eigenvalues has a real part of around 14 1/s).

Similar analysis is carried out in Fig. 5.19, except that the cut-off frequency of the power filter is increased to 75 rad/s. The previous observations are generally confirmed, although deviations from the original model are a bit larger. This is attributed to the closer time scales of the cascaded control.

Finally, the active power of PED 1 when load 1 is connected at $t = 3$ s is depicted

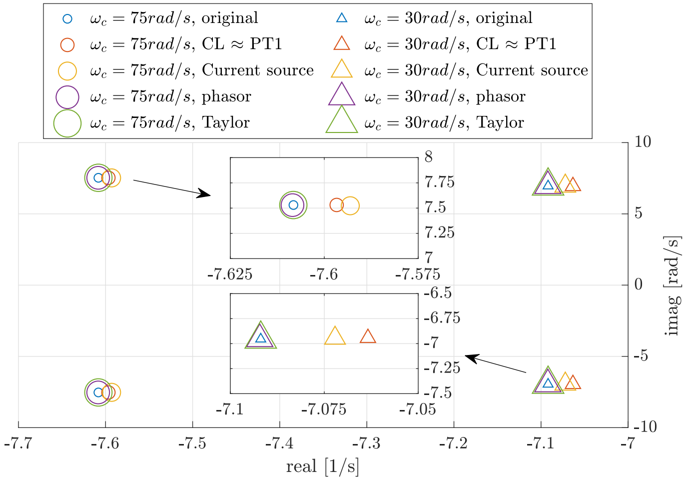

Figure 5.21.: Comparison of dominant eigenvalues of one grid-forming and one grid-supporting inverter for model simplifications.

in Fig. 5.20. The deviation is the largest when the inner loops are entirely neglected. All other models preserve the voltage controller and are close to the original model, although some deviations are observed in the period directly after the load connection. These are attributable not only to the dominant, but also to faster modes.

In summary, it is concluded that the proposed reduced order model which preserves the voltage controller and uses a phasor and first-order Taylor approximation for C_f and L_2, respectively, approximates the original model well. The network transformation can slightly improve the phasor approximation of L_2 and can be used when the first-order approximation is not available due to software restrictions.

5.9.2. Grid-Supporting Droop Control

The outcome of the dominant modes for the case of one grid-forming and one grid-supporting inverter is given in Fig. 5.21. The small microgrid from Sec. 5.2.1 is used. No simplifications are applied to the grid-forming inverter.

Modes are slightly shifted to the right when approximating the current loop by a first order lag ('CL≈PT1'). Interestingly, the accuracy is not significantly deteriorated when the whole LCL filter is neglected, i.e. modelling the PED as a simple current source with a first order lag. The simplifications lead to a conservative stability assessment. Network simplifications with Taylor or phasor approximations do not significantly alter the eigenvalues.

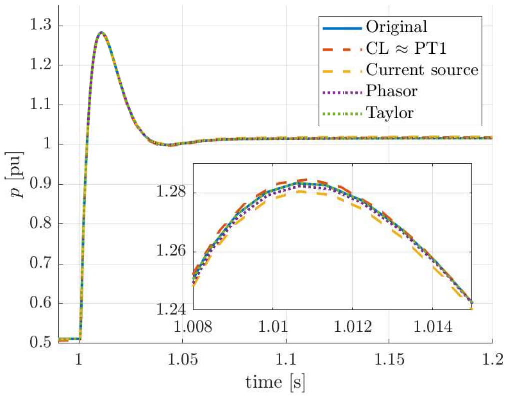

Figure 5.22.: Comparison time domain simulation results of one grid-forming and one grid-supporting inverter for model simplifications.

Fig. 5.22 illustrates the time-domain simulation results of the grid-forming controller for a load step at $t = 1$. In general, the original model is well approximated by all models and small deviations are observed for simplifications of the current loop and when a simple current source is used.

These results corroborate that the impact of the current loop and network dynamics is minor and dominant modes primarily depend in the PLL dynamics.

5.10. Case Study 7: Optimization of Synthetic Inertia for Wind Power Plants

The optimization of SI methods for wind power plants is covered in this section. At first, the objectives and constraints are defined as they differ from the previous optimizations. This is necessary due to the DFIG control, which is not grid-forming, but reacts to frequency fluctuations by providing SI [318, 258][2].

5.10.1. Objectives

Inverters and SM exhibit different dynamic behaviours during load fluctuations due to the differing time scales of their response. This also results in differing optimization objectives. During a load increase in the microgrid, SM initially provide active power through the rotor inertia which causes a significant drop in angular speed. After a few hundred milliseconds,

[2] The presented SI optimization was conducted by the author of this work.

the control of the governor becomes dominant and caters for the frequency recovery until a stable operating point is reached. On the other hand, the dynamics of PED are to a large extent dominated by the controller. Their dynamic response is quick to avoid overloading and potential damage of power electronics. Consequently, the frequency dip is less pronounced in a microgrid dominated by PED.

The optimization objectives are explicated referring to the Figures in Section 5.10.4. The differing dynamic behaviours are depicted in Fig. 5.23 and 5.24, where the active power of the wind turbine and the frequency in the microgrid during a load step are illustrated for various controller parameters. Whereas in the SM case in Fig. 5.24, there is a large frequency drop, referred to as frequency nadir [60], the frequency is rather smooth in the PED case in Fig. 5.23. The goal of the optimization in the PED case is to provide frequency support during the time span of 500 ms after the load step, which is marked in the figure. During this period, the DFIG should relieve the PED loading. Hence, the objective is to limit the frequency drop, which is a measure of the PED loading according to the droop characteristic. This optimization criterion can be formulated as the maximization of the minimum occurring frequency as follows:

$$max\Big(min\big(f(t)\big)\Big) \quad for\ t_{step} \leqslant t \leqslant t_{step} + 0.5\ s, \tag{5.1}$$

where $f(t)$ is the frequency in the microgrid and t_{step} is the time when the load step occurs.

On the other hand, a pronounced frequency drop is observed in case of a SM in Fig. 5.24. Here, the optimization objective is to limit the nadir. Therefore, the optimization criterion can be formulated similar to (5.1), but for the entire time span after the load jump:

$$max\Big(min\big(f(t)\big)\Big) \quad for\ t_{step} \leqslant t \leqslant \infty. \tag{5.2}$$

It is noted that the optimization criterion is not as straightforward in case of the PED compared to the SM. The nadir is a criterion that has been used for a long time in stability studies involving traditional power systems dominated by SM. Having said that, no such criterion exists for inverter dominated power systems. In this work, the considered time span is limited to 500 ms after the load jump in case of the PED. This is the critical interval where active power should be provided by the SI method to limit the transients and where rate of change of frequency relays may be triggered. However, the slow modes introduced by the SI control may cause the frequency to drop below the steady state value later, as is observed in Fig. 5.23.

5.10.2. Constraints

Controllers tuned with respect to a good transient response can introduce lightly damped modes to the system. Therefore, a constraint of the optimization is that the frequency must stay within a corridor around the steady state from $4s$ after the load step onwards. The deviation is limited to $+/-5\%$ of the total frequency change as depicted in Fig. 5.23, or with regard to the nadir in Fig. 5.24.

5.10.3. Parameter Ranges

The optimized parameters are the proportional factor of the frequency gradient SI k_{SI} and the proportional and integral gain of the slow PLL $k_{p,PLL}$ and $k_{i,PLL}$. The parameter ranges are given in Table 5.10.

Table 5.10.: Ranges of optimized parameters.

Parameter	k_{SI}	$k_{p,PLL}$	$k_{i,PLL}$
Range	$[1, 100]$	$[0.1, 30]$	$[0.1, 30]$

5.10.4. Time Domain Simulation

This Section covers the results of time domain simulations for optimized controller parameters for the microgrid with two nodes from Sec. 5.2.1 with a nominal voltage of 20 kV. At the first node, static load 1 and either a PED or a SM are connected. The DFIG and static load 2 are connected to the second node. Although the microgrid consists of only two nodes, conclusions for the dynamics of larger microgrids can be drawn. The data of the microgrid and the components are given in Appendix E.

The PED and SM always utilize grid-forming droop control (original droop without VI), whereas the DFIG is either droop controlled (grid-supporting) or simple PQ-control. The following figures illustrate the active power of the DFIG and the microgrid frequency when load 2 is connected at $t = 1$ s. The controller parameters are optimized separately for each case.

5.10.4.1. DFIG with Battery storage system

The results for a combination of PED and DFIG without droop control are shown in Fig. 5.23a.). The apparent power of the DFIG hardly changes when the SI is turned off and the frequency drops to almost its steady state value. When the DFIG provides frequency gradient SI (df/dt), its active power rises almost instantly when the load changes and

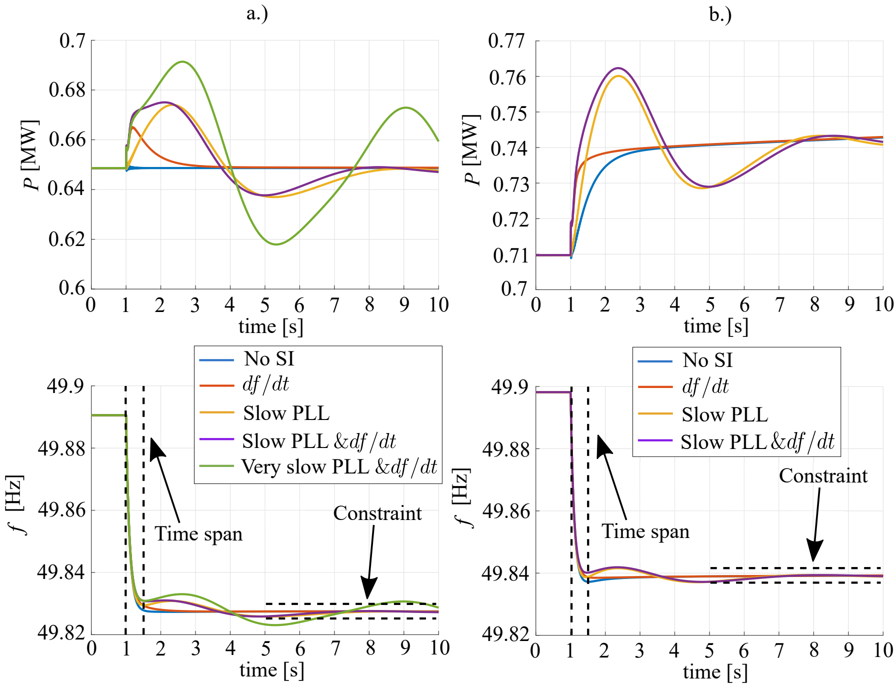

Figure 5.23.: Active power of DFIG and microgrid frequency when combined with a grid-forming inverter. a.) DFIG without droop control, b.) DFIG with grid-supporting droop control

lasts until about $t = 3s$. The frequency drop after 500 ms is 97.6 % of the steady state value.

Providing SI with a slow PLL results in an active power that peaks at around $t = 2.4$s and the introduction of a low frequency mode. The frequency drop in the relevant time span is similar to the df/dt case with 97.5 % of the steady state value.

When the slow PLL is combined with the df/dt SI, the instant active power increase is similar to the df/dt case, but is more sustained. The frequency drop is 95.2 %. Another case is added to Fig. 5.23 a.), where a non optimal parameter set was used for the PLL. When this very slow PLL is used in connection with df/dt SI, the systems shows extensive oscillations. The constraint of the frequency corridor is violated and the frequency drop is 95.1 % after 500 ms, which is only insignificantly smaller than in the former case. This confirms the ability of the optimization algorithm to find optimal solutions without violating constraints.

Fig. 5.23 b.) illustrates the simulation outcome for a microgrid with PED and

DFIG with activated droop control. When no SI is provided by the DFIG, the active power rises slowly as a reaction to the filtered frequency measurement in accordance to the grid-supporting droop in equation (3.53). The frequency drops slightly below its steady state value. With df/dt SI as well as with a slow PLL, the frequency drop is at 97.6 % of the non SI case. It is observed again that the active power rises steeply for df/dt SI, while it oscillates with a peak at $t \approx 2.3$ s for the slow PLL. The frequency drop is lowest with 95.2 % for the combined SI scenario. In this case, the active power combines the characteristics of the two SI methods and exhibits a steep increase in the moment after the load step and then oscillates.

In conclusion, the influence of the SI methods on the frequency drop when the microgrid contains a DFIG and a PED is minor. The frequency drop is similar for the two SI methods and it is slightly lower when they are combined. The df/dt leads to an almost instant and steep active power increase due to the frequency transient. On the other hand, employing the slow PLL, the active power provision is delayed but lasts longer. The reason is that the active power depends on the angle difference between the PLL and the actual grid angle. As the angle difference is the integral of the angular speed deviation, it takes some time until active power is provided. The slow PI controller of the PLL causes the subsequent oscillations. As described in Sec. 5.10.1, one drawback of the slow PLL SI is that the frequency falls below its steady state value at around 3.5 s in Fig. 5.23 a.) and b.).

5.10.4.2. DFIG with Synchronous Machine

For the scenario of a microgrid with DFIG and SM, the optimizations are conducted with and without droop control of the DFIG, similar to the former Section. The outcome without droop control is shown in Fig. 5.24 a.). The active power output is smooth when no SI is applied and the frequency nadir is at about $49.53Hz$, which is significantly lower than the steady state. Again, the active power rise is steep for the df/dt control and a damped oscillation is observed here. The frequency drop is at 84.7% with regard to the non SI case. The active power increase is less steep and the frequency drops lower to 88.1% when the slow PLL is employed. The combined SI case exhibits the lowest frequency drop with 78.3%, although the active power increase is less steep at the beginning, when compared to the df/dt control.

In Fig. 5.24 b.) the simulation results for a droop controlled DFIG are given. When no SI is applied, the frequency drops to about $49.58Hz$, which is a bit higher than in the former scenario without droop control as the DFIG also supports the steady state frequency by adjusting its active power. The frequency drop is about the same with 86.5 % and

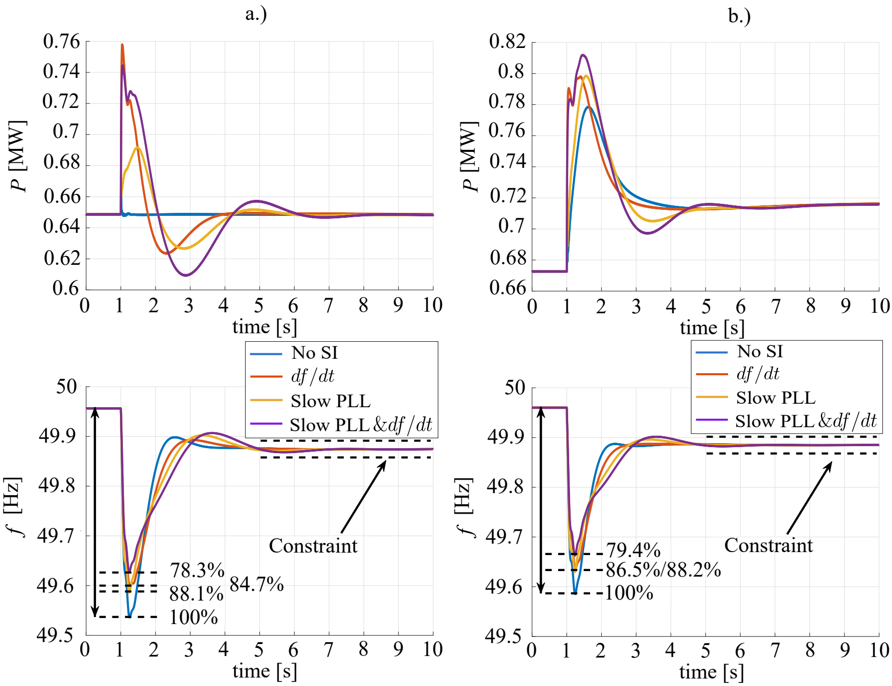

Figure 5.24.: Active power of DFIG and microgrid frequency when combined with a SM. a.) DFIG without droop control, b.) DFIG with grid-supporting droop control

88.2 % for the df/dt SI and the slow PLL, respectively. If the SI methods are combined, the frequency drop is 79.4 % and the active power again combines the characteristics of both SI methods.

It is seen that the impact of SI is larger for the SM scenario compared to the microgrid with PED. The df/dt control and the slow PLL again perform rather similar. Combining both SI methods results in a significant decrease of the nadir.

5.10.4.3. Optimized parameters

The optimized parameter sets for some of the scenarios described are given in Table 5.11. It becomes apparent that the grid-forming PED has a stabilizing effect on the microgrid in comparison to the SM. This is seen in the larger values for k_{SI} and the lower values for the PLL controller gains, which are equivalent to a more aggressive tuning of the SI controllers. Moreover, when the frequency gradient SI is combined with the slow PLL, k_{SI} has to be tuned less aggressive (smaller) to ensure the stability of the system.

Table 5.11.: Optimized synthetic inertia parameters

DFIG with droop control combined with PED			
	k_{SI}	$k_{p,PLL}$	$k_{i,PLL}$
df/dt	42	-	-
Slow PLL	-	0.6	1.3
Slow PLL & df/dt	40	0.6	1.2
DFIG with droop control combined with SM			
	k_{SI}	$k_{p,PLL}$	$k_{i,PLL}$
df/dt	34	-	-
Slow PLL	-	3.5	5.3
Slow PLL & df/dt	26	2.7	5.7

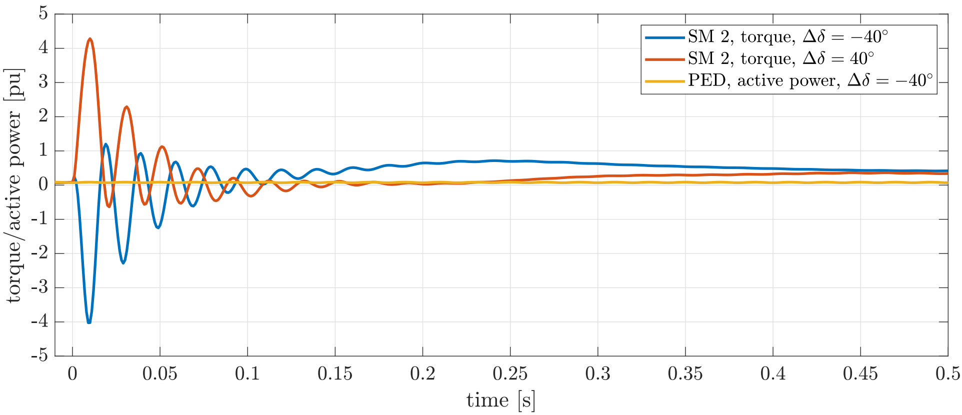

Figure 5.25.: Loadings of SM and PED for positive and negative angle deviations.

5.11. Case Study 8: Synchronization

This section investigates the loadings of SM and the breaker between an islanded microgrid and an external grid in case of imprecise voltage alignment at breaker closure [319, 320][3]. The two node microgrid from Fig. 5.3 is used with two SM and two static loads for EMT-simulations. The voltage level is 20 kV and the line has a length of 10 km. The SM are loaded with an active power of about 0.07 pu before the breaker closing. The loading before the closing is kept low to minimize its impact on the stresses occurring after closure. However, diesel gensets usually do not run idle which is why the minimal loading remains.

Example time-domain simulations are given in Fig. 5.25 for voltage angle deviations $\Delta\delta$ and breaker closure at $t = 0$ s. A positive $\Delta\delta$ means that the microgrid voltage angle leads the external grid. If the microgrid angle lags by $-40°$, the torque of SM 2 becomes

[3] The presented synchronization studies were conducted by the author of this work.

Table 5.12.: Parameters of base scenario.

H	R'	X'	R/X	LL
$1.07\ s$	$0.161\ \Omega$/km	$0.19\ \Omega$/km	0.847	10 km

negative after an initial back swing in the positive direction. It reaches a minimum of about -4 pu and oscillates with fundamental frequency. When $\Delta\delta$ is $40°$, the torque reaches large positive values above 4 pu. Negative torques at breaker closure occur when the microgrid angle lags and the external grid provides active power to the microgrid and accelerates the rotors of the SM. On the other hand, positive torques at closure occur when the microgrid angle leads and the rotors are decelerated. The maximum loading (torque) occurs during the first swing after breaker closing. Therefore, the SM control does not affect the loading due to its large time constants.

The simulation of a PED is also depicted in Fig. 5.25. It becomes apparent that PED can handle voltage angular changes well and are not overloaded. Hence, it is focused on SM.

Fig. 5.26 compares the voltage deviations investigated in this work with the maximum admissible deviations according to the standard in [59] for the multi-MVA class. It is looked at deviations that go far beyond the standard constraints. In this way, the impact of faulty operation of the synchrocheck is examined. Moreover, the severity of violations of the guideline and their impact on component loadings is assessed [321].

The voltage of the external grid is kept constant at $v_{external} = 1$ pu as it is assumed that the impact of the microgrid on the external grid is minor. The SM in the microgrid are controlled to cause deviations in voltage angle $\Delta\delta$, amplitude Δv and frequency Δf. The following figures illustrate the maximum torques of the SM and maximum breaker currents of time-domain simulations for breaker closing with various deviations. Unless stated otherwise, the frequency deviation is 20 mH. A certain frequency deviation is necessary for the angle to vary and to allow for closing at a certain value. The 20 mH deviation was shown to have a minor impact on the loadings.

The parameters of the base scenario are given in Table 5.12. The parameters are varied to explore the impact of the inertia constant H, the line R/X (the absolute value of the line impedance remains constant) ratio and the line length LL.

5.11.1. Angle Deviation

The maximum torques of the two SM and breaker currents for angle deviations are depicted in Fig. 5.27. The amplitude deviation is zero and the frequency discrepancy is 20 mH.

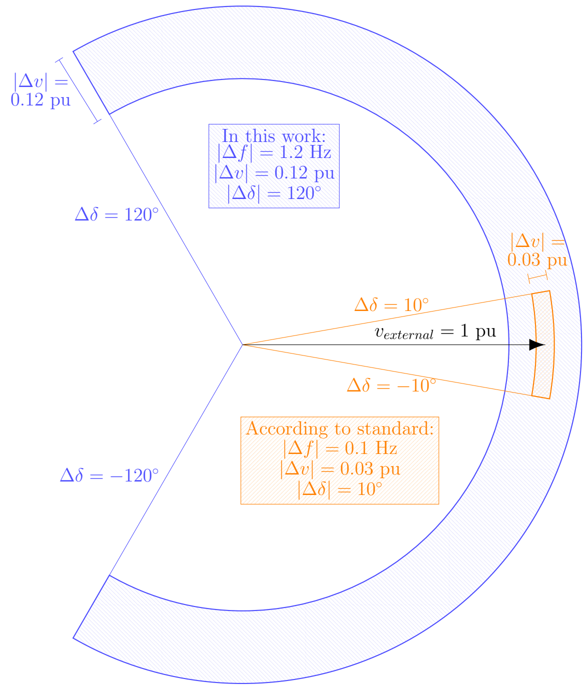

Figure 5.26.: Comparison of voltage deviations examined in this work and feasible deviations according to [59].

Torques reach high values and SM 1 is loaded heavier than SM 2, as SM 1 is closer to the breaker. The increase is especially steep towards larger $\Delta\delta$ (microgrid angle leads). The fact that the SM are slightly loaded before the closing contributes to this behaviour. The torque of SM 2 seems to reach a maximum at around $-90°$ and resembles a sine wave.

The impact of the inertia constant H is insignificant. A higher R/X-ratio compared to the base scenario slightly decreases the torque of SM 2 for negative angles. Increasing the line length leads to significantly lower loadings of SM 2.

The currents over the breaker increase almost linearly with positive and negative angle deviations and reach high levels (pu base of SM is used). Only the line length LL has a significant impact.

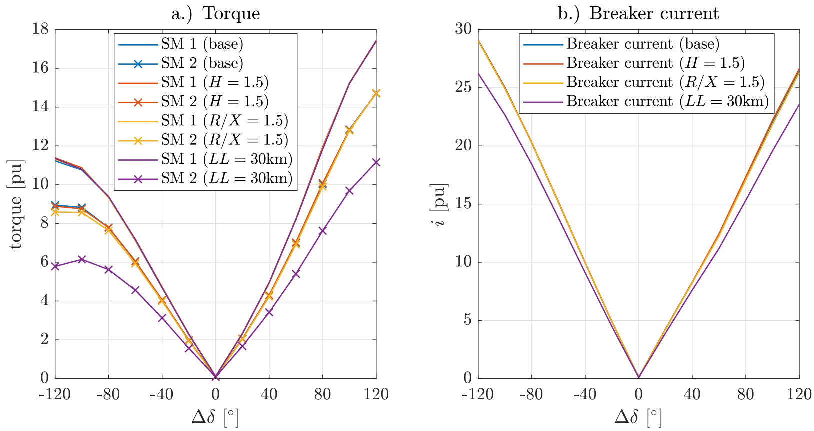

Figure 5.27.: Maximum torques and breaker currents for angle deviations.

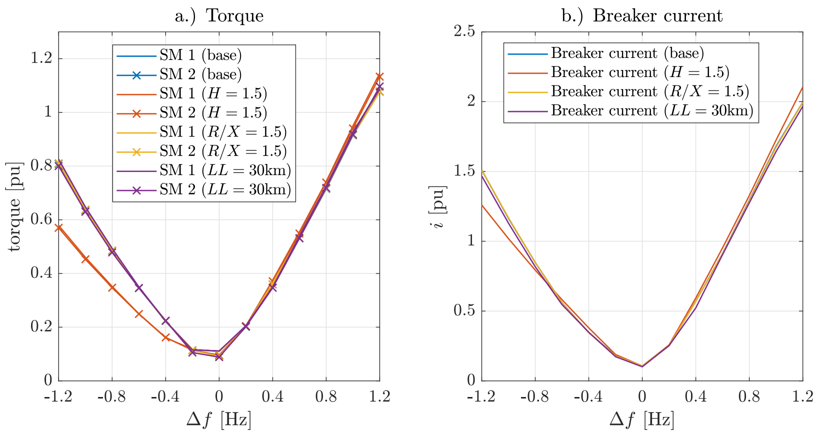

Figure 5.28.: Maximum torques and breaker currents for frequency deviations.

5.11.2. Frequency Deviation

The outcome for frequency deviations is given in Fig. 5.28. Both for torque and current, the loading has a parabolic shape. In comparison to angle deviations, the loadings are much lower. Differences between the torques of SM 1 and 2 are minor. Here, the inertia constant H has an impact. It decreases the loading for negative and increases the loading for positive frequency discrepancies.

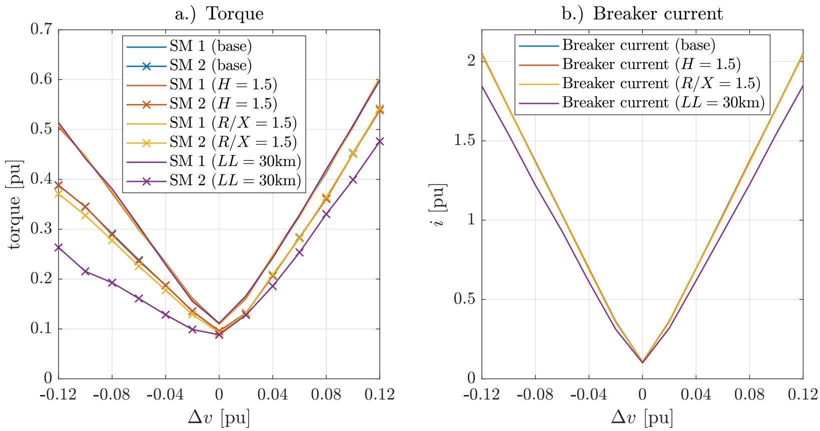

Figure 5.29.: Maximum torques and breaker currents for amplitude deviations.

5.11.3. Amplitude Deviation

The burden for amplitude deviations is shown in Fig. 5.29. The surge is rather linear to both sides here. The level of the torques are even lower than for frequency deviations, but the currents are larger. However, the burden is far less severe in comparison to angle deviations.

The burden of SM 1 is heavier. A higher R/X-ratio slightly decreases the torque of SM 2 for negative deviations. Longer lines lower the stresses for both positive and negative discrepancies.

5.11.4. Combination of Angle with Frequency/Amplitude Deviation

The previous sections show that the loadings of angle differences are by far and away the most severe. This section investigates the effect of combining the angle deviation with frequency or amplitude discrepancies. The combinations are selected to reinforce each other. For example, negative angles and negative frequencies both lead to a higher acceleration at breaker closing causing larger torques. Similarly, negative amplitudes should theoretically also accelerate the rotor because of an increased active power transmission from the bulk power system to the microgrid. The parameters of the base scenario are used.

It becomes apparent in Fig. 5.30 that the combination angle and frequency have a minor impact and that torques and currents are slightly higher for negative and a bit lower for positive values compared to the base scenario. The effect of combining angle with frequency deviations is more significant. However, it is unexpected that loadings are

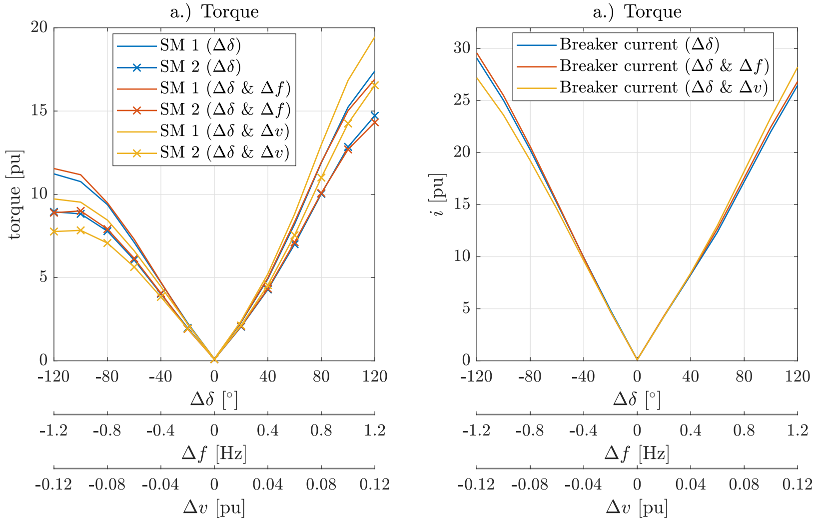

Figure 5.30.: Maximum torques and breaker currents for combinations angle with frequency/amplitude deviations.

lowered for negative voltage deviations. The explanation is that lower excitation of the SM and the decreased stator voltage decreases the overall power transmitted to the SM. This effect overcompensates the increased power transmission over the breaker due to the amplitude difference between microgrid and external grid at the moment the breaker closes.

5.11.5. Fast Synchronization

It is now looked at scenarios where the microgrid has either a frequency of -1 or 1 Hz. This may be the case when the microgrid needs to synchronize very quickly, e.g. due to looming instability. A large frequency difference with the external grid leads to a quicker alignment of the voltage angles. Another reason for the frequency deviations can be a mismatch of load and generation in a microgrid. The large frequency differences make it hard for the synchrocheck to close exactly at zero angle deviation. Hence, it is interesting to look at combinations of frequency and angle deviations around $\Delta\delta = 0°$. Furthermore, it may be possible to cancel out the loading due to frequency discrepancies with certain angle deviations.

The results for maximum occurring currents over the breaker are illustrated in Fig. 5.31. The burden of the SM is low for frequency deviations. It is more interesting to look at the currents over the breaker as they reflect the disturbances imposed on the external

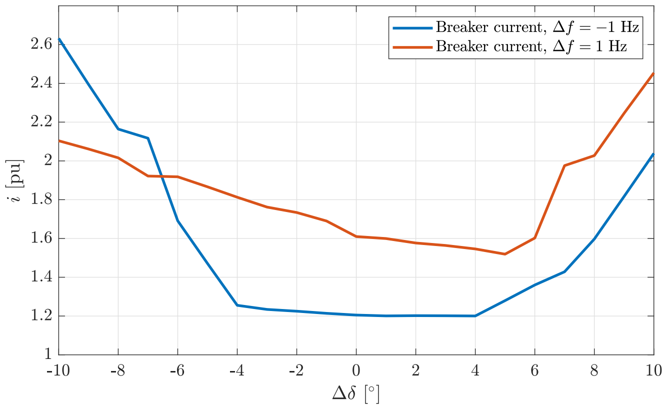

Figure 5.31.: Maximum currents for combinations of frequency deviations with small angle deviations.

grid. These are of importances for grid codes that may allow larger frequency deviations in future.

The lines can be separated in two parts. In the first part, the current loading is mainly affected by the frequency deviation and the curve is rather flat. This goes from $-4°$ to $4°$ for $\Delta f = -1$ Hz and from $0°$ to $5°$ for $\Delta f = 1$ Hz. Outside these ranges, the curves exhibit larger gradients which can be attributed to the impact of the angle deviations. For $\Delta f = 1$ Hz, the minimum is at $\Delta\delta = 5°$, which means that the combined deviations cancel each other out, because the current is lower than at $\Delta\delta = 5°$. However, this effect is hardly significant.

In conclusion, the impact of frequency deviations of $+/-1$ Hz on the external grid is moderate as long as the associated angle deviations are limited to the range mentioned above. The effectiveness of cancelling out the effects of frequency deviations with certain angle deviations is low.

6. Discussion

6.1. Summary and Conclusion

This work identifies the increased amount of PED as one of the key challenges of future power systems. Microgrids can be regarded as models for modern power systems due to the high share of PED. Their definition, benefits and current research aspects are described. A classification of the stability of microgrids is provided and compared to the stability of conventional power systems. The various time frames of dynamic phenomena in microgrids are detailed.

The main focus of this work is the small-signal stability of islanded microgrids. Modal analysis is identified as a suitable method to analyse the stability. Due to its systematic approach and flexibility, it is preferred over other methods, such as impedance or Lyapunov's direct method.

Furthermore, a classification of model order reduction techniques, including parameter optimizations, polynomial approximations and state truncations, is given. Singular perturbation theory is used extensively in conventional power systems and is also applied in this work.

The modelling of DER for microgrid stability studies is elaborated. Considered DER with a significant effect on microgrid stability are inverters, DFIG and diesel SM. Numerous control approaches for the power sharing are introduced with a special focus on droop control and its variants. SI methods for DFIG based on frequency gradient and PLL tuning are explicated. The LCL filter design as well as the tuning of inner control loops and PLL are detailed. Model-order reduction techniques are applied to the inner control loops of PED and a fifth order model for the grid-forming PED that preserves the dynamics of the voltage controller is proposed.

Besides DER, the modelling of the network lines plays a vital role in the efficient and yet accurate simulation of microgrids that is necessary for population based heuristic optimization. These criteria are satisfied by the modelling in the $dq0$ reference frame. The network differential equations can also be approximate by a first-order Taylor expansion or they are fully neglected in the phasor model. Only balanced grids are regarded.

A suitable optimization algorithm is required for the simultaneous optimization of a large set of DER controller parameters. Due to the intricacy of the optimization problem and the fact that a strictly mathematical formulation is impossible, EA is selected. The basic genetic operators are introduced. The computationally demanding fitness function necessitates the design of an efficient EA, that reaches the optimum within a limited amount of fitness evaluations. A BSP tree is at the core of the EA, impeding the repeated evaluation of similar individuals and paving the way for the assessment of the diversity of individuals. Benchmark functions are used to efficiently parametrize the EA. The framework that links the EA, the scenario simulation and results analysis, and forms the basis of the controller parameter optimizations of this work, is introduced.

The chapter on case studies starts with the validation of the network and SM models used in this work by comparison of time-domain simulations to Simulink's Simscape power systems toolbox, which features EMT simulation. The outcome is similar for PED dominated microgrids, whereas there is a small discrepancy in the SM models, which is attributable to the implementation of the Simulink SM model that is not exactly known.

Next, the EA developed in this work is evaluated by comparing its performance to a conventional EA. The proposed EA is found to perform considerably better than the conventional EA, especially when the number of fitness evaluations is low. For the most complex benchmark function, the conventional EA does not outperform the proposed EA, even if the number of fitness evaluations is ten times larger, because the conventional EA easily remains stuck in local optima. The proposed EA prevents this by promoting the diversity in the population. The superiority of the proposed EA is also demonstrated for a highly constrained DER controller optimization problem.

A thorough parameter sensitivity analysis for PED based on optimized parameter sets is conducted, incorporating parameters that have so far not been considered in literature on microgrid small-signal stability. Parameters that are attributable to control system stability as well as power supply and balance stability, according to the classification of the IEEE Task Force on microgrid stability, are included.

Regarding grid-forming droop controlled PED, the strong impact of the feed-forward gain of the voltage controller, the measurement filter cut-off frequency and the virtual resistor is notable, whereas the influence of the voltage droop coefficient is minor. This shows that the inner loop tuning affects the dominant modes and highlights the importance of implementing the VI. Moreover, it allows some degree of freedom in the selection of the voltage droop coefficient, i.e. to tune it with regard to steady-state power sharing, for example. The tuning of the PLL has by far the greatest effect on the stability of grid-supporting PED.

On the basis of the sensitivity analysis, the simultaneous optimization of a large set of relevant PED controller parameters, including voltage controller parameters and the measurement filter cut-off frequency, is performed for a small microgrid with two nodes. It becomes apparent that the optimized system is very stable, especially when only grid-forming PED are present. This corroborates the increased level of stability of such systems, when the controller parameters a thoroughly optimized. A high measurement filter cut-off frequency is preferable for grid-forming PED. The influence of the R/X ratio of the lines is minor in general.

Next, benchmark scenarios are developed to analyse the controller parameters under various conditions. The R/X ratio and the line length are varied in the small two-node microgrid. Furthermore, SM may be present or not and their parameters are also optimized in the former case. To limit the complexity of the optimization, the voltage controller parameters and the measurement filter cut-off frequency are fixed. Only grid-forming control is regarded and the performance of several droop variants is compared.

It is again shown that microgrids with grid-forming PED and thoroughly optimized parameter sets are very stable and are able to rapidly share the load after transients, which confirms the scientific statement from Sec. 1.4. The larger time constants of SM shift the dominant eigenvalues towards the unstable region, but the damping still remains acceptable. The difference in the outcome for different droop variants is rather small. The FTD has some advantages due to its flexibility and can be adjusted depending on the presence of SM. The FTD also enhances the performance of SM. However, it is confirmed that the presence and optimized tuning of the VI is critical for stability, whereas the impact of the choice of the droop variant is comparatively low. Hence, analysis of microgrid stability in any context, for example network reconfiguration [45] or placement of PED [288], should always be based on a well-designed and optimized controller with VI to get meaningful results.

The subsequent case study considers the Cigre benchmark LV microgrid with 38 nodes. Worst case scenarios regarding the outage of the largest load or PV plant are analysed. Four DER are optimized. Besides the controller parameters, also the placement of the SM is incorporated in the optimization.

The larger number of DER deteriorates the stability, although modes are still well inside the left half plane. It becomes apparent that the parameters found in the previous benchmark optimization of the small microgrid cannot simply be transferred to the larger system. In particular, the share of SM among the DER has a strong impact. The AVR and GOV can be tuned much more aggressively for a low share of SM. On the other hand, the parameters from the small benchmark microgrid do not violate any voltage, frequency or power sharing constraints in the larger network.

A drawback of the modal analysis used in this work is that it guarantees only local stability. However, the very stable nature of the investigated PED dominated systems, with eigenvalues deep inside the left half plane, suggests that such systems are generally stable also for further operating points, assuming that a thorough controller design and parameter optimization is conducted.

The optimized parameter sets are used to evaluate the validity of model order reduction approaches under realistic conditions. The approximation of LV lines with phasor models or by a first order Taylor expansion is generally valid due to the high R/X ratio and the low time constants. The simplification of the current controller leads to acceptable deviations, whereas entirely neglecting the inner loops, as often seen for grid-forming controllers in literature, is an oversimplification, because eigenvalues are sensitive to the voltage controller tuning. On the other hand, the proposed fifth order model preserves the dynamics of the voltage controller and well approximates the original model, corroborating the scientific statement from Sec. 1.4. Regarding the grid-supporting control, a simple current source model is still a good approximation. This corroborates that the dynamics predominantly depend on the PLL tuning.

The tuning of SI methods for DFIG is optimized in the subsequent study case. The DFIG is either combined with a PED or a SM in a small MV microgrid. It is shown that the impact of the choice of the SI methods on the frequency drop after load changes is minor when the microgrid is dominated by PED. When a SM is present, the influence of SI is more pronounced. The slow PLL and df/dt control perform rather similar and the combination leads to a significant decrease of the nadir.

Finally, the inaccurate synchronization of the microgrid with the bulk power system and its impact on the loading of microgrid components is studied. The most severe stress is attributed to voltage angle deviations, which causes much higher SM torques and breaker currents than frequency or magnitude discrepancies. The line length has a significant impact on loadings, whereas the inertia constant and the R/X ratio do not. Combined angle and magnitude or frequency deviations can slightly increase the burden compared to pure angle discrepancies in some cases. The results suggest that frequency and magnitude deviation constraints may be eased in future grid codes due to the relatively low burden in comparison to angle deviations.

In conclusion, the scientific statement from Sec. 1.4 which states the high degree of stability of microgrids dominated by PED when controller parameters are thoroughly optimized is underpinned by the results. The validity of the proposed model order reduction of grid-forming converters, which preserves the dynamics of the voltage controller, is proven.

6.2. Outlook

PED and SM have a strong impact on the microgrid stability. However, there are further components that should be incorporated in the stability analysis. One example are induction motors which account for 23% of the load in MV systems and can cause lightly damped oscillations in microgrids with droop controlled PED [272]. A composite load model with induction machines in the dq reference frame was recently developed in [274]. Several pairs of low- and medium-frequency eigenvalues are introduced when considering composite loads.

Another natural extension is the incorporation of DFIG models in the dq frame instead of using Simulink's built in model. This will allow for a closer analysis of the dominant modes in systems with DFIG. Moreover, the stability of the df/dt SI control must be further investigated. A number of issues of this type of control are mentioned in [17], also regarding problems with the voltage support. Moreover, the PLL modelling and type selection [157] should be investigated further and harmonics are to be incorporated in the stability assessment.

It is shown in this thesis that the measurement filter time constant of grid-forming droop controlled inverters has a strong impact on dominant modes. The selection of proper higher order filters for the handling of harmonics, while implementing low time constants, is an important task for future research.

The stability is evaluated on the basis of worst case scenarios in this work. However, given that modal analysis only ensures local stability and that manifold scenarios are possible, stochastic approaches are worth considering. Probabilistic approaches based on fluctuating wind and PV generation are proposed in [315, 322]. Markov chains and Markov jump linear systems are used to optimized a MV feeder in [284]. An interesting method to analytically determine the stability of linear systems subject to parameter variation is presented in [323] using a bilateral sum matrix approach.

The focus is placed on the dominant modes in this work. Future analysis should incorporate harmonics and unbalance as part of the optimized parameter tuning. The modelling in the $dq0$ reference frame should be extended with the dynamic phasor approach [324, 325, 326]. Moreover, modal analysis can be complemented with impedance based approaches [110].

Besides small-signal stability, transient events and short-circuits should also be considered in the controller design [29]. It is shown in [327] that the frequency droop coefficient also affects the transient stability. Hence, transient criteria are to be included in its optimization. In addition, aspects of secondary control should be considered in the model [328]. This is another step towards the practical realization of a microgrid.

It is shown in this work that the share of SM in a microgrid strongly affects the stability and the optimized parameter tuning. This should be considered for the implementation of further benchmark scenarios, besides the incorporation of additional models, such as induction machines, as mentioned. To allow for the comparableness of DER controllers, agreed benchmark scenarios should be established in the research community and used in publications. This would entail better understanding of the feasibility of proposed controllers and ease the identification of advantages and shortcomings. Ideally, publications should be accompanied by the provision of the data and models used, as implementing models on the basis of the written papers is a laborious and error-prone task. Similar approaches to establish standardized benchmarking exist for static and quasi-dynamic optimization of power systems [329].

This leads to the question which software should be used to model and simulate the benchmark scenarios for PED dominated power systems. The software should be open source and available for everyone. Simulink is used in this work and is popular in academic research due to free research licensing. It is a software for graphical programming and is often scripted with Matlab. Matlab is an old programming language and reaches its limits for projects with increased complexity, as experienced in the course of this work.

A very promising and fully open source candidate for future research on power systems is the Julia programming language [330], which has gained a lot of popularity lately. It was designed to have machine performance without sacrificing human convenience, or, in other words, to combine the performance of C++ with the convenience of Python. It is a general purpose language, but these characteristics make it particularly popular in numerical computing and a feature-rich ecosystem for the modelling, simulation and stability analysis of dynamic systems [331] has been developed by a quickly growing community in recent years, including a very wide range of solvers. Open source toolboxes for the simulation of low inertia power systems in the $dq0$ frame are already available [332]. Furthermore, the fully code-based modelling approach has advantages over graphical programming as it eases development processes, such as test-driven development, which enhances the productivity and reliability of models, especially with growing complexity.

Besides modelling and simulation, the optimization algorithm in this work also has room for improvements. The constraints violation handling is not yet efficient as it clearly distinguishes between individuals with or without violations and always assigns worse fitness to the former. This hampers the search in the area around the boarder to infeasible solutions. A more advanced approach would be to assign weighting factors to the constraints which are adjusted according to the incidence of violations in the population. In simple terms, this would mean that if the frequency of violations in the population is low or decreasing, the weighting factors of violations are also decreased, meaning that their effect on the fitness becomes smaller. In contrast, if there are to many violations and the EA is in danger of getting stuck in infeasible areas, the weighting of violations in increased.

Another aspect of the EA that can be enhanced is the parameter tuning. This is a difficult task as parameters are numerous and depend on one another. The selection of a certain parameter can introduce new parameters that need to be optimized (e.g. the selection of a certain crossover operator introduces new parameters for the tuning of this specific crossover). It is, therefore, hard to write an optimization algorithm to automate the tuning of the EA. In future, an optimization algorithm that can handle such a large number of parameters and their dependencies is required.

The mutation with GAS has not led to the expected improvement. A reason could be that the GAS leads the algorithm directly to a local optimum and aggravates the diversity, which must be further investigated.

This thesis analyses the small-signal stability of islanded microgrids. However, a number of aspects pertaining to the modelling and tuning of DER controllers are generally transferable to low inertia bulk power systems. The author hopes that a tiny contribution to the imminent challenge of drastically increasing the share of DER in power systems and the reduction of CO_2 emissions was made.

A. Composite Microgrid Model Example

A.1. Inverter

At first the model of an inverter in his individual $dq0$ reference frame is derived. The low-pass filtered active and reactive power are expressed as

$$p_{LPF} = \frac{\omega_c}{s+\omega_c}(v_{c,d}i_{L2,d} + v_{c,q}i_{L2,q}), \tag{A.1}$$

$$q_{LPF} = \frac{\omega_c}{s+\omega_c}(i_{L2,q} - v_{c,q}i_{L2,d}). \tag{A.2}$$

This leads to the small-signal dynamic model:

$$\Delta\dot{p}_{LPF} = -\omega_c\Delta p_{LPF} + \omega_c(i_{L2,d,0}\Delta v_c, d + i_{L2,q,0}\Delta v_{c,q} + v_{c,d,0}\Delta i_{L2,d} + v_{c,q,0}\Delta i_{L2,q}), \tag{A.3}$$

$$\Delta\dot{q}_{LPF} = -\omega_c\Delta q_{LPF} + \omega_c(i_{L2,q,0}\Delta v_c, d - i_{c,d,0}\Delta v_{c,q} - v_{c,q}\Delta i_{L2,d} + v_{c,q,0}\Delta i_{L2,q}) \tag{A.4}$$

From the droop equations (3.35) and (3.36), it follows that

$$\omega_{Droop} = \omega_0 - m_\omega(p_{LPF} - p_0) \tag{A.5}$$

$$v^*_{c,d} = v_0 - m_q(q_{LPF} - q_0) \tag{A.6}$$

$$v^*_{c,q} = 0. \tag{A.7}$$

Hence, the linearized small-signal models of the frequency and voltage in the two axes are

$$\Delta\omega_{Droop} = -m_\omega\Delta p_{LPF} \tag{A.8}$$

$$\Delta v^*_{c,d} = -m_q\Delta q_{LPF} \tag{A.9}$$

$$\Delta v^*_{c,q} = 0. \tag{A.10}$$

To convert the output of the inverter model to a common reference frame that rotates with ω_{ref}, the angle between the dq frame and the common DQ frame is defined as

$$\theta_{diff} = \int(\omega_{Droop} - \omega_{ref})dt. \tag{A.11}$$

The small signal model can then be derived as

$$\Delta\dot{\theta}_{diff} = \Delta\omega_{Droop} - \Delta\omega_{ref} = -m_\omega \Delta p_{LPF} - \Delta\omega_{ref}. \tag{A.12}$$

The voltage controller shown in Fig. 3.14 is described by the following state equations:

$$\dot{\nu_d} = v^*_{c,d} - v_{c,d}, \tag{A.13}$$

$$\dot{\nu_q} = v^*_{c,q} - v_{c,q}, \tag{A.14}$$

and the algebraic equations

$$i^*_{L1,d} = k_{i,v}\nu_d + k_{p,v}(v^*_{c,d} - v_{c,d}) - \omega_n C_f v_{c,q} + FF_v i_{L2,d}, \tag{A.15}$$

$$i^*_{L1,q} = k_{i,v}\nu_q + k_{p,v}(v^*_{c,q} - v_{c,q}) - \omega_n C_f v_{c,d} + FF_v i_{L2,q}. \tag{A.16}$$

The small-signal model of the voltage controller can then be formulated:

$$\Delta\dot{\nu_d} = \Delta v^*_{c,d} - \Delta v_{c,d}, \tag{A.17}$$

$$\Delta\dot{\nu_q} = \Delta v^*_{c,q} - \Delta v_{c,q}, \tag{A.18}$$

$$\Delta i_{L1,d}* = k_{i,v}\Delta\nu_d + k_{p,v}(\Delta v^*_{c,d} - \Delta v_{c,d}) - \omega_n C_f \Delta v_{c,q} + FF_v \Delta i_{L2,d}, \tag{A.19}$$

$$\Delta i_{L1,q}* = k_{i,v}\Delta\nu_q + k_{p,v}(\Delta v^*_{c,q} - \Delta v_{c,q}) - \omega_n C_f \Delta v_{c,d} + FF_v \Delta i_{L2,q}. \tag{A.20}$$

The linearized small-signal model for the current controller is similar to the voltage controller:

$$\Delta\dot{\varsigma_d} = \Delta i^*_{L1,d} - \Delta i_{L1,d}, \tag{A.21}$$

$$\Delta\dot{\varsigma_q} = \Delta i^*_{L1,q} - \Delta i_{L1,q}, \tag{A.22}$$

$$\Delta v^*_{i,d} = k_{i,c}\Delta\varsigma_d + k_{p,c}(\Delta i^*_{L1,d} - \Delta i_{L1,d}) - \omega_n L_1 \Delta v_{L1,q}, \tag{A.23}$$

$$\Delta v^*_{i,q} = k_{i,c}\Delta\varsigma_q + k_{p,c}(\Delta i^*_{L1,q} - \Delta i_{L1,q}) - \omega_n L_1 \Delta i_{L1,d}. \tag{A.24}$$

Finally, the linearized model of the LCL-filter is derived. The current of the inverter-side inductor is expressed as:

$$\Delta\dot{i}_{L1,d} = \frac{R_1}{L_1}\Delta i_{L1,d} + \omega_n \Delta i_{L1,q} - \frac{1}{L_1}\Delta v_{c,d} + \frac{1}{L_1}\Delta v_{i,d}, \tag{A.25}$$

$$\Delta\dot{i}_{L1,q} = -\frac{R_1}{L_1}\Delta i_{L1,q} - \omega_n \Delta i_{L1,d} - \frac{1}{L_1}\Delta v_{c,q} + \frac{1}{L_1}\Delta v_{i,q}. \tag{A.26}$$

The voltage of the filter capacitor is expressed as

$$\Delta \dot{v}_{c,d} = \frac{1}{C_f}\Delta i_{L1,d} + \omega_n \Delta v_{c,q} - \frac{1}{C_f}\Delta i_{L2,d}, \tag{A.27}$$

$$\Delta \dot{v}_{c,q} = \frac{1}{C_f}\Delta i_{L1,q} - \omega_n \Delta v_{c,d} - \frac{1}{C_f}\Delta i_{L2,q}. \tag{A.28}$$

The current of the grid-side inductor is defined as

$$\Delta \dot{i}_{L2,d} = \frac{1}{L_2}\Delta u_{c,d} - \frac{R_2}{L_2}\Delta i_{L2,d} + \omega_n \Delta i_{L2,q} - \frac{1}{L_2}\Delta v_{g,d}, \tag{A.29}$$

$$\Delta \dot{i}_{L2,q} = \frac{1}{L_2}\Delta u_{c,q} - \frac{R_2}{L_2}\Delta i_{L2,q} - \omega_n \Delta i_{L2,d} - \frac{1}{L_2}\Delta v_{g,q}. \tag{A.30}$$

The output variables $i_{L2,dq}$ and input variables have to be transformed to the respective reference frame using the transformation matrix from (3.8):

$$i_{L2,DQ} = K_a i_{L2,dq} = \begin{bmatrix} cos(\theta_{diff}) & -sin(\theta_{diff}) \\ sin(\theta_{diff}) & cos(\theta_{diff}) \end{bmatrix} i_{L2,dq}. \tag{A.31}$$

$$v_{g,dq} = K_a^{-1} v_{g,DQ} = \begin{bmatrix} cos(\theta_{diff}) & sin(\theta_{diff}) \\ -sin(\theta_{diff}) & cos(\theta_{diff}) \end{bmatrix} v_{g,DQ}. \tag{A.32}$$

The transformations are linearized as follows:

$$\Delta i_{L2,DQ} = K_{a,0}\Delta i_{L2,dq} + \begin{bmatrix} -i_{L2,d,0}sin(\theta_{diff,0}) - i_{L2,q,0}cos(\theta_{diff,0}) \\ i_{L2,d,0}cos(\theta_{diff,0}) - i_{L2,q,0}sin(\theta_{diff,0}) \end{bmatrix} \Delta\theta_{diff} \tag{A.33}$$

$$\Delta v_{g,dq} = K_{a,0}^{-1}\Delta v_{g,DQ} + \begin{bmatrix} -v_{g,D,0}sin(\theta_{diff,0}) + v_{g,Q,0}cos(\theta_{diff,0}) \\ -v_{g,D,0}cos(\theta_{diff,0}) - v_{g,Q,0}sin(\theta_{diff,0}) \end{bmatrix} \Delta\theta_{diff}, \tag{A.34}$$

where

$$K_{a,0} = \begin{bmatrix} cos(\theta_{diff,0}) & -sin(\theta_{diff,0}) \\ sin(\theta_{diff,0}) & cos(\theta_{diff,0}) \end{bmatrix} \tag{A.35}$$

and

$$K_{a,0}^{-1} = \begin{bmatrix} cos(\theta_{diff,0}) & sin(\theta_{diff,0}) \\ -sin(\theta_{diff,0}) & cos(\theta_{diff,0}) \end{bmatrix}. \tag{A.36}$$

The subscript $_0$ marks the equilibrium point.

(A.3) - (A.34) are combined to obtain the complete 13th order small-signal state-space model of a single grid-forming droop controlled inverter:

$$\Delta \dot{x}_{inv,i} = A_{inv,i}\Delta x_{inv,i} + B_{inv,i}\Delta v_{g,DQ} + B_{\omega com,i}\Delta\omega_{com}, \tag{A.37}$$

$$\begin{bmatrix} \Delta\omega_i \\ \Delta i_{g,DQ,i} \end{bmatrix} = \begin{bmatrix} C_{inv,\omega,i} \\ C_{inv,c,i} \end{bmatrix} \Delta x_{inv,i}, \tag{A.38}$$

where $\Delta x_i nv, i = [\Delta\theta_{diff,i} \quad \Delta p_{LPF,i} \quad \Delta q_{LPF,i} \quad \Delta\nu_{d,i} \quad \Delta\nu_{q,i} \quad \Delta\varsigma_{d,i} \quad \Delta\varsigma_{q,i} \quad \Delta i_{L1,d,i} \quad \Delta i_{L1,}$ $\Delta v_{c,d,i} \quad \Delta v_{c,q,i} \quad \Delta i_{L2,d,i} \quad \Delta i_{L2,q,i}]$ and the matrices $A_{inv,i}$, $B_{inv,i}$, $B_{\omega com,i}$, $C_{inv,\omega,i}$ and $C_{inv,c,i}$ are given in the Appendix B. Using the model of one individual inverter, the small-signal model of the two parallel inverters in the microgrid can be derived as

$$\Delta \dot{x}_{inv} = A_{inv}\Delta x_{inv} + B_{inv}\Delta v_{g,DQ}, \tag{A.39}$$

$$\Delta i_{g,DQ} = C_{inv,c}\Delta x_{inv}, \tag{A.40}$$

where $\Delta x_{inv} = \begin{bmatrix} \Delta x_{inv,1} & \Delta x_{inv,1} \end{bmatrix}^T$; $\Delta v_{g,DQ} = \begin{bmatrix} \Delta v_{g,DQ,1} & \Delta v_{g,DQ,2} \end{bmatrix}^T$;

$$A_{inv} = \begin{bmatrix} A_{inv,1} + B_{\omega com,1}C_{inv,\omega,1} & 0 \\ 0 & A_{inv,2} + B_{\omega com,2}C_{inv,\omega,2} \end{bmatrix};$$

$$B_{inv} = \begin{bmatrix} B_{inv,1} & 0 \\ 0 & B_{inv,2} \end{bmatrix}; \quad C_{inv,c} = \begin{bmatrix} C_{inv,c,1} & 0 \\ 0 & C_{inv,c,2} \end{bmatrix};$$

A.2. Network and Load Model

The microgrid lines are modelled as simple RL passive elements, which is an accurate approximation for LV microgrids [76]. The loads are also represented with a simple linear RL model. Similar to the LCL-filter linearization, the network and load equations in the DQ frame can then be expressed as:

$$\Delta \dot{i}_{line,DQ} = A_{net}\Delta i_{line,DQ} + B_{net}\Delta v_{g,DQ}, \tag{A.41}$$

$$\Delta \dot{i}_{load,DQ} = A_{load}\Delta i_{load,DQ} + B_{load}\Delta v_{g,DQ}, \tag{A.42}$$

where

$$A_{net} = \begin{bmatrix} -\frac{R_{line,1}}{L_{line,1}} & \omega_n & 0 & 0 \\ -\omega_n & -\frac{R_{line,1}}{L_{line,1}} & 0 & 0 \\ 0 & 0 & -\frac{R_{line,2}}{L_{line,2}} & \omega_n \\ 0 & 0 & -\omega_n & -\frac{R_{line,2}}{L_{line,2}} \end{bmatrix}; \tag{A.43}$$

$$B_{net} = \begin{bmatrix} \frac{1}{L_{line,1}} & 0 & -\frac{1}{L_{line,1}} & 0 & 0 & 0 \\ 0 & \frac{1}{L_{line,1}} & 0 & -\frac{1}{L_{line,1}} & 0 & 0 \\ 0 & 0 & \frac{1}{L_{line,2}} & 0 & -\frac{1}{L_{line,2}} & 0 \\ 0 & 0 & 0 & \frac{1}{L_{line,2}} & 0 & -\frac{1}{L_{line,2}} \end{bmatrix}. \tag{A.44}$$

$[i_{Line,DQ}]_{4\times1}$ is the vector of the line currents and $[v_{g,DQ}]_{6\times1}$ is the vector of the network node voltages. Note that in contrast to [76], the frequency $\omega = \omega_n$ is assumed constant.

As the coefficient matrix of the load model is very similar to the network model, it is refrained from showing it here.

A.3. Complete Microgrid Model

A large resistor r_N is set between each node and ground to establish a well defined voltage [76]. The small-signal model of the nodes then becomes:

$$\Delta v_{g,DQ} = R_N(M_{inv}\Delta i_{g,DQ} + M_{load}\Delta i_{load,DQ} + M_{net}\Delta i_{Line,DQ}), \tag{A.45}$$

where the matrice M_{inv} maps the DER coupling points to the network nodes, M_{load} maps load coupling points to the network nodes and M_{net} maps the lines to the network nodes. Given the topology of the microrid in Fig. 3.35, if $y = 2$ is the number of DER, $k = 2$ is the number of lines, $x = 3$ is the number of loads and $z = 3$ is the number of nodes, the matrices are:

$$R_N = \begin{bmatrix} r_N & & \\ & \ddots & \\ & & r_N \end{bmatrix}_{2z\times2z}; M_{inv} = \begin{bmatrix} 1 & 0 & 0 & 0 \\ 0 & 1 & 0 & 0 \\ 0 & 0 & 0 & 0 \\ 0 & 0 & 0 & 0 \\ 0 & 0 & 1 & 0 \\ 0 & 0 & 0 & 1 \end{bmatrix}_{2z\times2y}; R_N = \begin{bmatrix} -1 & & \\ & \ddots & \\ & & -1 \end{bmatrix}_{2z\times2x};$$

$$M_{net} = \begin{bmatrix} -1 & 0 & 0 & 0 \\ 0 & -1 & 0 & 0 \\ 1 & 0 & -1 & 0 \\ 0 & 1 & 0 & -1 \\ 0 & 0 & 1 & 0 \\ 0 & 0 & 0 & 1 \end{bmatrix}_{2z\times2k}.$$

This leads to the complete 36 order $(2k + 2x + 13y)$ small-signal model:

$$\begin{bmatrix} \Delta \dot{x}_{inv} \\ \Delta \dot{i}_{line,DQ} \\ \Delta \dot{i}_{load,DQ} \end{bmatrix} = A_{sys} \begin{bmatrix} \Delta x_{inv} \\ \Delta i_{line,DQ} \\ \Delta i_{load,DQ} \end{bmatrix}, \tag{A.46}$$

where

$$A_{sys} = \begin{bmatrix} A_{inv} + B_{inv} R_N M_{inv} C_{inv,c} & B_{inv} R_N M_{net} & B_{inv} R_N M_{load} \\ B_{net} R_N M_{inv} C_{inv,c} & A_{net} + B_{net} R_N M_{net} & B_{net} R_N M_{load} \\ B_{load} R_N M_{inv} C_{inv,c} & B_{load} R_N M_{net} & A_{load} B_{load} R_N M_{load} \end{bmatrix}.$$

It is seen that the linearized state-space model becomes complex and error-prone even for a small microgrid. The intricacy increases for larger microgrids with various types of DER. Therefore, it is advisable to resort to appropriate software that linearizes the model and automatically forms the state-space representation. In this work, the Simulink Control Design Toolbox is used for this purpose. To build the network state space model in the $dq0$ reference frame, it is made use of the open source software introduced in [145].

B. State-Space Model of Grid-Forming Droop Controlled Inverter

$$
Ainv,i =
\left[\begin{array}{ccccccccccccc}
0 & -m_{\omega} & 0 & 0 & 0 & 0 & 0 & 0 & 0 & 0 & 0 & 0 & 0 \\
0 & -\omega_c & 0 & 0 & 0 & 0 & 0 & 0 & 0 & \omega_c i_{L2,d,0} & \omega_c i_{L2,q,0} & \omega_c v_{c,d,0} & \omega_c v_{c,q,0} \\
0 & 0 & -\omega_c & 0 & 0 & 0 & 0 & 0 & 0 & \omega_c i_{L2,q,0} & -\omega_c i_{L2,d,0} & -\omega_c v_{c,q,0} & \omega_c v_{c,d,0} \\
0 & 0 & -m_q & 0 & 0 & 0 & 0 & 0 & 0 & -1 & 0 & 0 & 0 \\
0 & 0 & 0 & 0 & 0 & 0 & 0 & 0 & 0 & 0 & -1 & 0 & 0 \\
0 & 0 & -m_q k_{p,v} & k_{i,v} & 0 & 0 & 0 & -1 & 0 & -k_{p,v} & -\omega_n C_f & FF_v & 0 \\
0 & 0 & 0 & 0 & k_{i,v} & 0 & 0 & 0 & -1 & \omega_n C_f & -k_{p,v} & 0 & FF_v \\
0 & -m_{\omega} i_{L1,q,0} & \frac{-m_q k_{p,v} k_{p,c}}{L_1} & \frac{k_{i,v} k_{p,c}}{L_1} & 0 & \frac{k_{i,c}}{L_1} & 0 & \frac{-k_{p,c}-R_f}{L_1} & \omega_0 - \omega_n & \frac{-k_{p,v} k_{p,c}-1}{L_1} & -\frac{\omega_n C_f k_{p,c}}{L_1} & \frac{k_{p,c} FF_v}{L_1} & 0 \\
0 & m_{\omega} i_{L1,d,0} & 0 & 0 & \frac{k_{i,v} k_{p,c}}{L_1} & 0 & \frac{k_{i,c}}{L_f} & \omega_n - \omega_0 & \frac{-k_{p,c}-R_f}{L_1} & \frac{\omega_n C_f k_{p,c}}{L_1} & \frac{-k_{p,u} k_{p,c}-1}{L_1} & 0 & \frac{k_{p,c} FF_v}{L_1} \\
0 & -m_{\omega} v_{c,q,0} & 0 & 0 & 0 & 0 & 0 & \frac{1}{C_f} & 0 & 0 & \omega_0 & -\frac{1}{C_f} & 0 \\
0 & m_{\omega} v_{c,d,0} & 0 & 0 & 0 & 0 & 0 & 0 & \frac{1}{C_f} & -\omega_0 & 0 & 0 & -\frac{1}{C_f} \\
\frac{v_{g,D,0} sin(\alpha_0) - v_{g,Q,0} cos(\alpha_0)}{L_2} & -m_{\omega} i_{L2,q,0} & 0 & 0 & 0 & 0 & 0 & 0 & 0 & \frac{1}{L_2} & 0 & -\frac{R_2}{L_2} & \omega_0 \\
\frac{v_{g,D,0} cos(\alpha_0) - v_{g,Q,0} sin(\alpha_0)}{L_2} & m_{\omega} i_{L2,d,0} & 0 & 0 & 0 & 0 & 0 & 0 & 0 & 0 & \frac{1}{L_2} & -\omega_0 & -\frac{R_2}{L_2}
\end{array}\right]; \quad \text{(B.1)}
$$

$$B_{inv,i} = \begin{bmatrix} 0 & \cdots & 0 & -\frac{cos(alpha_0)}{L_2} & -\frac{sin(\alpha_0)}{L_2} \\ 0 & \cdots & 0 & \frac{sin(alpha_0)}{L_2} & -\frac{cos(\alpha_0)}{L_2} \end{bmatrix}^T_{2\times 13} ; B_{\omega com,i} = \begin{bmatrix} -1 & 0 & 0 & \dots & 0 \end{bmatrix}^T_{1\times 13};$$

$$C_{inv,\omega,i} = \begin{cases} \begin{bmatrix} 0 & -m_\omega & 0 & \cdots & 0 \end{bmatrix}_{1\times 13} & i = 1 \\ \begin{bmatrix} 0 & \cdots & 0 \end{bmatrix}_{1\times 13} & i \neq 1 \end{cases} \quad C_{inv,c,i} = \begin{bmatrix} -i_{L2,d,0}sin(\alpha_0) - i_{L2,q,0}cos(\alpha_0) & 0 & \cdots & 0 & cos(\alpha_0) & -sin(\alpha_0) \\ i_{L2,d,0}cos(\alpha_0) - i_{L2,q,0}sin(\alpha_0) & 0 & \cdots & 0 & sin(\alpha_0) & -cos(\alpha_0) \end{bmatrix}^T_{2\times 13};$$

C. Cigre Benchmark Microgrid Data

Lines:

All lines between node 1 and 10: $R' = 0.162\ \Omega/km$, $X' = 0.0832\ \Omega/km$.

Lines $3-11, 4-12, 12-13, 13-14, 14-15, 6-16, 9-17, 10-18$: $R' = 0.822\ \Omega/km$, $X' = 0.0847\ \Omega/km$.

Line $1-19$: $R' = 0.2647\ \Omega/km$, $X' = 0.2847\ \Omega/km$.

Line $1-20$ and all lines between node 20 and 27: $R' = 0.4917\ \Omega/km$, $X' = 0.2847\ \Omega/km$.

Lines $21-28, 28-29, 23-33, 33-34$: $R' = 1.3207\ \Omega/km$, $X' = 0.321\ \Omega/km$.

Lines $29-30, 28-31, 29-32, 33-35, 34-36, 26-37, 27-38$: $R' = 2.0167\ \Omega/km$, $X' = 0.3343\ \Omega/km$.

Lines $23-33, 33-34$: $R' = 1.3207\ \Omega/km$, $X' = 0.321\ \Omega/km$.

PV:

Power factor = 0.95 (ind.), use factor 1.5 for high PV case. $S_{n,PV1} = 33$ kVA, $S_{n,PV2} = 18$ kVA, $S_{n,PV3} = 6$ kVA, $S_{n,PV4} = 9$ kVA, $S_{n,PV5} = 6$ kVA, $S_{n,PV6} = 18$ kVA.

Loads:

Power factor = 0.95 (ind.), use factor 0.5 for apparent power in high PV case.

$S_{n,L1} = 41.3$ kVA, $S_{n,L2} = 4.2$ kVA, $S_{n,L3} = 14.6$ kVA, $S_{n,L4} = 15.4$ kVA, $S_{n,L5} = 9.8$ kVA, $S_{n,L6} = 13.2$ kVA, $S_{n,L7} = 25.1$ kVA, $S_{n,L8} = 5.3$ kVA, $S_{n,L9} = 6.5$ kVA, $S_{n,L10} = 8.3$ kVA, $S_{n,L11} = 2.1$ kVA, $S_{n,L12} = 6.6$ kVA, $S_{n,L13} = 4.2$ kVA, $S_{n,L14} = 2.1$ kVA.

D. LV Power Electronic Device and Diesel Synchonous Machine Data

Grid-forming PED:
$V_n = 400$ V, $S_n = 10$ kVA, $m_\omega = 0.005$, $m_v = 0.05$, $\omega_c = 60$, $v_0 = 1$, $f_0 = 1$, $R_{vi} = 0.12\ \Omega$, $L_{vi} = 0.68$ mH, $k_{p,v} = 3$, $k_{i,v} = 200$, $FF_v = 1$, $k_{p,c} = 0.73$, $k_{i,c} = 50$, $FF_c = 1$, $L_1 = 1.5$ mH, $R_1 = 0.1\ \Omega$, $C_f = 70\ \mu F$, $L_2 = 0.36$ mH.

Grid-supporting PED:
$m_\omega = 0.002$, $m_v = 0.08$, $\omega_c = 60$, $v_0 = 1$, $f_0 = 1$, $V_n = 400$, $k_{p,c} = 0.73$, $k_{i,c} = 50$, $FF_c = 1$, $L_1 = 1.5$ mH, $R_1 = 0.1\ \Omega$, $C_f = 70\ \mu F$, $L_2 = 0.36$ mH.

SM:
$S_n = 10$ kVA, $V_n =$ 400V, $x_{ls} = 0.064$ pu, $x_{md} = 1.65$ pu, $x_{lkq1} = 0.41$ pu, $x_{mq} = 1.159$ pu, $x_{lkq2} = 0$ pu, $x_{lfd} = 0.468$ pu, $x_{lkd} = 0.07$ pu, $r_s = 0.062$ pu, $r_{rkq1} = 0.111$ pu, $r_{kq2} = 0$ pu, $r_{fd} = 0.0674$ pu, $r_{kd} = 0.147$ pu.

AVR:
$k_{p,AVR} = 0.0845$, $k_{i,AVR} = 0.0945$, $K_A = 400$, $T_A = 0.2$ s, $T_E = 0.8$ s, $K_E = 1$, $e_{xfd,1} = 5.6$, $E_{xfd,2} = 4.4$, $s_{Efd,1} = 0.86$, $s_{Efd,2} = 0.5$, $T_r = 0.02$.

Governor:
$k_{p,GOV} = 1$, $k_{i,GOV} = 100$, $\tau_1 = 0.07$ s, $\tau_2 = 0.125$ s, $K_1 = 1.15$, $K_2 = 1$, $K_3 = 1$.

E. Synthetic Intertia for Wind Power Plants Data

DFIG:

$r_s = 0.023$ pu, $H = 4.32$ s, $l_s = 0.18$ pu, $S_n = 1.67$ MVA, $l_m = 2.9$ pu, $V_n = 1.975$ kV.

MV PED [226]:

$L_1 = 1.11$ mH, $m_\omega = 0.01$ pu, $C_f = 0.09$ mF, $V_n = 3.35$ kV, $L_2 = 0.3$ mH, $m_\omega = 0.01$ pu, $S_n = 3$ MVA, $m_v = 0.005$ pu, $V_n = 3.35$ kV, $\omega_c = 60$ rad/s.

MV Line:

$V_n = 20$ kV, $\underline{Z}_L^{'} = 0.12 + j0.33$ Ω/km, Length $= 20$ km.

Load:

$S_{n,load1} = 1.5$ MVA (PF: 0.95(ind.)), $S_{n,load2} = 0.5$ MVA (PF: 0.95(ind.)).

List of Figures

1.1. Microgrid schematic [20]. 3
1.2. Simulation and optimization framework. 7

2.1. Hierarchical microgrid control. 13
2.2. Stability classification of conventional power systems [62]. 15
2.3. Classification of microgrid stability [65]. 20
2.4. Time frames of dynamic phenomena. 22
2.5. Source and load subsystems for impedance-based stability analysis. 30

3.1. Natural abc and rotating dq (zero sequence omitted) reference frame. . . 41
3.2. Comparison of signals in the abc and $dq0$ frame. 42
3.3. Reference frames in power system simulation. 44
3.4. Single line diagrams of LV and MV line models. 45
3.5. PLL models. 47
3.6. DER controller types. 49
3.7. Power flow over an RL-line. 52
3.8. Droop control with feed-forward gain. 55
3.9. Virtual frame transformation with simplified line power flow. 56
3.10. Comparison of virtual synchronous machine and droop control. 58
3.11. LCL-filter with VI. 60
3.12. Overview of inverter with LCL-filter. 62
3.13. Overview of grid-forming droop controlled inverter with LCL-filter. 64
3.14. Overview of grid-forming droop controlled inverter with LCL-filter. 65
3.15. Magnitude and phase response of the closed loop transfer function of the voltage controller ($v_{c,d}/v_{c,d}^*$). 68
3.16. Phase response of the closed loop transfer function $i_{L2,d}/v_{c,d}^*$. 69
3.17. Model order reduction of grid-forming inverter. 70
3.18. Microgrid simplification. 71
3.19. Overview of different types of grid-feeding inverters with LCL-filter. . . . 72
3.20. Overview of grid-supporting inverter with LCL-filter. 73

3.21. Model order reduction of grid-supporting inverter. 74
3.22. Grid-forming and grid-feeding SM. 75
3.23. Cross section of three-phase two pole SM. 76
3.24. Reference frames for SM coupling with the power system. 78
3.25. AVR model AC5A to control stator voltage v_s. 79
3.26. AVR saturation function. 80
3.27. AVR model AC1A to control stator voltage v_s. 80
3.28. Governor for LV applications. 81
3.29. Governor for MV applications. 81
3.30. DFIG wind power plant control. 83
3.31. Deloaded operation for several operating points [257]. 84
3.32. PLL dynamics. 85
3.33. Combination of frequency gradient SI and grid-supporting droop control. . 86
3.34. Voltages alignment of microgrid and external grid with synchrocheck. . . 88
3.35. Example microgrid and composite state-space model. 89

4.1. Benchmark functions 95
4.2. Basic flowchart of a EA. 97
4.3. Encoding of chromosomes 98
4.4. Example for stochastic universal sampling. 100
4.5. Crossover mechanisms. 102
4.6. Constraints Handling. 104
4.7. Solution space (left) and root of BSP (right) [309]. 106
4.8. Solution space (left) and BSP tree with two solutions (right)[309]. 107
4.9. Solution space (left) and BSP tree with three solutions (right)[309]. . . . 108
4.10. Solution space (left) and BSP tree with a closed subspace (right)[309]. . 108
4.11. Mutation with guided anisotropic search [309]. 109
4.12. Diversity of solutions according to the size of their subspace [309]. 110
4.13. Flowchart of implemented EA. 112
4.14. Benchmark functions 113
4.15. Simulation and optimization framework. 116

5.1. Small microgrid with two nodes. 118
5.2. Cigre benchmark LV network [312]. 119
5.3. Voltages alignment of microgrid and external grid with synchrocheck. . . 119
5.4. Model validation results. 120
5.5. Cost over the generations for microgrid optimization. 123

5.6. Dominant eigenvalues of the microgrid with two grid-forming inverters for various parameter ranges (parameters increase with marker size). 124
5.7. Dominant eigenvalues of the microgrid with one grid-forming and one grid-supporting inverter for various parameter ranges (parameters increase with marker size). 126
5.8. Comparison of dominant eigenvalues of grid-forming inverters for optimized parameter sets. 129
5.9. Comparison of time-domain simulation results of grid-forming inverters for optimized parameter sets. 130
5.10. Comparison of dominant eigenvalues of one grid-forming and one grid-supporting inverter for optimized parameter sets. 132
5.11. Comparison of time-domain simulation results of one grid-forming and one grid-supporting inverter for optimized parameter sets. 132
5.12. Response to load step. 138
5.13. Dominant eigenvalues when optimized according to area criterion or eigenvalue real part. 139
5.14. Response to load step ($^+$parameters from Sec. 5.7). 142
5.15. Dominant eigenvalues when optimized according to area criterion or eigenvalue real part ($^+$parameters from Sec. 5.7). 143
5.16. Comparison of dominant eigenvalues of two grid-forming inverters for model simplifications. 145
5.17. Comparison of time domain simulation results of two grid-forming inverters for model simplifications. 145
5.18. Comparison of dominant eigenvalues for grid-forming inverters for model simplifications and $w_c = 30$ rad/s. 146
5.19. Comparison of dominant eigenvalues for grid-forming inverters for model simplifications and $w_c = 75$ rad/s. 147
5.20. Comparison of time domain simulations for grid-forming inverters for model simplifications with $\omega_c = 75$ rad/s and $FF_v = 0.2$. 147
5.21. Comparison of dominant eigenvalues of one grid-forming and one grid-supporting inverter for model simplifications. 148
5.22. Comparison time domain simulation results of one grid-forming and one grid-supporting inverter for model simplifications. 149
5.23. Active power of DFIG and microgrid frequency when combined with a grid-forming inverter. a.) DFIG without droop control, b.) DFIG with grid-supporting droop control 152

5.24. Active power of DFIG and microgrid frequency when combined with a SM. a.) DFIG without droop control, b.) DFIG with grid-supporting droop control 154
5.25. Loadings of SM and PED for positive and negative angle deviations. . . . 155
5.26. Comparison of voltage deviations examined in this work and feasible deviations according to [59]. 157
5.27. Maximum torques and breaker currents for angle deviations. 158
5.28. Maximum torques and breaker currents for frequency deviations. 158
5.29. Maximum torques and breaker currents for amplitude deviations. 159
5.30. Maximum torques and breaker currents for combinations angle with frequency/amplitude deviations. 160
5.31. Maximum currents for combinations of frequency deviations with small angle deviations. 161

Bibliography

[1] Svante Arrhenius. “On the influence of carbonic acid in the air upon the temperature of the ground”. In: *The London, Edinburgh, and Dublin Philosophical Magazine and Journal of Science* 41.251 (Apr. 1896), pp. 237–276. ISSN: 1941-5982. DOI: 10.1080/14786449608620846. (Visited on 06/06/2020).

[2] Thomas C. Peterson, William M. Connolley, and John Fleck. “The Myth of the 1970s Global Cooling Scientific Consensus”. In: *Bull. Amer. Meteor. Soc.* 89.9 (Sept. 2008). Publisher: American Meteorological Society, pp. 1325–1338. ISSN: 0003-0007. DOI: 10.1175/2008BAMS2370.1. URL: https://journals.ametsoc.org/doi/10.1175/2008BAMS2370.1 (visited on 06/06/2020).

[3] R. K. Pachauri, Leo Mayer, and Intergovernmental Panel on Climate Change, eds. *Climate change 2014: synthesis report*. en. OCLC: 914851124. Geneva, Switzerland: Intergovernmental Panel on Climate Change, 2015. ISBN: 978-92-9169-143-2.

[4] M. R. Raupach et al. “Global and regional drivers of accelerating CO2 emissions”. en. In: *Proceedings of the National Academy of Sciences* 104.24 (June 2007), pp. 10288–10293. ISSN: 0027-8424, 1091-6490. DOI: 10.1073/pnas.0700609104. URL: http://www.pnas.org/cgi/doi/10.1073/pnas.0700609104 (visited on 06/07/2020).

[5] John Cook et al. “Quantifying the consensus on anthropogenic global warming in the scientific literature”. en. In: *Environ. Res. Lett.* 8.2 (May 2013). Publisher: IOP Publishing, p. 024024. ISSN: 1748-9326. DOI: 10.1088/1748-9326/8/2/024024. URL: https://doi.org/10.1088%2F1748-9326%2F8%2F2%2F024024 (visited on 06/06/2020).

[6] Riley E. Dunlap. “Climate Change Skepticism and Denial: An Introduction”. en. In: *American Behavioral Scientist* 57.6 (June 2013), pp. 691–698. ISSN: 0002-7642, 1552-3381. DOI: 10.1177/0002764213477097. URL: http://journals.sagepub.com/doi/10.1177/0002764213477097 (visited on 06/06/2020).

[7] William Nordhaus. “Climate Change: The Ultimate Challenge for Economics”. en. In: *American Economic Review* 109.6 (June 2019), pp. 1991–2014. ISSN: 0002-8282. DOI: 10.1257/aer.109.6.1991. URL: https://pubs.aeaweb.org/doi/10.1257/aer.109.6.1991 (visited on 06/07/2020).

[8] Nicholas Stern. "The Structure of Economic Modeling of the Potential Impacts of Climate Change: Grafting Gross Underestimation of Risk onto Already Narrow Science Models". en. In: *Journal of Economic Literature* 51.3 (Sept. 2013), pp. 838–859. ISSN: 0022-0515. DOI: 10.1257/jel.51.3.838. URL: https://www.aeaweb.org/articles?id=10.1257/jel.51.3.838 (visited on 06/07/2020).

[9] Brian Vad Mathiesen, Henrik Lund, and Kenneth Karlsson. "100% Renewable energy systems, climate mitigation and economic growth". en. In: *Applied Energy*. The 5th Dubrovnik Conference on Sustainable Development of Energy, Water and Environment Systems, held in Dubrovnik September/October 2009 88.2 (Feb. 2011), pp. 488–501. ISSN: 0306-2619. DOI: 10.1016/j.apenergy.2010.03.001. URL: http://www.sciencedirect.com/science/article/pii/S0306261910000644 (visited on 06/07/2020).

[10] Thomas Klaus, Carla Vollmer, and Kathrin Werner. *Energy target 2050: 100 % renewable electricity supply*. en. 2010.

[11] Xi Fang et al. "Smart Grid — The New and Improved Power Grid: A Survey". In: *IEEE Communications Surveys Tutorials* 14.4 (2012). Conference Name: IEEE Communications Surveys Tutorials, pp. 944–980. ISSN: 1553-877X. DOI: 10.1109/SURV.2011.101911.00087.

[12] *dena-Studie Systemdienstleistungen 2030 - Sicherheit und Zuverlässigkeit einer Stromversorgung mit hohem Anteil erneuerbarer Energien*. Tech. rep. Berlin: Deutsche Energie Agentur GmbH, 2014.

[13] and S. Chaitusaney. "Impacts of inverter-based distributed generation control modes on short-circuit currents in distribution systems". In: *2012 7th IEEE Conference on Industrial Electronics and Applications (ICIEA)*. July 2012, pp. 1645–1650. DOI: 10.1109/ICIEA.2012.6360989.

[14] Pieter Tielens and Dirk Van Hertem. "The relevance of inertia in power systems". In: *Renewable and Sustainable Energy Reviews* 55 (Mar. 2016), pp. 999–1009. ISSN: 1364-0321. DOI: 10.1016/j.rser.2015.11.016. URL: http://www.sciencedirect.com/science/article/pii/S136403211501268X (visited on 10/04/2018).

[15] T. L. Vandoorn et al. "Review of primary control strategies for islanded microgrids with power-electronic interfaces". In: *Renewable and Sustainable Energy Reviews* 19 (Mar. 2013), pp. 613–628. ISSN: 1364-0321. DOI: 10.1016/j.rser.2012.11.062. URL: http://www.sciencedirect.com/science/article/pii/S1364032112006764 (visited on 10/13/2018).

[16] W. He et al. “Providing inertial support from wind turbines by adjusting phase-locked loop response”. In: *2014 IEEE PES General Meeting | Conference Exposition* (July 2014), pp. 1–5.

[17] D. Duckwitz and B. Fischer. “Modeling and Design of df/dt -Based Inertia Control for Power Converters”. In: *IEEE Journal of Emerging and Selected Topics in Power Electronics* 5.4 (Dec. 2017), pp. 1553–1564. ISSN: 2168-6777. DOI: 10.1109/JESTPE.2017.2703814.

[18] Gustav Lammert et al. “International industry practice on modelling and dynamic performance of inverter based generation in power system studies”. en. In: *Cigre Science and Engineering* (2017), p. 13.

[19] K. Yamashita et al. “Industrial Recommendation of Modeling of Inverter-Based Generators for Power System Dynamic Studies With Focus on Photovoltaic”. In: *IEEE Power and Energy Technology Systems Journal* 5.1 (Mar. 2018), pp. 1–10. ISSN: 2332-7707. DOI: 10.1109/JPETS.2018.2806744.

[20] *Microgrids & Vehicle-Grid Integration | Grid Integration Group*. URL: https://gridintegration.lbl.gov/microgrids-vehicle-grid-integration (visited on 12/27/2020).

[21] Nikos Hatziargyriou. *Microgrids: Architectures and Control*. en. OCLC: 1087331705. Wiley-IEEE Press, 2014. ISBN: 978-1-118-72064-6 978-1-118-72068-4 978-1-118-72067-7 978-1-118-72065-3.

[22] Johannes Schiffer et al. “A survey on modeling of microgrids - From fundamental physics to phasors and voltage sources”. In: *Automatica* 74 (Dec. 2016), pp. 135–150. ISSN: 0005-1098. DOI: 10.1016/j.automatica.2016.07.036. URL: http://www.sciencedirect.com/science/article/pii/S0005109816303041 (visited on 03/12/2018).

[23] A. Kwasinski and C. N. Onwuchekwa. “Dynamic Behavior and Stabilization of DC Microgrids With Instantaneous Constant-Power Loads”. In: *IEEE Transactions on Power Electronics* 26.3 (Mar. 2011), pp. 822–834. ISSN: 0885-8993. DOI: 10.1109/TPEL.2010.2091285.

[24] Robert Lasseter et al. *Integration of distributed energy resources. The CERTS Microgrid Concept*. en. Tech. rep. LBNL–50829, 799644. Apr. 2002, LBNL–50829, 799644. DOI: 10.2172/799644. URL: http://www.osti.gov/servlets/purl/799644-dfXsZi/native/ (visited on 05/30/2019).

[25] F D Kanellos, A I Tsouchnikas, and N D Hatziargyriou. "Micro-Grid Simulation during Grid-Connected and Islanded Modes of Operation". en. In: *International Conference on Power Systems Transients*. Montreal: International Conference on Power Systems Transients, 2005, p. 6.

[26] A. Soleimanisardoo, H. K. Karegar, and H. H. Zeineldin. "Differential Frequency Protection Scheme Based on Off-Nominal Frequency Injections for Inverter-Based Islanded Microgrids". In: *IEEE Transactions on Smart Grid* (2018), pp. 1–1. ISSN: 1949-3053. DOI: 10.1109/TSG.2017.2788851.

[27] S. F. Zarei and M. Parniani. "A Comprehensive Digital Protection Scheme for Low-Voltage Microgrids with Inverter-Based and Conventional Distributed Generations". In: *IEEE Transactions on Power Delivery* 32.1 (Feb. 2017), pp. 441–452. ISSN: 0885-8977. DOI: 10.1109/TPWRD.2016.2566264.

[28] Adolf J. Schwab. *Elektroenergiesysteme: Erzeugung, Übertragung und Verteilung elektrischer Energie*. de. 5. Auflage. OCLC: 1001339792. Berlin: Springer Berlin, 2017. ISBN: 978-3-662-55315-2 978-3-662-55316-9.

[29] A. D. Paquette and D. M. Divan. "Virtual Impedance Current Limiting for Inverters in Microgrids With Synchronous Generators". In: *IEEE Transactions on Industry Applications* 51.2 (Mar. 2015), pp. 1630–1638. ISSN: 0093-9994. DOI: 10.1109/TIA.2014.2345877.

[30] E. A. Mohamed et al. "Digital coordination strategy of protection and frequency stability for an islanded microgrid". In: *Transmission Distribution IET Generation* 12.15 (2018), pp. 3637–3646. ISSN: 1751-8687. DOI: 10.1049/iet-gtd.2018.0264.

[31] Ian A. Hiskens. "Significance of Load Modelling in Power System Dynamics". In: *SYMPOSIUM OF SPECIALISTS IN ELECTRIC OPERATIONAL AND EXPANSION PLANNING*. Folrianopolis, Brazil: SYMPOSIUM OF SPECIALISTS IN ELECTRIC OPERATIONAL and EXPANSION PLANNING, 2006.

[32] A. Hooshyar and R. Iravani. "Microgrid Protection". In: *Proceedings of the IEEE* 105.7 (July 2017), pp. 1332–1353. ISSN: 0018-9219. DOI: 10.1109/JPROC.2017.2669342.

[33] A. Ghassemi, S. Bavarian, and L. Lampe. "Cognitive Radio for Smart Grid Communications". In: *2010 First IEEE International Conference on Smart Grid Communications*. Oct. 2010, pp. 297–302. DOI: 10.1109/SMARTGRID.2010.5622097.

[34] Babak Arbab-Zavar et al. “Smart Inverters for Microgrid Applications: A Review”. en. In: *Energies* 12.5 (Mar. 2019), p. 840. ISSN: 1996-1073. DOI: 10.3390/en12050840. URL: https://www.mdpi.com/1996-1073/12/5/840 (visited on 03/11/2019).

[35] C. P. Nguyen and A. J. Flueck. “Modeling of communication latency in smart grid”. In: *2011 IEEE Power and Energy Society General Meeting*. July 2011, pp. 1–7. DOI: 10.1109/PES.2011.6039815.

[36] Y. Yan et al. “A Survey on Smart Grid Communication Infrastructures: Motivations, Requirements and Challenges”. In: *IEEE Communications Surveys Tutorials* 15.1 (2013), pp. 5–20. ISSN: 1553-877X. DOI: 10.1109/SURV.2012.021312.00034.

[37] S. Palm and P. Schegner. “Fundamentals of detectability and detection methods of unintentional electrical islands”. In: *2015 IEEE Eindhoven PowerTech*. June 2015, pp. 1–6. DOI: 10.1109/PTC.2015.7232390.

[38] P. Mahat and and B. Bak-Jensen. “Review of islanding detection methods for distributed generation”. In: *2008 Third International Conference on Electric Utility Deregulation and Restructuring and Power Technologies*. Apr. 2008, pp. 2743–2748. DOI: 10.1109/DRPT.2008.4523877.

[39] Ku Nurul Edhura Ku Ahmad, Jeyraj Selvaraj, and Nasrudin Abd Rahim. “A review of the islanding detection methods in grid-connected PV inverters”. In: *Renewable and Sustainable Energy Reviews* 21 (May 2013), pp. 756–766. ISSN: 1364-0321. DOI: 10.1016/j.rser.2013.01.018. URL: http://www.sciencedirect.com/science/article/pii/S136403211300049X (visited on 04/03/2019).

[40] M. M. A. Abdelaziz, H. E. Farag, and E. F. El-Saadany. “Optimum Reconfiguration of Droop-Controlled Islanded Microgrids”. In: *IEEE Transactions on Power Systems* 31.3 (May 2016), pp. 2144–2153. ISSN: 0885-8950. DOI: 10.1109/TPWRS.2015.2456154.

[41] Neng Fan et al. “A mixed integer programming approach for optimal power grid intentional islanding”. en. In: *Energy Systems* 3.1 (Mar. 2012), pp. 77–93. ISSN: 1868-3967, 1868-3975. DOI: 10.1007/s12667-011-0046-5. URL: http://link.springer.com/10.1007/s12667-011-0046-5 (visited on 04/15/2019).

[42] H. Shao and J. Bialek. “When to island in the controlled islanding scheme to prevent imminent wide-area blackouts”. In: *2012 47th International Universities Power Engineering Conference (UPEC)*. Sept. 2012, pp. 1–6. DOI: 10.1109/UPEC.2012.6398544.

[43] H. Mohamad et al. "Feasibility study of an intentional islanding operation with a new adaptive load shedding". In: *2013 3rd International Conference on Electric Power and Energy Conversion Systems*. Oct. 2013, pp. 1–6. DOI: 10.1109/EPECS.2013.6713019.

[44] A. El-Zonkoly, M. Saad, and R. Khalil. "Optimal intentional islanding of distribution systems with DG using CLPSO". In: *2012 16th IEEE Mediterranean Electrotechnical Conference*. Mar. 2012, pp. 540–543. DOI: 10.1109/MELCON.2012.6196491.

[45] D. K. Dheer et al. "Effect of Reconfiguration and Meshed Networks on the Small-Signal Stability Margin of Droop-Based Islanded Microgrids". In: *IEEE Transactions on Industry Applications* 54.3 (May 2018), pp. 2821–2833. ISSN: 0093-9994. DOI: 10.1109/TIA.2018.2796590.

[46] J. M. Guerrero et al. "Hierarchical Control of Droop-Controlled AC and DC Microgrids—A General Approach Toward Standardization". In: *IEEE Transactions on Industrial Electronics* 58.1 (Jan. 2011), pp. 158–172. ISSN: 0278-0046. DOI: 10.1109/TIE.2010.2066534.

[47] F. Doost Mohammadi, H. Keshtkar Vanashi, and A. Feliachi. "State-Space Modeling, Analysis, and Distributed Secondary Frequency Control of Isolated Microgrids". In: *IEEE Transactions on Energy Conversion* 33.1 (Mar. 2018), pp. 155–165. ISSN: 0885-8969. DOI: 10.1109/TEC.2017.2757012.

[48] Z. Zhao et al. "Multiple-Time-Scales Hierarchical Frequency Stability Control Strategy of Medium-Voltage Isolated Microgrid". In: *IEEE Transactions on Power Electronics* 31.8 (Aug. 2016), pp. 5974–5991. ISSN: 0885-8993. DOI: 10.1109/TPEL.2015.2496869.

[49] J. C. Vasquez et al. "Modeling, Analysis, and Design of Stationary-Reference-Frame Droop-Controlled Parallel Three-Phase Voltage Source Inverters". In: *IEEE Transactions on Industrial Electronics* 60.4 (Apr. 2013), pp. 1271–1280. ISSN: 0278-0046. DOI: 10.1109/TIE.2012.2194951.

[50] D. E. Olivares et al. "Trends in Microgrid Control". In: *IEEE Transactions on Smart Grid* 5.4 (July 2014), pp. 1905–1919. ISSN: 1949-3053. DOI: 10.1109/TSG.2013.2295514.

[51] Simon Eberlein. "Genetic Algorithm for Unit Commitment and Economic Dispatch in Microgrids considering Network Topology". MA thesis. Stuttgart, Germany: University of Stuttgart, 2014.

[52] SMA. *Sunny Island Generator - White Paper*. 2012.

[53] Farid Katiraei et al. *PV Hybrid Mini-Grids: Applicable Control Methods for Various Situations*. en. 2012.

[54] N. Hatziargyriou et al. "Microgrids". In: *IEEE Power and Energy Magazine* 5.4 (July 2007), pp. 78–94. ISSN: 1540-7977. DOI: 10.1109/MPAE.2007.376583.

[55] Lubna Mariam, Malabika Basu, and Michael F. Conlon. "Microgrid: Architecture, policy and future trends". In: *Renewable and Sustainable Energy Reviews* 64 (Oct. 2016), pp. 477–489. ISSN: 1364-0321. DOI: 10.1016/j.rser.2016.06.037. URL: http://www.sciencedirect.com/science/article/pii/S1364032116302635 (visited on 07/12/2019).

[56] P Asmus and M Lawrence. *Market data: microgrids*. 2016.

[57] T. L. Vandoorn et al. "Transition From Islanded to Grid-Connected Mode of Microgrids With Voltage-Based Droop Control". In: *IEEE Transactions on Power Systems* 28.3 (Aug. 2013), pp. 2545–2553. ISSN: 0885-8950. DOI: 10.1109/TPWRS.2012.2226481.

[58] C. Cho et al. "Active Synchronizing Control of a Microgrid". In: *IEEE Transactions on Power Electronics* 26.12 (Dec. 2011), pp. 3707–3719. ISSN: 0885-8993. DOI: 10.1109/TPEL.2011.2162532.

[59] "IEEE Standard for Interconnecting Distributed Resources with Electric Power Systems". In: *IEEE Std 1547-2003* (July 2003), pp. 1–28. DOI: 10.1109/IEEESTD.2003.94285.

[60] Prabha Kundur. *Power System Stability and Control*. Vol. 7. New York: McGraw-hill, 1994.

[61] Jan Machowski, Janusz W. Bialek, and J. R. Bumby. *Power system dynamics: stability and control*. en. 2nd ed. OCLC: ocn232130756. Chichester, U.K: Wiley, 2008. ISBN: 978-0-470-72558-0.

[62] P. Kundur et al. "Definition and classification of power system stability IEEE/CIGRE joint task force on stability terms and definitions". In: *IEEE Transactions on Power Systems* 19.3 (Aug. 2004), pp. 1387–1401. ISSN: 0885-8950. DOI: 10.1109/TPWRS.2004.825981.

[63] Carson W. Taylor. *Power system voltage stability*. The EPRI power system engineering series. New York [u.a.]: McGraw-Hill, 1994. ISBN: 978-0-07-063184-7.

[64] B. Gao, G. K. Morison, and P. Kundur. "Voltage stability evaluation using modal analysis". In: *IEEE Transactions on Power Systems* 7.4 (Nov. 1992), pp. 1529–1542. ISSN: 0885-8950. DOI: 10.1109/59.207377.

[65] M. Farrokhabadi et al. “Microgrid Stability Definitions, Analysis, and Examples”. In: *IEEE Transactions on Power Systems* (2019), pp. 1–1. ISSN: 0885-8950. DOI: 10.1109/TPWRS.2019.2925703.

[66] Ehsan Nasr-Azadani et al. “Stability Analysis of Unbalanced Distribution Systems With Synchronous Machine and DFIG Based Distributed Generators”. In: *IEEE Transactions on Smart Grid* 5.5 (Sept. 2014). Conference Name: IEEE Transactions on Smart Grid, pp. 2326–2338. ISSN: 1949-3061. DOI: 10.1109/TSG.2014.2321709.

[67] Gauthier Delille, Bruno Francois, and Gilles Malarange. “Dynamic Frequency Control Support by Energy Storage to Reduce the Impact of Wind and Solar Generation on Isolated Power System’s Inertia”. In: *IEEE Transactions on Sustainable Energy* 3.4 (Oct. 2012). Conference Name: IEEE Transactions on Sustainable Energy, pp. 931–939. ISSN: 1949-3037. DOI: 10.1109/TSTE.2012.2205025.

[68] Gauthier Delille et al. “Experimental validation of a novel approach to stabilize power system frequency by taking advantage of Load Voltage Sensitivity”. In: *2015 IEEE Eindhoven PowerTech*. June 2015, pp. 1–6. DOI: 10.1109/PTC.2015.7232697.

[69] Bharatkumar V. Solanki, Claudio A. Cañizares, and Kankar Bhattacharya. “Practical Energy Management Systems for Isolated Microgrids”. In: *IEEE Transactions on Smart Grid* 10.5 (Sept. 2019). Conference Name: IEEE Transactions on Smart Grid, pp. 4762–4775. ISSN: 1949-3061. DOI: 10.1109/TSG.2018.2868130.

[70] Jorge Elizondo et al. “Enhanced critical clearing time estimation and fault recovery strategy for an inverter-based microgrid with IM load”. In: *2016 IEEE Power and Energy Society General Meeting (PESGM)*. ISSN: 1944-9933. July 2016, pp. 1–5. DOI: 10.1109/PESGM.2016.7741312.

[71] Mostafa Farrokhabadi et al. “Battery Energy Storage System Models for Microgrid Stability Analysis and Dynamic Simulation”. In: *IEEE Transactions on Power Systems* 33.2 (Mar. 2018). Conference Name: IEEE Transactions on Power Systems, pp. 2301–2312. ISSN: 1558-0679. DOI: 10.1109/TPWRS.2017.2740163.

[72] R. Belkacemi et al. “Experimental Transient Stability Analysis of MicroGrid systems: Lessons learned”. In: *2015 IEEE Power Energy Society General Meeting*. ISSN: 1932-5517. July 2015, pp. 1–5. DOI: 10.1109/PESGM.2015.7286637.

[73] Xiongfei Wang, Frede Blaabjerg, and Weimin Wu. “Modeling and Analysis of Harmonic Stability in an AC Power-Electronics-Based Power System”. In: *IEEE Transactions on Power Electronics* 29.12 (Dec. 2014). Conference Name: IEEE

Transactions on Power Electronics, pp. 6421–6432. ISSN: 1941-0107. DOI: 10.1109/TPEL.2014.2306432.

[74] Mauricio Cespedes and Jian Sun. "Impedance Modeling and Analysis of Grid-Connected Voltage-Source Converters". In: *IEEE Transactions on Power Electronics* 29.3 (Mar. 2014), pp. 1254–1261. ISSN: 0885-8993, 1941-0107. DOI: 10.1109/TPEL.2013.2262473.

[75] Bernd Kulicke. *Digitale Simulation elektromagnetischer und –mechanischer Ausgleichsvorgänge*. 2011.

[76] N. Pogaku, M. Prodanovic, and T. C. Green. "Modeling, Analysis and Testing of Autonomous Operation of an Inverter-Based Microgrid". In: *IEEE Transactions on Power Electronics* 22.2 (Mar. 2007), pp. 613–625. ISSN: 0885-8993. DOI: 10.1109/TPEL.2006.890003.

[77] Y. A. I. Mohamed and E. F. El-Saadany. "Adaptive Decentralized Droop Controller to Preserve Power Sharing Stability of Paralleled Inverters in Distributed Generation Microgrids". In: *IEEE Transactions on Power Electronics* 23.6 (Nov. 2008), pp. 2806–2816. ISSN: 0885-8993. DOI: 10.1109/TPEL.2008.2005100.

[78] Heverton Pereira et al. "High Performance Reduced Order Models for Wind Turbines with Full-Scale Converters Applied on Grid Interconnection Studies". en. In: *Energies* 7.11 (Nov. 2014), pp. 7694–7716. ISSN: 1996-1073. DOI: 10.3390/en7117694. URL: http://www.mdpi.com/1996-1073/7/11/7694 (visited on 06/08/2019).

[79] J. Sun. "Small-Signal Methods for AC Distributed Power Systems: A Review". In: *IEEE Transactions on Power Electronics* 24.11 (Nov. 2009), pp. 2545–2554. ISSN: 0885-8993. DOI: 10.1109/TPEL.2009.2029859.

[80] Zhikang Shuai et al. "Microgrid stability: Classification and a review". In: *Renewable and Sustainable Energy Reviews* 58 (May 2016), pp. 167–179. ISSN: 1364-0321. DOI: 10.1016/j.rser.2015.12.201. URL: http://www.sciencedirect.com/science/article/pii/S1364032115015841 (visited on 05/16/2018).

[81] Shuya Wang et al. "A review on the small signal stability of microgrid". In: *2016 IEEE 8th International Power Electronics and Motion Control Conference (IPEMC-ECCE Asia)*. May 2016, pp. 1793–1798. DOI: 10.1109/IPEMC.2016.7512566.

[82] Xiaobo Wang. "Modal Analysis of Large Interconnected Power Systems". PhD thesis. Erlangen: University of Erlangen/Nuernberg, 1997.

[83] I. J. Perez-Arriaga, G. C. Verghese, and F. C. Schweppe. “Selective Modal Analysis with Applications to Electric Power Systems, PART I: Heuristic Introduction”. In: *IEEE Transactions on Power Apparatus and Systems* PAS-101.9 (Sept. 1982), pp. 3117–3125. ISSN: 0018-9510. DOI: 10.1109/TPAS.1982.317524.

[84] I. P. Nikolakakos et al. “Stability Evaluation of Interconnected Multi-Inverter Microgrids Through Critical Clusters”. In: *IEEE Transactions on Power Systems* 31.4 (July 2016), pp. 3060–3072. ISSN: 0885-8950. DOI: 10.1109/TPWRS.2015.2476826.

[85] X. Tang, W. Deng, and Z. Qi. “Investigation of the Dynamic Stability of Microgrid”. In: *IEEE Transactions on Power Systems* 29.2 (Mar. 2014), pp. 698–706. ISSN: 0885-8950. DOI: 10.1109/TPWRS.2013.2285585.

[86] A. U. Krismanto and N. Mithulananthan. “Identification of modal interaction and small signal stability in autonomous microgrid operation”. In: *Transmission Distribution IET Generation* 12.1 (2018), pp. 247–257. ISSN: 1751-8687. DOI: 10.1049/iet-gtd.2017.1219.

[87] Z. Miao, A. Domijan, and L. Fan. “Investigation of Microgrids With Both Inverter Interfaced and Direct AC-Connected Distributed Energy Resources”. In: *IEEE Transactions on Power Delivery* 26.3 (July 2011), pp. 1634–1642. ISSN: 0885-8977. DOI: 10.1109/TPWRD.2011.2114372.

[88] A. Aderibole et al. “Domain of Stability Characterization for Hybrid Microgrids Considering Different Power Sharing Conditions”. In: *IEEE Transactions on Energy Conversion* 33.1 (Mar. 2018), pp. 312–323. ISSN: 0885-8969. DOI: 10.1109/TEC.2017.2743105.

[89] Andrew Donald Paquette. “Power quality and inverter-generator interactions in microgrids”. PhD thesis. Georgia Institute of Technology, Jan. 2014. (Visited on 07/14/2018).

[90] Dharmendra Kumar Dheer, Nimish Soni, and Suryanarayana Doolla. “Improvement of small signal stability margin and transient response in inverter-dominated microgrids”. In: *Sustainable Energy, Grids and Networks* 5 (Mar. 2016), pp. 135–147. ISSN: 2352-4677. DOI: 10.1016/j.segan.2015.12.005. URL: http://www.sciencedirect.com/science/article/pii/S2352467715000776 (visited on 05/21/2018).

[91] Zheng Zeng, Huan Yang, and Rongxiang Zhao. "Study on small signal stability of microgrids: A review and a new approach". In: *Renewable and Sustainable Energy Reviews* 15.9 (Dec. 2011), pp. 4818–4828. ISSN: 1364-0321. DOI: 10.1016/j.rser.2011.07.069. URL: http://www.sciencedirect.com/science/article/pii/S1364032111003145 (visited on 05/20/2018).

[92] Z. He et al. "Fault Detection and Classification in EHV Transmission Line Based on Wavelet Singular Entropy". In: *IEEE Transactions on Power Delivery* 25.4 (Oct. 2010), pp. 2156–2163. ISSN: 0885-8977. DOI: 10.1109/TPWRD.2010.2042624.

[93] N. Bottrell, M. Prodanovic, and T. C. Green. "Dynamic Stability of a Microgrid With an Active Load". In: *IEEE Transactions on Power Electronics* 28.11 (Nov. 2013), pp. 5107–5119. ISSN: 0885-8993. DOI: 10.1109/TPEL.2013.2241455.

[94] E. Barklund et al. "Energy Management in Autonomous Microgrid Using Stability-Constrained Droop Control of Inverters". In: *IEEE Transactions on Power Electronics* 23.5 (Sept. 2008), pp. 2346–2352. ISSN: 0885-8993. DOI: 10.1109/TPEL.2008.2001910.

[95] T. S. Sreeram et al. "Hopf bifurcation analysis in droop controlled islanded microgrids". In: *International Journal of Electrical Power & Energy Systems* 90 (Sept. 2017), pp. 208–224. ISSN: 0142-0615. DOI: 10.1016/j.ijepes.2017.01.028. URL: http://www.sciencedirect.com/science/article/pii/S0142061516308377 (visited on 05/20/2018).

[96] Z. Shuai et al. "Dynamic Stability Analysis of Synchronverter-Dominated Microgrid Based on Bifurcation Theory". In: *IEEE Transactions on Industrial Electronics* 64.9 (Sept. 2017), pp. 7467–7477. ISSN: 0278-0046. DOI: 10.1109/TIE.2017.2652387.

[97] Johannes Schiffer. "Stability and power sharing in microgrids". en. PhD thesis. Berlin: Technische Universitaet Berlin, Aug. 2015. URL: https://depositonce.tu-berlin.de//handle/11303/4878 (visited on 03/12/2018).

[98] Hassan Khalil. *Nonlinear Systems*. 3. New Jersey: Prentice hall, 2002.

[99] M. Kabalan, P. Singh, and D. Niebur. "Large Signal Lyapunov-Based Stability Studies in Microgrids: A Review". In: *IEEE Transactions on Smart Grid* 8.5 (Sept. 2017), pp. 2287–2295. ISSN: 1949-3053. DOI: 10.1109/TSG.2016.2521652.

[100] L. Luo and S. V. Dhople. "Spatiotemporal Model Reduction of Inverter-Based Islanded Microgrids". In: *IEEE Transactions on Energy Conversion* 29.4 (Dec. 2014), pp. 823–832. ISSN: 0885-8969. DOI: 10.1109/TEC.2014.2348716.

[101] Federico Milano. *Power System Modelling and Scripting*. en. Vol. 0. Power Systems. Berlin, Heidelberg: Springer Berlin Heidelberg, 2010. ISBN: 978-3-642-13668-9 978-3-642-13669-6. DOI: 10.1007/978-3-642-13669-6. URL: http://link.springer.com/10.1007/978-3-642-13669-6 (visited on 05/07/2019).

[102] N. Soni, S. Doolla, and M. C. Chandorkar. "Analysis of Frequency Transients in Isolated Microgrids". In: *IEEE Transactions on Industry Applications* 53.6 (Nov. 2017), pp. 5940–5951. ISSN: 0093-9994. DOI: 10.1109/TIA.2017.2746619.

[103] F. Andrade et al. "Study of large-signal stability of an inverter-based generator using a Lyapunov function". In: *IECON 2014 - 40th Annual Conference of the IEEE Industrial Electronics Society*. Oct. 2014, pp. 1840–1846. DOI: 10.1109/IECON.2014.7048752.

[104] P. Vorobev et al. "High-Fidelity Model Order Reduction for Microgrids Stability Assessment". In: *IEEE Transactions on Power Systems* 33.1 (Jan. 2018), pp. 874–887. ISSN: 0885-8950. DOI: 10.1109/TPWRS.2017.2707400.

[105] P. Vorobev et al. "A framework for development of universal rules for microgrids stability and control". In: *2017 IEEE 56th Annual Conference on Decision and Control (CDC)*. Dec. 2017, pp. 5125–5130. DOI: 10.1109/CDC.2017.8264418.

[106] Robert D. Middlebrook. "Input Filter Considerations in Design and Application of Switching Regulators". In: 1976.

[107] Mohamed Belkhayat. "Stability for AC Power Systems with Regulated Loads". Ph.D. Dissertation. Purdue University, 1997.

[108] Xiaogang Feng, Jinjun Liu, and F. C. Lee. "Impedance specifications for stable DC distributed power systems". In: *IEEE Transactions on Power Electronics* 17.2 (Mar. 2002), pp. 157–162. ISSN: 0885-8993. DOI: 10.1109/63.988825.

[109] J. Sun. "Impedance-Based Stability Criterion for Grid-Connected Inverters". In: *IEEE Transactions on Power Electronics* 26.11 (Nov. 2011), pp. 3075–3078. ISSN: 0885-8993. DOI: 10.1109/TPEL.2011.2136439.

[110] M. Amin and M. Molinas. "Small-Signal Stability Assessment of Power Electronics Based Power Systems: A Discussion of Impedance- and Eigenvalue-Based Methods". In: *IEEE Transactions on Industry Applications* 53.5 (Sept. 2017), pp. 5014–5030. ISSN: 0093-9994. DOI: 10.1109/TIA.2017.2712692.

[111] B. Wen et al. “AC Stability Analysis and dq Frame Impedance Specifications in Power-Electronics-Based Distributed Power Systems”. In: *IEEE Journal of Emerging and Selected Topics in Power Electronics* 5.4 (Dec. 2017), pp. 1455–1465. ISSN: 2168-6777. DOI: 10.1109/JESTPE.2017.2728640.

[112] H. Liu, X. Xie, and W. Liu. “An Oscillatory Stability Criterion Based on the Unifieddq-Frame Impedance Network Model for Power Systems With High-Penetration Renewables”. In: *IEEE Transactions on Power Systems* 33.3 (May 2018), pp. 3472–3485. ISSN: 0885-8950. DOI: 10.1109/TPWRS.2018.2794067.

[113] B. Wen et al. “Analysis of D-Q Small-Signal Impedance of Grid-Tied Inverters”. In: *IEEE Transactions on Power Electronics* 31.1 (Jan. 2016), pp. 675–687. ISSN: 0885-8993. DOI: 10.1109/TPEL.2015.2398192.

[114] Bo Wen. “Stability Analysis of Three-Phase AC Power Systems Based on Measured D-Q Frame Impedances”. en. PhD thesis. Blacksburg: Virginia Polytechnic Institute and State University, Jan. 2015. URL: https://vtechworks.lib.vt.edu/handle/10919/51202 (visited on 03/29/2018).

[115] D. Dong et al. “Analysis of Phase-Locked Loop Low-Frequency Stability in Three-Phase Grid-Connected Power Converters Considering Impedance Interactions”. In: *IEEE Transactions on Industrial Electronics* 62.1 (Jan. 2015), pp. 310–321. ISSN: 0278-0046. DOI: 10.1109/TIE.2014.2334665.

[116] S. Zhou et al. “An Improved Design of Current Controller forLCL-Type Grid-Connected Converter to Reduce Negative Effect of PLL in Weak Grid”. In: *IEEE Journal of Emerging and Selected Topics in Power Electronics* 6.2 (June 2018), pp. 648–663. ISSN: 2168-6777. DOI: 10.1109/JESTPE.2017.2780918.

[117] W. Wu et al. “Damping Methods for Resonances Caused by LCL-Filter-Based Current-Controlled Grid-Tied Power Inverters: An Overview”. In: *IEEE Transactions on Industrial Electronics* 64.9 (Sept. 2017), pp. 7402–7413. ISSN: 0278-0046. DOI: 10.1109/TIE.2017.2714143.

[118] M. Amin and M. Molinas. “Understanding the Origin of Oscillatory Phenomena Observed Between Wind Farms and HVdc Systems”. In: *IEEE Journal of Emerging and Selected Topics in Power Electronics* 5.1 (Mar. 2017), pp. 378–392. ISSN: 2168-6777. DOI: 10.1109/JESTPE.2016.2620378.

[119] Turhan Hilmi Demiray. “Simulation of Power Sytsem Dynamics using Dynamic Phasor Models”. PhD thesis. Zurich, Switzerland: ETH Zurich, 2008.

[120] *Simulink User’s Guide*. The MathWorks, Inc., 2019.

[121] P. Fritzson. "Front Matter". In: *Principles of Object-Oriented Modeling and Simulation with Modelica 3.3: A Cyber-Physical Approach*. IEEE, 2015. ISBN: 978-1-118-98916-6. DOI: 10.1002/9781118989166.fmatter. URL: https://ieeexplore.ieee.org/document/7027391 (visited on 08/04/2019).

[122] L. Fortuna, G. Nunnari, and A. Gallo. *Model Order Reduction Techniques with Applications in Electrical Engineering*. en. London: Springer London, 1992. ISBN: 978-1-4471-3200-4 978-1-4471-3198-4. DOI: 10.1007/978-1-4471-3198-4. URL: http://link.springer.com/10.1007/978-1-4471-3198-4 (visited on 06/29/2020).

[123] Wenqiang Hu, Zaijun Wu, and Venkata Dinavahi. "Dynamic Analysis and Model Order Reduction of Virtual Synchronous Machine Based Microgrid". In: *IEEE Access* (2020). Conference Name: IEEE Access, pp. 1–1. ISSN: 2169-3536. DOI: 10.1109/ACCESS.2020.3001076.

[124] Panagiotis N. Papadopoulos et al. "Black-box dynamic equivalent model for microgrids using measurement data". In: *Transmission Distribution IET Generation* 8.5 (May 2014). Conference Name: Transmission Distribution IET Generation, pp. 851–861. ISSN: 1751-8695. DOI: 10.1049/iet-gtd.2013.0524.

[125] F. O. Resende and J. A. Pecas Lopes. "Development of Dynamic Equivalents for MicroGrids using System Identification Theory". In: *2007 IEEE Lausanne Power Tech*. July 2007, pp. 1033–1038. DOI: 10.1109/PCT.2007.4538457.

[126] Y. Gu, N. Bottrell, and T. C. Green. "Reduced-Order Models for Representing Converters in Power System Studies". In: *IEEE Transactions on Power Electronics* 33.4 (Apr. 2018), pp. 3644–3654. ISSN: 0885-8993. DOI: 10.1109/TPEL.2017.2711267.

[127] E. Davison. "A method for simplifying linear dynamic systems". In: *IEEE Transactions on Automatic Control* 11.1 (Jan. 1966), pp. 93–101. ISSN: 0018-9286. DOI: 10.1109/TAC.1966.1098264.

[128] X. Guo et al. "Dynamic Phasors-Based Modeling and Stability Analysis of Droop-Controlled Inverters for Microgrid Applications". In: *IEEE Transactions on Smart Grid* 5.6 (Nov. 2014), pp. 2980–2987. ISSN: 1949-3053. DOI: 10.1109/TSG.2014.2331280.

[129] S. V. Iyer, M. N. Belur, and M. C. Chandorkar. "A Generalized Computational Method to Determine Stability of a Multi-inverter Microgrid". In: *IEEE Transactions on Power Electronics* 25.9 (Sept. 2010), pp. 2420–2432. ISSN: 0885-8993. DOI: 10.1109/TPEL.2010.2048720.

[130] V. Mariani et al. "Model Order Reductions for Stability Analysis of Islanded Microgrids With Droop Control". In: *IEEE Transactions on Industrial Electronics* 62.7 (July 2015), pp. 4344–4354. ISSN: 0278-0046. DOI: 10.1109/TIE.2014.2381151.

[131] Petar Kokotovic. *Singular Perturbation Methods in Control Analysis and Design*. 3rd ed. London: John O'Reilly, 1999.

[132] Yoash Levron and Juri Belikov. "Modeling power networks using dynamic phasors in the dq0 reference frame". In: *Electric Power Systems Research* 144 (Mar. 2017), pp. 233–242. ISSN: 0378-7796. DOI: 10.1016/j.epsr.2016.11.024. URL: http://www.sciencedirect.com/science/article/pii/S0378779616305120 (visited on 03/12/2018).

[133] R.H. Park. "Two Reaction Theory of Synchronous Machines". In: *AIEE Transactions* (1929).

[134] Paul C. Krause et al. *Analysis of electric machinery and drive systems*. en. Third edition. IEEE Press series on power engineeering. Hoboken, New Jersey: Wiley, 2013. ISBN: 978-1-118-02429-4.

[135] D. Baimel et al. "Dynamic Modeling of Networks, Microgrids, and Renewable Sources in the dq0 Reference Frame: A Survey". In: *IEEE Access* 5 (2017), pp. 21323–21335. DOI: 10.1109/ACCESS.2017.2758523.

[136] Bernd R. Oswald. *Berechnung von Drehstromnetzen: Berechnung stationärer und nichtstationärer Vorgänge mit symmetrischen Komponenten und Raumzeigern*. de. 3., korrigierte und erweiterte Auflage. Lehrbuch. OCLC: 979563271. Wiesbaden: Springer Vieweg, 2017. ISBN: 978-3-658-14404-3 978-3-658-14405-0.

[137] Bikash Pal and Balarko Chaudhuri. *Robust control in power systems.* Springer Science & Business Media, 2005.

[138] J. Belikov and Y. Levron. "Uses and Misuses of Quasi-static Time-varying Phasor Models in Power Systems". In: *IEEE Transactions on Power Delivery* (2018), pp. 1–1. ISSN: 0885-8977. DOI: 10.1109/TPWRD.2018.2852950.

[139] Juri Belikov and Yoash Levron. "Comparison of time-varying phasor and dq0 dynamic models for large transmission networks". In: *International Journal of Electrical Power & Energy Systems* 93 (Dec. 2017), pp. 65–74. ISSN: 0142-0615. DOI: 10.1016/j.ijepes.2017.05.017. (Visited on 03/12/2018).

[140] T. Demiray, G. Andersson, and L. Busarello. “Evaluation study for the simulation of power system transients using dynamic phasor models”. In: *2008 IEEE/PES Transmission and Distribution Conference and Exposition: Latin America*. Aug. 2008, pp. 1–6. DOI: 10.1109/TDC-LA.2008.4641716.

[141] S. Almer and U. Jonsson. “Dynamic Phasor Analysis of Periodic Systems”. In: *IEEE Transactions on Automatic Control* 54.8 (Aug. 2009), pp. 2007–2012. ISSN: 0018-9286. DOI: 10.1109/TAC.2009.2023970.

[142] P. J. Hart, R. H. Lasseter, and T. M. Jahns. “Reduced-order harmonic modeling and analysis of droop-controlled distributed generation networks”. In: *2016 IEEE 7th International Symposium on Power Electronics for Distributed Generation Systems (PEDG)*. June 2016, pp. 1–9. DOI: 10.1109/PEDG.2016.7527023.

[143] Z. Miao et al. “Dynamic Phasor-Based Modeling of Unbalanced Radial Distribution Systems”. In: *IEEE Transactions on Power Systems* 30.6 (Nov. 2015), pp. 3102–3109. ISSN: 0885-8950. DOI: 10.1109/TPWRS.2014.2388154.

[144] S. Chandrasekar and R. Gokaraju. “Dynamic phasor modeling of type 3 DFIG wind generators (including SSCI phenomenon) for short circuit calculations”. In: *2015 IEEE Power Energy Society General Meeting*. July 2015, pp. 1–1. DOI: 10.1109/PESGM.2015.7286217.

[145] Y. Levron and J. Belikov. “Open-source software for modeling and analysis of power networks in the dq0 reference frame”. In: *2017 IEEE Manchester PowerTech*. June 2017, pp. 1–6. DOI: 10.1109/PTC.2017.7980912.

[146] Juri Belikov and Yoash Levron. “Integration of long transmission lines in large-scale dq0 dynamic models”. In: *Electrical Engineering* (June 2017), pp. 1–10. DOI: 10.1007/s00202-017-0582-7.

[147] S. Golestan and J. M. Guerrero. “Conventional Synchronous Reference Frame Phase-Locked Loop is an Adaptive Complex Filter”. In: *IEEE Transactions on Industrial Electronics* 62.3 (Mar. 2015), pp. 1679–1682. ISSN: 0278-0046. DOI: 10.1109/TIE.2014.2341594.

[148] S. Golestan et al. “Performance Improvement of a Prefiltered Synchronous-Reference-Frame PLL by Using a PID-Type Loop Filter”. In: *IEEE Transactions on Industrial Electronics* 61.7 (July 2014), pp. 3469–3479. ISSN: 0278-0046. DOI: 10.1109/TIE.2013.2282607.

[149] A. Timbus et al. "Synchronization methods for three phase distributed power generation systems - An overview and evaluation". In: *2005 IEEE 36th Power Electronics Specialists Conference*. June 2005, pp. 2474–2481. DOI: 10.1109/PESC.2005.1581980.

[150] Z. Zou and M. Liserre. "Modeling Phase-locked Loop-based Synchronization in Grid-interfaced Converters". In: *IEEE Transactions on Energy Conversion* (2019), pp. 1–1. ISSN: 0885-8969. DOI: 10.1109/TEC.2019.2939425.

[151] G. Franklin, J. Powell, and A. Emami-Naeini. *Feedback Control Of Dynamic Systems*. 4th ed. Prentice Hall, 2002.

[152] F. Hans, W. Schumacher, and L. Harnefors. "Small-Signal Modeling of Three-Phase Synchronous Reference Frame Phase-Locked Loops". In: *IEEE Transactions on Power Electronics* 33.7 (July 2018), pp. 5556–5560. ISSN: 0885-8993. DOI: 10.1109/TPEL.2017.2783189.

[153] W. Du, X. Chen, and H. Wang. "Parameter tuning of the PLL to consider the effect on power system small-signal angular stability". In: *IET Renewable Power Generation* 12.1 (2018), pp. 1–8. ISSN: 1752-1416. DOI: 10.1049/iet-rpg.2016.0835.

[154] T. Midtsund, J. A. Suul, and T. Undeland. "Evaluation of current controller performance and stability for voltage source converters connected to a weak grid". en. In: *The 2nd International Symposium on Power Electronics for Distributed Generation Systems*. Hefei, China: IEEE, June 2010, pp. 382–388. ISBN: 978-1-4244-5669-7. DOI: 10.1109/PEDG.2010.5545794. URL: http://ieeexplore.ieee.org/document/5545794/ (visited on 02/17/2019).

[155] S. Chung. "Phase-locked loop for grid-connected three-phase power conversion systems". In: *IEE Proceedings - Electric Power Applications* 147.3 (May 2000), pp. 213–219. ISSN: 1350-2352. DOI: 10.1049/ip-epa:20000328.

[156] Matthew J Korytowski. "EFFECTS OF THE PHASE LOCKED LOOP ON THE STABILITY OF A VOLTAGE SOURCE CONVERTER IN A WEAK GRID ENVIRONMENT". en. PhD thesis. Pittsburgh: University of Pittsburgh, 2014.

[157] M. Barnes. "Phase-locked loops for grid-tied inverters: Comparison and testing". In: *8th IET International Conference on Power Electronics, Machines and Drives (PEMD 2016)*. Apr. 2016, pp. 1–6. DOI: 10.1049/cp.2016.0304.

[158] A. Nagliero et al. "Synchronization techniques for grid connected wind turbines". In: *2009 35th Annual Conference of IEEE Industrial Electronics*. Nov. 2009, pp. 4606–4613. DOI: 10.1109/IECON.2009.5414859.

[159] J. Rocabert et al. “Control of Power Converters in AC Microgrids”. In: *IEEE Transactions on Power Electronics* 27.11 (Nov. 2012), pp. 4734–4749. ISSN: 0885-8993. DOI: 10.1109/TPEL.2012.2199334.

[160] H. Han et al. “Review of Power Sharing Control Strategies for Islanding Operation of AC Microgrids”. In: *IEEE Transactions on Smart Grid* 7.1 (Jan. 2016), pp. 200–215. ISSN: 1949-3053. DOI: 10.1109/TSG.2015.2434849.

[161] Q. C. Zhong and G. Weiss. “Synchronverters: Inverters That Mimic Synchronous Generators”. In: *IEEE Transactions on Industrial Electronics* 58.4 (Apr. 2011), pp. 1259–1267. ISSN: 0278-0046. DOI: 10.1109/TIE.2010.2048839.

[162] Q. C. Zhong et al. “Self-Synchronized Synchronverters: Inverters Without a Dedicated Synchronization Unit”. In: *IEEE Transactions on Power Electronics* 29.2 (Feb. 2014), pp. 617–630. ISSN: 0885-8993. DOI: 10.1109/TPEL.2013.2258684.

[163] S. Dong and Y. C. Chen. “Adjusting Synchronverter Dynamic Response Speed via Damping Correction Loop”. In: *IEEE Transactions on Energy Conversion* 32.2 (June 2017), pp. 608–619. ISSN: 0885-8969. DOI: 10.1109/TEC.2016.2645450.

[164] V. Natarajan and G. Weiss. “Synchronverters With Better Stability Due to Virtual Inductors, Virtual Capacitors, and Anti-Windup”. In: *IEEE Transactions on Industrial Electronics* 64.7 (July 2017), pp. 5994–6004. ISSN: 0278-0046. DOI: 10.1109/TIE.2017.2674611.

[165] Hirofumi Akagi. *Instantaneous power theory and applications to power conditioning*. en. Second edition. IEEE Press series on power engineering. OCLC: ocn975024781. Hoboken, New Jersey: IEEE Press/Wiley, 2017. ISBN: 978-1-118-36210-5.

[166] Remus Teodorescu, Marco Liserre, and Pedro Rodríguez. *Grid Converters for Photovoltaic and Wind Power Systems: Teodorescu/Grid Converters for Photovoltaic and Wind Power Systems*. en. Chichester, UK: John Wiley & Sons, Ltd, Jan. 2011. ISBN: 978-0-470-66705-7 978-0-470-05751-3. DOI: 10.1002/9780470667057. URL: http://doi.wiley.com/10.1002/9780470667057 (visited on 03/04/2019).

[167] M. Kim and A. Kwasinski. “Stability characterization of inverter based microgrids considering configuration changes”. In: *2015 17th European Conference on Power Electronics and Applications (EPE'15 ECCE-Europe)*. Sept. 2015, pp. 1–10. DOI: 10.1109/EPE.2015.7311741.

[168] R. An et al. "Analysis and design of cutoff frequency for power calculation low-pass filters in droop control". In: *2017 IEEE 3rd International Future Energy Electronics Conference and ECCE Asia (IFEEC 2017 - ECCE Asia)*. June 2017, pp. 1596–1600. DOI: 10.1109/IFEEC.2017.7992285.

[169] Y. Song et al. "A Distributed Framework for Stability Evaluation and Enhancement of Inverter-Based Microgrids". In: *IEEE Transactions on Smart Grid* 8.6 (Nov. 2017), pp. 3020–3034. ISSN: 1949-3053. DOI: 10.1109/TSG.2017.2684426.

[170] P. J. Hart et al. "Effect of power measurement filter properties on CERTS microgrid control performance". In: *2015 IEEE 6th International Symposium on Power Electronics for Distributed Generation Systems (PEDG)*. June 2015, pp. 1–8. DOI: 10.1109/PEDG.2015.7223064.

[171] G. M. S. Azevedo et al. "Enhanced power calculator for droop control in single-phase systems". In: *2011 IEEE Energy Conversion Congress and Exposition*. Sept. 2011, pp. 391–396. DOI: 10.1109/ECCE.2011.6063796.

[172] Z. Ren et al. "Power calculation method used in wireless parallel inverters under nonlinear load conditions". In: *2010 Twenty-Fifth Annual IEEE Applied Power Electronics Conference and Exposition (APEC)*. Feb. 2010, pp. 1674–1677. DOI: 10.1109/APEC.2010.5433456.

[173] E. T. Andrade et al. "A novel power calculation method for droop-control microgrid systems". In: *2012 Twenty-Seventh Annual IEEE Applied Power Electronics Conference and Exposition (APEC)*. Feb. 2012, pp. 2254–2258. DOI: 10.1109/APEC.2012.6166136.

[174] K. De Brabandere et al. "A Voltage and Frequency Droop Control Method for Parallel Inverters". In: *IEEE Transactions on Power Electronics* 22.4 (July 2007), pp. 1107–1115. ISSN: 0885-8993. DOI: 10.1109/TPEL.2007.900456.

[175] M. C. Chandorkar, D. M. Divan, and R. Adapa. "Control of parallel connected inverters in standalone AC supply systems". In: *IEEE Transactions on Industry Applications* 29.1 (Jan. 1993), pp. 136–143. ISSN: 0093-9994. DOI: 10.1109/28.195899.

[176] A. Engler and N. Soultanis. "Droop control in LV-grids". In: *2005 International Conference on Future Power Systems*. Nov. 2005, 6 pp.–6. DOI: 10.1109/FPS.2005.204224.

[177] J. He and Y. W. Li. "An Enhanced Microgrid Load Demand Sharing Strategy". In: *IEEE Transactions on Power Electronics* 27.9 (Sept. 2012), pp. 3984–3995. ISSN: 0885-8993. DOI: 10.1109/TPEL.2012.2190099.

[178] A. Tuladhar et al. "Control of parallel inverters in distributed AC power systems with consideration of line impedance effect". In: *IEEE Transactions on Industry Applications* 36.1 (Jan. 2000), pp. 131–138. ISSN: 0093-9994. DOI: 10.1109/28.821807.

[179] J. C. Vasquez et al. "Adaptive Droop Control Applied to Voltage-Source Inverters Operating in Grid-Connected and Islanded Modes". In: *IEEE Transactions on Industrial Electronics* 56.10 (Oct. 2009), pp. 4088–4096. ISSN: 0278-0046. DOI: 10.1109/TIE.2009.2027921.

[180] Y. W. Li and C. Kao. "An Accurate Power Control Strategy for Power-Electronics-Interfaced Distributed Generation Units Operating in a Low-Voltage Multibus Microgrid". In: *IEEE Transactions on Power Electronics* 24.12 (Dec. 2009), pp. 2977–2988. ISSN: 0885-8993. DOI: 10.1109/TPEL.2009.2022828.

[181] J. M. Guerrero et al. "Decentralized Control for Parallel Operation of Distributed Generation Inverters Using Resistive Output Impedance". In: *IEEE Transactions on Industrial Electronics* 54.2 (Apr. 2007), pp. 994–1004. ISSN: 0278-0046. DOI: 10.1109/TIE.2007.892621.

[182] R. Wai, Q. Zhang, and Y. Wang. "A Novel Voltage Stabilization and Power Sharing Control Method Based on Virtual Complex Impedance for an Off-Grid Microgrid". In: *IEEE Transactions on Power Electronics* 34.2 (Feb. 2019), pp. 1863–1880. ISSN: 0885-8993. DOI: 10.1109/TPEL.2018.2831673.

[183] Y. A. I. Mohamed et al. "Seamless Formation and Robust Control of Distributed Generation Microgrids via Direct Voltage Control and Optimized Dynamic Power Sharing". In: *IEEE Transactions on Power Electronics* 27.3 (Mar. 2012), pp. 1283–1294. ISSN: 0885-8993. DOI: 10.1109/TPEL.2011.2164939.

[184] J. M. Guerrero et al. "Control Strategy for Flexible Microgrid Based on Parallel Line-Interactive UPS Systems". In: *IEEE Transactions on Industrial Electronics* 56.3 (Mar. 2009), pp. 726–736. ISSN: 0278-0046. DOI: 10.1109/TIE.2008.2009274.

[185] T. Wu et al. "A Unified Virtual Power Decoupling Method for Droop-Controlled Parallel Inverters in Microgrids". In: *IEEE Transactions on Power Electronics* 31.8 (Aug. 2016), pp. 5587–5603. ISSN: 0885-8993. DOI: 10.1109/TPEL.2015.2497972.

[186] P. Li et al. "Dynamic Power Conditioning Method of Microgrid Via Adaptive Inverse Control". In: *IEEE Transactions on Power Delivery* 30.2 (Apr. 2015), pp. 906–913. ISSN: 0885-8977. DOI: 10.1109/TPWRD.2014.2323083.

[187] Y. Li and Y. W. Li. "Power Management of Inverter Interfaced Autonomous Microgrid Based on Virtual Frequency-Voltage Frame". In: *IEEE Transactions on Smart Grid* 2.1 (Mar. 2011), pp. 30–40. ISSN: 1949-3053. DOI: 10.1109/TSG.2010.2095046.

[188] Y. Li and Y. W. Li. "Virtual frequency-voltage frame control of inverter based low voltage microgrid". In: *2009 IEEE Electrical Power Energy Conference (EPEC)*. Oct. 2009, pp. 1–6. DOI: 10.1109/EPEC.2009.5420973.

[189] A. Trivedi, D. K. Jain, and M. Singh. "A modified droop control method for parallel operation of VSI's in microgrid". In: *2013 IEEE Innovative Smart Grid Technologies-Asia (ISGT Asia)*. Nov. 2013, pp. 1–5. DOI: 10.1109/ISGT-Asia.2013.6698752.

[190] J. W. Simpson-Porco, F. Dörfler, and F. Bullo. "Voltage Stabilization in Microgrids via Quadratic Droop Control". In: *IEEE Transactions on Automatic Control* 62.3 (Mar. 2017), pp. 1239–1253. ISSN: 0018-9286. DOI: 10.1109/TAC.2016.2585094.

[191] A. Elrayyah, F. Cingoz, and Y. Sozer. "Construction of Nonlinear Droop Relations to Optimize Islanded Microgrid Operation". In: *IEEE Transactions on Industry Applications* 51.4 (July 2015), pp. 3404–3413. ISSN: 0093-9994. DOI: 10.1109/TIA.2014.2387484.

[192] N. Soni, S. Doolla, and M. C. Chandorkar. "Improvement of Transient Response in Microgrids Using Virtual Inertia". In: *IEEE Transactions on Power Delivery* 28.3 (July 2013), pp. 1830–1838. ISSN: 0885-8977. DOI: 10.1109/TPWRD.2013.2264738.

[193] J. Hu et al. "Virtual Flux Droop Method—A New Control Strategy of Inverters in Microgrids". In: *IEEE Transactions on Power Electronics* 29.9 (Sept. 2014), pp. 4704–4711. ISSN: 0885-8993. DOI: 10.1109/TPEL.2013.2286159.

[194] Y. Zhang, L. Xie, and Q. Ding. "Interactive Control of Coupled Microgrids for Guaranteed System-Wide Small Signal Stability". In: *IEEE Transactions on Smart Grid* 7.2 (Mar. 2016), pp. 1088–1096. ISSN: 1949-3053. DOI: 10.1109/TSG.2015.2495233.

[195] J. M. Guerrero et al. “Output impedance design of parallel-connected UPS inverters with wireless load-sharing control”. In: *IEEE Transactions on Industrial Electronics* 52.4 (Aug. 2005), pp. 1126–1135. ISSN: 0278-0046. DOI: 10.1109/TIE.2005.851634.

[196] O. Mo, S. D’Arco, and J. A. Suul. “Evaluation of Virtual Synchronous Machines With Dynamic or Quasi-Stationary Machine Models”. In: *IEEE Transactions on Industrial Electronics* 64.7 (July 2017), pp. 5952–5962. ISSN: 0278-0046. DOI: 10.1109/TIE.2016.2638810.

[197] Y. Hirase et al. “Analysis of Resonance in Microgrids and Effects of System Frequency Stabilization Using a Virtual Synchronous Generator”. In: *IEEE Journal of Emerging and Selected Topics in Power Electronics* 4.4 (Dec. 2016), pp. 1287–1298. ISSN: 2168-6777. DOI: 10.1109/JESTPE.2016.2581818.

[198] N. Soni, S. Doolla, and M. C. Chandorkar. “Inertia Design Methods for Islanded Microgrids Having Static and Rotating Energy Sources”. In: *IEEE Transactions on Industry Applications* 52.6 (Nov. 2016), pp. 5165–5174. ISSN: 0093-9994. DOI: 10.1109/TIA.2016.2597281.

[199] M. Ashabani and Y. A. I. Mohamed. “Novel Comprehensive Control Framework for Incorporating VSCs to Smart Power Grids Using Bidirectional Synchronous-VSC”. In: *IEEE Transactions on Power Systems* 29.2 (Mar. 2014), pp. 943–957. ISSN: 0885-8950. DOI: 10.1109/TPWRS.2013.2287291.

[200] J. Alipoor, Y. Miura, and T. Ise. “Power System Stabilization Using Virtual Synchronous Generator With Alternating Moment of Inertia”. In: *IEEE Journal of Emerging and Selected Topics in Power Electronics* 3.2 (June 2015), pp. 451–458. ISSN: 2168-6777. DOI: 10.1109/JESTPE.2014.2362530.

[201] Hassan Bevrani, Toshifumi Ise, and Yushi Miura. “Virtual synchronous generators: A survey and new perspectives”. In: *International Journal of Electrical Power & Energy Systems* 54 (Jan. 2014), pp. 244–254. ISSN: 0142-0615. DOI: 10.1016/j.ijepes.2013.07.009. (Visited on 10/06/2018).

[202] S. D’Arco and J. A. Suul. “Virtual synchronous machines — Classification of implementations and analysis of equivalence to droop controllers for microgrids”. In: *2013 IEEE Grenoble Conference*. June 2013, pp. 1–7. DOI: 10.1109/PTC.2013.6652456.

[203] D. Arricibita, P. Sanchis, and L. Marroyo. "Virtual synchronous generators classification and common trends". In: *IECON 2016 - 42nd Annual Conference of the IEEE Industrial Electronics Society*. Oct. 2016, pp. 2433–2438. DOI: 10.1109/IECON.2016.7793025.

[204] S. D'Arco, J. A. Suul, and O. B. Fosso. "Small-signal modelling and parametric sensitivity of a Virtual Synchronous Machine". In: *2014 Power Systems Computation Conference*. Aug. 2014, pp. 1–9. DOI: 10.1109/PSCC.2014.7038410.

[205] H. Wu et al. "Small-Signal Modeling and Parameters Design for Virtual Synchronous Generators". In: *IEEE Transactions on Industrial Electronics* 63.7 (July 2016), pp. 4292–4303. ISSN: 0278-0046. DOI: 10.1109/TIE.2016.2543181.

[206] J. Alipoor, Y. Miura, and T. Ise. "Stability Assessment and Optimization Methods for Microgrid With Multiple VSG Units". In: *IEEE Transactions on Smart Grid* 9.2 (Mar. 2018), pp. 1462–1471. ISSN: 1949-3053. DOI: 10.1109/TSG.2016.2592508.

[207] J. Liu, Y. Miura, and T. Ise. "Comparison of Dynamic Characteristics Between Virtual Synchronous Generator and Droop Control in Inverter-Based Distributed Generators". In: *IEEE Transactions on Power Electronics* 31.5 (May 2016), pp. 3600–3611. ISSN: 0885-8993. DOI: 10.1109/TPEL.2015.2465852.

[208] Salvatore D'Arco, Jon Are Suul, and Olav B. Fosso. "A Virtual Synchronous Machine implementation for distributed control of power converters in SmartGrids". In: *Electric Power Systems Research* 122 (May 2015), pp. 180–197. ISSN: 0378-7796. DOI: 10.1016/j.epsr.2015.01.001. URL: http://www.sciencedirect.com/science/article/pii/S0378779615000024 (visited on 05/06/2019).

[209] S. D'Arco and J. A. Suul. "Equivalence of Virtual Synchronous Machines and Frequency-Droops for Converter-Based MicroGrids". In: *IEEE Transactions on Smart Grid* 5.1 (Jan. 2014), pp. 394–395. ISSN: 1949-3053. DOI: 10.1109/TSG.2013.2288000.

[210] C. Dou et al. "Improved droop control based on virtual impedance and virtual power source in low-voltage microgrid". In: *Transmission Distribution IET Generation* 11.4 (2017), pp. 1046–1054. ISSN: 1751-8687. DOI: 10.1049/iet-gtd.2016.1492.

[211] W. Yao et al. "Design and Analysis of the Droop Control Method for Parallel Inverters Considering the Impact of the Complex Impedance on the Power Sharing". In: *IEEE Transactions on Industrial Electronics* 58.2 (Feb. 2011), pp. 576–588. ISSN: 0278-0046. DOI: 10.1109/TIE.2010.2046001.

[212] J. He and Y. W. Li. "Analysis, Design, and Implementation of Virtual Impedance for Power Electronics Interfaced Distributed Generation". In: *IEEE Transactions on Industry Applications* 47.6 (Nov. 2011), pp. 2525–2538. ISSN: 0093-9994. DOI: 10.1109/TIA.2011.2168592.

[213] X. Wang et al. "Virtual-Impedance-Based Control for Voltage-Source and Current-Source Converters". In: *IEEE Transactions on Power Electronics* 30.12 (Dec. 2015), pp. 7019–7037. ISSN: 0885-8993. DOI: 10.1109/TPEL.2014.2382565.

[214] X. Wu, C. Shen, and R. Iravani. "Feasible Range and Optimal Value of the Virtual Impedance for Droop-Based Control of Microgrids". In: *IEEE Transactions on Smart Grid* 8.3 (May 2017), pp. 1242–1251. ISSN: 1949-3053. DOI: 10.1109/TSG.2016.2519454.

[215] Y. Zhu et al. "A Virtual Impedance Optimization Method for Reactive Power Sharing in Networked Microgrid". In: *IEEE Transactions on Power Electronics* 31.4 (Apr. 2016), pp. 2890–2904. ISSN: 0885-8993. DOI: 10.1109/TPEL.2015.2450360.

[216] P. Zhang et al. "Power decoupling strategy based on 'virtual negative resistor' for inverters in low-voltage microgrids". In: *IET Power Electronics* 9.5 (2016), pp. 1037–1044. ISSN: 1755-4535. DOI: 10.1049/iet-pel.2015.0137.

[217] J. Schiffer et al. "Voltage Stability and Reactive Power Sharing in Inverter-Based Microgrids With Consensus-Based Distributed Voltage Control". In: *IEEE Transactions on Control Systems Technology* 24.1 (Jan. 2016), pp. 96–109. ISSN: 1063-6536. DOI: 10.1109/TCST.2015.2420622.

[218] H. Mahmood, D. Michaelson, and J. Jiang. "Accurate Reactive Power Sharing in an Islanded Microgrid Using Adaptive Virtual Impedances". In: *IEEE Transactions on Power Electronics* 30.3 (Mar. 2015), pp. 1605–1617. ISSN: 0885-8993. DOI: 10.1109/TPEL.2014.2314721.

[219] Qing-Chang Zhong and Tomas Hornik. *Control of Power Inverters in Renewable Energy and Smart Grid Integration: Zhong/Control*. en. Chichester, West Sussex, United Kingdom: John Wiley & Sons, Ltd., Dec. 2012. ISBN: 978-1-118-48180-6 978-0-470-66709-5. DOI: 10.1002/9781118481806. URL: http://doi.wiley.com/10.1002/9781118481806 (visited on 05/28/2020).

[220] Joachim Specovius. *Grundkurs Leistungselektronik: Bauelemente, Schaltungen und Systeme*. de. 7., aktualisierte und überarb. Aufl. Lehrbuch. OCLC: 913015356. Wiesbaden: Springer Vieweg, 2015. ISBN: 978-3-658-03308-8 978-3-658-03309-5.

[221] Suleiman M. Sharkh et al. *Power Electronic Converters for Microgrids*. en. Singapore: John Wiley & Sons, Singapore Pte. Ltd, Apr. 2014. ISBN: 978-0-470-82405-4 978-0-470-82403-0. DOI: 10.1002/9780470824054. URL: http://doi.wiley.com/10.1002/9780470824054 (visited on 05/07/2019).

[222] Seddik Bacha, Iulian Munteanu, and Antoneta Iuliana Bratcu. *Power Electronic Converters Modeling and Control*. en. Advanced Textbooks in Control and Signal Processing. London: Springer London, 2014. ISBN: 978-1-4471-5477-8 978-1-4471-5478-5. DOI: 10.1007/978-1-4471-5478-5. (Visited on 03/15/2019).

[223] D. Pan et al. "Analysis and Design of Current Control Schemes for LCL-Type Grid-Connected Inverter Based on a General Mathematical Model". In: *IEEE Transactions on Power Electronics* 32.6 (June 2017), pp. 4395–4410. ISSN: 0885-8993. DOI: 10.1109/TPEL.2016.2602219.

[224] Marco Liserre *, Frede Blaabjerg, and Antonio Dell'Aquila. "Step-by-step design procedure for a grid-connected three-phase PWM voltage source converter". en. In: *International Journal of Electronics* 91.8 (Aug. 2004), pp. 445–460. ISSN: 0020-7217, 1362-3060. DOI: 10.1080/00207210412331306186. URL: http://www.tandfonline.com/doi/abs/10.1080/00207210412331306186 (visited on 03/04/2019).

[225] M. Rizo et al. "Voltage Control Architectures for the Universal Operation of DPGS". In: *IEEE Transactions on Industrial Informatics* 11.2 (Apr. 2015), pp. 313–321. ISSN: 1551-3203. DOI: 10.1109/TII.2015.2389657.

[226] Aris Gkountaras. *Modeling techniques and control strategies for inverter dominated microgrids*. en. Vol. 2. Berlin: Universitaetsverlag der TU Berlin, 2017.

[227] A. A. Rockhill et al. "Grid-Filter Design for a Multimegawatt Medium-Voltage Voltage-Source Inverter". In: *IEEE Transactions on Industrial Electronics* 58.4 (Apr. 2011), pp. 1205–1217. ISSN: 0278-0046. DOI: 10.1109/TIE.2010.2087293.

[228] M. Liserre, F. Blaabjerg, and S. Hansen. "Design and control of an LCL-filter-based three-phase active rectifier". In: *IEEE Transactions on Industry Applications* 41.5 (Sept. 2005), pp. 1281–1291. ISSN: 0093-9994. DOI: 10.1109/TIA.2005.853373.

[229] I. J. Gabe, V. F. Montagner, and H. Pinheiro. "Design and Implementation of a Robust Current Controller for VSI Connected to the Grid Through an LCL Filter". In: *IEEE Transactions on Power Electronics* 24.6 (June 2009), pp. 1444–1452. ISSN: 0885-8993. DOI: 10.1109/TPEL.2009.2016097.

[230] Amirnaser Yazdani and Reza Iravani. *Voltage-Sourced Converters in Power Systems*. en. Hoboken, NJ, USA: John Wiley & Sons, Inc., Jan. 2010. ISBN: 978-0-470-55157-8 978-0-470-52156-4. DOI: 10.1002/9780470551578. (Visited on 02/17/2019).

[231] Poh Chiang Loh and D. G. Holmes. "Analysis of multiloop control strategies for LC/CL/LCL-filtered voltage-source and current-source inverters". In: *IEEE Transactions on Industry Applications* 41.2 (Mar. 2005), pp. 644–654. ISSN: 0093-9994. DOI: 10.1109/TIA.2005.844860.

[232] Y. Tao et al. "Analysis and Mitigation of Inverter Output Impedance Impacts for Distributed Energy Resource Interface". In: *IEEE Transactions on Power Electronics* 30.7 (July 2015), pp. 3563–3576. ISSN: 0885-8993. DOI: 10.1109/TPEL.2014.2339849.

[233] Yemi Ojo, Jeremy Watson, and Ioannis Lestas. "A Review of Reduced-Order Models for Microgrids: Simplifications vs Accuracy". In: *arXiv:2003.04923 [math]* (Mar. 2020). arXiv: 2003.04923. URL: http://arxiv.org/abs/2003.04923 (visited on 03/23/2020).

[234] T. C. Green and M. Prodanović. "Control of inverter-based micro-grids". In: *Electric Power Systems Research*. Distributed Generation 77.9 (July 2007), pp. 1204–1213. ISSN: 0378-7796. DOI: 10.1016/j.epsr.2006.08.017. URL: http://www.sciencedirect.com/science/article/pii/S037877960600191X (visited on 03/31/2019).

[235] N. Kroutikova, C. a Hernandez-Aramburo, and T. C. Green. "State-space model of grid-connected inverters under current control mode". In: *IET Electric Power Applications* 1.3 (May 2007), pp. 329–338. ISSN: 1751-8660. DOI: 10.1049/iet-epa:20060276.

[236] A. H. Kasem Alaboudy, H. H. Zeineldin, and J. Kirtley. "Microgrid Stability Characterization Subsequent to Fault-Triggered Islanding Incidents". In: *IEEE Transactions on Power Delivery* 27.2 (Apr. 2012), pp. 658–669. ISSN: 0885-8977. DOI: 10.1109/TPWRD.2012.2183150.

[237] Daniel Scott Prull. "Design and integration of an isolated microgrid with a high penetration of renewable generation". PhD thesis. University of California, Berkeley, 2008.

[238] Arthur Fitzgerald. *Electric Machinery*. New York, NY: McGraw-Hill, 2003.

[239] Melkebeek, J.A. *Electrical machines and drives*. en. New York, NY: Springer Berlin Heidelberg, 2018. ISBN: 978-3-319-72729-5.

[240] Chee-Mun Ong. *Dynamic simulation of electric machinery: using MATLAB/SIMULINK*. Vol. 5. Prentice hall PTR Upper Saddle River, NJ, 1998.

[241] Liwei Wang. "Modeling of ac machines using a voltage-behind-reactance formulation for simulation of electromagnetic transients in power systems". eng. PhD thesis. University of British Columbia, 2010. DOI: 10.14288/1.0069215. URL: https://open.library.ubc.ca/cIRcle/collections/ubctheses/24/items/1.0069215 (visited on 07/23/2018).

[242] S. Krishnamurthy, T. M. Jahns, and R. H. Lasseter. "The operation of diesel gensets in a CERTS microgrid". In: *2008 IEEE Power and Energy Society General Meeting - Conversion and Delivery of Electrical Energy in the 21st Century*. July 2008, pp. 1–8. DOI: 10.1109/PES.2008.4596500.

[243] Les Hajagos and D.C. Lee. "IEEE Recommended Practice for Excitation System Models for Power System Stability StudiesLes". In: *IEEE Std 421.5-2005 (Revision of IEEE Std 421.5-1992)* (Apr. 2006), pp. 1–93. DOI: 10.1109/IEEESTD.2006.99499.

[244] S. Eberlein, A. Heider, and K. Rudion. "Modelling and Control Optimization of Diesel Synchronous Generators in LV Microgrids". In: *2018 IEEE PES Innovative Smart Grid Technologies Conference Europe (ISGT-Europe)*. Oct. 2018, pp. 1–6. DOI: 10.1109/ISGTEurope.2018.8571786.

[245] Les Hajagos, Robert Thornton-Jones, and Leonardo Lima. "IEEE Recommended Practice for Excitation System Models for Power System Stability Studies". In: *IEEE Std 421.5-2016 (Revision of IEEE Std 421.5-2005)* (Aug. 2016), pp. 1–207. DOI: 10.1109/IEEESTD.2016.7553421.

[246] Johanna Salazar, Fernando Tadeo, and Cesar Prada. "Modelling of Diesel Generator Sets That Assist Off-Grid Renewable Energy Micro-grids". en. In: *Renewable Energy and Sustainable Development* 1.1 (Aug. 2015), pp. 72–80. ISSN: 2356-8569. DOI: 10.21622/resd.2015.01.1.072. URL: http://apc.aast.edu/ojs/index.php/RESD/article/view/01.1.072 (visited on 03/20/2018).

[247] K. E. Yeager and J. R. Willis. "Modeling of emergency diesel generators in an 800 megawatt nuclear power plant". In: *IEEE Transactions on Energy Conversion* 8.3 (Sept. 1993), pp. 433–441. ISSN: 0885-8969. DOI: 10.1109/60.257056.

[248] L. N. Hannett et al. "Validation of Nuclear Plant Auxiliary Power Supply By Test". In: *IEEE Transactions on Power Apparatus and Systems* PAS-101.9 (Sept. 1982), pp. 3068–3074. ISSN: 0018-9510. DOI: 10.1109/TPAS.1982.317551.

[249] *Model the dynamics of three-phase asynchronous machine - Simulink - MathWorks*. URL: https://de.mathworks.com/help/physmod/sps/powersys/ref/asynchronousmachine.html (visited on 01/13/2020).

[250] Gonzalo Abad et al. *Doubly Fed Induction Machine: Modeling and Control for Wind Energy Generation Applications*. Wiley-IEEE Press, 2011. ISBN: 978-1-118-10496-5. DOI: 10.1002/9781118104965.fmatter. URL: https://ieeexplore.ieee.org/xpl/articleDetails.jsp?arnumber=6047771 (visited on 04/12/2018).

[251] W. He, X. Yuan, and J. Hu. "Inertia Provision and Estimation of PLL-Based DFIG Wind Turbines". In: *IEEE Transactions on Power Systems* 32.1 (Jan. 2017), pp. 510–521. ISSN: 0885-8950. DOI: 10.1109/TPWRS.2016.2556721.

[252] J. B. Ekanayake, L. Holdsworth, and N. Jenkins. "Comparison of 5th order and 3rd order machine models for doubly fed induction generator (DFIG) wind turbines". In: *Electric Power Systems Research* 67.3 (Dec. 2003), pp. 207–215. ISSN: 0378-7796. DOI: 10.1016/S0378-7796(03)00109-3. (Visited on 04/23/2018).

[253] Francisco Diaz-Gonzalez et al. "Participation of wind power plants in system frequency control: Review of grid code requirements and control methods". en. In: *Renewable and Sustainable Energy Reviews* 34 (June 2014), pp. 551–564. ISSN: 1364-0321. DOI: 10.1016/j.rser.2014.03.040. URL: http://www.sciencedirect.com/science/article/pii/S1364032114002019 (visited on 01/14/2020).

[254] Xue Yingcheng and Tai Nengling. "Review of contribution to frequency control through variable speed wind turbine". en. In: *Renewable Energy* 36.6 (June 2011), pp. 1671–1677. ISSN: 0960-1481. DOI: 10.1016/j.renene.2010.11.009. URL: http://www.sciencedirect.com/science/article/pii/S0960148110005112 (visited on 01/14/2020).

[255] RogÉrio G. de Almeida and J. A. Pecas Lopes. "Participation of Doubly Fed Induction Wind Generators in System Frequency Regulation". In: *IEEE Transactions on Power Systems* 22.3 (Aug. 2007), pp. 944–950. ISSN: 1558-0679. DOI: 10.1109/TPWRS.2007.901096.

[256] Z. Zhang et al. "Coordinated frequency regulation by doubly fed induction generator-based wind power plants". In: *IET Renewable Power Generation* 6.1 (Jan. 2012), pp. 38–47. ISSN: 1752-1416. DOI: 10.1049/iet-rpg.2010.0208.

[257] Davood Raoofsheibani, Ehsan Abbasi, and Klaus Pfeiffer. "Provision of primary control reserve by DFIG-based wind farms in compliance with ENTSO-E frequency grid codes". In: *IEEE PES Innovative Smart Grid Technologies, Europe*. ISSN: 2165-4824. Oct. 2014, pp. 1–6. DOI: 10.1109/ISGTEurope.2014.7028810.

[258] Simon Eberlein and Krzysztof Rudion. "Influence of PLL on Synthetic Inertia of DFIG Wind Turbine in Droop Controlled Microgrids". In: *IET Renewable Power Generation, Copenhagen*. IET Renewable Power Generation, Copenhagen (2018).

[259] D. Zhang et al. "Impacts of PLL on the DFIG-based WTG's electromechanical response under transient conditions: analysis and modeling". In: *CSEE Journal of Power and Energy Systems* 2.2 (June 2016), pp. 30–39. DOI: 10.17775/CSEEJPES.2016.00019.

[260] J. Ma et al. "Research on the Impact of DFIG Virtual Inertia Control on Power System Small-Signal Stability Considering the Phase-Locked Loop". In: *IEEE Transactions on Power Systems* 32.3 (May 2017), pp. 2094–2105. ISSN: 0885-8950. DOI: 10.1109/TPWRS.2016.2594781.

[261] J. Hu et al. "Modeling of Grid-Connected DFIG-Based Wind Turbines for DC-Link Voltage Stability Analysis". In: *IEEE Transactions on Sustainable Energy* 6.4 (Oct. 2015), pp. 1325–1336. ISSN: 1949-3029. DOI: 10.1109/TSTE.2015.2432062.

[262] J. Morren et al. "Wind turbines emulating inertia and supporting primary frequency control". In: *IEEE Transactions on Power Systems* 21.1 (Feb. 2006), pp. 433–434. ISSN: 0885-8950. DOI: 10.1109/TPWRS.2005.861956.

[263] N. W. Miller, K. Clark, and M. Shao. "Frequency responsive wind plant controls: Impacts on grid performance". In: *2011 IEEE Power and Energy Society General Meeting* (July 2011), pp. 1–8.

[264] H. Geng, Xinze Xi, and Geng Yang. "Small-signal stability of power system integrated with ancillary-controlled large-scale DFIG-based wind farm". In: *IET Renewable Power Generation* 11.8 (2017), pp. 1191–1198. ISSN: 1752-1416. DOI: 10.1049/iet-rpg.2016.0078.

[265] X. Xi, H. Geng, and G. Yang. "Enhanced model of the doubly fed induction generator-based wind farm for small-signal stability studies of weak power system". In: *IET Renewable Power Generation* 8.7 (Sept. 2014), pp. 765–774. ISSN: 1752-1416. DOI: 10.1049/iet-rpg.2013.0394.

[266] J. Ma, Y. Shen, and Y. Zhang. “Dynamic characteristics of DFIG frequency oscillation of wind turbines with virtual inertia control”. In: *The Journal of Engineering* 2017.13 (2017), pp. 2525–2529. DOI: 10.1049/joe.2017.0782.

[267] I. D. Margaris et al. “Frequency Control in Autonomous Power Systems With High Wind Power Penetration”. In: *IEEE Transactions on Sustainable Energy* 3.2 (Apr. 2012), pp. 189–199. ISSN: 1949-3029. DOI: 10.1109/TSTE.2011.2174660.

[268] C.W. Taylor and W.W. Price. “Standard load models for power flow and dynamic performance simulation”. In: *IEEE Transactions on Power Systems* 10.3 (Aug. 1995), pp. 1302–1313. ISSN: 0885-8950. DOI: 10.1109/59.466523.

[269] Inés Romero Navarro, Lunds universitet, and Institutionen för industriell elektroteknik och automation. “Dynamic load models for power systems: estimation of time-varying parameters during normal operation”. en. OCLC: 186507903. PhD thesis. Lund: Dept. of Industrial Electrical Engineering and Automation [Institutionen foer industriell elektroteknik och automation], Univ., 2002.

[270] Adam John Collin. “Advanced Load Modelling for Power System Studies”. en. PhD thesis. University of Edinburgh, 2013.

[271] Koji Yamashita and Sergio Martinez Villanueva. “Initial Results of International Survey on Industrial Practice on Power System Load Modelling Conducted by CIGRE WG C4.605”. en. In: 2011, p. 9.

[272] A. Kahrobaeian and Y. A. I. Mohamed. “Analysis and Mitigation of Low-Frequency Instabilities in Autonomous Medium-Voltage Converter-Based Microgrids With Dynamic Loads”. In: *IEEE Transactions on Industrial Electronics* 61.4 (Apr. 2014), pp. 1643–1658. ISSN: 0278-0046. DOI: 10.1109/TIE.2013.2264790.

[273] J. Chen and J. Chen. “Stability Analysis and Parameters Optimization of Islanded Microgrid With Both Ideal and Dynamic Constant Power Loads”. In: *IEEE Transactions on Industrial Electronics* 65.4 (Apr. 2018), pp. 3263–3274. ISSN: 0278-0046. DOI: 10.1109/TIE.2017.2756588.

[274] Zhuoli Zhao et al. “Dynamic modeling, sensitivity assessment, and design of VSC-based microgrids with composite loads”. en. In: *J. Power Electron.* 20.1 (Jan. 2020), pp. 245–259. ISSN: 1598-2092, 2093-4718. DOI: 10.1007/s43236-019-00031-4. URL: http://link.springer.com/10.1007/s43236-019-00031-4 (visited on 04/06/2020).

[275] C. Jin et al. "A seamless transfer strategy of islanded and grid-connected mode switching for microgrid based on droop control". In: *2012 IEEE Energy Conversion Congress and Exposition (ECCE)*. Sept. 2012, pp. 969–973. DOI: 10.1109/ECCE.2012.6342714.

[276] Y. Wang et al. "Small-Signal Stability Analysis of Inverter-Fed Power Systems Using Component Connection Method". In: *IEEE Transactions on Smart Grid* 9.5 (Sept. 2018), pp. 5301–5310. ISSN: 1949-3053. DOI: 10.1109/TSG.2017.2686841.

[277] Nagaraju Pogaku. "Analysis, Control and Testing of Inverter-Based Distributed Generation in Standalone and Grid-Connected". en. PhD thesis. London: Imperial College London, 2006.

[278] K. Yu et al. "Analysis and Optimization of Droop Controller for Microgrid System Based on Small-Signal Dynamic Model". In: *IEEE Transactions on Smart Grid* 7.2 (Mar. 2016), pp. 695–705. ISSN: 1949-3053. DOI: 10.1109/TSG.2015.2501316.

[279] Kwang Y. Lee and Mohamed A. El-Sharkawi. *Modern heuristic optimization techniques: theory and applications to power systems*. en. Piscataway, N.J. : Hoboken, N.J: IEEE Press ; Wiley-Interscience, 2008. ISBN: 978-0-471-45711-4.

[280] Jizhong Zhu. *Optimization of power system operation*. en. IEEE Press series on power engineering. Piscataway, N.J. : Chichester: Wiley-IEEE, 2009. ISBN: 978-0-470-29888-6.

[281] S. Dong and Y. C. Chen. "A Method to Directly Compute Synchronverter Parameters for Desired Dynamic Response". In: *IEEE Transactions on Energy Conversion* 33.2 (June 2018), pp. 814–825. ISSN: 0885-8969. DOI: 10.1109/TEC.2017.2771401.

[282] Simon Eberlein, Marius Radloff, and Krzysztof Rudion. "Small-Signal Stability Optimization of LV Microgrids with Grid-Forming and Grid-Supporting Inverters". en. In: *Cired International Conference on Electricity Distribution*. Madrid, 2019, p. 5.

[283] H. Bevrani and S. Shokoohi. "An Intelligent Droop Control for Simultaneous Voltage and Frequency Regulation in Islanded Microgrids". In: *IEEE Transactions on Smart Grid* 4.3 (Sept. 2013), pp. 1505–1513. ISSN: 1949-3053. DOI: 10.1109/TSG.2013.2258947.

[284] S. Liu, X. Wang, and P. X. Liu. "A Stochastic Stability Enhancement Method of Grid-Connected Distributed Energy Storage Systems". In: *IEEE Transactions on Smart Grid* 8.5 (Sept. 2017), pp. 2062–2070. ISSN: 1949-3053. DOI: 10.1109/TSG.2015.2514286.

[285] Z. Peng et al. "The Application of Microgrids Based on Droop Control With Coupling Compensation and Inertia". In: *IEEE Transactions on Sustainable Energy* 9.3 (July 2018), pp. 1157–1168. ISSN: 1949-3029. DOI: 10.1109/TSTE.2017.2773512.

[286] I. Chung et al. "Control Methods of Inverter-Interfaced Distributed Generators in a Microgrid System". In: *IEEE Transactions on Industry Applications* 46.3 (May 2010), pp. 1078–1088. ISSN: 0093-9994. DOI: 10.1109/TIA.2010.2044970.

[287] M. A. Hassan and M. A. Abido. "Optimal Design of Microgrids in Autonomous and Grid-Connected Modes Using Particle Swarm Optimization". In: *IEEE Transactions on Power Electronics* 26.3 (Mar. 2011), pp. 755–769. ISSN: 0885-8993. DOI: 10.1109/TPEL.2010.2100101.

[288] D. K. Dheer et al. "Effect of placement of droop based generators in distribution network on small signal stability margin and network loss". In: *International Journal of Electrical Power & Energy Systems* 88 (June 2017), pp. 108–118. ISSN: 0142-0615. DOI: 10.1016/j.ijepes.2016.12.014. (Visited on 12/19/2018).

[289] Thomas Weise. *Global Optimization Algorithms - Theory and Application*. en. Second. 2009.

[290] Jonas Winkler. "Sequenzoptimierung eines synthetischen bifunktionalen Proteins durch multikriterielle genetische Algorithmen". de. PhD thesis. Essen: Universitaet Duisburg-Essen, 2012.

[291] T. Baeck, DB Fogel, and Michalewicz Z. *Handbook of evolutionary computation*. New York: Oxford University Press, 1997.

[292] L. Davis. *Handbook of genetic algorithms*. New York: Van Nostrand Reinhold, 1991.

[293] T. Baeck and H. Schwefel. "An Overview of Evolutionary Algorithms for Parameter Optimization". In: *Evolutionary Computation* 1.1 (Mar. 1993), pp. 1–23. ISSN: 1063-6560. DOI: 10.1162/evco.1993.1.1.1.

[294] D. B. Fogel and J. W. Atmar. "Comparing genetic operators with gaussian mutations in simulated evolutionary processes using linear systems". en. In: *Biol. Cybern.* 63.2 (June 1990), pp. 111–114. ISSN: 1432-0770. DOI: 10.1007/BF00203032. URL: https://doi.org/10.1007/BF00203032 (visited on 06/04/2019).

[295] D. H. Wolpert and W. G. Macready. "No free lunch theorems for optimization". In: *IEEE Transactions on Evolutionary Computation* 1.1 (Apr. 1997), pp. 67–82. ISSN: 1089-778X. DOI: 10.1109/4235.585893.

[296] D. B. Fogel and A. Ghozeil. "A note on representations and variation operators". In: *IEEE Transactions on Evolutionary Computation* 1.2 (July 1997), pp. 159–161. ISSN: 1089-778X. DOI: 10.1109/4235.687882.

[297] Hans-Paul Schwefel. *Evolution and Optimum Seeking*. en. New York: John Wiley & Sons, 1995.

[298] P. J. Angeline, G. M. Saunders, and J. B. Pollack. "An evolutionary algorithm that constructs recurrent neural networks". In: *IEEE Transactions on Neural Networks* 5.1 (Jan. 1994), pp. 54–65. ISSN: 1045-9227. DOI: 10.1109/72.265960.

[299] Robert Ghanea-Hercock. *Applied Evolutionary Algorithms in Java*. en. New York: Springer-Verlag, 2003. ISBN: 978-0-387-95568-1. URL: https://www.springer.com/gp/book/9780387955681 (visited on 06/05/2019).

[300] James E. Baker. "Reducing Bias and Inefficiency in the Selection Algorithm". In: *Proceedings of the Second International Conference on Genetic Algorithms on Genetic Algorithms and Their Application*. event-place: Cambridge, Massachusetts, USA. Hillsdale, NJ, USA: L. Erlbaum Associates Inc., 1987, pp. 14–21. ISBN: 978-0-8058-0158-3. URL: http://dl.acm.org/citation.cfm?id=42512.42515 (visited on 06/05/2019).

[301] Gilbert Syswerda. "Uniform Crossover in Genetic Algorithms". In: *Proceedings of the 3rd International Conference on Genetic Algorithms*. San Francisco, CA, USA: Morgan Kaufmann Publishers Inc., 1989, pp. 2–9. ISBN: 978-1-55860-066-9. URL: http://dl.acm.org/citation.cfm?id=645512.657265 (visited on 06/04/2019).

[302] Kalyanmoy Deb and Ram Bhushan Agrawal. "Simulated Binary Crossover for Continuous Search Space". In: *Complex Systems* 9 (1995).

[303] Francisco Herrera, Manuel Lozano, and Ana M. Sánchez. "A taxonomy for the crossover operator for real-coded genetic algorithms: An experimental study". In: *Int. J. Intell. Syst.* 18 (2003), pp. 309–338. DOI: 10.1002/int.10091.

[304] A. Rogers and A. Prugel-Bennett. “Genetic drift in genetic algorithm selection schemes”. In: *IEEE Transactions on Evolutionary Computation* 3.4 (Nov. 1999), pp. 298–303. ISSN: 1089-778X. DOI: 10.1109/4235.797972.

[305] Henry Fuchs. “On visible surface generation by a priori tree structures”. en. In: *Proceedings of the 7th annual conference on Computer graphics and interactive techniques*. Seattle, Washington, USA, 1980, p. 10.

[306] Jan Schaefer. *KD-Baeume*. University of Bielefeld, 2018. URL: https://www.techfak.uni-bielefeld.de/~mhanheid/lehre/alggeo/kdbaeume.pdf.

[307] S. Y. Yuen and C. K. Chow. “A Genetic Algorithm That Adaptively Mutates and Never Revisits”. In: *IEEE Transactions on Evolutionary Computation* 13.2 (Apr. 2009), pp. 454–472. ISSN: 1089-778X. DOI: 10.1109/TEVC.2008.2003008.

[308] C. K. Chow and S. Y. Yuen. “An Evolutionary Algorithm That Makes Decision Based on the Entire Previous Search History”. In: *IEEE Transactions on Evolutionary Computation* 15.6 (Dec. 2011), pp. 741–769. ISSN: 1089-778X. DOI: 10.1109/TEVC.2010.2040180.

[309] Marius Radloff. “Evolutionary algorithm for optimization compute-intensive fitness functions”. MA thesis. Stuttgart, Germany: University of Stuttgart, 2019.

[310] Anya Heider. “Optimierung der Regelparameter dezentraler Energieanlagen mittels künstlicher Intelligenz”. MA thesis. Stuttgart, Germany: University of Stuttgart, 2018.

[311] J.G. Digalakis and K.G. Margaritis. “On benchmarking functions for genetic algorithms”. en. In: *International Journal of Computer Mathematics* 77.4 (Jan. 2001), pp. 481–506. ISSN: 0020-7160, 1029-0265. DOI: 10.1080/00207160108805080. URL: http://www.tandfonline.com/doi/abs/10.1080/00207160108805080 (visited on 01/20/2020).

[312] “Benchmark Systems for Network Integration of Renewable and Distributed Energy Resources”. EN. In: *Cigre Electra* (2014). Library Catalog: e-cigre.org. URL: https://e-cigre.org/publication/ELT_273_8-benchmark-systems-for-network-integration-of-renewable-and-distributed-energy-resources (visited on 06/23/2020).

[313] J. Elizondo et al. “Robust small signal stability for microgrids under uncertainty”. In: *2015 IEEE 6th International Symposium on Power Electronics for Distributed Generation Systems (PEDG)*. June 2015, pp. 1–8. DOI: 10.1109/PEDG.2015.7223059.

[314] M. C. Pulcherio, M. S. Illindala, and R. K. Yedavalli. “Robust Stability Region of a Microgrid Under Parametric Uncertainty Using Bialternate Sum Matrix Approach”. In: *IEEE Transactions on Power Systems* 33.5 (Sept. 2018), pp. 5553–5562. ISSN: 0885-8950. DOI: 10.1109/TPWRS.2018.2815980.

[315] A. U. Krismanto, N. Mithulananthan, and I. Kamwa. “Oscillatory stability assessment of microgrid in autonomous operation with uncertainties”. In: *IET Renewable Power Generation* 12.4 (2018), pp. 494–504. ISSN: 1752-1416. DOI: 10.1049/iet-rpg.2017.0579.

[316] A. Adib et al. “On Stability of Voltage Source Inverters in Weak Grids”. In: *IEEE Access* 6 (2018), pp. 4427–4439. DOI: 10.1109/ACCESS.2017.2788818.

[317] Simon Eberlein and Krzysztof Rudion. “Small-signal stability modelling, sensitivity analysis and optimization of droop controlled inverters in LV microgrids”. en. In: *International Journal of Electrical Power & Energy Systems* 125 (Feb. 2021), p. 106404. ISSN: 0142-0615. DOI: 10.1016/j.ijepes.2020.106404. (Visited on 08/17/2020).

[318] Simon Eberlein and Krzysztof Rudion. “Influence of PLL on synthetic inertia of DFIG wind turbine in droop controlled microgrids”. en. In: *The Journal of Engineering* 2019.18 (July 2019), pp. 5314–5319. ISSN: 2051-3305. DOI: 10.1049/joe.2018.9316. URL: https://digital-library.theiet.org/content/journals/10.1049/joe.2018.9316 (visited on 08/05/2019).

[319] S. Eberlein and K. Rudion. “Influence of inaccurate low voltage microgrid synchronization on synchronous generators”. In: *2018 IEEE International Energy Conference (ENERGYCON)*. June 2018, pp. 1–6. DOI: 10.1109/ENERGYCON.2018.8398754.

[320] Simon Eberlein and Krzysztof Rudion. “Influence of Inaccurate Medium Voltage Microgrid Synchronization on Synchronous Generators”. en. In: *CIRED Workshop* 0424 (2018), p. 4.

[321] S. Eberlein and K. Rudion. “Investigation of resynchronisation process and its influence on microgrid components”. In: *CIRED Workshop 2016*. June 2016, pp. 1–4. DOI: 10.1049/cp.2016.0719.

[322] S. Liu, P. X. Liu, and X. Wang. “Stability Analysis of Grid-Interfacing Inverter Control in Distribution Systems With Multiple Photovoltaic-Based Distributed Generators”. In: *IEEE Transactions on Industrial Electronics* 63.12 (Dec. 2016), pp. 7339–7348. ISSN: 0278-0046. DOI: 10.1109/TIE.2016.2592864.

[323] M. Pulcherio et al. “Robust Microgrid Clustering in a Distribution System With Inverter-Based DERs”. In: *IEEE Transactions on Industry Applications* 54.5 (Sept. 2018), pp. 5152–5162. ISSN: 0093-9994. DOI: 10.1109/TIA.2018.2853039.

[324] Markus Mirz et al. “DPsim-A dynamic phasor real-time simulator for power systems”. In: *SoftwareX* 10 (July 2019), p. 100253. ISSN: 2352-7110. DOI: 10.1016/j.softx.2019.100253. URL: http://www.sciencedirect.com/science/article/pii/S2352711018302760 (visited on 08/25/2019).

[325] M. Mirz et al. “Dynamic phasors to enable distributed real-time simulation”. In: *2017 6th International Conference on Clean Electrical Power (ICCEP)*. June 2017, pp. 139–144. DOI: 10.1109/ICCEP.2017.8004805.

[326] Markus Mirz, Jan Dinkelbach, and Antonello Monti. “DPsim-Advancements in Power Electronics Modelling Using Shifted Frequency Analysis and in Real-Time Simulation Capability by Parallelization”. en. In: *Energies* 13.15 (July 2020), p. 3879. ISSN: 1996-1073. DOI: 10.3390/en13153879. URL: https://www.mdpi.com/1996-1073/13/15/3879 (visited on 08/01/2020).

[327] Taoufik Qoria et al. “Critical Clearing Time Determination and Enhancement of Grid-Forming Converters Embedding Virtual Impedance as Current Limitation Algorithm”. In: *IEEE Journal of Emerging and Selected Topics in Power Electronics* 8.2 (June 2020). Conference Name: IEEE Journal of Emerging and Selected Topics in Power Electronics, pp. 1050–1061. ISSN: 2168-6785. DOI: 10.1109/JESTPE.2019.2959085.

[328] X. Wu and C. Shen. “Distributed Optimal Control for Stability Enhancement of Microgrids With Multiple Distributed Generators”. In: *IEEE Transactions on Power Systems* 32.5 (Sept. 2017), pp. 4045–4059. ISSN: 0885-8950. DOI: 10.1109/TPWRS.2017.2651412.

[329] Jens Weibezahn and Mario Kendziorski. “Illustrating the Benefits of Openness: A Large-Scale Spatial Economic Dispatch Model Using the Julia Language”. en. In: *Energies* 12.6 (Jan. 2019). Number: 6 Publisher: Multidisciplinary Digital Publishing Institute, p. 1153. DOI: 10.3390/en12061153. URL: https://www.mdpi.com/1996-1073/12/6/1153 (visited on 04/12/2020).

[330] Jeff Bezanson et al. *Julia: A Fresh Approach to Numerical Computing*. en. Nov. 2014. URL: https://arxiv.org/abs/1411.1607v4 (visited on 08/15/2020).

[331] Christopher Rackauckas and Qing Nie. "DifferentialEquations.jl – A Performant and Feature-Rich Ecosystem for Solving Differential Equations in Julia". en. In: *Journal of Open Research Software* 5.1 (May 2017). Number: 1 Publisher: Ubiquity Press, p. 15. ISSN: 2049-9647. DOI: 10.5334/jors.151. URL: http://openresearchsoftware.metajnl.com/articles/10.5334/jors.151/ (visited on 08/15/2020).

[332] Rodrigo Henriquez-Auba et al. "LITS.jl – An Open-Source Julia based Simulation Toolbox for Low-Inertia Power Systems". In: *arXiv:2003.02957 [cs, eess, math]* (Mar. 2020). arXiv: 2003.02957. URL: http://arxiv.org/abs/2003.02957 (visited on 08/14/2020).